

Fundamental Investigations on Interrupted Machining of Challenging Materials with MQL

Zur Erlangung des akademischen Grades eines

Dr.-Ing.

von der Fakultät Maschinenbau

der Technischen Universität Dortmund

genehmigte Dissertation

Youssef Alammari, M.Sc.

aus

Riad (Saudi Arabien)

Tag der mündlichen Prüfung: 07.12.2023

1. Gutachter: Prof. Dr.-Ing. Prof. h.c. Dirk Biermann
2. Gutachter: Univ.-Prof. Dr.-Ing. Hans-Christian Möhring

Dortmund, 2023

Bibliografische Information der Deutschen Nationalbibliothek

Die Deutsche Nationalbibliothek verzeichnet diese Publikation in der Deutschen Nationalbibliografie, detaillierte bibliographische Daten sind im Internet über www.dnb.de abrufbar.

ISBN 978-3-8027-8926-7

Acknowledgement

I thank Allah (الحمد لله) for all the blessings he bestows upon me among which was the ability and strength to undertake and complete this work. I would like to thank my mother Munirah Aldighiri for her unconditional love and support and to remember and honor my late father Hindi Alammari. My heartfelt thanks go to my wife Afrah Alghunaim for her understanding, companionship and love and for our children Badr, Anas and Omar. Without the support of my family, I would have been overwhelmed long before reaching my goals.

This dissertation was written during my time at the Institute of Machining Technology (ISF) in TU Dortmund as a doctoral student. My special appreciation and sincere thanks go to my doctoral supervisor Prof. Dr.-Ing. Prof. h.c. Dirk Biermann for the opportunity, his constant encouragement, personal support, and trust. I have always appreciated the joint discussions and scientific exchange. I would like also to thank Prof. Dr.-Ing Hans-Christian Möhring for being the co-referee for my dissertation and Prof. Dr.-Ing. Dipl.Wirt.Ing. Wolfgang Tillmann for being a member in the examination committee. I also thank apl. Prof. PD Dr.-Ing. Dipl.-Inform. Andreas Zabel for being the chairman of the committee and for his support during my studies at ISF.

I am thankful to Qassim University in Saudi Arabia for their support especially the awarded doctoral scholarship granted through the cultural office of the Royal Embassy of Saudi Arabia in Berlin.

My thanks go to the current and former members of the ISF, especially to the colleagues from the machining department, for the good cooperation and the many discussions. In particular, I would like to thank Dr.-Ing. Ivan Iovkov and Jannis Saelzer as direct group leaders for their valuable support. I also thank Dr.-Ing. Jan Nickel and Sebastian Berger for their support and critical suggestions and reviews. I want to extend my appreciation to my colleagues at ISF: Gero Polus, Nils Felinks, Martin Sicking, Tobias Wolf, Pascal Volke, Milan Bücken, Florian Vogel, Robert Schmidt, Julian Gerken, Timo Rinschede, Gabriel Brock and Erik Krumme. My thanks go also to my current and former office colleagues at ISF: Sebastian Michel, Dr.-Ing. Ekrem Oezkaya and Dr. Jian Weng. Furthermore, I would like to thank Michael Kater for his support in the measurement technology. I extend my appreciation to Tobias Hoffmann, Michael Wedekind, Muhidin Sarajlic, Jörg Eichmann and Martin Gerwert for their technical assistance. Many thanks goes to Nicole Kneppé for her support especially in editing and proofreading. I would like to thank all supervised graduate and undergraduate students: Felipe Barbosa Reis, Ahmed Elkholey, Kayzad Mistry, Jörn Haberland, Philipp Protsch and Georges Morcos. I also appreciate the support provided from Gühring KG through Dr.-Ing. Nicolas Beer and Mr. Tobias Müller related to cutting tools.

Special thanks and appreciations go to my brother Ahmad Alammari for his continuous support, encouragement and joyful doctoral-life discussions. I would like to thank my sister Zainab and hold dear the unforgettable moments of her visit with her husband, Muhammad Alshaya, and her family during Eid al-Fitr 1443AH (May, 2022). I also extend my thanks my sister Layla and my brothers Muhammad and Hasan.

Kurzfassung

Eine nachhaltige Fertigung zielt darauf ab, die Ressourcennutzung zu optimieren und gleichzeitig die Produktivität aufrechtzuerhalten sowie die Gesundheit und die Umwelt zu schützen. Eine Möglichkeit, dies zu erreichen, ist die Reduzierung des Energie- und Kühlschmierstoffverbrauchs bei der Bearbeitung, wodurch jedoch die Produktivität und die Wirtschaftlichkeit eingeschränkt werden können. Um dieser Herausforderung zu begegnen, streben aktuelle technologische Fortschritte danach, neue Ansätze für eine nachhaltige Fertigung zu finden. Ein solcher Ansatz beinhaltet die Untersuchung grundlegender tribologischer Aspekte bei der Spanbildung. Das Ziel ist ein besseres Verständnis des tribologischen Systems bei der Zerspanung zu erlangen, um die Gesamtleistung zu verbessern und damit letztlich die Nachhaltigkeit zu erhöhen. Die Bearbeitung von schwer zerspanbaren Werkstoffen stellt aufgrund der hohen mechanischen und thermischen Belastungen eine zusätzliche Herausforderung dar. Kontinuierliche Bearbeitungsvorgänge, bei denen die Schneide über einen längeren Zeitraum in Kontakt mit dem Werkstück bleibt, schränken die Zugänglichkeit der Schneide ein und verringern die Wirksamkeit von Kühlschmiermedien. Diese Herausforderung wird verstärkt, wenn Techniken wie die Minimalmengenschmierung (MMS) verwendet werden, bei der eine kleine Menge Schmierstoff durch Druckluft zerstäubt wird. Eine vielversprechende Methode zur Verbesserung der MMS-Performance bei der kontinuierlichen Bearbeitung schwer zerspanbarer Materialien stellt die Unterbrechung des kontinuierlichen Werkzeugeingriffs dar, wodurch definierte Kühl- und Schmierzeiten ermöglicht werden. Die Bestimmung des Einflusses von Schnitt- und Unterbrechungszeiten auf die Verringerung des Werkzeug-Span-Kontakts erfordert jedoch weitere Forschung. In dieser Arbeit wird der Einfluss der unterbrochenen Bearbeitung mit MMS auf schwer zerspanbare Werkstoffe, insbesondere eines austenitischen Edelstahl 1.4305 und Nickelbasis-Superlegierung Inconel 718, untersucht. Um die Auswirkungen der Unterbrechung auf die Reduzierung des Werkzeug-Span-Kontakts zu bewerten, werden Orthogonalschnittversuche durchgeführt. Dabei konnte beobachtet werden, dass sich bei einer ausreichenden Unterbrechungszeit der Kontakt zwischen Werkzeug und Span während der initialen Spanbildung (IPCF) signifikant verringert. Neben der Quantifizierung der Adhäsion an der Spanfläche, der Analyse der Spankrümmung und der Untersuchung der mechanischen Belastungen wurde eine thermische Modellierung durchgeführt, um eine Korrelation zwischen dem IPCF-Übergangsschnittweg und der damit verbundenen Übergangstemperatur herzustellen. Es zeigt sich, dass der Übergangsschnittweg und die Temperatur für die beiden Werkstoffe selbst bei unterschiedlichen Bearbeitungsbedingungen innerhalb enger Bereiche liegen. Die Erkenntnisse aus dieser Grundlagenforschung liefern wertvolle Erkenntnisse für die Optimierung und Implementierung gezielter MMS-Anwendungen. Die grundlegenden Untersuchungen werden durch praktische Fallstudien ergänzt, bei denen MMS zum Bohren von Inconel 718 mit verschiedenen Unterbrechungsansätzen eingesetzt wird. Die Fallstudien zielen darauf ab, das Potenzial und die Grenzen zu erforschen, die mit einer unterbrochenen Bearbeitung in einem ansonsten kontinuierlichen Bearbeitungsvorgang verbunden sind. Untersucht wird die Anzahl der Unterbrechungszyklen, die von einem niedrigen Bereich beim Bohren mit Entspannungshüben bis hin zu einem relativ hohen Bereich beim vibrationsunterstützten Bohren (VAD) reicht, für das ein hydraulischer VAD-Aktuator entwickelt und hergestellt wurde. Beim Bohren mit Entspannungshüben konnte eine verbesserte Werkzeugstandzeit beobachtet werden, jedoch wird auch die Abtragsleistung beeinträchtigt. Bei den VAD-Untersuchungen wurden Probleme im Zusammenhang mit vorzeitigen Ausbrüchen der Schneidkante der Schneidkante beobachtet, wodurch potenzielle positive tribologische Effekte übersehen worden sein könnten. Dies ist auf die typischerweise erhöhten mechanischen Belastungen beim VAD zurückzuführen.

Abstract

Sustainable manufacturing aims to optimize resource utilization while maintaining productivity along with protecting the health and the environment. However, reducing energy and metalworking fluid consumption during machining can hinder productivity and lead to economic constraints. Recent technological advances have attempted to address this challenge by proposing new approaches for sustainable manufacturing. One such approach involves the study of fundamental tribological aspects during chip formation. Investigations at the fundamental level have the potential to be applied to various machining operations. The objective is to gain a better understanding of the tribological system during machining in order to improve overall performance and ultimately increase sustainability. Machining difficult-to-cut materials presents additional challenges due to high mechanical and thermal loads. Continuous machining operations, where the cutting edge remains in prolonged contact with the workpiece, limit exposure to the environment and reduce the effectiveness of metalworking fluids. This challenge is compounded when near-dry techniques such as minimum quantity lubrication (MQL) are used, in which a small amount of lubricant is atomized by compressed air. Interrupting machining continuity offers a promising method for improving MQL performance in the continuous machining of difficult-to-cut materials. By briefly interrupting contact between the tool and the workpiece, interrupted machining allows for controlled thermal input through finite cooling and re-lubrication periods. However, determining the influence of cutting and interruption periods on reducing the severity of tool-chip contact requires further research. This study fundamentally investigates the influence of interrupted machining with MQL on difficult-to-cut materials, specifically austenitic stainless steel 1.4305 and nickel-based superalloy Inconel 718. An orthogonal cutting setup is used to evaluate the effect of interruption on tool-chip contact reduction. A significant reduction in chip-tool contact was observed to occur within a finite cutting distance during the initial period of chip formation (IPCF) with a sufficient interruption period. In addition to quantifying adhesion on the rake face, analyzing the chip curl geometry, and investigating the mechanical loads, thermal modeling was employed to establish a correlation between IPCF transition cutting distance and an associated transition temperature. It is found that the transition distance and temperature fall within narrow ranges for the two materials, even under different machining conditions. The findings from this fundamental research provide valuable insights for optimizing and implementing targeted MQL applications. The fundamental investigations are complemented by practical case studies using MQL to drill Inconel 718 with different interruption approaches. The case studies aim to explore the potential and limitations associated with enabling interrupted machining in an otherwise continuous machining operation. The range of interruption cycle frequencies is investigated from a low range using a peck drilling technique to a relatively higher interruption cycle range using vibration-assisted drilling (VAD). The VAD investigations involve the design and construction of a hydraulic actuator. Improved tool life was observed in peck drilling, although the material removal rate is compromised. Challenges associated with premature loss of cutting edge due to increased mechanical load typical of VAD were observed, which might have overlooked potential positive tribological effects.

Table of Content

	Page
Abbreviations.....	VII
Formula symbols.....	XI
Chapter 1: Introduction.....	1
Chapter 2: Background and Literature Review.....	3
2.1 Sustainability in machining.....	3
2.1.1 Sustainability in production systems.....	3
2.1.2 Sustainability issues in machining.....	4
2.1.3 Enhancing sustainability in machining.....	7
2.2 Fundamental chip formation.....	9
2.2.1 Analytical models for predicting the shear angle and cutting forces.....	11
2.3 Tribology in machining.....	14
2.3.1 Friction conditions within tool-chip contact.....	14
2.3.2 Cutting fluids action within tool-chip contact.....	18
2.4 Thermal characteristics of interrupted machining.....	20
2.4.1 The influence of interrupted machining on tool wear.....	20
2.4.2 Models for transient temperature propagation in interrupted machining.....	22
2.5 Vibration assisted machining (VAM).....	24
2.5.1 The orientation of superimposed oscillations in VAM.....	24
2.5.2 Actuation devices used in VAM.....	28
2.5.3 Modelling of VAM.....	31
Chapter 3: Objectives and Methodology.....	37
Chapter 4: Experimental Boundary Conditions.....	39
4.1 Workpiece materials.....	39
4.1.1 Workpiece material: Inconel 718.....	39
4.1.2 Workpiece material: Austenitic stainless steel 1.4305.....	41
4.2 Cutting tool material.....	42
4.3 Machine tools.....	43
4.3.1 Machine tool for orthogonal cutting investigations.....	43
4.3.2 Machine tool for drilling investigations.....	44
4.4 Hydraulic aggregate for vibration assisted drilling.....	45

4.5 Preparation of minimum quantity lubrication (MQL)	46
4.5.1 MQL in orthogonal cutting investigations	46
4.5.2 MQL in drilling investigations	47
4.6 In-situ process variables measurement technology	48
4.6.1 Mechanical load	48
4.6.2 Temperature measurement	50
4.6.3 Displacement measurement	51
4.6.4 High speed video recording	52
4.7 Ex-situ analysis technology	53
Chapter 5: Adhesion on the Rake Face in Interrupted Orthogonal Cutting	55
5.1 Methodology and experimental setup	55
5.1.1 Tools and materials	55
5.1.2 Adhesion area quantification on the rake face using AGLM	56
5.2 Assessment of AGLM for adhesion area quantification on the rake face in continuous orthogonal machining	59
5.2.1 Sensitivity of AGLM to change in primary electron acceleration voltage	62
5.2.2 AGLM in comparison with K-mean Clustering Algorithm	64
5.2.3 AGLM in comparison with EDS elemental mapping	66
5.3 Interrupted Orthogonal Machining of Inconel 718 under MQL	69
5.3.1 Adhesion area quantification	69
5.3.2 Tool-chip contact length	70
5.3.3 Mechanical load	72
5.3.4 Apparent coefficient of friction	74
5.4 Chapter conclusions	76
Chapter 6: Initial Period of Chip Formation	77
6.1 Methodology and experimental setup	77
6.2 Initial period of chip formation (IPCF) and correlated low tool-chip contact	79
6.2.1 Mechanical load in IPCF	79
6.2.2 Contact zone within tool-chip interface in IPCF	80
6.2.3 Lubricant penetration within tool-chip interface	81
6.2.4 Chip contact-side surface condition	82
6.2.5 Chip curl and the identification of a transition criteria	83
6.3 IPCF in interrupted orthogonal cutting	86

6.3.1 Austenitic stainless steel 1.4305.....	86
6.3.2 Inconel 718	89
6.4 Chapter conclusions.....	94
Chapter 7: Thermal Modelling of the Initial Period of Chip Formation	95
7.1 Transient thermal modelling at IPCF	95
7.1.1 Determination of heat flux at tool-chip interface	95
7.2 Results of transient temperature in IPCF – Inconel 718	100
7.2.1 Input parameters	100
7.2.2 Model results validation at steady state.....	101
7.2.3 Determination of heat flux reduction factor within IPCF	102
7.2.4 Heat flux and temperature results.....	103
7.3 Results of transient temperature in IPCF – austenitic stainless steel 1.4305.....	107
7.3.1 Input parameters	107
7.3.2 Model results validation at steady state.....	108
7.3.3 Heat flux and temperature results.....	109
7.4 Chapter conclusions.....	111
Chapter 8: Case Studies on the Influence of Interrupted Machining on Drilling Inconel 718 under MQL.....	113
8.1 Peck drilling Investigations	114
8.1.1 Tool wear and maximum tool life in peck drilling	114
8.1.2 Chip form in peck drilling	116
8.1.3 Borehole roughness in peck drilling.....	119
8.2 Design and development of a hydraulic VAD actuator	120
8.3 VAD investigations	123
8.3.1 VAD experimental setup	123
8.3.2 VAD experimental plan and constraints	124
8.3.3 VAD experimental results	126
8.4 Chapter conclusions.....	132
Chapter 9: Summary and Outlook	133
References.....	137

Abbreviations

Term	Meaning
2D	Two Dimensional
3D	Three Dimensional
AG	Aktiengesellschaft
AGLM	Adhesion Gray Level Masking
AISI	American Iron and Steel Institute
ASTM	American Society for Testing and Materials
BCC	Body Centered Cubic
BCT	Body Centered Tetragonal
BSE	Back Scatter Electron
BUE	Built Up Edge
CCD	Charged Coupled Device
CF	Cutting Fluid
CFRP	Carbon Fiber Reinforced Plastic
CIRP	College International pour la Recherche en Productique
CNC	Computer Numerical Control
COF	Coefficient of Friction
CVD	Chemical Vapor Deposition
DIN	Deutsches Institut für Normung
DLR	Deutsches Zentrum für Luft- und Raumfahrt
ED	Einschaltdauer
EDM	Electrical Discharge Machining
EDS	Energy Dispersive X-ray Spectroscopy
EN	Europäische Norm
FBGA	Field Programmable Gate Array
FCC	Face Centered Cubic
FE	Finite Element
FVM	Focus Variation Microscopy
GUI	Graphical User Interface
HLP	Hydraulic oil class according to standard: DIN 51524-2

HPJAM	High Pressure Jet Assisted Machining
HSK	Hohlschaftkegel
HV	Hardness Vickers or acceleration voltage
IPCF	Initial Period of Chip Formation
ISF	Instituts für Spanende Fertigung
ISO	International Organization for Standardization
KG	Kommanditgesellschaft
LCO ₂	Liquid Carbon Dioxide
LED	Light Emitting Diode
LN ₂	Liquid Nitrogen
MATLAB	Matrix Laboratory
MMS	Minimalmengenschmierung
MQL	Minimum Quantity Lubrication
MRR	Material Removal Rate
MWF	Metal Working Fluid
NbC	Niobium Carbide
NG	Nenngröße
OP	Output
PD	Proportional Derivative
PDE	Partial Deferential Equation
PI	Proportional Integral
PID	Proportional Integral Derivative
PTFE	Polytetrafluoroethylene
PV	Process Variable
PVD	Physical Vapor Deposition
RIO	Reconfigurable Input Output
RPM	Revolution per minute
SAS	Société par Actions Simplifiée
SDD	Silicon Drift Detector
SE	Secondary Electron
SEM	Scanning Electron Microscope
SHPB	Split Hopkinson Pressure Bar
SP	Set Point

TiC	Titanium Carbide
TiN	Titanium Nitride
TiAlN	Titanium Aluminum Nitride
UNS	Unified Numbering System
USB	Universal Serial Bus
VAD	Vibration Assisted Drilling
VAM	Vibration Assisted Machining
VGA	Video Graphics Array
WC	Wolframcarbide
WD	Working Distance
WDS	Wavelength Dispersive Spectrometry
WP	Workpiece

Formula symbols

Large letter symbols

Symbol	Unit	Meaning
A	μm	Vibration amplitude
A_{adh}	mm^2	Adhesion area
A_{p}	mm^2	Pixel size
A_{pp}	μm	Vibration peak-to-peak amplitude
A_{r}	mm^2	Real area of contact
A_{ϕ}	mm^2	Shear plane area
COF	--	Apparent coefficient of friction
COF_{fit}	--	Fit of coefficient of friction
COF_{max}	--	Maximum coefficient of friction
COF_{min}	--	Minimum coefficient of friction
E_{c}	J	Cutting energy
F	N	Resultant force
F_{c}	N	Cutting force
F_{N}	N	Normal force
F_{p}	N	Passive force
F_{t}	N	Tangential force
F_{x}	N	Axial force in x-direction
F_{y}	N	Axial force in y-direction
F_{z}	N	Axial force in z-direction or drilling axial force
F_{γ}	N	Shear force on the rake face
$F_{\gamma\text{n}}$	N	Normal force on the rake face
F_{ϕ}	N	Shear force along shear plane
$F_{\phi\text{n}}$	N	Normal force on the shear plane
HV	kV	SEM acceleration voltage
H_z	mm	Axial uncut chip thickness per cutting edge
$H_{z\text{max}}$	mm	Maximum axial uncut chip thickness per cutting edge
K	m^2/s	Thermal diffusivity
K'_{Λ}		Vibration amplitude ratio with respect to peak-to-peak amplitude
K_{Λ}	--	Vibration amplitude ratio with respect to amplitude
K_{f}	--	Vibration frequency ratio
L	mm	Fluid penetration length
L_{c}	mm	Cutting length
L_{ci}	mm	Individual cutting length
L_{int}	mm	Individual interruption length
MRR	mm^3/s	Material removal rate

M_z	Nm	Torque
N	min^{-1}	Spindle rotational speed
N_{\max}	min^{-1}	Maximum spindle rotational speed
N_z	--	Number of flutes
P	kW	Nominal motor power
P_{\max}	kW	Maximum spindle power
Q	cm^3/rev	Volumetric flow rate
Q_{air}	Nl/min	Air flow rate
Q_{oil}	ml/h	Oil flow rate
R	N	Resultant force on shear plane
R'	N	Resultant force on the rake face
R_2	--	Secondary shear zone heat flux partition ratio
R_a	μm	A roughness value
R_c	mm	Distance from initial curl center
R_z	μm	A roughness value
S_m	--	Standard deviation multiplier
T	$^{\circ}\text{C}$	Temperature
T_{∞}	$^{\circ}\text{C}$	Ambient temperature
T_f	$^{\circ}\text{C}$	Flank temperature
T_{fl}	$^{\circ}\text{C}$	Oil flashing point
T_{room}	$^{\circ}\text{C}$	Room temperature
\bar{T}_{tr}	$^{\circ}\text{C}$	Mean transition temperature
W	J	Work per cutting interval
WB	μm	Flank wear
WD	mm	SEM working distance
Z	mm	Axial position
Z_0	mm	Initial axial position
Z_{surface}	mm	Surface altitude

Small letter symbols

Symbol	Unit	Meaning
a_c	--	Fluid penetration length fraction
a_e	mm	Radial depth of cut in milling
a_{\max}	m/s^2	Maximum acceleration
a_p	mm	Axial depth of cut in milling
a_s	mm	Constant defining logarithmic spiral
b	mm	Chip width
b_s	--	A constant defining logarithmic spiral
c	J/kgK	Specific Heat
c_L	mm	Initial chip curl arc length
c_r	mm	Initial chip curl radius

d	mm	Drilling tool diameter
d_{fo}	μm	Pyrometer fiber optic diameter
f	mm	Feed
f_{frr}	Hz	Recording frame rate
f_{int}	Hz	Interruption frequency
f_N	Hz	Rotation frequency
f_n	Hz	Natural frequency
f_{os}	Hz	Vibration frequency
f_s	Hz	Sampling frequency
f_z	mm	Feed per tooth
g	--	Gray level
g_c	--	highest adhesion gray level value
g_s	--	Lowest adhesion gray level value
h	mm	Uncut chip thickness
h_c	mm	Chip thickness
h_{conv}	W/m^2	Heat convection coefficient
h_{max}	mm	maximum uncut chip thickness
h_z	mm	Uncut chip thickness per cutting edge
i	--	Interval number
k	W/mK	Thermal conductivity
k_c	$\text{kN}/\mu\text{m}$	Dynamometer stiffness
k_f	--	COF evolution rate
l	mm	Drilling depth
l_c	mm	Tool-chip contact length
l_{cs}	mm	Measured sticking length
l_l	μm	Cut-off length
l_f	mm	Drilling length or tool life
l_p	mm	Pecking distance
l_r	mm	Relative retraction distance
l_{ref}	mm	Relative depth
l_{st}	mm	Calculated sticking zone length
l_T	mm	Drilling length with temperature measurement
n	--	Number of interruption intervals
n_{adh}	--	Number of adhesion pixels
n_c	--	Number of cutting intervals
n_p	--	Number of adhesion pixels
p	MPa	Normal pressure
p_0	MPa	Maximum pressure
p_{air}	bar	Air pressure
p_{max}	bar	Maximum pressure
p_{oil}	bar	MQL oil pressure

\dot{q}	W/m ²	Heat flux
\dot{q}_{IPCF}	W/m ²	Transient heat flux in initial period of chip formation
\dot{q}_{tool}	W/m ²	Tool heat flux
r	mm	Radial position
r_c	--	Chip thickness ratio
r_s	mm	Distance from spiral center
r_β	μm	Cutting edge radius
s	mm	Distance
s_0	mm	Transition distance
\bar{s}_0	mm	Mean transition distance
s_c	mm	Distance along chip curvature
s_i	--	Start distance of cutting interval
s_{os}	μm	Sinusoidal displacement
s_p	mm	Probe line distance
t	s	Time
t_{cut}	s	Cutting period between interruptions
t_d	s	Dwell time
t_{int}	s	Interruption time
t_v	mm	Deformation affected zone depth
v	m/s	Velocity
v_c	m/min	Cutting speed
v_{ch}	m/s	Chip velocity
v_{ch0}	m/s	Average chip velocity
v_f	m/min	Feed velocity
v_{fx}	mm/min	Maximum traverse velocity in x-direction
v_{fy}	mm/min	Maximum traverse velocity in y-direction
v_{fz}	mm/min	Maximum traverse velocity in z-direction
v_{max}	m/min	Maximum velocity
x	mm	Length in x-direction, distance from cutting edge or x- Cartesian coordinate
x_c	mm	x- Cartesian coordinates of initial chip curl center
x_{max}	mm	Maximum traverse in x-direction
y	mm	Length in y-direction or y- Cartesian coordinate
y_c	mm	y- Cartesian coordinates of initial chip curl center
y_{max}	mm	Maximum traverse in y-direction
z	mm	Length in z-direction
z_{max}	mm	Maximum traverse in z-direction

Greek symbols

Symbol	Unit	Meaning
μ	--	Sliding Coefficient of friction

α	m^2/s	Thermal diffusivity
α_o	$^\circ$	Flank face angle
β	--	A parameter between 0 and 1
β_{COF}	--	Coefficient of friction reduction factor
β_r	--	Ratio of shear stress at the rake face to the yield stress of the chip
γ_o	$^\circ$	Rake face angle
δ	μm	Displacement
ζ	--	Rake face stress distribution exponent
η	mm^2/s	Viscosity
θ	$^\circ$	Angular position
θ_0	$^\circ$	Initial angular position
λ	μm	Wavelength
λ_1	μm	Pyrometer wavelength 1
λ_2	μm	Pyrometer wavelength 2
λ_c	mm	Cut-off wavelength
λ_f	$^\circ$	Friction angle
$\lambda_{f'}^{\prime}$	$^\circ$	Apparent friction angle
λ_o	$^\circ$	Inclination angle in oblique cutting
μ	--	Sliding coefficient of friction
μ_g	--	Adhesion gray level mean
ρ	kg/m^3	Density
σ	MPa	Normal stress
σ_{D}	MPa	Compressive yield stress
σ_s	--	Standard deviation
σ_{T}	$^\circ$	Drilling tool point angle
τ	MPa	Shear stress
τ_1	MPa	Material's shear flow stress
τ_{aB}	MPa	Asperities shear strength
τ_{aB}	MPa	Shear strength of the material
τ_{F}	MPa	Shear yield stress
τ_{ϕ}	MPa	Shear stress on shear plane
ϕ	$^\circ$	Shear angle
ϕ_1	$^\circ$	Slip angle
ϕ_v	$^\circ$	Phase angle between spindle rotation and superimposed vibration
χ	--	Multiples of h defining length of contact on rake face
ω	rad/s	Vibration frequency
ω_c	--	Chip velocity distribution exponent

Chapter 1: Introduction

Sustainable manufacturing entails the optimal utilization of resources while maintaining high productivity levels. Various methods and practices have been explored to enhance overall sustainability in production. Key concerns are about protecting the environment, as well as the health and safety of workers and consumers. In machining, reducing energy and metalworking fluid (MWF) consumption are crucial aspects. However, sometimes, these practices can lead to a decrease in productivity, creating economic constraints in their implementation. Balancing the economic and ecological aspects of sustainability has always posed a challenge. In response, recent technological advancements have been proposed and investigated, seeking to redefine established practices and introduce new approaches and solutions with sustainability as a primary objective. One such effort involves fundamental investigations into chip formation in machining, which holds the potential to be extended to various machining operations. The aim is to gain a better understanding of the process and facilitate more resource-efficient production while preserving economic viability.

Sustainable machining encounters additional challenges when working with difficult-to-cut materials, primarily due to the significant mechanical and thermal loads involved. In continuous machining operations, the cutting edge remains in contact with the workpiece for extended periods, limiting its exposure to the environment and reducing the effectiveness of metal working fluids, especially near the cutting edge where they are most needed. This challenge is further intensified when utilizing near-dry techniques such as minimum quantity lubrication (MQL), given its poor inherent thermal properties. MQL involves the atomization and delivery of a small amount of cutting oil through compressed air, which has a lower heat capacity compared to the liquids used in flood cooling methods. As a result, the demand for enhanced lubricating and cooling capabilities of MQL becomes even more critical when dealing with difficult-to-cut materials.

To enable MQL and further enhance its performance in continuous machining operations for difficult-to-cut materials, one promising method is interrupting machining continuity. During interrupted machining, when the tool momentarily breaks contact with the workpiece, there is an opportunity to effectively control the thermal input to the machining system by allowing finite periods of cooling and re-lubrication. Also, interruptions facilitate the production of smaller chips that improves chip evacuation. The determination of optimal cutting and interruption periods remains a subject that requires further research.

In this work, two difficult-to-cut materials are investigated: austenitic stainless steel 1.4305 and nickel-based superalloy Inconel 718, with more focus on the latter. The investigation utilizes an orthogonal cutting setup to evaluate the influence of interrupted machining with MQL on the adhesions occurring on the uncoated tool's rake face. During the investigation, the interruption length is varied to understand its effect on the occurrence of reduced tool-chip contact. Subsequent to the cutting interruption, a distinct finite cutting length ending at the end of the initial period of chip formation (IPCF) shows a significant reduction in chip-tool contact. This finding holds valuable insights into optimizing MQL applications for enhanced machining performance. Reduced tool-chip contact leads to a decrease in the work done during machining, subsequently benefiting overall energy consumption.

Further investigations related to the thermal behavior in interrupted machining are carried out, taking into consideration the effect of IPCF. The transient temperature increase that takes place at the beginning of cutting is modeled using a hybrid analytical and finite element approach. The analytical

method, with experimentally obtained input parameters, allows the determination and distribution of input heat flux along the flank face to be precisely considered, while its magnitude during both interruption and cutting intervals is taken into account. A 2D section of the tool's temperature field is obtained by numerically solving the partial differential heat equation of individual finite elements. As a result, critical transition temperatures corresponding to finite cutting distances during IPCF are determined.

In addition to investigating the impact of interrupted machining with MQL fundamentally, this dissertation takes a practical approach by exploring its application in drilling Inconel 718. Through case studies, the research aims to uncover potential challenges and facilitate the translation of fundamental findings into practical implementation. To assess the influence of interrupted drilling, the interruption cycle frequency is systematically varied using diverse drilling techniques. These techniques include peck drilling, operating within a low-frequency cycle range, and relatively higher cycle frequency through vibration-assisted drilling (VAD). For the VAD investigation, a custom-built hydraulic actuator is employed, enabling control over vibration amplitude and frequency, thus covering an extended range of parameter variations.

By combining minimal consumption of MWF, and the use of uncoated tools, sustainability can directly be influenced. These promising attributes serve as strong motivation for conducting fundamental research focused on machining tribology to enhance the performance of sustainable methods such as near-dry machining. Interrupted machining can be a viable and sustainable solution for machining difficult-to-cut materials. This dissertation discusses fundamental aspects related to the feasibility of enhancing the performance of MQL using interrupted machining for difficult-to-cut materials.

Chapter 2: Background and Literature Review

The literature review starts with a brief overview of sustainability in machining. Next, fundamental chip formation modelling is introduced including description of well-known theories related to tool-chip interface tribology system in orthogonal machining. The research related to the effect of interrupted machining on machinability and machining tribological system are introduced and reviewed. The chapter concludes by an overview of vibration assisted machining and state-of-the-art vibration assisted drilling actuators.

2.1 Sustainability in machining

This section is an overview of the sustainability concept in machining. It starts by introducing the general definition of sustainability in production systems followed by introducing the main aspects of sustainability issues related to machining. Moreover, sustainability-relevant solutions in machining research literature are presented. This section provides a context for the current work within machining research.

2.1.1 Sustainability in production systems

Awareness about minimizing the negative impact on the environment, preserving resources, and protecting the health and well-being of workers and consumers has been gaining more attention and research in the last few decades (Jayal et al., 2010). Applying sustainable manufacturing techniques that uphold the aforementioned principles while maintaining high quality and productivity goals has become a priority in the manufacturing sector. As shown in Figure 2.1, the environment, economy, and society are the main three sustainability groups that are reciprocally affected by the production process. Interactions within the sustainability system are dynamic. Energy consumption and the use of metalworking fluids (MWF) are considered major sources of sustainability issues in machining.

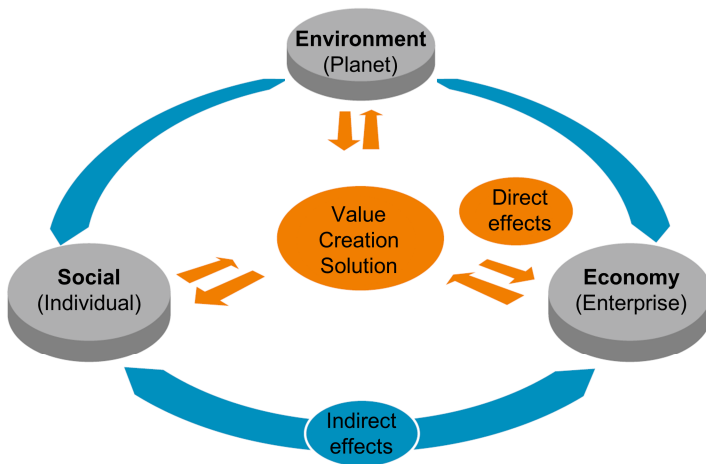


Figure 2.1 Sustainability Dynamic model; (Stark and Lindow, 2017)

It is estimated that the industry sector consumed 50% of the global energy demand in 2018, with the potential to increase by over 30% within 30 years. Within the industry sector, the manufacturing sector is the largest energy consumer, accounting for more than 80% of the sector's energy consumption (U.S. Energy Information Administration, 2019). Machining processes, such as milling, turning, grinding, etc., are significant manufacturing techniques in terms of energy consumption (Dambhare et al., 2015).

In general, power production, which is essential for modern manufacturing processes, is responsible for approximately 24% of CO₂ emissions. These emissions are major contributors to the increase in greenhouse gas concentration in the atmosphere, resulting in global warming and negative environmental changes (Finnveden et al., 2009). Energy consumption is one significant contributor to environmental impact, but materials production and waste in various forms (gas, liquid, and solid) also play a role. Ensuring the health and well-being of workers and consumers is an integral part of sustainability, in addition to environmental protection. Furthermore, economic concerns for producers and consumers are at the forefront of sustainability considerations. The following sections will address machining-specific concerns related to sustainability.

2.1.2 Sustainability issues in machining

Machining is considered to have the highest energy utilization and waste production in the manufacturing industry (Dambhare et al., 2015). Energy is consumed in machining, either directly or indirectly, during the production of cutting tools, preparation of workpiece materials, tool changing, machine tool operations, and the cutting process itself (Mativenga and Rajemi, 2011). Figure 2.2 provides a brief summary of the energy and material flow in machining.

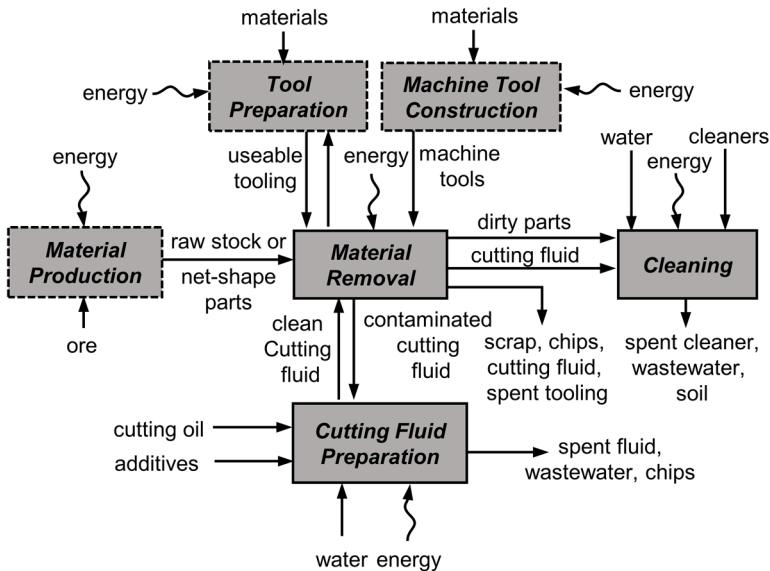


Figure 2.2 Energy and material flow chart for machining sustainably; adapted from (Dahmus et al. 2004)

For cutting tools, materials such as tungsten carbide require the application of manufacturing techniques with intensive energy demands, such as sintering (Goldwitz, 2002). Coating techniques, such as physical vapor deposition (PVD) or chemical vapor deposition (CVD), are commonly used for producing high-quality cutting tools. These coating techniques are estimated to consume 1 to 2 MJ per cutting tool (Goldwitz, 2002).

On the other hand, workpiece manufacturing consumes a large amount of energy relative to the machining process. High-demand workpiece materials such as steel and aluminum require a significant amount of energy for production. Steel, for example, requires up to 31 MJ/kg, while aluminum consumes about 219 MJ/kg (Chapman and Roberts, 1983).

The tool changing process also contributes to energy consumption in machining. The energy consumption of the machine tool drive system may vary from one cycle to another depending on the specific machining process being performed. A significant percentage of the total energy usage in machining is attributed to tool changing (Pusavec et al., 2010b). In addition to the actual cutting operations, other operations require additional energy consumption (Camposeco-Negrete, 2013). Examples of non-cutting operations used in auxiliary systems include cooling, filtration, and hydraulic systems, which utilize pumps and fans to circulate machine tool fluids. The startup of motors and the quick motion of the drives also contribute to higher energy consumption (Rajemi et al., 2009).

In comparison to the energy consumption of non-cutting operations, cutting energy may account for less than 15% of the total energy utilization in mass production factories (Zhao et al., 2017). However, in small-scale applications, this percentage increases to around 66%. Figure 2.3 compares the energy consumption breakdown between mass production systems and small-scale applications.

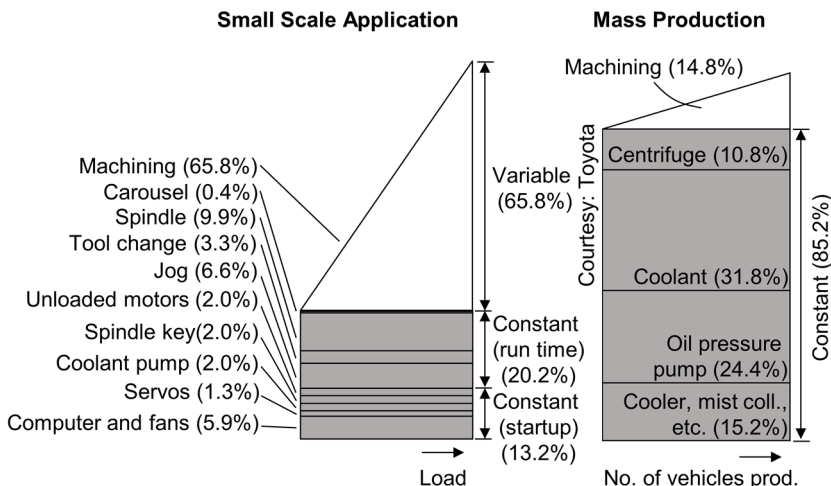


Figure 2.3 Energy use breakdown in machining, (Left) In small scale machining application; (Kordonowy, 2002), (Right) In mass production machining; (Gutowski et al. 2005/Toyota)

The energy spent on the actual cutting process depends on various factors. Factors such as workpiece material, cutting fluids, tool quality and geometry, and cutting parameters have a significant

influence on energy consumption. For example, the specific cutting energy for steels ranges between 2.7 J/m³ and 9.3 J/m³, while for aluminum alloys it ranges between 0.4 J/m³ and 1.1 J/m³ (Zhao et al., 2017). The required quality of the machined products also contributes to determining the cutting energy required (Hanafi et al., 2012). Furthermore, energy conversion in machine tools is not fully utilized, resulting in inevitable energy losses in the form of heat and noise.

In addition to energy consumption, the use of metalworking fluids (MWF) is another major concern for machining sustainability, particularly in relation to the environment and society. MWFs are used in machining for cooling, lubricating, and evacuating generated chips. Conventionally, emulsions or straight oils are used as MWFs during the cutting process. On one hand, depending on the requirements of the machining task, emulsions can provide better heat transfer due to the excellent heat capacity of water, making them suitable for high cutting speed applications. On the other hand, straight oils provide a better lubrication effect for low cutting speed applications (Weinert, 2004).

In general, metalworking fluids (MWF) have an impact on health and are considered a critical health risk for workers (Schultheiss et al., 2013). MWFs contain non-biodegradable and toxic mineral oil, which is refined from crude oil, typically in varying concentrations (Pervaiz et al., 2018). Roughly, two liters of crude oil are required to extract around 160 L of MWF oil, and the byproducts of this process are emitted into the environment (Pusavec et al., 2010a). Degradation of MWFs due to mist, vapor, or bacterial growth can cause health issues related to the skin and/or respiratory system (Ghani et al., 2014). Inappropriate disposal of MWFs poses a high potential risk for soil and water contamination. MWFs also contain additives that have an impact on health and the environment. For example, the phased-out additive 1,1,1-Trichloroethane (TCA) is associated with high levels of ozone layer depletion (Dahmus and Gutowski, 2004). Water-soluble MWFs are susceptible to the growth of microorganisms, which can lead to a change in pH value and cause corrosion problems for the machine tool (Ghosh and Rao, 2015). Chemical additives and pesticides are used to control the growth of microorganisms, which in turn have environmental and health impacts (Shokrani et al., 2012). Approximately 80% of operators' infections are due to MWFs, caused by direct skin contact during their work (Debnath et al., 2014).

MWF consumption varies depending on the application technique. Flood cooling, on one hand, is known to consume a large amount of MWF compared to minimum quantity lubrication (MQL). While MWF in flood cooling is typically water-based and circulated, the estimated waste is relatively high, ranging from 10% to 30% annually due to vaporization or being wasted with evacuated chips (Dahmus et al., 2004). The proper disposal of cutting fluids is a highly controlled and expensive process, which can cost as much as the replacement fluid itself, adding a substantial amount to the overall cost of MWF.

While MWF is necessary in many machining applications to meet production demands, its impact on sustainability can be significant. As a result, many researchers are investigating solutions to reduce its negative impacts while maintaining product quality and productivity. The flood technique is the conventional method for supplying MWF in machining. However, the associated energy consumption of auxiliary equipment and disposal costs are quite significant. Other methods, such as minimum quantity lubrication (MQL), cryogenic machining, high-pressure jet-assisted machining (HPJAM), and the use of solid lubricants, to name a few, are being developed and researched as alternatives to the flood cooling strategy.

2.1.3 Enhancing sustainability in machining

Dry machining is considered to be the optimal solution for eliminating MWF and the associated sustainability issues in machining (Devillez et al., 2011). Cast iron, particularly gray cast iron, is well-suited for dry machining due to the characteristics of short chips, low cutting forces, low cutting temperature, and the lubricating effect of included graphite (Klocke and Eisenbläter, 1997). However, dry machining may not be technically feasible or economically viable for many machining applications and materials. This is due to excessive heat generation caused by chip formation and the friction between the tool and workpiece. Concerns such as accelerated tool wear, premature tool failure, poor productivity, and poor product quality are significant challenges in dry machining. Additionally, the formation of metallic dust is another issue associated with dry machining (Siniawski and Bowman, 2009). Therefore, near-dry lubrication/cooling strategies have gained more consideration in recent decades.

In minimum quantity lubrication (MQL), a small amount of lubricant oil is pneumatically atomized and supplied to the cutting region, with oil droplets typically ranging from 15 to 40 μm in diameter (Masoudi et al., 2017). MQL utilizes a minute amount of MWF, typically at a flow rate of 10–50 ml/h, which is orders of magnitude lower than the amount used in flood cooling techniques (Weinert et al., 2004). The air pressure used in MQL ranges from 2 to 23 bars (Rahim and Sasahara, 2011). External air compressors are utilized with MQL, which are the main concern for environmental impact due to their energy consumption (Fernando et al., 2021). It is estimated that the CO_2 emissions when turning 1 kg of AISI 1040 are comparable to conventional flood strategies in terms of power consumption (Campatelli, 2014). However, the cleaning and handling of scraps in MQL are almost comparable to dry machining, which significantly alleviates the environmental impact. Table 2.1 provides a comparison and summary of conventional and state-of-the-art cooling and lubrication methods and their effectiveness.

Table 2.1 Effectiveness and application of various cooling and lubrication strategies; (Jawahir et al. 2016)

Effect of the cooling and lubrication strategy		Flood <i>Emulsion/oil</i>	Dry <i>comp. air</i>	MQL <i>oil</i>	Cryogenic <i>LN₂</i>	Hybrid <i>LN₂+MQL</i>
Primary	<i>Cooling</i>	Good	Poor	Marginal	Excellent	Excellent
	<i>Lubrication</i>	Excellent	Poor	Excellent	Marginal	Excellent
	<i>Chip removal</i>	Good	Good	Marginal	Good	Good
Secondary	<i>Machine cooling</i>	Good	Poor	Poor	Marginal	Marginal
	<i>Workpiece cooling</i>	Good	Poor	Poor	Good	Good
	<i>Dust/Particle Control</i>	Good	Poor	Marginal	Good	Good
	<i>Production Quality (Surface Integrity)</i>	Good	Poor	Marginal	Marginal	Excellent
Sustainability Concern		<i>Water pollution, microbial infestation, and high cost</i>	<i>Poor surface integrity due to thermal damage</i>	<i>Harmful oil vapor</i>	<i>Initial cost</i>	<i>Initial cost, oil vapor</i>

Cryogenic lubrication, mainly using liquefied nitrogen (LN₂) or liquid carbon dioxide (LCO₂) (Jawahir et al., 2016), is another option for avoiding the flood cooling strategy. Cryogenic methods can achieve low temperatures below -153 °C (120K) (Jawahir et al., 2016). Cryogenic cooling is employed to lower the temperature of the tool and workpiece (Shokrani et al., 2012). In the case of LN₂, fractional distillation of liquefied air is used as a production method. Air is compressed using compressors to achieve high pressure, then cooled to ambient temperature, and finally allowed to expand to low pressure. During the expansion process, oxygen, nitrogen, and argon can be separated (Castle, 2007; Timmerhaus, 2007). Generating LN₂ consumes a considerable amount of energy and utility resources (Pusavec et al., 2010a). However, it has been reported by Aggarwal et al. (2007) that energy consumption using cryogenic lubrication during machining is more economical compared to flood cooling, which justifies its use.

Other cooling and lubrication techniques being researched include high-pressure jet-assisted machining (HPJAM), the use of solid lubricants, and modified cutting tools. In HPJAM, MWF is supplied to the cutting zones at high pressures, reaching several hundreds of bars (Wertheim, 1992). The extreme pressure is investigated to penetrate within the contact zones for machining difficult-to-cut materials (Ezugwu et al., 2005; Zareena et al., 2005; Mia and Dhar, 2015). Achieving high pressure requires a significant amount of energy through the use of pumps. However, the relatively low consumption of MWF and the reduced machining power achieved by minimizing the tool-chip contact may offset the high energy use of high-pressure pumps (Pusavec et al., 2010b).

Solid lubricants, such as molybdenum disulphide (MoS₂), graphite, and occasionally other solid lubricants like calcium fluoride, cerium fluoride, boron nitride, and tungsten disulphides, are used as alternatives to the flood cooling strategy (Lawal et al., 2013). These solid lubricants typically have an average particle size of 1 to 10 µm (Pusavec et al., 2020) and provide lubrication due to their lamellar structure (Lawal et al., 2013). Particularly in high contact pressure and temperature within cutting zones, where conventional lubricants reach their limit or flashing point, solid lubricants can offer enhanced performance (Sterle et al., 2018). Solid lubricants are supplied to the cutting zones in various ways, such as mixing with compressed air (Rao et al., 2008), electrostatic induction (Reddy et al., 2015), suspension in MQL oil (Moura et al., 2015), or more recently, mixing with liquid carbon dioxide (LCO₂) (Pusavec et al., 2020). Solid lubricants demonstrate promising machining performance, especially in terms of avoiding the flood cooling strategy and enhancing near-dry lubrication techniques like MQL. However, investigations regarding their sustainability, particularly in relation to potential prolonged exposure health hazards, are still being researched.

Other researchers have explored alternative approaches aimed at increasing tool life through cutting process parameter optimization, improving tool utilization, or enhancing tool design, which are appealing topics for many researchers. In many cases, these approaches have a direct effect on sustainability. Optimizing cutting process parameters, specifically cutting speed, feed, and depth, using modern optimization methods has been shown to be effective for sustainability. (Hanafi et al., 2012) applied gray relational theory and Taguchi optimization methods to minimize surface roughness and cutting power.

Improving cutting tool utilization by distributing the tool wear across multiple regions of cutting inserts has shown a significant increase in tool life. (Schultheiss et al., 2013) investigated cutting tool utilization in secondary machining operations in turning and milling. They explored methods such as facing followed by longitudinal turning and turning in opposite feed directions, resulting in wear on two sides of the insert nose. They reported approximately a 15% reduction in cycle time and 12% less energy consumption. The concept of distributing wear across different regions of the tool was also investigated using circular rotary inserts by (Armagero, 1994a and 1994b). (Lei and

Liu, 2002) reported a significant increase in tool life, more than 60 times, using rotary inserts. However, the design of complex tool holders remains an issue for this approach.

Cutting inserts modified with holes in the rake face and flank face through electrical discharge machining (EDM) were investigated by (Dhananchezian and Kumar, 2011). Cryogenic LN₂ was supplied at 3 bars through the holes and compared with the flood cooling strategy. In the turning of Ti6Al4V, external supply of flood coolant using a 5% emulsion was used. The modified inserts showed a reduction of up to 39% in tool flank wear and 35% in surface roughness. However, a critical assessment of this approach is still required to evaluate the necessary pressure to overcome high tool-chip contact stresses.

Modifying cutting tools through flank face retraction has been shown to improve tool life in turning inserts by up to 70% (Denkena et al., 2017). (Beer et al., 2014) reported a 50% increase in tool life for solid carbide twist drilling tools using the flank face retraction strategy. In this approach, the flank face of the drilling tool was modified by grinding a retraction channel behind the cutting edge to enhance cutting fluid flow near the cutting zones. (Bücker et al., 2020) optimized the design of rake face retraction in twist drilling tools for improved performance and tool life when drilling Inconel 718.

Structured and textured cutting tools utilize the concept of artificially created surfaces to enhance the tribological performance between parts in contact (Özel et al., 2021). In machining, this approach aims to reduce friction, resulting in lower heat generation and subsequently lower temperatures. These key factors contribute to improved tool wear resistance and reduced cutting forces. The effectiveness of lubrication is enhanced by retaining lubricant or debris in the generated channels, promoting a lubricant film at the tool-chip and tool-workpiece interfaces (Özel et al., 2021).

The choice of the best solution among the aforementioned options can be a challenging task. However, continuous sustainability-oriented developments and research in various aspects of machining can lead to overall improvement in sustainability. Fundamental research on chip formation, focusing on the tribological phenomena within the tool-chip and tool-workpiece interfaces, can contribute to understanding the main effects and requirements needed for better resource utilization. This understanding can ultimately lead to the production of high-quality products with enhanced economic performance, as well as improved health and environmental protection. The next section introduces and discusses the fundamental principles of chip formation.

2.2 Fundamental chip formation

During the cutting process, the tool wedge penetrates into the workpiece and creates a chip through cutting and forming processes. The chip formation process is commonly represented in the orthogonal plane according to DIN 6581. The nomenclature of the orthogonal section is shown in Figure 2.4. The tool has a rake face denoted as A_r and a flank face denoted as A_{α} , which are joined at the cutting edge denoted as S . The rake face angle, γ_0 , is inclined to the vertical line either in a positive or negative orientation. The flank face angle, sometimes referred to as the clearance angle, α_0 , is the angle between the machined surface and the tool. The cutting speed, v_c , represents the scalar rate of relative motion between the tool and the workpiece. The uncut chip thickness is denoted as h , and the chip thickness is denoted as h_c . Shearing occurs in two zones: the primary shear zone, which is at an average angle to the cutting direction known as the shear angle, ϕ , and the secondary shear zones, located between the rake face of the tool and the chip, the flank face and workpiece, and around the cutting edge. The chip curls away from the rake face at a distance known as the contact length, l_c , with an average speed of v_{ch0} .

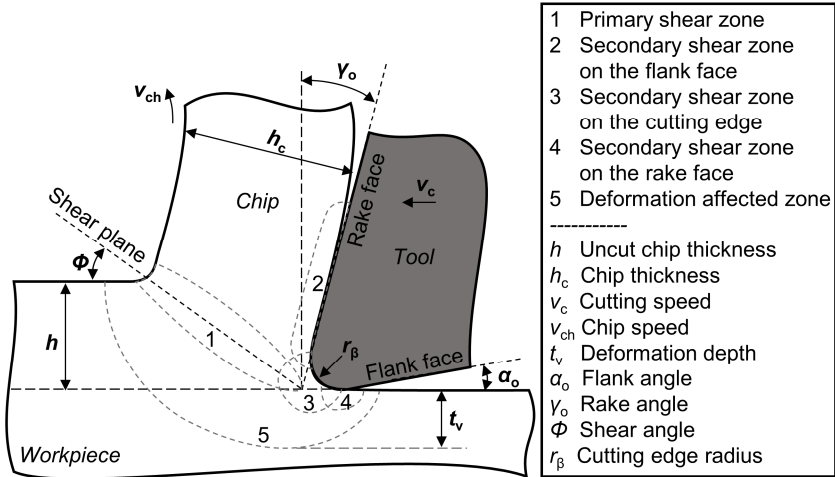


Figure 2.4 Chip formation in orthogonal plane representation; adapted from (Warnecke 1974)

An early representation of chip formation was known as the card model (Piispanen, 1948). The card model, as shown in Figure 2.5 (left), simply represents the shearing process that occurs during chip formation. It depicts a deck of cards inclined at an angle equal to the shear angle, moving relative to each other in a process called the lamellar slip structure as the tool advances towards them. The cards eventually slide relative to each other and accumulate, rising up on the rake face. This model, despite its simplicity, represents many physical actions occurring during chip formation, as the thickness of the cards can be related to the spacing of structural defects in workpiece materials (Shaw, 1950). However, it is important to note that the formation of the lamellar structure is only applicable under specific conditions. Additionally, the card model assumes that shear occurs in a thin plane, while in reality, it occurs within a finite width.

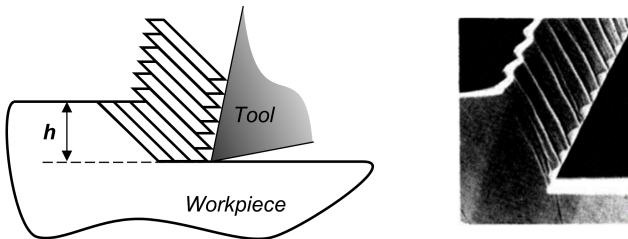


Figure 2.5 (Left) Card model schematic - adapted from (Piispanen, 1948), (Right) Chip formation of single crystal β -brass under SEM showing lamellar slip structure; (Ueda and Iwata, 1980)

Machining operations are classified into two main categories: orthogonal or oblique (Merchant, 1944), as shown in Figure 2.6. In orthogonal machining, the orientation of the cutting edge is perpendicular to the direction of cutting velocity. Therefore, two-dimensional analysis is straightforward. In oblique machining, there is an angle between the cutting edge and the cutting

velocity vector, known as the inclination angle λ_o , which results in an additional force component. According to (Usui et al., 1978a), chip formation in oblique cutting can be interpreted as a piling up of orthogonal cuttings along the cutting edge, using the minimum energy approach. The energy method is applicable to single-edge cutting operations and other operations such as plain milling, as long as the inclination angle is not too large (Usui et al., 1978a). Thus, orthogonal analysis in chip formation is significant and useful for fundamental chip formation analysis.

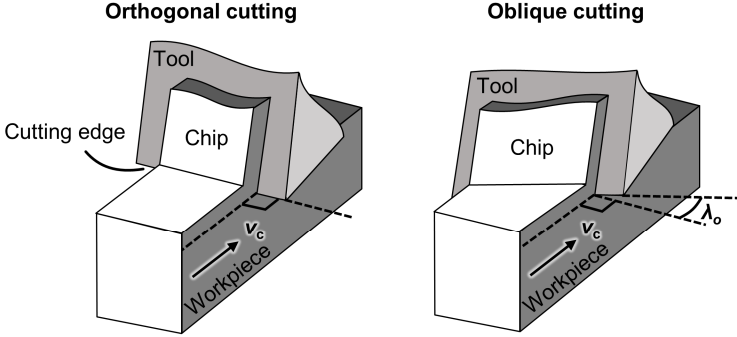


Figure 2.6 Orthogonal and oblique cutting; adapted from (Klocke et al., 2008)

2.2.1 Analytical models for predicting the shear angle and cutting forces

It is possible to measure cutting forces in orthogonal cutting using dynamometers, which are available in various types and sizes. Typically, the dynamometer is attached to either the tool holder or the workpiece. Orthogonal cutting can be achieved using different workpiece configurations, such as pipes or disks in turning machines, thin cuboids in broaching machines, or custom-built machines specifically designed for orthogonal cutting research. In orthogonal cutting, the force component parallel to the cutting velocity vector is known as the cutting force (F_c), while the force perpendicular to it is called the passive force (F_p). By vectorially adding these forces, the resultant force (R) can be calculated. Merchant (1944) studied the relationships between the resultant force and other perpendicular force combinations and represented them using the so-called Merchant circle, as shown in Figure 2.7. By applying the principle of minimum energy, the shear angle (ϕ) can be calculated. Various geometric relationships can be derived from Merchant's circles, leading to the following relationships:

$$\tau_\phi = \frac{|\vec{F}_\phi|}{A_\phi} = \frac{|\vec{R}| \cos(\phi + \lambda_f - \gamma_o)}{A_\phi} \quad (2.1)$$

$$|\vec{R}| = \frac{\tau_\phi}{\sin \phi \cos(\phi + \lambda_f - \gamma_o)} \cdot b \cdot h \quad (2.2)$$

$$|\vec{F}_c| = |\vec{R}| \cdot \cos(\lambda_f - \gamma_o) \quad (2.3)$$

$$|\vec{F}_p| = |\vec{R}| \cdot \sin(\lambda_f - \gamma_o) \quad (2.4)$$

where τ_ϕ is the shear stress on the shear plane, A_ϕ is the shear plane area, λ_f is the friction angle on the rake face and b is the chip width. Substituting 2.2 in 2.3 and 2.4 results:

$$|\vec{F}_c| = \frac{\cos(\lambda_f - \gamma_o) \cdot \tau_\phi}{\sin \phi \cos(\phi + \lambda_f - \gamma_o)} \cdot b \cdot h \quad (2.5)$$

$$|\vec{F}_p| = \frac{\sin(\lambda_f - \gamma_o) \cdot \tau_\phi}{\sin \phi \cos(\phi + \lambda_f - \gamma_o)} \cdot b \cdot h \quad (2.6)$$

Applying minimum energy principle:

$$\frac{\partial E_c}{\partial \phi} = 0 \quad (2.7)$$

Since the cutting energy, E_c , is calculated as the product of cutting force F_c and cutting distance L_c , and the cutting distance is not a function of the shear angle, it can be simplified as follows:

$$\frac{L_c \cdot \partial |\vec{F}_c|}{\partial \phi} = 0 \quad (2.8)$$

The shear angle becomes:

$$\phi = \frac{\pi}{4} - \frac{1}{2} \cdot (\lambda_f - \gamma_o) \quad (2.9)$$

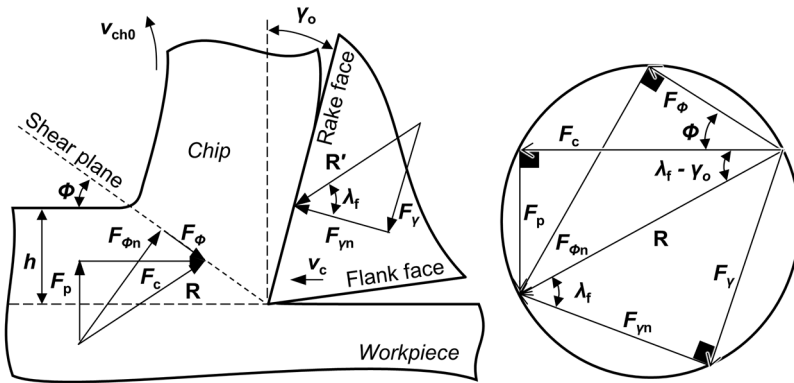


Figure 2.7 Cutting forces circle diagram; according to (Merchant, 1944)

While the graphical method mentioned above is widely accepted in the machining community as a convenient approximation of chip formation, it is important to note that the calculation of tool-chip friction using the geometrical approach can only represent the macro case. The friction within the tool-chip interface is more complex and can vary significantly at the micro level. Additionally, assumptions such as a thin shearing plane, a sharp cutting edge, and continuous chip formation need to be critically examined when using the analytical approach described earlier.

(Hucks, 1951) developed an equation for the shear angle by applying Mohr's slip theory to the orthogonal machining process. Unlike the models proposed by Merchant, this theory allows for consideration of a material-specific slip angle rather than the idealized angle of 45° . It is important to note that the shear angle does not necessarily have to be equal to the angle indicating the actual position of the sliding surface. So far, the direction of the shear plane has been determined purely

geometrically based on ideal considerations. In Hucks' theory, a square surface finite element on the rake face is considered, which experiences both shear and compressive loads. The angle between the rake face and the principal stress direction is solely determined by the coefficient of friction between the rake face and the chip. This relationship helps explain why different shear angles result at different cutting speeds. The coefficient of friction is dependent on the cutting speed, which in turn changes the principal stress direction. The slip direction is inclined by a material-dependent angle with respect to the principal stress directions. For steel in general, the slip plane forms at 45° to the principal stress direction, since the maximum shear stress occurs at this angle. This results a principal stress and slip directions relative to the rake face. The slip angle ϕ_1 , which is identical to shear angle in this case, can be calculated as:

$$\phi_1 = \varphi - \frac{1}{2} \arctan(2\mu) + \gamma_o \quad (2.10)$$

where μ is the sliding coefficient of friction and angle φ is given as:

$$\varphi = 45 - \frac{1}{2} \arcsin\left(\frac{\sigma_D - 2\tau_F}{\sigma_D}\right) \quad (2.11)$$

here, σ_D is the compressive yield stress of the material and τ_F is the shear yield stress

In their study, (Lee and Shaffer, 1951) applied the theory of plasticity using a slip-line field to enhance the prediction of the shear angle proposed by Merchant, which utilizes the minimum energy principle. They observed that the maximum shear stress occurs on a plane oriented at a shear angle through the chip root, passing through the cutting edge at point C. The material is assumed to be rigid-perfectly plastic, with no shear or normal stress along the edge AB, which intersects the chip at a 45° angle to the shear plane. Segment AC represents a portion located at the rake face. The rectangular region ABC is considered to be plastically rigid and subjected to a uniform state of stress. Any point within the region ABC can be represented using a single Mohr's circle diagram. The shear angle is given by the following equation:

$$\phi = \frac{\pi}{4} + \gamma_o - \lambda_f \quad (2.12)$$

This method has a few shortcomings. Firstly, it misrepresents the physics of the process, as the shear zone is planar rather than triangular. Secondly, it assumes that the normal and shear stresses are equal on segment AC (representing sliding friction), which does not accurately represent the actual case.

The secondary shear zone near the rake face also affects the shear angle. In a similar approach to (Merchant, 1945), (Rowe and Spick, 1967) utilizes a global minimum energy solution to predict the shear angle. In this approach, the work done on both the shear plane and the rake face is taken into account using the Hamiltonian principle: $d/d\phi = (F \cdot v) = 0$ It is assumed that the material is perfectly plastic with no strain hardening. From this analysis, the following relationship was derived:

$$\cos \gamma \cos(2\phi - \gamma_o) - \beta_r \cdot \chi \cdot \sin \phi = 0 \quad (2.13)$$

where β_r is the ratio of shear stress at the rake face to the yield stress of the chip (maximum is $\beta = 1$ for sticking condition) and χ is the multiples of h defining length of contact on rake face.

The value of ϕ satisfying this equation for chosen values of γ_o , β_r , and χ can be found by plotting the following two families of curves as function of ϕ :

$$A = \beta_r \sin^2 \phi, \text{ and } B = \frac{1}{\chi} \cos \gamma_o \cos(2\phi - \gamma_o) \quad (2.14)$$

The intersection of two curves from each family gives the predicted shear plane angle. Knowledge about friction angle and the contact length are necessary to predict shear plane angle.

Incorporating the strain hardening effect, (Oxley, 1989) developed a slip-line theory model with increased analysis complexity. This model requires iterative construction of the slip-line field. It assumes a thin shear zone, chip equilibrium, and a uniform shear stress in the secondary deformation zone at the tool-chip interface. The minimum energy principles are applied in this model. It allows for the variation of flow stress properties considering strain, strain rate, and temperature. To find solutions in the model, a 'velocity-modified temperature' approach is utilized. The thermal properties of the work and tool materials are taken into account as functions of temperatures, and the heat partitioning factors are considered.

The analytical models mentioned above are widely recognized as well-received models for chip formation within the scientific community. In a comprehensive review conducted by the CIRP working group for "Modelling of Machining Operations" in 1998, Luttervelt et al. provided an overview of the research related to chip formation (1998). Additionally, a more recent CIRP keynote paper by (Arrazola et al., 2013) presented a comprehensive review of analytical and numerical models for fundamental chip formation. In the following section, an overview and background on the role of friction during chip formation will be discussed.

2.3 Tribology in machining

2.3.1 Friction conditions within tool-chip contact

As discussed in the previous section, machining involves severe frictional conditions that have a significant impact on the chip formation process. Understanding the friction conditions within the tool-chip interface is crucial and can greatly contribute to improving machining efficiency and the development of analytical models. However, the friction conditions in machining are complex, and conventional dry sliding representations are not sufficient to describe the actual case. The friction conditions within the tool-chip interface directly affect the metal cutting process and chip formation. To illustrate the challenges associated with applying conventional friction laws to machining, a brief overview of these laws is provided. It becomes evident that the applicability of these laws to the machining case is limited.

The qualitative laws of friction were first postulated by Amonton in the late 17th century and later expanded upon by Coulomb in the 19th century, leading to a better understanding of the complex phenomenon of friction (Popova et al., 2015). It has been established that dry sliding friction between two solid surfaces is governed by a tangential force, F_t , that causes relative motion and is proportional to the normal force, F_N , at the interface. The constant of proportionality is referred to as the coefficient of friction.

$$\mu = \frac{F_t}{F_N} \quad (2.15)$$

It is essential to differentiate between the real and apparent areas of contact. The real contact area, also known as the bearing area, exists at a microscopic level due to surface roughness and is limited to discrete contact spots (Bhushan, 2013). This real contact area, where interatomic interactions take place, is smaller than the apparent geometrical contact area, as depicted in Figure 2.8. Therefore, the frictional characteristics of the contact are defined by the real contact area (A_r). During the initial

stages of contact, only a few points are in contact. As the normal force increases, the surfaces come closer, resulting in more asperities making contact. Depending on the normal and shear stresses at the contact, various forms of surface deformation can occur, including elastic, plastic, viscoelastic, or viscoplastic deformation (Bhushan, 2013). The magnitude of the real area of contact can be determined as:

$$A_r = \frac{F_N}{p} \quad (2.16)$$

where p is the pressure required to plastically deform the asperities. The frictional force required to cause a slide is the force required to cause enough shearing stress at contact asperities. The friction force is therefore give as:

$$F_N = A_r \tau_{aB} \quad (2.17)$$

where τ_{aB} is the asperities shear strength of the softer material. In Equation 2.16 and 2.17, the coefficient of friction is found to be independent of the apparent area of contact but dependent on the applied normal load, F_N , which leads to an increase in the real area of contact. As the normal load increases, the real area of contact expands, resulting in partial subsurface plastic flow and shearing of asperities. With further increase in the normal load, the real and apparent areas of contact eventually become equal, resulting in a sticking condition where relative motion is only possible through subsurface plastic flow. In such cases, the linear proportional relationship between the normal load and frictional force is no longer valid. The slip movement occurs within the workpiece materials rather than at the interface. Therefore, when the real area of contact becomes a significant fraction of the apparent area, the proportionality between the normal load and the real area of contact becomes no longer valid.

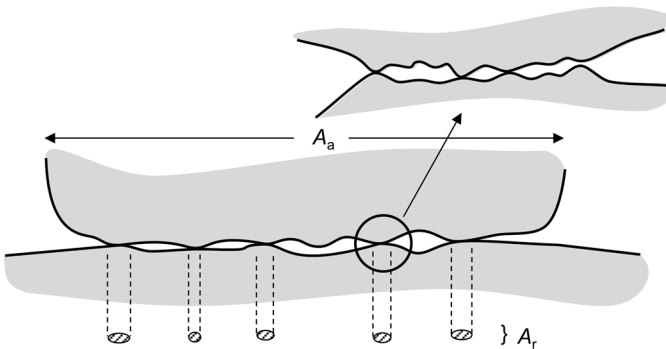


Figure 2.8 Apparent and real areas of contact; (Bhushan, 2013)

In machining, the presence of high normal pressure, elevated temperatures, and non-uniform stress distribution within the tool-chip and tool-workpiece interface creates a highly complex tribological system. In such cases, the concept of dry sliding friction may not be adequate or even applicable to accurately characterize the system. The magnitude of the coefficient of friction in metal cutting differs significantly from that of lightly loaded metal pairs under sliding conditions. In metal cutting, the continuous generation of new surfaces that are chemically active and free from contaminants further complicates the frictional conditions. While a single coefficient of friction is conventionally

used to describe friction, it may not be sufficient to capture all the friction conditions that occur in machining. Nevertheless, it can provide a general understanding of the overall frictional behavior.

Friction plays a significant role in the cutting process. It directly affects the shear in the primary shear zone at the tool-chip interface. The friction condition at the interface can impact the resultant force, R' , calculated on the rake face (as shown in Figure 2.7), which in turn affects the opposite force on the shear plane, as discussed by Merchant in the previous section. There is a direct coupling between friction and shearing in machining, as highlighted by (Shaw, 1993). Consequently, cutting forces are influenced by friction-related characteristics, such as an increased tool-chip contact length or the shear yield strength of the contact, as identified by (Trent, 1977).

A generally accepted understanding of friction within the tool-chip contact is based on the sticking/sliding concept. In this concept, sticking conditions occur near the cutting edge, while sliding occurs beyond the sticking region in the direction of chip flow. (Zorev, 1966) developed a model that illustrated seizure along the rake face, followed by a sliding region, as shown in Figure 2.9. The seizure is caused by the shear stress exceeding the yield stress of the material. The normal stress on the rake face was assumed to follow an exponentially decaying distribution represented as following:

$$p(x) = p_0 \left(1 - \left(\frac{x}{l_c} \right)^\zeta \right) \quad (2.18)$$

where l_c is the contact length, x is the distance from the cutting edge along the rake face and ζ is the pressure distribution exponent. This model viewed the seized zone as a special built up edge (a thin boundary layer). The compressive stress causes the frictional forces to exceed the shear yield stress of the material. Thus a “saturated” frictional condition could be obtained at high normal pressures. as following:

$$\tau(x) = \tau_{\alpha B} \quad (2.19)$$

where $\tau_{\alpha B}$ is the shear strength of the material. At lower values of normal pressure, it becomes:

$$\tau(x) = \mu p(x) \quad (2.20)$$

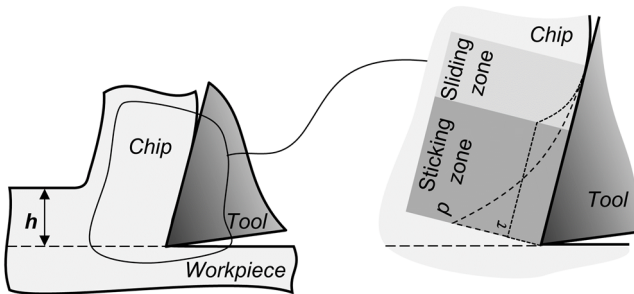


Figure 2.9 Sticking and sliding zones and stresses distribution within tool-chip interface; adapted from (Zorev, 1963)

Using a transparent tool, (Doyle et al., 1979) defined three regions of chip contact. The seizure zone, where plastic flow occurs within the material, is located near the cutting edge. The formation of a

built-up edge (BUE) is one observation of this type of contact, particularly for workpiece materials with relatively high strain hardening when machined at low cutting speeds (Trent, 1977).

A built-up edge (BUE) has significant effects on surface finish, dimensional accuracy, and tool life. It also alters cutting tool geometry and introduces high variability in the cutting process. Cutting forces can fluctuate up to 50% when BUE is present, compared to only 10% without BUE (Oxley, 1988). The formation of BUE is caused by strain hardening surpassing thermal softening. Only materials with a tendency for strain hardening can exhibit BUE. The material that sticks to the rake face continues to undergo strain hardening as shearing occurs. If no thermal softening takes place, the material accumulates as BUE. The relative angle of the BUE to the rake face can be positive, negative, or neutral. Extensive studies on BUE geometry have been conducted by Heginbotham and Gogia (1961). Increasing the cutting speed can reduce BUE formation by magnifying the effect of thermal softening.

Strain hardening and thermal softening can also have an impact on chip formation itself. In some materials, the interplay between strain hardening and thermal softening occurs not only at the tool-chip interface but also within the material itself. This results in a phenomenon known as shear banding, where the chip thickness ratio undergoes significant and frequent changes, leading to a serrated chip. There are two categories of inhomogeneous strain associated with shear banding: fracture/rewelding and adiabatic shear. While only a few materials, such as titanium, exhibit fracture/rewelding, many others show adiabatic shear banding. As the cutting velocity reaches a critical point, the chip formation transitions from continuous to discontinuous. The chips become thicker and hotter as the shear plane rotates (reducing the shear angle, thereby increasing the chip thickness ratio). Eventually, the thermal softening process takes over, causing the shear to localize into a narrow band, effectively liquefying the material at the cut/uncut interface. The cycle then repeats, with the uncut material initiating the shear process again (at a higher shear angle value), and the shear plane starting to rotate downward once more. Shear banding occurring within the workpiece material during chip formation may not be directly influenced by the friction within the tool-chip interface, but rather by the workpiece's strain hardening and thermal properties. Nonetheless, its cyclic behavior can influence the stresses that occur within the tool-chip contact.

High mechanical loads are present within the sticking zone and decrease as the distance increases away from the cutting edge. The sliding zone occurs at a certain distance away from the cutting edge, following the sticking zone and a transition zone. In the sliding zone, the chip undergoes elastic recovery and rubs against the tool. Crater wear on the rake face exhibits similarities to these zones.

In the sliding zone, the presence of oxygen can influence the contact between the tool and the chip. One hypothesis suggests that the use of lubricants creates a barrier to the environment, which can extend the tool life in some cases (Shaw, 1984). In the seizure zone, as the chip flows over the tool, it depletes the layer of contaminants, gradually exposing a clean contact surface. Additionally, the increased temperature in this zone promotes contact welding (Shaw, 1984). Since there is no relative movement between the tool and the chip in the seizure zone, the grain boundaries within the work material extend parallel to the rake face over a significant distance. Cutting experiments using a quick stop device have revealed strong adhesion of the chip to the tool, resulting in ductile fracture occurring within the material rather than at the tool-chip interface. These observations indicate a strong welding effect that is stronger than the material strength (Trent, 1977). The sliding zone in the steady state occurs within a very small area relative to the overall contact region (Trent, 1977). The steady state is reached when oxides and contaminant layers (such as lubricants) are abraded, and the temperature reaches a plateau.

Coolants and lubricants influence the friction within tool-chip interface mainly by heat dissipation and lubrication effects. Their influence and general interpretations on their working action are discussed in the following section.

2.3.2 Cutting fluids action within tool-chip contact

In machining operations, Metalworking fluids (MWF) are used to enhance productivity and product quality. As discussed earlier, MWF have three main functions: cooling, lubrication, and chip removal (Weinert et al., 2004). Due to localized friction within the tool-chip and tool-workpiece interfaces and the process of plastic deformation occurring at shear zones, energy transformation occurs and heat is generated. Therefore, it is necessary to dissipate the heat to prevent excessive temperatures. For materials with relatively high thermal conductivity, such as steel, the majority of the generated heat (up to 75%) is transferred away by the chips from the cutting zones (Kronenberg, 1954). However, a considerable fraction of the heat is still transmitted to the tool and the workpiece. In the case of low thermal conductivity materials, such as nickel-base alloys, the heat transfer is less effective and localized around the chip formation zones, resulting in high temperatures.

MWF flow around the cutting zones contributes to heat dissipation, resulting in reduced cutting temperatures. This reduction in temperature leads to reduced tool wear (El Baradie, 1996), allowing for the use of higher cutting parameters, such as high cutting speeds, for improved productivity. Another important function of MWF is lubrication. It reduces friction within the tool-chip and tool-workpiece interfaces at the rake face and flank face, respectively. It is generally believed that MWF functions as a lubricant at low cutting speeds (e.g., straight oil) and primarily as a coolant at high cutting speeds (e.g., emulsions) (Weinert et al., 2004). Additionally, MWF plays a crucial role in chip transport and evacuation, especially in operations like drilling where there is limited space available (Cselle, 1995).

The exact working principle of metal working fluids in affecting the friction within the tool-chip contact is still being researched. It has been reported by (Boothroyd, 1975) that many common lubricants have little effect on the cutting process, while chemicals that are considered uncommon for lubrication applications have shown particular effectiveness in machining, such as carbon tetrachloride (CCl_4), despite being a highly toxic compound. (Usui et al., 1961) coated a fresh cut surface with CCl_4 and observed a significant influence on chip formation. It was assumed that a chemical reaction, rather than a physical mechanism, formed a layer with low shear strength.

Boundary lubrication is unlikely to exist in machining due to the high stresses within the tool-chip interface. However, the lubrication action in machining is quite complex. A commonly accepted view is that the lubricant penetrates small channels within the tool-chip interface through capillary action, reducing the sticking zone (Williams and Tabor, 1977), as shown in Figure 2.10 (left). It is assumed that the shear strength of the contact is lowered by the formation of a low shear strength layer through chemical attack or physical adsorption.

Surface roughness in the lightly loaded region (i.e., the sliding zone) near the point where the chip leaves the contact can result in the real area of contact being smaller than the apparent area of contact. This provides an opportunity for the lubricant fluid to penetrate through microchannels in that area. The penetration of the fluid is also influenced by the balance between the fluid pressure gradient and the relative motion between the chip and the tool working against it (Childs, 2006).

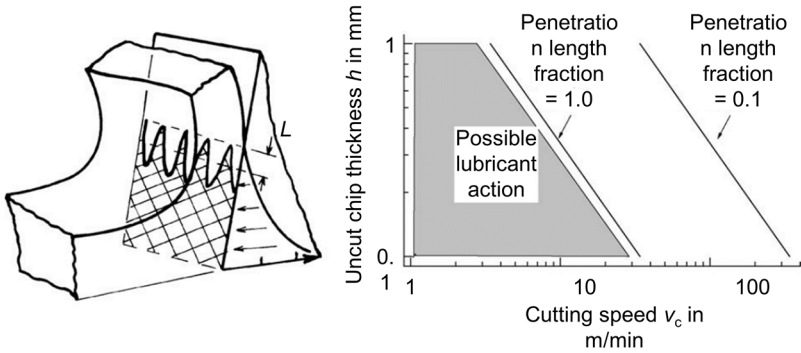


Figure 2.10 Cutting fluid penetration within tool-chip interface; (Childs, 2006)

In Figure 2.10 (left), the schematic illustration demonstrates the penetration of fluid within the tool-chip contact. At a certain distance from the cutting edge, the fluid partially penetrates the contact, forming a length denoted as L . The effectiveness of lubrication is determined by the ratio of L to the length of the channels, known as the penetration length fraction a_c . When a_c approaches 1, lubrication is considered to be possible. However, lubrication becomes ineffective for fraction values below 0.1. The efficiency of lubrication is also influenced by the cutting speed and the uncut chip thickness, as shown in Figure 2.10 (right). For example, effective lubrication may occur at a penetration length fraction of $a_c = 0.16$ for cutting speeds ranging from $v_c = 20$ m/min to $v_c = 30$ m/min, with an uncut chip thickness of $h = 0.1$ mm.

Conventionally, researchers have indirectly investigated the tribological conditions within the tool-chip interface by measuring mechanical loads, observing chip morphology, or assessing adhesion marks on tool surfaces. However, despite the experimental challenges of visualizing cutting fluid distribution within the tool-chip interface during the cutting process, a few studies have attempted to directly reveal the hidden contact. Transparent tools made of sapphire glass have been utilized for direct observation of the contact zone, as described by (Wright, 1990).

(Madhavan et al., 1995, 2002) used an oil-ink mixture to investigate the penetration of the mixture within the interface using a transparent tool. They observed the penetration of oil into the sliding zone, while no fluid penetration was observed in the sticking zone. It is worth mentioning that they used different terms for the sticking and sliding zones based on a different perspective. Hwang and (Chandrasekar, 2011) investigated the tool-chip interface in the presence of cutting fluids using sapphire tools and were able to observe a reduction in the tool-chip contact length. (Huang et al., 2007) mixed a fluorescence dye with cutting fluid to enhance the visibility of the cutting fluids through a sapphire tool. (Moscoso et al., 2005) investigated low-frequency, high-amplitude vibration-assisted machining using a sapphire tool and a lead workpiece to visualize the lubricant during a full vibration cycle. Soft materials were used in previous investigations due to the vulnerability of transparent tools to lose their optical characteristics or breakdown during machining. The interaction between conventional opaque tool materials such as cemented carbide and higher strength workpiece materials is still rather challenging for direct observation. Moreover, Combination of transparent tools with soft workpiece materials results a weak analogy to common tool and workpiece materials due to different thermal, mechanical, and surface properties.

Visualization of cutting fluid within the tool-chip interface provides important insights into the working mechanism of cutting fluids under machining conditions. As mentioned earlier, the choice of material pairs can significantly influence the tribological conditions and friction behavior within the contact. In addition to direct observation methods, indirect experimental investigations are also conducted for material pairs relevant to industrial applications under realistic machining conditions. Denkena et al. (2021) employed high-speed recording of the machining process combined with digital particle velocimetry to study the effect of chip sliding velocity on the frictional behavior within the tool-chip interface. These investigations were carried out on the orthogonal plane using a sapphire glass plate, a steel AISI 4140 workpiece, and a cemented carbide tool.

It is important to keep in mind that the classification of friction into friction zones within tool-chip contact, as mentioned above, is related to the steady-state condition. A transient tribological condition does exist at the beginning of the cut (Davim et al., 2019). The transient behavior lasts a finite distance longer than the uncut chip thickness, where chip formation has already been well established. Within the transient friction condition, the apparent friction coefficient increases rapidly. The reason behind this phenomenon has been attributed to the effect of various forms of contaminants, including lubricants and oxides (Davim et al., 2019). A longer cutting distance is required to sweep off these contaminants from the tool-chip contact.

(Davim et al., 2019) observed that different materials exhibit different transient and steady-state frictional behaviors. Ductile materials tend to have a longer transient friction distance in comparison to materials with relatively high strength and brittle behavior. Additionally, it has been observed that the coefficient of friction for materials with a longer transient friction condition progressively increases at steady-state. In contrast, materials with a shorter transient condition exhibit a well-defined constant steady-state coefficient of friction. The underlying mechanisms of these observations are still being researched. In the current work, more discussions are provided for the transient friction behavior, which is referred to as the initial period of chip formation (IPCF).

In order to benefit from the low contact within the transient region, the cutting may be limited to a certain distance before reaching the steady-state. Interrupted machining can facilitate the utilization of this concept. In the following sections, reviews about research topics related to interrupted machining, in general, with a specific focus on interrupted machining realized through tool/workpiece vibration (i.e., vibration-assisted machining), are provided.

2.4 Thermal characteristics of interrupted machining

2.4.1 The influence of interrupted machining on tool wear

Interrupted machining allows for cyclic mechanical and thermal loads to be imposed on the tool/workpiece tribological system. In some machining operations, such as milling, interrupted machining is inherent. In contrast, continuous machining operations, such as turning and drilling, require special arrangements to achieve interrupted machining. While cyclic loads may, under certain conditions, excite system dynamics and induce thermal fatigue, other researchers have reported favorable effects of interrupted machining (e.g., milling) compared to continuous machining regarding tool life. (Stephenson and Ali, 1992) demonstrated that both mean and maximum temperatures are lower in intermittent cutting than those in continuous cutting under the same cutting conditions. (Kitagawa et al., 1997) reported that tool life can increase up to 10 times in milling compared to turning when using a relatively high cutting speed ($v_c = 200$ m/min) for machining Inconel 718 with a cemented carbide tool (K10) under the use of cutting fluids.

According to Kitagawa's investigations, interrupted cutting reduces both maximum and mean cutting temperatures. A reduction of 100 K in maximum tool temperature was observed to influence tool wear by a factor of two to three. The transient increase in temperature resulting from the short cutting distance, as well as the cooling period during interruption, contribute to a longer tool life in milling. Furthermore, during interruption, the tool-chip and tool-workpiece contact zones are exposed to cutting fluids, which enhances the performance of the fluids. Figure 2.11, adapted from (Kitagawa et al., 1997), represents a typical temperature profile in interrupted machining compared to continuous machining. At the start of the cutting interval, the temperature increases rapidly. The cutting process is then interrupted before the temperature reaches a steady state. The temperature then reduces to a lower level depending on the surrounding medium. The heating cycle repeats again at the next cutting interval.

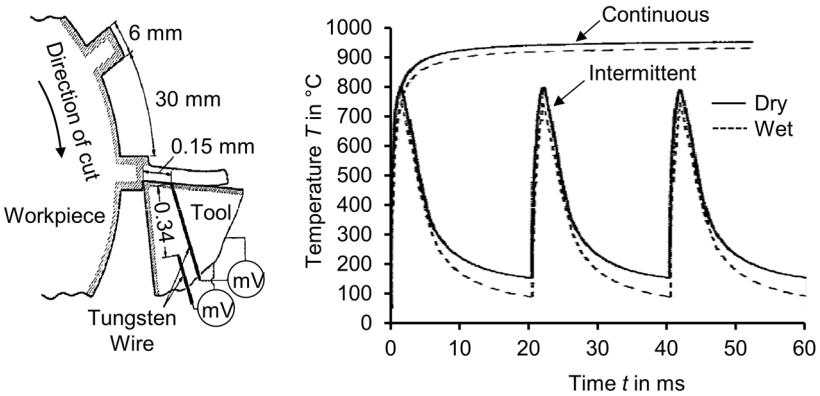


Figure 2.11 Tool temperature in interrupted machining; adapted from (Kitagawa et al., 1997)

The evolution of temperature in interrupted machining, specifically in modulation machining where vibration is superimposed on the feed, has been investigated by (Kountanya, 2009). In his investigation, the Green's function approach introduced by (Stephenson and Ali, 1992) for predicting temperature in machining was applied to modulated turning. He concluded that modulation reduces average cutting temperatures due to interspersed cooling periods. Additionally, a higher modulation frequency was reported to significantly reduce the cutting temperature.

Interrupted machining in continuous machining operations, such as turning, can be achieved using the turn-milling technique. In this technique, the conventional operations of turning and milling are combined into one operation (Schulz and Spur, 1990). In turn-milling, both the workpiece and the tool are given a rotary movement. The tool engages the workpiece intermittently, allowing a period of time for cooling down and exposure to the environment. (Karaguzel et al., 2015) investigated tool wear using the turn-milling operation. Difficult-to-cut materials such as Ti6Al4V, Inconel 718, and Waspaloy were investigated under dry conditions, flood cooling, and minimum quantity lubrication (MQL). Their results for tool life in Waspaloy are shown in Figure 2.12.

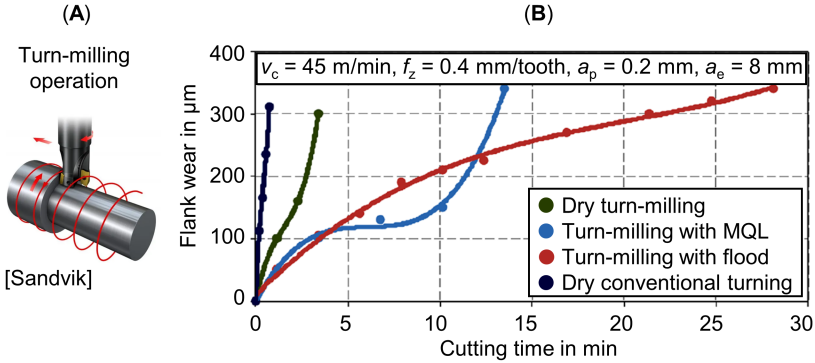


Figure 2.12 (A) Turn-milling operation schematic; (Courtesy: Sandvik). (B) Conventional turning tool life in comparison with turn-milling Waspaloy; (Karaguzel et al., 2015)

A significant increase in tool life, ranging from 2 to 10 times, was observed when using turn-milling compared to conventional turning. Even under dry conditions, more than double the tool life was reported when comparing turn-milling to conventional turning with cutting fluids. These observations indicate a significant relationship between interrupted machining and tool life. They also suggest the presence of severe tribological conditions within the tool-chip and tool-workpiece interfaces in continuous machining operations, leading to accelerated tool wear, especially for difficult-to-cut materials.

Turn-milling is a promising technique for achieving interrupted machining in turning. Its implementation is possible with modern multi-axis turning centers equipped with multiple spindles. For other continuous machining operations, such as drilling, interrupted machining can be achieved using special arrangements, including the use of actuators that impose vibration along various directions, as will be discussed in the following sections.

It can be inferred from the literature presented in this section that interrupted machining can lead to better tool life due to decreased average and maximum temperatures. Nonetheless, the exact mechanism of the effect of temperature on the tribological conditions during transient chip formation, occurring at the start of cutting, is still being investigated, and only a few studies have addressed this topic.

2.4.2 Models for transient temperature propagation in interrupted machining

As discussed in the previous section, interrupted machining affects tool life. The temperature during machining is shown to play an important role in bringing about this favorable effect. Measuring temperature in machining can be quite challenging, especially within the chip-tool interface, as the temperature distribution changes considerably along the rake face with a steep temperature field. Additionally, the transient behavior occurring in interrupted machining, which lasts for a very short time, poses an additional challenge for experimental temperature investigations. Researchers have experimentally investigated temperature measurement using different techniques, as reviewed in a CIRP keynote paper by (Davies et al., 2007). In addition to experimental temperature measurement, analytical and numerical models provide detailed insight into the transient temperature behavior both spatially and temporally.

(Trigger and Chao, 1951) conducted pioneering research on determining cutting temperatures in continuous cutting. They created a model that takes into account the heat source in the shear plane and computes the average temperature of the chip in the shear zone. Other researchers have built upon Trigger and Chao's model for continuous cutting. (Komanduri and Hou, 2000) surveyed these contributions and suggested their own method for analyzing the orthogonal continuous cutting process, which accounts for the impact of the shear plane heat source. They later incorporated a heat source caused by friction at the interface of the tool and chip (Komanduri and Hou, 2001a) and included both the shear and frictional heat sources in the temperature distribution calculation (Komanduri and Hou, 2001b). While most research on cutting temperature has focused on continuous cutting operations, several studies have also been conducted on interrupted cutting operations.

In interrupted machining, transient temperature modeling is highly relevant. Only a few researchers have addressed this problem and developed complete analytical or numerical models with experimental validation. Interrupted cutting is characterized by the production of discontinuous chips and non-steady-state cyclic conditions of forces, heat sources, and temperatures. The fluctuating heat sources and resulting temperature fields create cyclic thermal loads on both the tool and workpiece.

(Stephenson and Ali, 1992) adopted a method of approximating the tool geometry with a semi-infinite rectangular corner to model the punctual transient temperatures in the tool during interrupted cutting. They investigated the impact of different types of heat source distributions (uniform, linear, and exponential) along the rake face, as well as time-varying heat source intensities in the form of square wave heat inputs. Their model suggested that interrupted cutting leads to lower tool temperatures compared to continuous cutting due to the cooling effect during non-cutting periods. They explained that the Green's function for temperatures in a semi-infinite corner, caused by an instantaneous point source at a surface point and assuming adiabatic conditions at the boundaries, can be obtained by multiplying the Green's function for three mutually perpendicular instantaneous plane sources in semi-infinite half-spaces, which intersect to form an eighth space or corner. Consequently, the transient temperature field at a point in the corner at time t can be expressed as a solution to the governing differential equation for transient heat conduction in a continuous medium. The identification of input heat flux can be difficult, as it involves determining the spatial and temporal distribution of the heat flux of the instantaneous, punctual heat sources and the Green's function of the relevant geometry. Stephenson and Ali utilized the steady-state cutting temperature model developed by (Loewen and Shaw, 1954), which involves calculating the total amount of frictional energy dissipated at the chip-tool interface per unit time and per unit area, based on parameters such as the friction force, chip velocity, chip contact length, and chip width. The analytical model by (Stephenson and Ali, 1992) is a fundamental approach in transient temperature modeling that has been accepted and implemented by many researchers, such as (Karaguzel et al., 2016) and (Augspurger et al., 2020).

(Jen and Anagonye, 2001) extended the model of (Stephenson and Ali, 1992) to include the initial transient response to the tool temperature and non-uniform heat flux distribution. (Jen et al., 2003) developed three-dimensional nonlinear transient heat conduction equations, which were numerically solved to study their effect on transient temperature. (Potdar and Zehnder, 2002) developed a finite element model for investigating transient temperature behavior based on a friction model with critical stress criteria. (Lazoglu and Altintas, 2002) developed a numerical model based on finite difference for transient temperature fields.

(Jiang et al., 2013) used an analytical model for contact length to determine the time-dependent spatial heat source distribution on the rake face during the milling process. They validated their approach by integrating thermocouples into the tool and used a least square optimization algorithm proposed by (Beck et al., 1985) to solve the inverse heat conduction problems and determine the heat flux into the tool and workpiece.

To accurately model cutting temperatures, it is important to consider the contact properties between the cutting tool and chip, particularly the complex frictional interactions at the tool-chip interface. Previous studies have used simplified friction models, such as Coulomb friction. However, (Zorev, 1963) showed that the tool-chip interface has two distinguishable regions: the sticking region and the sliding region. Nevertheless, this distinction is not quite accurate for precise modeling since friction properties also depend on temperature, pressure, and sliding velocity.

Recently, (Karaguzel, 2021) proposed a hybrid model that combines analytical and numerical methods taking into consideration zonal contact. The model determines heat flux analytically and uses a numerical transient heat conduction model to calculate temperature within the tool. The Matlab PDE Toolbox was used to develop the numerical model. A similar approach is utilized in this dissertation for thermal modeling in IPCF, but with variations in how heat flux is defined spatially and temporally based on experimental data, as explained in Chapter 7.

A fundamental understanding of the transient temperature behavior is important to establish an analogical connection between interruption characteristics and the favorable tribological effects related to enhancing cutting fluids' performance and effectiveness.

As discussed earlier in this chapter, the enabling of interrupted machining in continuous machining operations requires additional measures. In turning, the effectiveness and applicability of the turn-milling strategy have been observed. However, in drilling, further adaptation must be applied. One approach to introduce interruptions along the drilling process is through vibration-assisted machining, where superimposed oscillations are utilized. In the following section, the details of VAM and its application in machining, particularly in drilling, will be discussed.

2.5 Vibration assisted machining (VAM)

As discussed in previous sections, prolonged tool-chip contact leads to severe tribological condition that adversely affects chip formation. For continuous machining operations, one method is to interrupt the cut via controlled superimposed oscillations.

2.5.1 The orientation of superimposed oscillations in VAM

Vibration-assisted machining (VAM) is a commonly used term in the literature to describe the use of superimposed oscillations in machining. The superimposition of oscillations can be applied either along the cutting velocity or parallel to the uncut chip thickness (i.e., feed). In some cases, elliptical vibration is also employed, where oscillations occur simultaneously in two directions.

Superimposed oscillations in the cutting speed direction achieve tool-chip disengagement along the rake face. The cutting fluid can penetrate the contact region periodically and influence the lubricating effect. However, applying vibration in the cutting speed direction does not guarantee discontinuous chip formation, as the chip thickness remains the same. On the other hand, superimposing the vibration in the direction parallel to the uncut chip thickness or the feed can result in full tool disengagement due to the variable uncut chip thickness, which can reach zero under

specific conditions. Consequently, segmented chips can be generated. In fact, some researchers have even used the former type of vibration to produce particulate materials (Mann et al., 2007).

In elliptical vibration, the superimposed vibrations occur parallel to both the cutting speed and the uncut chip thickness directions simultaneously (Moriwaki and Shamoto, 1995). This approach minimizes variations in the uncut chip thickness. The tool has a velocity component in the direction of chip flow during the vibration cycle, effectively minimizing or even reversing the tool-chip frictional force. Elliptical mode VAM has been used for machining complex geometries and precision surface microstructures (Shamoto et al., 2005; Brehl et al., 2006; Guo and Ehmman, 2013). Figure 2.13 summarizes the three types of superimposed vibrations.

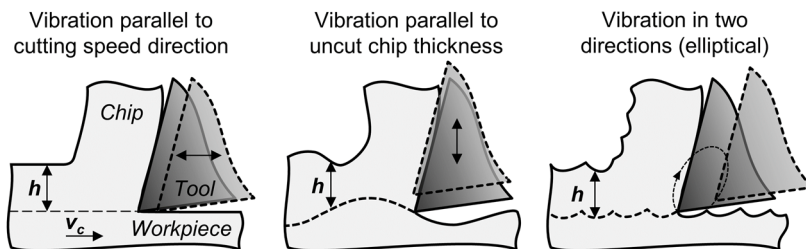


Figure 2.13 Different types of superimposed vibrations in VAM

Frequent exposure of the tool-chip contact to the environment, particularly cutting fluids, alters the chip formation mechanism. The positive effects of chip evacuation, improved tool wear, reduced friction, and the targeted use of cutting fluids enhance overall machining performance and sustainability. The fundamental requirements and characteristics of superimposed vibration are crucial to ensure the proper application of VAM.

Historically, Vibration Assisted Machining (VAM) was first pioneered in the late 1950s for macro-scale machining (Brehl et al., 2008). Early work by Isaev and Anokhin (1961) discussed ultrasonic vibration in metal cutting, while Skelton (1979) investigated the effect of superimposed vibration on cutting forces in turning using an electrohydraulic tool holder. The interest in VAM gained more traction in the 1990s for turning using diamond tools to reduce thermo-chemical wear caused by the chemical activity between diamond tools and ferrous materials. Moriwaki and Shomato studied the use of diamond tools under VAM to machine austenitic stainless steel (Moriwaki and Shomato, 1991), glass (Moriwaki and Shomato, 1992), and hardened steel (Shomato and Moriwaki, 1999). Diamond tools were shown to exhibit extended tool life when machining these materials using VAM, leading to economical production. Improvements in surface quality were also compared with conventional machining.

When machining steel using diamond tools, excessive tool wear occurs due to increased chemical activity under high mechanical and thermal loads in conventional machining. However, VAM disrupts the severe contact conditions and potentially reduces temperatures, thereby reducing thermo-chemical wear. VAM has been applied in machining different materials using various machining operations. Table 2.2 provides a list of selected VAM works in the literature.

Table 2.2 Selected VAM literature

Workpiece material	Machining operation			
	Milling	Turning	Drilling	Deep hole drilling
Steel or stainless steel	- Nath et al., 2007 - Ding et al., 2010	- Miyake et al., 2018 - Kataoka and Shamoto, 2019,	- Neugebauer and Stoll, 2004 - Mann et al., 2011 - Paulsen et al., 2020	
Aluminum alloys	- Verma and Pandey, 2019		- Jallageas et al., 2013 - Pecat and Meyer, 2013 - Paulsen et al., 2020	- Chu et al., 2018
Copper alloys			- Mann et al., 2011	- Heisel et al., 2008 - Bleicher et al., 2019
Titanium alloys	- Tong et al., 2019	- Patil et al., 2014, - Sugihara and Enomoto, 2016, - Sui et al., 2017	- Okamura et al., 2006, - Mann et al., 2011 - Sadek et al., 2014, - Brinksmeier et al., 2015 - Pecat et al., 2016, - Schumski et al., 2019, - Yang et al., 2019, - Paulsen et al., 2020	
Nickel alloys	- Hsu et al., 2007	- Babitsky et al., 2003 - Nath and Rahman, 2008	- Liao et al., 2007 - Mann et al., 2011	- Baghlani et al. 2013
Composites			- Tekeyama and Kato, 1991 - Ramkumar et al., 2004 - Liu et al., 2005 - Arul et al., 2006 - Pecat et al., 2014 - Bleicher et al., 2018, - Hussein et al., 2018 - Feng et al., 2019 - Dong et al., 2019 - Xu et al., 2019	
Bones			- Alam et al., 2009	

In addition to enabling diamond tool machining of steel, VAM is highly effective in creating functional surfaces and enhancing the machinability in challenging machining operations, such as

drilling and deep hole drilling, particularly for difficult-to-cut metallic and composite materials. However, there are only a few studies that have addressed the drilling of Nickel alloys (e.g., Inconel 718) using VAD. There is a scarcity of research in the literature regarding the application of sustainable lubrication techniques, such as MQL, in conjunction with VAD, as reported by (Pecat et al., 2014), (Pecat et al., 2016), (Hussein et al., 2018), (Yan et al., 2019), and (Paulsen et al., 2020). A more comprehensive investigation of the effects of MQL under VAD for Nickel alloys still requires further elaboration.

The kinematics of the two types of 1D VAM are fundamentally different. However, in both cases, a sinusoidal displacement of $s_{os} = A \cdot \sin(2\pi f_{os}t)$, where A is the vibration amplitude, f_{os} is the vibration frequency in Hz and t is time in seconds, is superimposed on tool motion, either in the cutting direction or the feed direction.

VAM in cutting speed direction

For vibration in the cutting direction, the superimposed vibration velocity must exceed the average cutting velocity, $A \cdot 2\pi f_{os} > v_c$, in order to ensure interrupted cutting (Brehl and Dow, 2008). In this case, the instantaneous cutting velocity can reach zero, and its direction is periodically reversed over a full cycle of vibration. As a result, the tool retracts for a defined period of time with respect to the chip. For instance, a cutting speed of $v_c = 45$ m/min requires a vibration amplitude of $A = 3 \mu\text{m}$ and a vibration frequency of $f_{os} = 40$ kHz to achieve interruptions (Moriwaki and Shamoto, 1991). Therefore, ultrasonic vibration might potentially be applicable in some applications. However, it is important to consider system compliance in practice, as it can influence the minimum requirements of vibration characteristics for interrupted machining.

Direct observation of lubricant fluid penetration into the tool-chip contact during modulated orthogonal cutting in the cutting speed direction was reported by (Moscoso et al., 2005). They used a transparent sapphire tool to cut lead at a very low cutting velocity of $v_c = 0.3$ m/min. Their observation showed minimal fluid penetration into the tool-chip contact without applying superimposed vibration to the tool, similar to conventional machining conditions. However, when superimposed vibration was applied to the tool, causing the contact to disengage, cutting fluid was observed to penetrate the contact area. Indirect observations also indicated a reduction in the coefficient of friction.

Superimposed vibrations in the cutting direction can be effective in interrupting the severe tribological conditions within the tool-chip contact, allowing cutting fluid to penetrate the contact and influence the temperature. However, the practical implementation of this type of VAM using industrial machining parameters is still under research. Achieving the critical vibration velocity condition ($A \cdot 2\pi f_{os} > v_c$) at relatively high cutting velocities is challenging. Many investigations reported in the literature on VAM in the cutting velocity direction have used very low cutting speeds. The combination of vibration amplitude and frequency required to achieve higher velocity levels for ensuring tool-chip separation poses fundamental challenges. The available actuation technology generally suggests low achievable amplitudes at high frequencies (Bleicher, 2018).

Furthermore, VAM in the cutting speed direction does not guarantee discrete chips, as the uncut chip thickness remains constant. This is particularly challenging in drilling, where smaller chips are desirable for enhancing machinability. Additionally, applying superimposed oscillations in the cutting direction during drilling requires the oscillations to be superimposed on tool rotation (Mann et al., 2009). Therefore, the application of VAM in the direction of cutting speed is beyond the scope of this study. Instead, further attention will be given to superimposed oscillations parallel to the uncut chip thickness in drilling.

VAM in feed direction

When the oscillations are superimposed in the direction parallel to the uncut chip thickness (i.e., feed direction), the tool-chip contact can be disrupted when the instantaneous uncut chip thickness reaches zero during the vibration cycle. The variation in uncut chip thickness occurs due to the instantaneous difference between the current position of the oscillating tool and the machined surface generated by previous cutting passes.

In this case, the vibration speed, which depends on the vibration amplitude and frequency, also has a critical condition. It must be greater than the feed velocity (Babitsky et al., 2003). In the feed direction, the vibration velocity is much lower compared to the cutting speed direction. For example, a feed rate of $f = 0.05$ mm at a cutting speed of $v_c = 20$ m/min results in a feed velocity of $v_f = 0.0084$ m/min (Babitsky et al., 2003), which is a significantly lower value compared to the cutting speed. Additionally, the frequency ratio and amplitude ratio are important factors in ensuring tool-chip contact disruption (Bleicher et al., 2019). The amplitude ratio K'_A , which represents the ratio of the peak-to-peak vibration amplitude (A_{pp}) to the feed (f), must be $K'_A > 1$ (Bleicher et al., 2019). This ratio can also be represented as $K'_A = A/H_z$, where A is the vibration amplitude and H_z is the axial uncut chip thickness per tooth or $H_z = f/2$ for a drilling tool with two cutting edges. The frequency ratio K_f , which is the ratio of the vibration frequency (f_{os}) to the rotational frequency (f_s), must not be an even number (Toews et al., 1998). The effect of these parameters on ensuring tool-chip contact disruption will be discussed later.

2.5.2 Actuation devices used in VAM

Different frequencies and amplitudes can be applied in VAM. Vibration superimposed in the cutting speed direction typically requires vibration in the ultrasonic range, where the frequency is above $f_{os} = 20$ kHz, and amplitudes are usually less than $A = 5$ μ m. Ultrasonic vibration is generated using a piezoelectric actuator composed of a piezoelectric stack that converts input electrical energy into mechanical strain. The actuator output is tuned and amplified using an ultrasonic horn or sonotrode, to which the tool or sometimes the workpiece is attached at its end. Ultrasonic vibration is necessary to surpass the critical speed at which tool disengagement becomes possible, as discussed previously. However, high levels of vibration speed may not be necessary when the vibration is applied in the feed direction. When disengagement is required in the feed direction, low-frequency high-amplitude vibration is typically applied. This type of VAM is sometimes referred to as modulated machining in the literature.

For vibration superimposed in the feed direction, the vibration amplitude is relatively large, typically within a few hundred micrometers, and the frequency is usually less than 100 Hz. In drilling operations, this type of VAM is commonly used to achieve small chips and enable intermittent contact, resulting in lower drilling temperatures (Yang et al., 2019). Therefore, this section briefly reviews the methods and devices belonging to this type of VAM for drilling, referred to as vibration-assisted drilling (VAD).

(Sugihara et al., 2016) utilized the numerically-controlled NC axis of a machine tool to apply ultra-low vibration frequencies in the feed direction for dry machining of Ti6Al4V alloy. They reported a significant reduction in tool crater wear and discussed the correlation between cutting and non-cutting times, as well as the effectiveness of superimposed vibration. (Miyake et al., 2018) developed a low-frequency vibration machine tool for turning operations. This tool allows superimposed vibration in the feed direction, synchronized with spindle rotation, to be applied in the x- and/or z-axis. For example, their developed machine tool is capable of turning tapered shapes under superimposed vibration in the feed direction. The setting of superimposed vibrations is

integrated into the machine's NC program. This new technique is based on interrupting the cut during turning to avoid continuous chips, providing more flexibility in setting vibration and cutting parameters for different materials and operations. However, the specific mechanisms used to superimpose the vibration into the machine axes were not disclosed in their study.

Devices based on different configurations and operating principles have been developed for low-frequency applications. These mechanisms include linear motors (Chhabra et al., 2002), piezo actuators, magnetostrictive actuators, air cylinders, and mechanical ball screw systems (Mann, 2010). High-frequency and low-amplitude vibration devices primarily consist of piezoelectric actuators. Electro-mechanical systems are suitable for medium-range amplitudes and frequencies, while mechanical and hydraulic systems are designed for low-frequency and high-amplitude applications. Figure 2.14 categorizes actuation systems into different groups based on their achievable amplitude and frequency, as reported by (Bleicher et al., 2019).

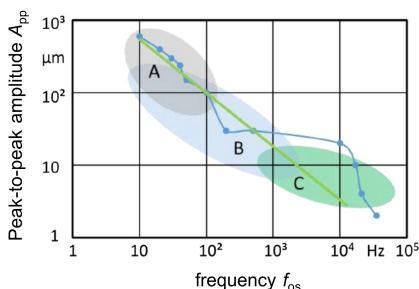


Figure 2.14 VAM actuator categories based on their achievable amplitude at variable frequencies, (A) Mechanical or hydraulic systems, (B) Electro-mechanical actuators, (C) Piezoelectric actuators; (Bleicher et al., 2018)

In Figure 2.15, several VAD devices with different operating principles are depicted. One such device, shown in Figure 2.15 (A), is a spindle unit from LTI motion GmbH/KEPA Group AG, which utilizes active magnetic bearings to generate vibration. This spindle unit allows for 3D movement in six degrees of freedom and enables trochoidal or helical machining in the presence of VAM. The spindle has a power rating of 6.5 kW at 12000 rpm. In addition to enabling VAD, the contact-free operation of magnetic bearings contributes to a longer spindle life. However, the complexity of dynamics control and process stability are some challenges associated with this particular system (Bleicher et al., 2019). Another type of VAD tool holder, developed by MITIS SAS, operates based on a mechanical principle, as shown in Figure 2.15 (B). The tool holder consists of a set of roller bearings, some of which have undulated rolling surfaces. The vibration frequency of these tool holders is fixed and correlated to the rotation frequency. In certain configurations, the amplitude can be adjusted by using a bearing stack with multiple undulated rolling surfaces that are phase-shifted relative to each other (Peigne, 2014). A piezo-electrically and hydraulically actuated horizontal spindle unit, developed by (Bleicher et al., 2018), is shown in Figure 2.15 (C). This spindle unit is capable of 3D movement in the x-, y-, and z-directions. It has a rated power of 6.5 kW and a maximum speed of 30000 min⁻¹. Air bearings are used to suspend the spindle rotor, while a hydraulic actuator applies vibration in the axial direction. Piezoelectric actuators with flexural hinges actuate the radial directions, specifically in the x and y directions. Mann (2010) developed a piezoelectric actuated tool holder for low-frequency, high-amplitude VAD applications, as shown in Figure 2.15 (D). The tool holder consists of a piezoelectric stack with a compression limit of

1800N. The rated unloaded displacement of the stack was $120\mu\text{m}$ at an applied voltage of +150V. A linear ball-spline bearing is employed to decouple torsion and bending from reaching the piezoelectric stack, as the stack is sensitive to such types of loads. To minimize the effect of large mass inertia on system dynamics, the vibration is applied only locally at the cutting tool.

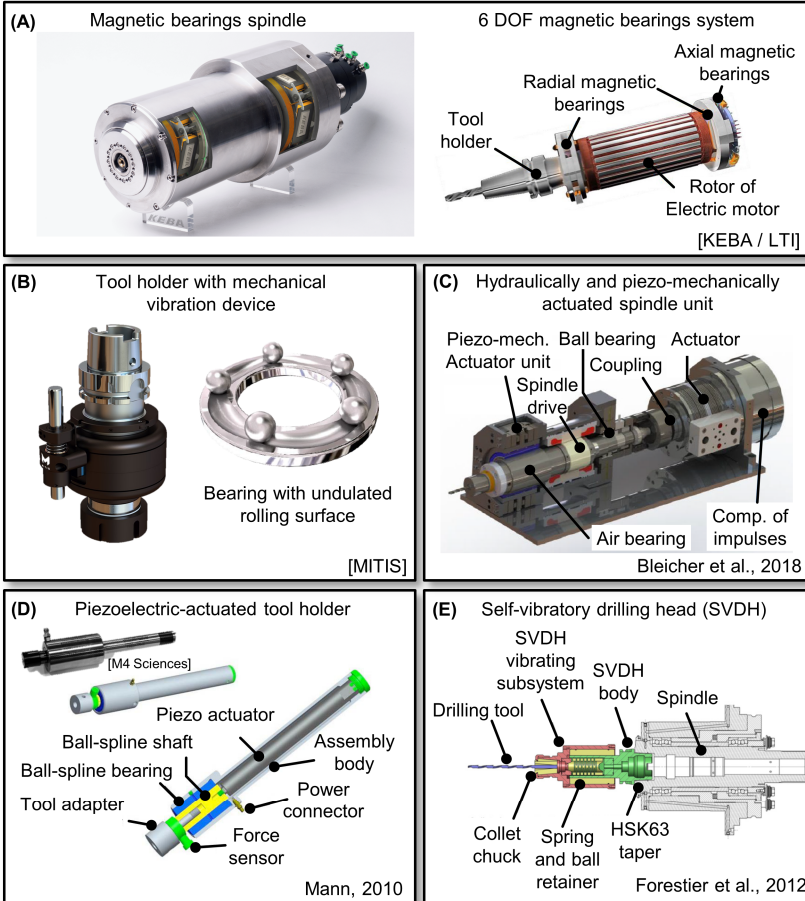


Figure 2.15 Devices for vibration assisted drilling (VAD), (A) Magnetic bearing spindle with six degrees of freedom; (Courtesy: LTI motion GmbH/KEPA AG), (B) Mechanical tool holder for VAD; (Courtesy: MITIS SAS), (C) Hydraulically and piezoelectrically actuated spindle unit; (Bleicher et al., 2018), (D) Piezoelectric-based tool holder for low-frequency high-amplitude VAD; (Mann, 2010). (E) Self-vibratory drilling head; (Forestier et al., 2012)

A self-vibratory drilling tool holder, shown in Figure 2.15 (E), was developed by (Paris et al., 2005), (Guibert et al., 2008), and (Forestier et al., 2012). This tool holder incorporates a set of springs to add flexibility to the system, where axial vibrations are self-excited by the drilling energy without

the need for external power, similar to the phenomenon of chatter. This configuration offers the advantage of being applicable in high-speed drilling operations. However, careful tuning of the added flexibility is a critical requirement to achieve satisfactory performance.

A recent extensive review of devices used in vibration-assisted machining was conducted by Zheng et al. (2020). Various devices used in different VAM applications were reviewed, including electro-hydraulic, electromagnetic, and piezoelectric devices in single or multi-directional VAM applications. In general, devices based on resonance and self-excited vibration are typically fixed in frequency and amplitude, while non-resonant vibration devices allow for more flexibility in selecting the frequency and amplitude.

2.5.3 Modelling of VAM

The literature also includes investigations into the fundamental aspects of VAM, including kinematics, dynamics, and thermomechanical behavior, where analytical or numerical models were proposed. Detailed kinematics of 1D and 2D VAM were presented by (Cerniway, 2002) and (Ladonne et al., 2015). Finite element (FE) modeling for turning Inconel 718 under VAM was carried out by (Babitsky et al., 2004), providing numerical results of the stress/strain state, cutting forces, and contact conditions at the tool/workpiece interface, compared with cutting experiments. (Mitrofanov et al., 2005) conducted thermomechanical FE modeling of ultrasonic vibration turning, while (Ahmed et al., 2007) proposed a 3D FE model of forces in ultrasonically assisted turning of Inconel 718. Numerous numerical investigations have been performed on VAM, but only a few analytical models have been proposed. (Nategh et al., 2012), (Razavi et al., 2012a), and (Razavi et al., 2012b) developed kinematic and dynamic analytical models of vibration-assisted oblique turning, validated by experimental investigations using aluminum workpieces.

Furthermore, there is limited research in the literature regarding the tribological behavior at the tool/workpiece interface under VAM. (Lotfi and Amini, 2016) conducted FE analysis and experimental investigations on the frictional behavior of the tool/chip interface in ultrasonic vibration machining of stainless steel 304. Temperature evolution models in interrupted machining, particularly for VAM, were addressed by (Kountanya, 2009). (Yan et al., 2018) proposed a mathematical model for the lubricant penetration of minimal quantity lubricant (MQL) under VAM in the turning process. Their investigation examined the capillary action that may occur between the tool and the workpiece, considering the varying micro-channel length due to applied vibration. The lubricant properties, cutting parameters, and VAM parameters were modeled and experimentally simulated. However, the experimental work performed to validate the proposed model of capillary rise was conducted in a laboratory environment where complications of the cutting process, such as heat, material flow, and deformation, were not considered. The cutting experiments were only performed to observe the effects of VAM under MQL on cutting forces, chip morphology, and tool wear.

The kinematic model for 1-D superimposed vibration in drilling, as described by Ladonne et al. (2015) with slight differences in variable symbols, will be provided in the following section. Using the kinematic model, several calculation examples will be presented to demonstrate the effects of vibration amplitude and frequency on the process.

Kinematic model of VAD

Conventional parameters such as feed, f , and spindle speed, N , describe tool's translation and rotation movements, respectively. The amplitude A and frequency f_{os} define the superimposed

oscillation movement. Assuming the vibration device generates a perfectly sinusoidal oscillation, the superimposed oscillations, s_{os} , can be expressed at each instant of time, t , using:

$$s_{os}(t) = A \cdot \sin(\omega \cdot t) \quad (2.21)$$

where

$$\omega = 2 \cdot \pi \cdot f_{os} \quad (2.22)$$

here, A is the amplitude and f_{os} is the oscillations frequency in Hz. The axial position, Z , and angular position, θ , of each point of the cutting edge, i , at radial position, r , can be calculated using Equations 2.23 and 2.24, respectively, for each instant of time, t , as:

$$Z(t, i, r) = Z_0(i, r) - \frac{f \cdot N}{60} \cdot t - A \cdot \sin(\omega \cdot t) \quad (2.23)$$

$$\theta(t, i, r) = \theta_0(i, r) - \frac{f \cdot \pi \cdot N}{60} \cdot t \quad (2.24)$$

Constants $Z_0(i, r)$ and $\theta_0(i, r)$ represent the axial and angular initial positions, respectively. With these equations, the axial trajectories of each edge of the tool can be plotted for different parameters. Figure 2.16 and Figure 2.17 provide examples that illustrate the effects of varying vibration amplitude and frequency.

These two graphs show that, depending on the value of the amplitude (for a given feed rate), cutting interruption can occur when the trajectories of the tool edges intersect. The boundary between continuous cutting and interrupted cutting corresponds to the point of tangency between two consecutive paths. Based on this, for a given feed rate f , oscillation frequency f_{os} , rotation speed N , and the number of flutes N_z , the amplitude corresponding to the boundary between continuous and interrupted cutting can be expressed as follows, where f_N represents the rotational frequency:

$$A_{limit} = \frac{f}{2 \cdot N_z \left| \sin\left(\frac{K_f \cdot \pi}{N_z}\right) \right|} \quad (2.25)$$

where

$$K_f = \frac{f_{os}}{f_N} = \frac{f_{os} \cdot 60}{N} \quad (2.26)$$

If the oscillation amplitude does not result in path intersection, the sinusoidal paths of the different cutting edges will not intersect. As a result, the cutting process remains continuous, with the vibratory assistance only affecting the thickness of the generated chips. In this scenario, the cutting height or the axial uncut chip thickness per cutting edge, H_z , can be determined by calculating the difference between two consecutive trajectories as follows:

$$H_z(t) = \frac{f}{N_z} + A \cdot \sin\left(\frac{K_f \cdot \pi}{N_z}\right) \cdot \cos\left(\omega \cdot t - \frac{K_f \cdot \pi}{N_z}\right) \quad \forall i, t \quad (2.27)$$

In this case, the axial uncut chip thickness is always positive and remains the same for each point on the cutting edges. As the cutting process is continuous, the surface formation will also be continuous. The surface altitude, $Z_{surface}(t, r)$, machined by cutting edge i , can be described at any given time instant t as follows:

$$Z_{surface}(t, \theta(t, i, r), r) = Z(t, i, r) \quad (2.28)$$

If the amplitude is set larger than the limit defined by Equation 2.25, the trajectories of the cutting edges will intersect. As a result, the edges will protrude out of the workpiece during the process, causing periodic interruptions in the cutting. Equation 2.28, which is used to define the cutting height, becomes inadequate in accurately describing the situation. To account for the discontinuity in VAD, a formula that describes the different configurations is required.

When the tool is engaged in the material, the axial uncut chip thickness will correspond to the distance between the surface at the bottom of the borehole and the cutting edge. On the other hand, when the tool is outside the material, there will be no cutting, and the axial uncut chip thickness will be zero. This can be expressed as follows:

$$H_z(t, i, r) = \begin{cases} Z_{surface}(t - dt, \theta(t, i, r), r) - s_{os}(t, i, r), & Z < Z_{surface} \\ 0, & else \end{cases} \quad (2.29)$$

Then, the surface position is updated at each time instant, t , during the calculation. If the cutting process is discontinuous, the surface formation will also be discontinuous. To calculate the surface position, both configurations need to be taken into account as follows:

$$Z_{surface}(t, \theta(t, i, r), r) == \begin{cases} Z(t, i, r), & Z < Z_{surface} \\ Z_{surface}(t - dt, \theta(t, i, r), r), & else \end{cases} \quad (2.30)$$

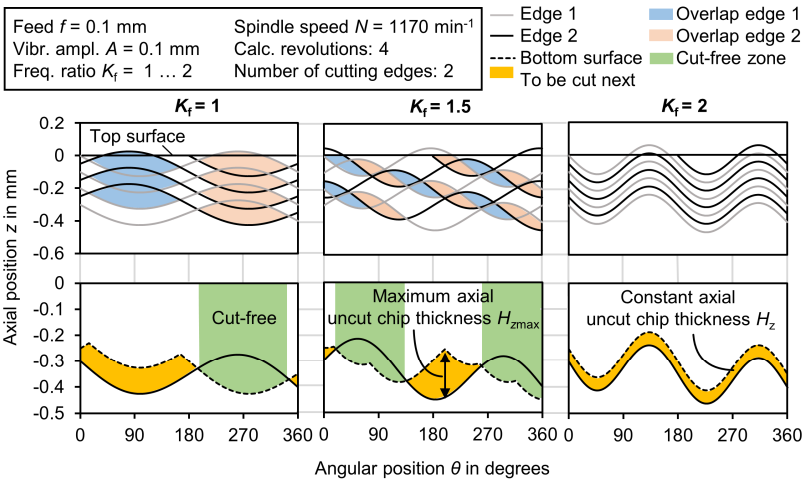


Figure 2.16 Superimposition of tool path in VAD, example of variable frequency ratio

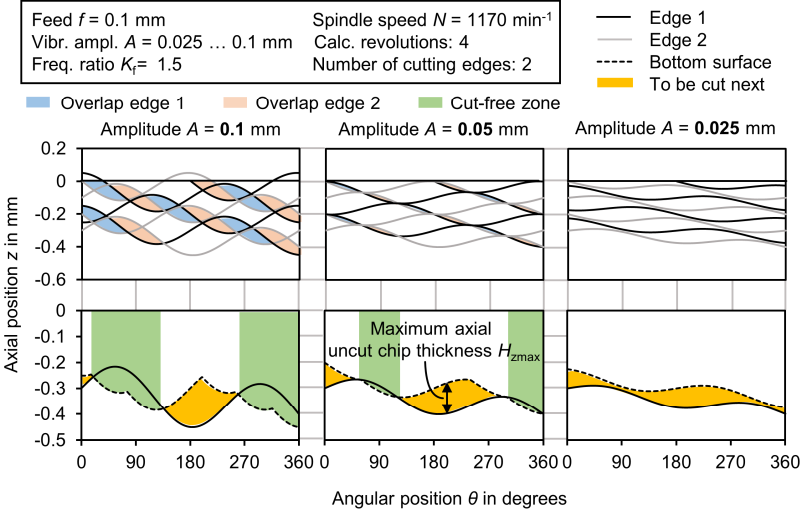


Figure 2.17 Superimposition of tool path in VAD, example of variable vibration amplitude

The minimum amplitude required to influence discrete chip formation in VAD, where the axial uncut chip thickness is zero, is given in Equation 2.25. The ratio necessary to ensure discrete chip formation, which is the ratio of vibration amplitude A to the axial uncut chip thickness per tooth H_z in the absence of superimposed vibration, is expressed as (Mann et al., 2011):

$$K'_A = A/H_z = 1/(2 \cdot \sin(\phi_v/2)) \tag{2.31}$$

where ϕ_v is the phase between spindle rotation and superimposed vibration, given by:

$$\phi_v = 2\pi(f_{os}/f_N - INT(f_{os}/f_N)) \tag{2.32}$$

Figure 2.18 illustrates the relationship between the ratio A/H_z and ϕ_v graphically. Since ϕ_v depends only on f_{os}/f_N in Equation 2.32, K'_A can also be plotted as a function of K_f , as shown in Figure 2.18 (B).

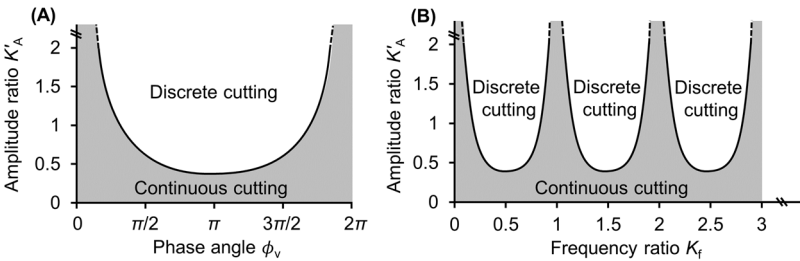


Figure 2.18 Frequency and amplitude relationships to ensure discrete chip formation in VAD. (A) Graphical representation as function of phase angle ϕ_v , (B) Graphical representation as function of frequency ratio; adapted from (Mann et al., 2011)

(Yang et al., 2019) developed analytical model for predicting drilling thrust force and torque in low frequency vibration assisted drilling. The stiffness of the vibration system has been considered and the amplitude and frequency of superimposed vibration was corrected accordingly. Several calculation element were considered depending on cutting edge morphology and cutting mechanism of VAD.

Chapter 3: Objectives and Methodology

Intensive energy consumption and the impact of metal-working fluids (MWF) are two major causes influencing sustainability in machining. Eliminating MWF by dry machining can be the optimal solution. However, this solution was proved to have limited applicability. Near-dry machining using the minimum quantity lubrication (MQL) approach is a promising technique with demonstrated capabilities. State-of-the-art understandings of the tribological system within tool-chip and tool-workpiece interfaces suggest fundamental limitations for MWF access into contact zones due to high mechanical and thermal loads. The theory of two-zone friction conditions (i.e. sticking and sliding) within the tool-chip interface proposes that MWF penetrates only within the sliding zone of the contact. Since MWF are mainly used to provide cooling, lubricating, and chip removal functions, the effectiveness of the lubricating qualities of MWF becomes quite limited within the contact zones leading to severe frictional conditions. Interrupting the cutting process allows the contact to be exposed to the environment and the heating cycle to be discontinued for a period of time.

Therefore, the main objective of this work is to fundamentally investigate the effectiveness of MWF, particularly MQL, in reducing tool-chip contact in interrupted orthogonal machining of Austenitic stainless steel 1.4305 and nickel-based superalloy Inconel 718. The research quantifies adhesion marks on the rake face during orthogonal cutting using a special method and measures the resulting contact zones from different cutting and interruption intervals. The research also investigates the initial period of chip formation (IPCF), which is characterized by minimal contact between the tool and chip, indicated by smaller tool-chip contact and low mechanical loads. The research further explores whether IPCF can be sustained in subsequent cutting intervals by varying the interruption length, which allows the tool to be exposed to the environment for different durations. To determine the distance at which IPCF ends, a sigmoid function is fitted to the average apparent coefficient of friction (COF), calculated from experimentally measured mechanical loads. The transition distance is evaluated at variable cutting speed to determine whether IPCF is a distance-related phenomenon.

Moreover, to determine the existence of a transition temperature corresponding to a transition distance, a two-dimensional (2D) transient thermal model by (Karaguzel, 2021) is adapted with some modifications to be applicable to IPCF. The model consists of two parts: one focuses on analytically identifying the input heat flux along the rake face and the cutting path using experimental data as input parameters, while the other calculates the tool's temperature field by numerically solving a transient partial differential heat equation using finite element method (FEM), accounting for tool's temperature-dependent thermal properties. To validate the model's results for the average rake face temperature, they are compared with the measurements obtained using a two-color ratio pyrometer at a specific cutting distance. The identification of the transition cutting distance and its associated transition temperature provides a deeper understanding of the underlying physical mechanics of the initial period of chip formation (IPCF).

As reported in the literature, inherently interrupted machining operations, such as milling, result in lower average temperatures and lower tool wear compared to continuous machining operations like turning and drilling. However, applying interruptions to continuous operations requires process adaptations. In this work, case studies were conducted on Inconel 718 to explore incorporating interruptions into drilling operation. These case studies aim to identify the challenges and opportunities associated with transferring the findings of fundamental investigations to practical applications. Initially, interrupted drilling is achieved using a custom peck drilling cycle. However,

using peck drilling is expected to result in a relatively long total process time with low material removal rate. In order to investigate a relatively higher range of cycle frequencies, a faster approach is required. Consequently, a hydraulic actuator is designed and constructed in-house to facilitate vibration-assisted drilling (VAD), enabling interruptions through superimposed oscillations on the feed. The actuator enables flexible selection of vibration amplitude and frequency. The effects of vibration amplitude and frequency are investigated against tool life and mechanical load.

High thermal and mechanical loads are expected to lead to severe tribological conditions within the tool-chip contact. These conditions result in adhesion, which is influenced by various complex physical and chemical interactions. The hypothesis of this research suggests that by introducing interruptions along the cutting path, the impervious contact region can be accessed by contaminants (e.g. lubricants), thereby mitigating the severity of the contact. As a result, interrupted machining is anticipated to yield positive outcomes from a tribological stand point. Figure 3.1 provides a schematic overview of the investigations conducted in this dissertation.

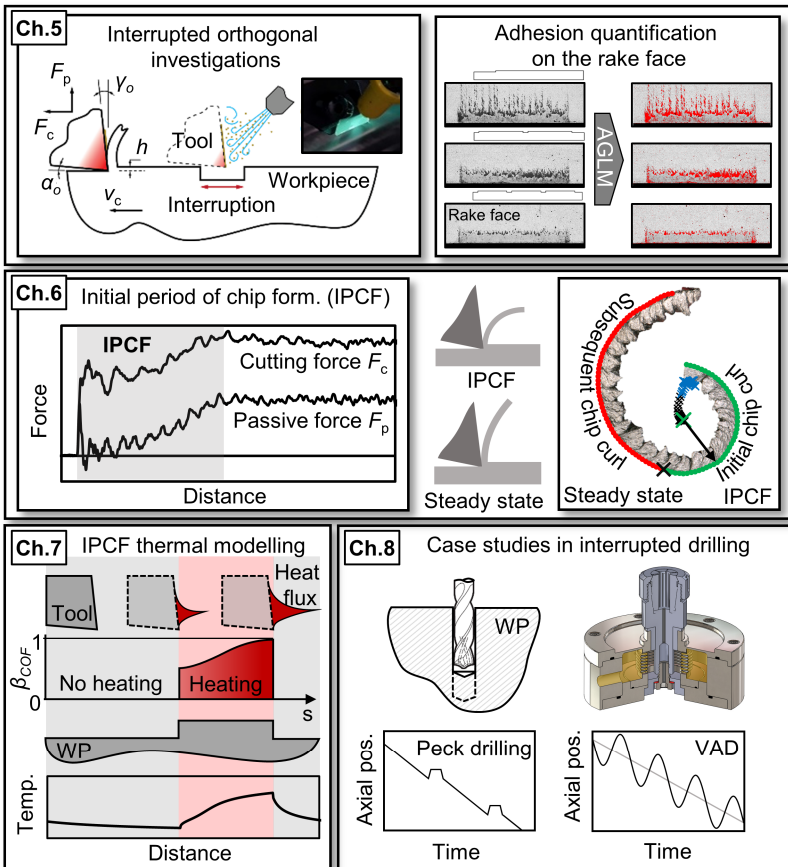


Figure 3.1 Investigations overview in this dissertation

Chapter 4: Experimental Boundary Conditions

In this chapter, workpiece materials, tools, machines, and measurement equipment used in the context of this thesis are described. The relevant properties and specifications of materials and equipment are listed. Descriptions of in-situ measurement techniques used to evaluate mechanical loads, displacement, temperature, and high-speed imaging are provided. The chapter also includes a description of ex-situ measurement techniques using various microscopes to determine surface conditions and morphology.

4.1 Workpiece materials

Two workpiece materials were considered in the context of this dissertation. One is the nickel-based superalloy Inconel 718, and the other is the austenitic stainless steel 1.4305. The two materials were selected due to their behavior related to adhesion tendency, relatively low thermal conductivity, and their special characteristics regarding machinability at different ranges of cutting speeds. The following section summarizes their properties and main characteristics.

4.1.1 Workpiece material: Inconel 718

Inconel 718 is the commercial name of the nickel-based superalloy NiCr19Fe19Nb5Mo3 (material number: 2.4886) according to the German standard DIN EN 10302. It is also known as UNS N07718 according to the American standard ASTM B637-18. The alloy offers high corrosion and creep resistance at elevated temperatures. Due to its desirable thermomechanical properties, this alloy finds applications where high temperatures and high mechanical loads exist (Bartolomies et al., 2021). For instance, it is used in the hot segments of aero engines and power generation turbines, rocket engine nozzles, nuclear reactors, and in the exhaust systems of performance automotive vehicles.

Inconel 718 contains a relatively large number of alloying elements and a significant amount of iron, therefore it is referred to as a nickel-iron superalloy. The choice of nickel as the solvent for these elements is justified by its face-centered-cubic (FCC) crystal structure (Reed, 2006). The chemical composition and mechanical properties, according to DIN EN 10302, are listed in Table 4.1.

Table 4.1 Chemical composition and mechanical properties of Inconel 718*

Chemical composition in wt.%					
Ni	Cr	Fe	Nb + Ta	Mo	Ti
50.0 to 55.0	17.0 to 21.0	Balance	4.7 to 5.5	2.8 to 3.3	0.6 to 1.2
Mn (max.)	Co	Cu (max.)	S (max.)	Si	Al
0.35	≤ 1.0	0.3	0.015	≤ 0.35	0.30 to 0.70
P (max.)	C	B			
0.015	0.02 to 0.08	0.002 to 0.006			
Mechanical Properties					
$R_{p0.2}$ in MPa	R_m in MPa	$A\%$			
1030 (min.)	1230 (min.)	12			

*According to DIN EN 10302

In general, nickel-based superalloys are complex alloys with various microstructural features that contribute to the control of the mechanical properties (Furrer and Fecht, 1999). The microstructure

includes the gamma (γ) phase with an FCC structure, where a continuous matrix phase is formed, and other phases reside within it. The microstructure of Inconel 718 is shown in Figure 4.1. The gamma prime (γ') and ordered gamma double prime (γ'') form hardening or precipitate phases. Precipitation hardening of Inconel 718 (+P) according to DIN EN 10302 is achieved by heating the material to between 710 and 730 °C for 8 hours, then oven cooling and holding it between 610 and 630 °C for a total heat treatment time of 18 hours.

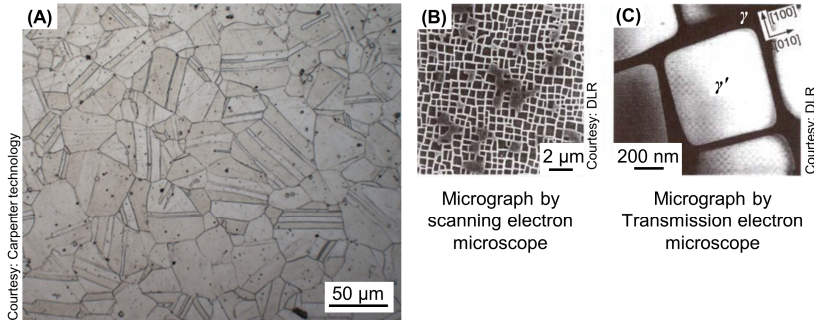


Figure 4.1 (A) Inconel 718 microstructure, (B) and (C) Micrographs showing typical γ and γ' phases of nickel-based superalloys

According to Reed (2006), nickel-iron superalloys like Inconel 718, which contain niobium, do not primarily strengthen through γ' but instead through a body-centered tetragonal (BCT) ordered compound of Ni_3Nb called γ'' . The γ'' precipitate exhibits a disc-shaped morphology, with a thickness often as small as 10 nm and a diameter of about 50 nm. Inconel 718 is widely used in polycrystalline cast-and-wrought form, offering excellent high-temperature properties up to operating temperatures of approximately 650 °C due to the coherency strains so imparted and the limited number of available slip systems operating in γ'' .

Pulidindi and Prakash (2020) found that Inconel 718 holds over 54% of the nickel superalloy market share, equivalent to over \$4 billion in 2019, making it the largest nickel superalloy used globally. The substantial lattice misfit between γ'' and γ enables the strain-hardening properties of Inconel 718 (Zhang et al., 2020). Inconel 718 consists of different percentages of constituent phases, approximately 3% γ' and approximately 20% γ'' (Mignanelli et al., 2017).

Nickel-iron alloys, which are strengthened by the γ'' phase, are prone to the formation of an orthorhombic Nb-rich δ phase in the overaged condition. This δ phase is inherently incoherent with γ and, therefore, does not confer strength even when present in significant quantities (Reed, 2006). Carbides and borides reside on the grain boundaries of the γ phase. A significant amount of hard carbides, such as TiC and NbC , which hinder dislocations, also contribute to the high abrasive behavior observed during machining (Zhou et al., 2012).

While this alloy can offer great advantages from an application and design perspective, it is considered one of the most difficult-to-cut materials due to its high material strength and low thermal conductivity. The thermal conductivity and specific heat of Inconel 718 are estimated to be $k = 10.1 \text{ W/mK}$ and $c = 0.43 \text{ J/gK}$ at 20°C, respectively (Kim and Lee, 2014). As a result, conductive heat transfer is limited through the workpiece and chips, leading to high temperatures being generated in the cutting zone (Bartolomies et al., 2021).

4.1.2 Workpiece material: Austenitic stainless steel 1.4305

The second workpiece material used in the context of this thesis is austenitic stainless steel 1.4305. According to DIN EN 10088-3, the material designation is X8CrNiS18-9 with a material number of 1.4305. In the American standard ASTM A582/A582M, it is designated as UNS S30300 or AISI grade 303. It is considered a free-machining stainless steel due to its high sulfur content. The chemical composition and mechanical properties of austenitic stainless steel 1.4305 are listed in Table 4.2

Table 4.2 Chemical composition and mechanical properties of austenitic stainless steel 1.4305*

Chemical composition in max. wt.%					
C	Si	Mn	P	S	Cr
0.1	1.00	2.00	0.045	0.15 to 0.35	17.0 to 19.0
Ni	N	Cu	Fe		
8.0 to 10.0	0.10	1.00	Balance		
Mechanical Properties					
$R_{p0.2}$ in MPa	R_m in MPa	$A\%$			
190 (min.)	500 to 750	35			

*According to DIN EN 10088-3

In general, austenitic stainless steels have many advantages from a metallurgical point of view. They can be made soft (i.e., with a yield strength around 200 MPa) or strong through cold working, achieving yield strengths of over 2000 MPa. Their austenitic (FCC, face-centered cubic) structure is very versatile in terms of toughness. Compared to ferritic (BCC, body-centered cubic) iron-based steel alloys, they maintain their strength over a broader range of elevated temperatures. Their corrosion resistance can be adjusted to withstand various environments. The austenitic grades are the most commonly used stainless steel grades mainly because, in many instances, they provide highly predictable levels of corrosion resistance along with excellent mechanical properties. Austenitic stainless steels are more highly alloyed and are more prone to higher work-hardening rates. The microstructure of austenitic stainless steel 1.4305 is shown in Figure 4.2.

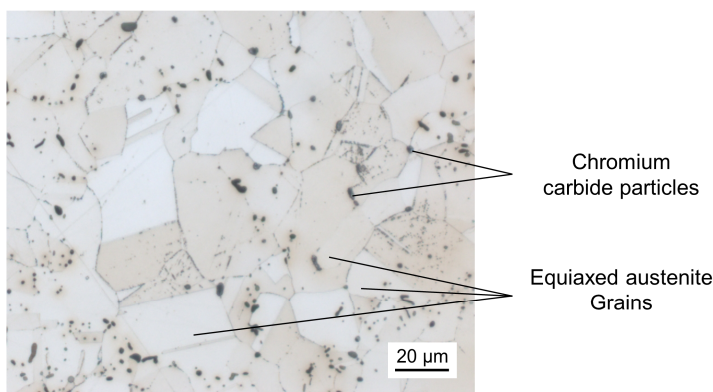


Figure 4.2 Austenitic stainless steel 1.4305 microstructure

Austenitic stainless steels are typically difficult-to-machine materials due to their work-hardening tendency. The yield-to-tensile ratio of austenitic stainless steel is very large, making it hard to break

chips. The higher strength and higher ductility of stainless steels also tend to increase cutting temperatures, necessitating the use of tools with higher heat resistance. Built-up edge (BUE) is another issue when machining stainless steels, as it affects the surface quality of machined products. Many attempts have been made to improve the machinability of these steels by adding free-machining elements, such as sulfur, lead, selenium, and tellurium (Akasawa et al., 2003). Higher sulfur levels are correlated with better machinability, and sulfur remains the popular additive choice, as other additives have their own disadvantages (e.g., lead toxicity). The role of sulfur as a machinability agent in stainless steels is very complex and not necessarily straightforward, but in general, sulfur has been extremely beneficial in increasing the machinability of stainless steels. Generally, as the molten metal cools and solidifies, sulfur combines with manganese to form manganese sulfide inclusions. Sulfide inclusions form weak planes that mechanically weaken the steel, allowing for chip breakage. The deformation caused by the severe bending of the chip during cutting leads to the chip breaking at the sulfide striations. Additionally, a small amount of manganese sulfide is deposited on the tool surface at the tool-chip interface, providing a solid lubricating layer between the chip and tool, thereby reducing friction. However, sulfides in stainless steels have disadvantages, especially when sulfur levels exceed 0.15%. It is well-documented that sulfides negatively affect the corrosion resistance and mechanical properties of stainless steels. Sulfur tends to form segregated films with low melting points during solidification. Since these films are low in strength, they may induce the formation of microcracks caused by solidification shrinkage stresses. Further processing of these materials can exacerbate the formation of cracks, resulting in poor processing yields. Sulfur affects corrosion resistance by locally depleting chromium from the matrix, causing it to precipitate as a sulfide. These manganese sulfide inclusions become exposed on the surface of the bar and serve as initiation sites for pitting corrosion (McGUIRE, 2008).

4.2 Cutting tool material

Cemented carbide tools (WC) were utilized in two different investigations. In orthogonal cutting experiments, uncoated tungsten carbide insert (TPGN160308 H13A), with a triangular shape and a cutting edge radius of $r_{\beta} = 8 \mu\text{m}$, was attached to the tool holder (CTFPL2525M16), both manufactured by Sandvik. The resulting rake angle was $\gamma_o = 6^\circ$, and the clearance angle was $\alpha_o = 5^\circ$. Similar geometry inserts from manufacturer Ceratizit (TPUN160308FN H10T) were also used.

For drilling investigations, coated and uncoated twist drilling tools of type 8521, with a diameter of $d = 6.8 \text{ mm}$ and a point angle $\sigma_T = 140^\circ$, were employed. These solid carbide drilling tools were supplied by manufacturer Gühring KG. The coated drilling tools were coated with a TiAlN/TiN multilayer coating. The tool geometry incorporates web thinning, a relieved cone, and a slightly concave main cutting edge with optimized cutting edge geometry. A brief summary of the tools is shown in Figure 4.3.

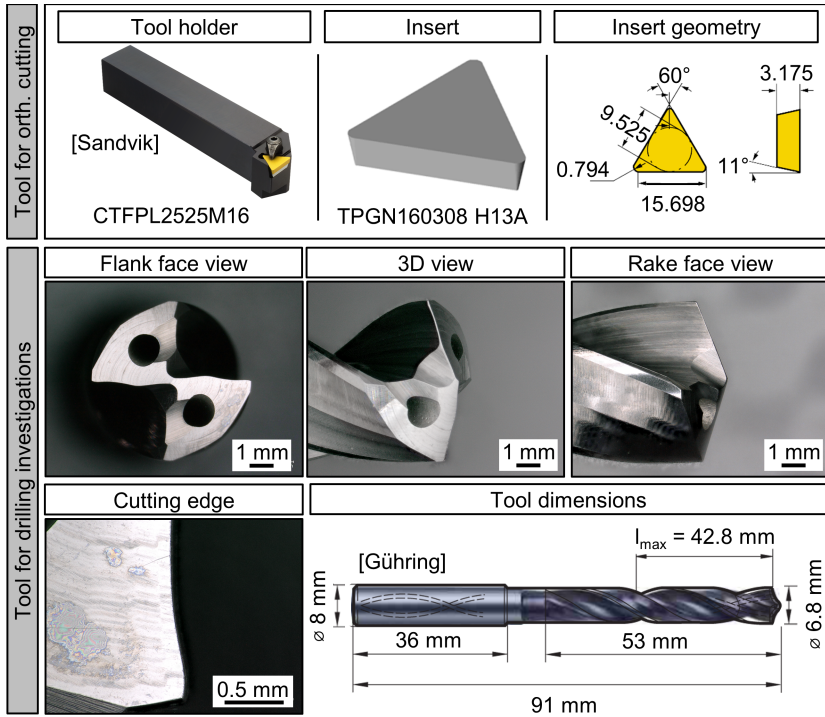


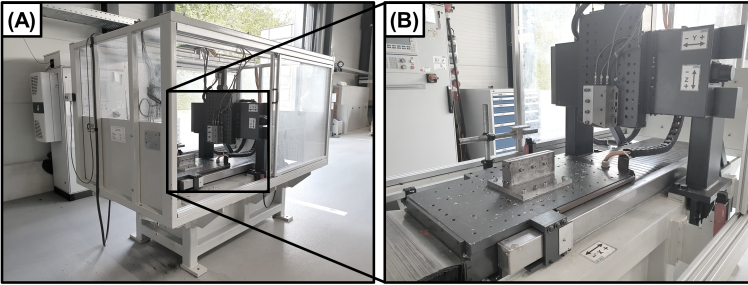
Figure 4.3 Cutting tools

4.3 Machine tools

Two machine tools were used. On one hand, a special machine tool was used for conducting orthogonal cutting experiments. On the other hand, drilling experiments were performed on a horizontal milling machine.

4.3.1 Machine tool for orthogonal cutting investigations

A custom-made machine tool was used to conduct orthogonal experiments in the context of this dissertation. The machine used for chip formation analysis is a special machine based on the model PFS 5558/1 from the company Heinz Berger Maschinenfabrik GmbH & Co. KG. It has three axes that are utilized for positioning and feed movement. The machine, along with its specifications, is shown in Figure 4.4.



Machine type: Chip formation analysis machine, **Model:** Berger PFS 5558/1

Axis	Range of travel	Max. acceleration	Max. speed
x-axis	900 mm	30 m/s ²	180 m/min
y-axis	200 mm	10 m/s ²	15 m/min
z-axis	95 mm	10 m/s ²	15 m/min

Figure 4.4 Machine tool for orthogonal cutting and chip formation analysis, (A) External view, (B) Internal view

The horizontal table is moved along the x-axis by linear direct drives, allowing for a maximum acceleration of $a_{\max} = 30 \text{ m/s}^2$ and a traverse path of $x_{\max} = 900 \text{ mm}$, resulting in a maximum speed of $v_{\max} = 180 \text{ m/min}$. This capability enables the coverage of a wide range of cutting speeds typically encountered in drilling and turning operations. The cross table, operating in the y-z plane, is driven by ball screws and has a range of motion of $y_{\max} = 200 \text{ mm}$ or $z_{\max} = 95 \text{ mm}$. The generous design of the working space ensures excellent accessibility to the effective point and facilitates the installation of various measuring devices. For instance, a dynamometer and a high-speed microscope can be employed for detailed process analysis. In this dissertation, the machine was utilized to investigate chip formation using both continuous and interrupted workpieces.

4.3.2 Machine tool for drilling investigations

The drilling investigations were carried out using a machine tool from GROB-WERKE GmbH & Co. KG, as shown in Figure 4.5. The machining center features a horizontally mounted spindle, commonly employed in the automotive industry, particularly in the production of cylinder heads, due to its advantageous chip removal facilitated by gravity. The 4-axis machining center, GROB BZ40CS, is equipped with a spindle capable of reaching maximum speeds of $N_{\max} = 24000 \text{ min}^{-1}$. The spindle-tool holder interface is designed as a hollow shank taper of type HSK-A63, enabling the direct connection of a rotary dynamometer, specifically the type 9125A from Kistler, for mechanical load measurement.



Machine type	CNC machining center
Model	GROB BZ 40 CS
Spindle orientation	Horizontal
Spindle interface	HSK-A63
Maximum spindle rotation speed	$N_{\max} = 24000 \text{ min}^{-1}$
Maximum Spindle power	$P_{\max} = 44 \text{ kW (40\%ED)}$ $P_{\max} = 34 \text{ kW (100\% ED)}$
Axes travel range X/Y/Z (mm)	500 / 500 / 500
Max. feed speeds X/Y/Z (mm/min)	40000 / 50000 / 60000

Figure 4.5 Machine tool for drilling investigation analysis and machine specifications

The machine spindle power is rated at $P = 34 \text{ kW}$ and can provide a maximum power of $P_{\max} = 44 \text{ kW}$. The spindle has a maximum range of motion in the x-direction, reaching $x_{\max} = 500 \text{ mm}$ at a maximum traverse speed of $v_{ix} = 40000 \text{ mm/min}$. In the y-direction, the maximum range of motion is $y_{\max} = 500 \text{ mm}$, with a maximum traverse speed of $v_{iy} = 50000 \text{ mm/min}$. Similarly, in the z-direction, the spindle can move up to $z_{\max} = 500 \text{ mm}$ at a maximum traverse speed of $v_{iz} = 60000 \text{ mm/min}$. An additional axis, the c-axis, allows for the rotation of the machine table up to 360° . The table pallet size measures 500 mm by 500 mm . A pumping unit is attached to the machine, capable of supplying metalworking fluids up to $p = 80 \text{ bar}$. Moreover, the machine is equipped with a modern programmable computer numerical control unit, the SINUMERIK 840D from Siemens AG.

4.4 Hydraulic aggregate for vibration assisted drilling

A compact hydraulic aggregate was modified and used in combination with a custom-built hydraulic actuator to enable vibration-assisted drilling investigations. The aggregate comprises a 3-phase electric motor rated at $P = 3 \text{ kW}$ with a fixed rotation speed of $N = 2810 \text{ min}^{-1}$. This electric motor drives a gear hydraulic pump, which is rated for a maximum pressure of $p_{\max} = 210 \text{ bar}$ and a volume flow rate of $Q = 2 \text{ cm}^3/\text{turn}$. The hydraulic pump is submerged in an 8-liter hydraulic tank. The hydraulic aggregate includes a manifold with various ports, allowing for the installation of modular valves with NG 6 port configuration according to DIN 24 340 form A. The hydraulic system incorporates a 4/4 fail-safe servo solenoid valve model 4WRPEH from Bosch Rexroth AG, equipped with an on-board electronics (OBE) module. Additionally, two pressure relief valves were installed on ports A and B. The aggregate is fitted with a return-line cooler, as shown in Figure 4.6. A detailed description of the hydraulic system and the developed actuator will be further discussed in Chapter 8.

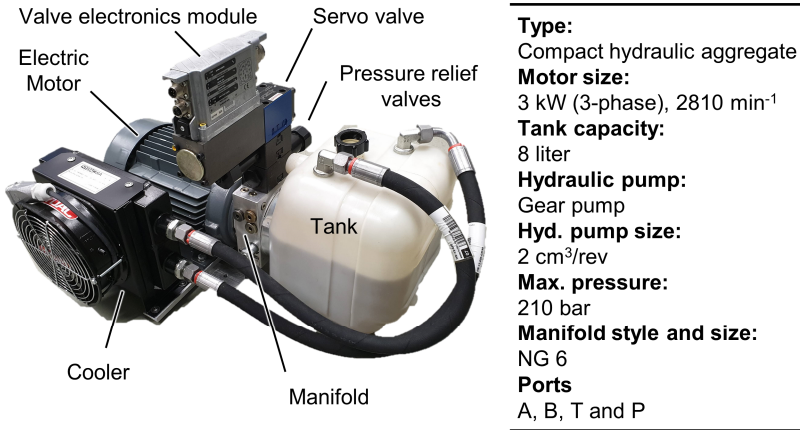


Figure 4.6 Compact hydraulic aggregate equipped with a servo valve

4.5 Preparation of minimum quantity lubrication (MQL)

The Minimum Quantity Lubrication (MQL) technique was used to supply lubricants to the cutting zones. In orthogonal investigations, the MQL aerosol is prepared remotely using a special aerosol generation device and supplied through a nozzle directed at the cutting zone. In drilling investigations, one-channel MQL is supplied through internal ducts within the tool. The MQL oil used in all cases was an Ester (80%) synthetic oil, specifically Vascomill MMS HD1, manufactured by Blasser Swisslube AG. This oil has a viscosity $\eta = 40 \text{ mm}^2/\text{s}$ at 40 °C and a flashing point at $T_{fl} = 200 \text{ °C}$. It contains 16% Sulfur.

4.5.1 MQL in orthogonal cutting investigations

Within the scope of the orthogonal investigations, an MQL aerosol generation device from HPM Technologie GmbH was utilized, as shown in Figure 4.7. The device has a maximum permissible pressure of $p_{\max} = 16 \text{ bar}$; however, only 6 bar was used. The MQL device consists of two mixing nozzles that pneumatically atomize oil using compressed air inside a tank. Additionally, the tank is supplied with additional compressed air to enable controllable MQL pressure and flow, with minimal impact on the air/oil mixing ratio settings. Maintaining a pressure difference of 1.5 bar between the nozzle pressure and the tank pressure is crucial to ensure proper airflow through the nozzles. The position of a needle located within the nozzles can be adjusted using a micrometer-like setting device to achieve variable aerosol quality. The output MQL aerosol supply was connected to an external nozzle, which was directed at the cutting tool during the orthogonal cutting investigations.

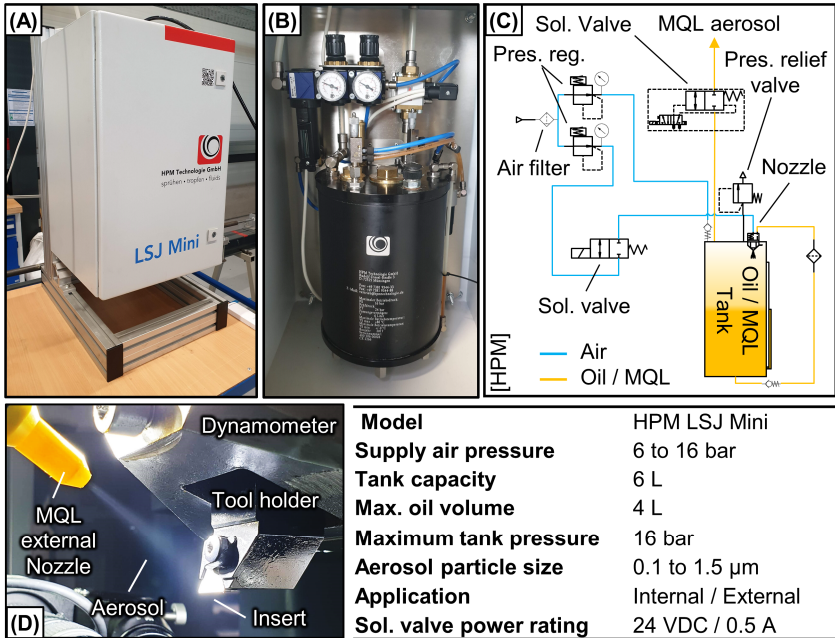


Figure 4.7 MQL aerosol generation device, (A) External view, (B) Internal view, (C) Pneumatic diagram, (D) MQL aerosol in application

4.5.2 MQL in drilling investigations

The integration of one-channel MQL into the horizontal milling machine GROB BZ40CS through a rotary union is shown in Figure 4.8, along with details of the equipment used and flow measurement devices. Compressed air is supplied from the utility at approximately 6 bar. The air pressure was boosted to 12 bar using a pneumatic booster from FESTO GmbH, specifically the type DPA-100-16-CRVZS20. A pressure regulator is employed to adjust and maintain the pressure. The MQL is generated using a special mixing nozzle connected to oil and compressed air supply lines. The actual aerosol generation occurs within this nozzle by atomizing the MQL medium with the assistance of a primary air stream. Furthermore, the measurement devices indicated in Figure 4.8 were utilized to record both air and oil volume flow rates. An air flow meter based on the calorimetric principle, manufactured by TESTO GmbH (type 6441), was used to measure the air flow rate. For oil flow rate measurement, a flow meter from Bronkhorst (type mini CORI-FLOW M12) was employed, which measures low quantity flow based on the Coriolis measuring principle. Since the oil passes through small tubes within the flow meter, a differential pressure is required. To achieve this, a pressurized oil tank located upstream was utilized, with the oil tank pressure set at 14 bar. A downstream needle valve was used to adjust the oil flow rate. The air flow meter provides current signals ranging from 4 mA to 20 mA. Flow meter signals were simultaneously measured in a data acquisition system along with mechanical loads during drilling operations. Separate current input modules (type 9203) from National Instrument Corporation were employed to process the current signals.

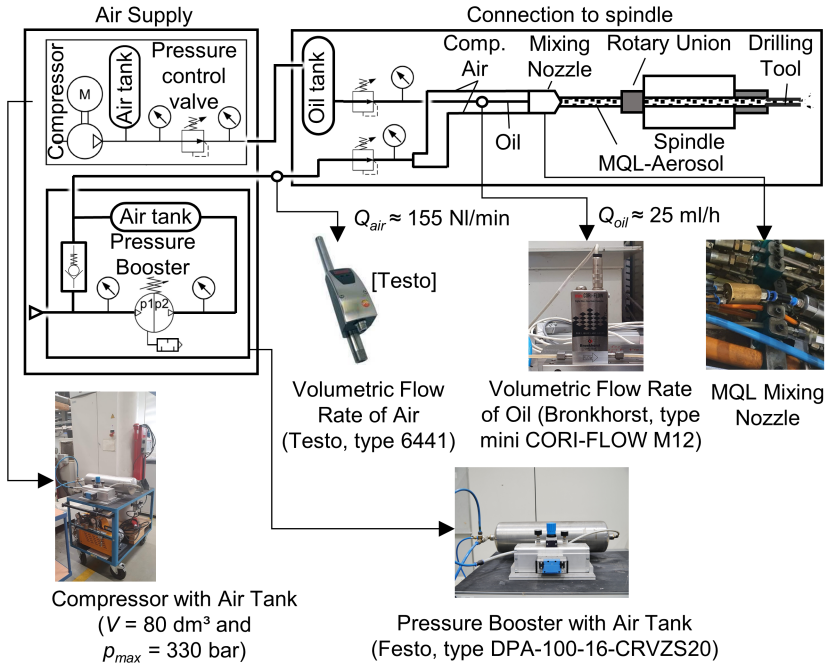


Figure 4.8 One-channel MQL setup used in drilling investigations with oil and air flow rates measurements

4.6 In-situ process variables measurement technology

In this section, a description of in-process variable measurements is provided. Measurements techniques of mechanical load, temperature, displacement, and high-speed video imaging are discussed.

4.6.1 Mechanical load

For the recording of the mechanical tool load, Three different piezoelectric dynamometers from Kistler Instrumente AG were used. The dynamometers are piezoelectric force transducers that generate a charge proportional to the strain caused by the applied mechanical load. A summary of the dynamometer specifications is shown in Figure 4.9.

The force measuring platform, type 9263, offers the possibility to measure mechanical loads of up to 10 kN in the x- and y-directions and 20 kN in the z-direction. This dynamometer was attached to a platform sliding on the cross rail of the Berger machine. According to the manufacturer of the dynamometer, its lowest natural frequency is $f_n > 2.5 \text{ kHz}$, stiffness $k_c \approx 2 \text{ kN}/\mu\text{m}$, with a response threshold of less than 0.1 N. For signal conditioning, Kistler KIAG SWISS type 5001 charge amplifiers were used to convert the charge signals to proportional voltage signals. The charge amplifiers amplify the signal using calibrated gain factors to within $\pm 10\text{V}$. Multi-channel data acquisition from TEAK Corporation KK type GX1 integrated recorder was used to collect the data

at a sampling frequency $f_s = 50$ kHz upon manual trigger before cutting occurrence. After proper analog-to-digital conversion, a computer was used to store and display the data.


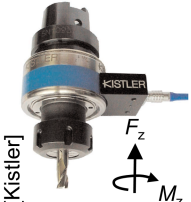
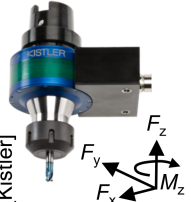
			
Dynamometer model	Kistler Kiag 9263	Kistler 9125A	Kistler 9170A
Signal conditioner	Kistler Kiag 5001	Kistler 5237	Kistler 5328B
Dynamometer type	Piezoelectric	Piezoelectric	Piezoelectric
Measurement directions	F_x, F_y, F_z	F_z, M_z	F_x, F_y, F_z, M_z
Load range	$F_x = -10 \dots 10$ kN $F_y = -10 \dots 10$ kN $F_z = 0 \dots 20$ kN	$F_z = -3 \dots 3$ kN $M_z = -50 \dots 50$ Nm	$F_x, F_y = 0 \dots 3$ kN $F_z = 0 \dots 18$ kN $M_z = 0 \dots 100$ Nm
Bandwidth	> 2.5 kHz (Lowest natural frequency)	1 kHz (cut-off frequency)	In x and y (2 kHz), In z (7.6 kHz)
Machine interface	N/A	HSK-A63 (DIN 69893-1)	HSK-A63 (DIN 69893-1)
Tool holder type	N/A	Collet chuck ER 32 (DIN 6499-B32)	Collet chuck ER 32 (DIN 6499-B32)
Maximum spindle speed	N/A	25000 min ⁻¹	20000 min ⁻¹

Figure 4.9 Dynamometers used in mechanical load measurements

For drilling investigations, the feed force and drilling torque were measured on the tool side with the aid of rotating dynamometers, specifically types 9125A and 9170A from Kistler Instrumente AG. The initial peck drilling investigations utilized the 9152A rotating dynamometer, which measures axial force within a range of $F_z = -3 \dots 3$ kN and torque within a range of $M_z = -50 \dots 50$ Nm. The 9170A rotating dynamometer was used for vibration-assisted drilling investigations due to its higher mechanical load capacity. It measures axial force within a range of $F_z = 0 \dots 18$ kN and torque within a range of $M_z = 0 \dots 100$ Nm. Although the rotary dynamometers have the capability to measure forces in the x- and y-directions, these measurements were not used in the investigations. The rotary dynamometers convert the charge signal into a digital signal using the electronics integrated in the rotor, which is then transmitted inductively to the stator. Signal conditioning devices, namely the type 5237 for the 9152A dynamometer and the type 5328B for the 9170A dynamometer, were used to process the signals. Both signal conditioning devices are from Kistler AG. They handle further data processing and convert the measured values into analog voltage signals within a range of ± 10 V. To collect the analog voltage signals, a voltage input module of type 9239 from National Instruments (NI) Corporation was connected to a USB-based data acquisition

system of type cDAQ 9172, also from the same manufacturer. The data is then communicated to the measuring computer at a sampling rate of $f_s = 10$ kHz.

4.6.2 Temperature measurement

To determine the thermal load, the two-color ratio pyrometer, Fire III, manufactured by Energy Engineering Aachen (en2AIX) GmbH, was used. The pyrometer operates at wavelengths $\lambda_1 = 1.675 \mu\text{m}$ and $\lambda_2 = 1.945 \mu\text{m}$. It has a maximum sampling rate of $f_s = 500$ kHz and a temperature range of $T = 250 \dots 1200$ °C. The pyrometer system utilized a fiber optic cable with a diameter of $d_{fo} = 330 \mu\text{m}$. The use of fiber optic technology enables measurements in confined spaces. Figure 4.10 illustrates the pyrometer's specifications and its optical schematic.

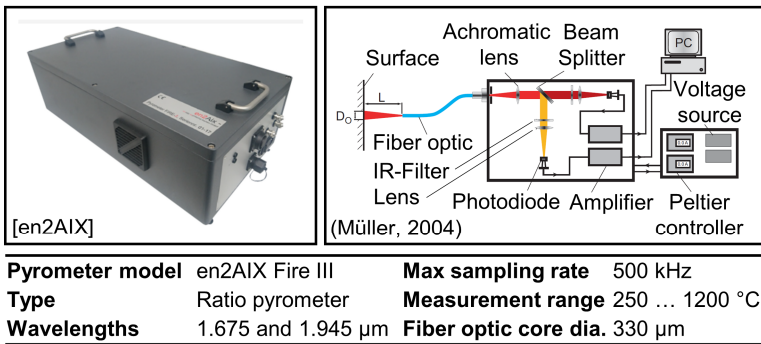
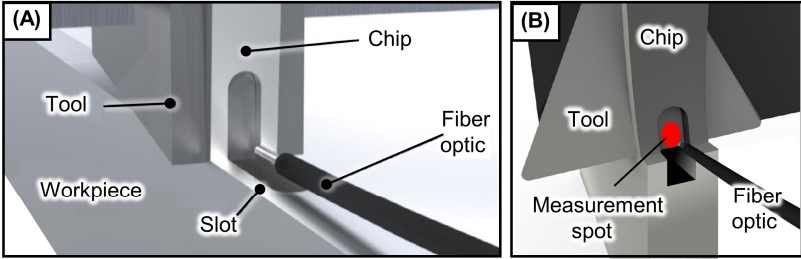


Figure 4.10 Two-color ratio pyrometer specifications

The actual measurement spot diameter in ratio pyrometric analysis depends on several factors, including the fiber optic core diameter, the fiber optic numerical aperture, and the distance to the measurement object. In addition to non-contact and high-speed temperature measurement, a major advantage of using ratio pyrometry compared to single-wavelength pyrometry is the assumption of negligible emissivity variation on the surfaces being measured. This assumption is based on the small difference between the two detected wavelengths. As a result, the emission coefficients for the slightly varying wavelengths 1 and 2 can be omitted from the calibration polynomial (Müller, 2004).

Temperature evaluation was conducted during orthogonal cutting. The pyrometer's fiber optic was positioned to measure the temperature of the chip-free side. Access to the rake face was facilitated by a small slot along the cutting path, as described by Saelzer et al. (2020). Figure 4.11 provides an overview of the temperature measurement procedure.



(Saelzer et al., 2020)

Figure 4.11 Rake face temperature measurement method, (A) The technique as illustrated by (Sealzer et al., 2020), (B) Temperature measurement as utilized in this work at the end of the workpiece

In drilling investigations, flank temperature was measured by impeding the fiber optic of the two-color pyrometer inside the workpiece at a distance of $l = 30$ mm from the borehole entrance and 1 mm away from the borehole wall. Once the tool reaches the axial position where the end of the fiber optic is placed, small parts of it become machined with the workpiece material as drilling progresses. Temperature measurement continues to be recorded for $l_T = 2$ mm of drilling length. The setup for temperature measurement in drilling operations is shown in Figure 4.12. A similar setup was used by Bückner (2022).

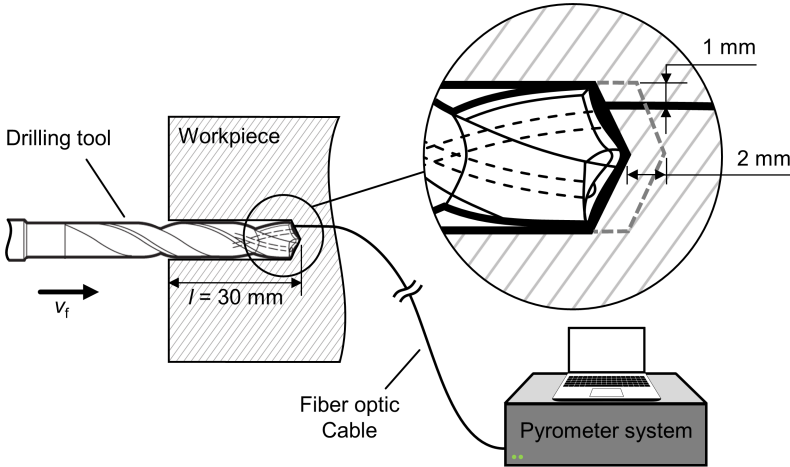


Figure 4.12 Temperature measurement in drilling operation

4.6.3 Displacement measurement

The position of the workpiece, which was set to oscillate in vibration-assisted drilling investigations, was measured using Laser displacement sensors of type LK-G32, manufactured by Keyence Corporation. These sensors operate based on the principle of laser triangulation. A semiconductor

laser generates a red beam ($\lambda = 650 \text{ nm}$), which is focused on the object being measured. The reflected light falls incident onto a charge-coupled device (CCD) array element at a specific angle determined by the distance. By analyzing the position of the light spot on the receiver element and the distance between the sender and receiver elements, the sensor calculates the distance to the measurement object. The measurement spot can range from $30 \text{ }\mu\text{m}$ in the middle of the measuring range to $250 \text{ }\mu\text{m}$ at the limits of the measurement range. The measurement range is $\pm 5 \text{ mm}$, with a resolution of $0.05 \text{ }\mu\text{m}$. The reference distance is 30 mm . Figure 4.13 illustrates the working principle of the sensor and provides relevant specifications.

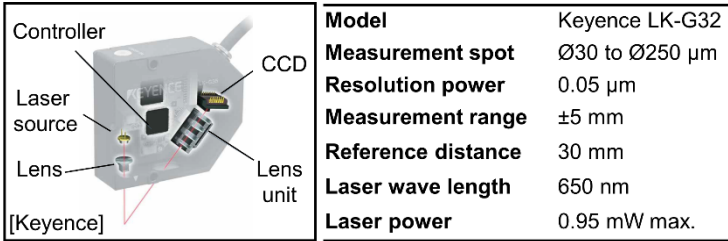


Figure 4.13 Working principle of laser triangulation and the displacement sensor system specifications

4.6.4 High speed video recording

A high-speed microscope system of type VHX 9000, manufactured by Keyence Corporation, was utilized to capture chip formation during orthogonal cutting experiments (see Figure 4.14). The microscope incorporates a monochrome camera, Keyence VW-600M, equipped with a complementary metal oxide semiconductor (CMOS) sensor. To enable magnification of up to $\times 500$, the camera was paired with a long-focal-distance objective lens, Keyence VH-Z50L. The microscope system allows for a frame rate of up to $f_{\text{fr}} = 4000 \text{ Hz}$ at VGA resolution (640×480 pixels) or a maximum of $f_{\text{fr}} = 230000 \text{ Hz}$ at lower resolution (160×32 pixels). However, recording at high frame rates posed a challenge in terms of light intensity. Although some light could be applied through the objective lens, additional external light was required. An Artrolux GmbH high throughput LED array light source was employed for this purpose. To ensure precise positioning of the microscope within the chip formation region, a 3-axis adjustable positioning mount was utilized. The selected frame rate for recording was $f_{\text{fr}} = 10000 \text{ Hz}$ at a resolution of 320×240 pixels.

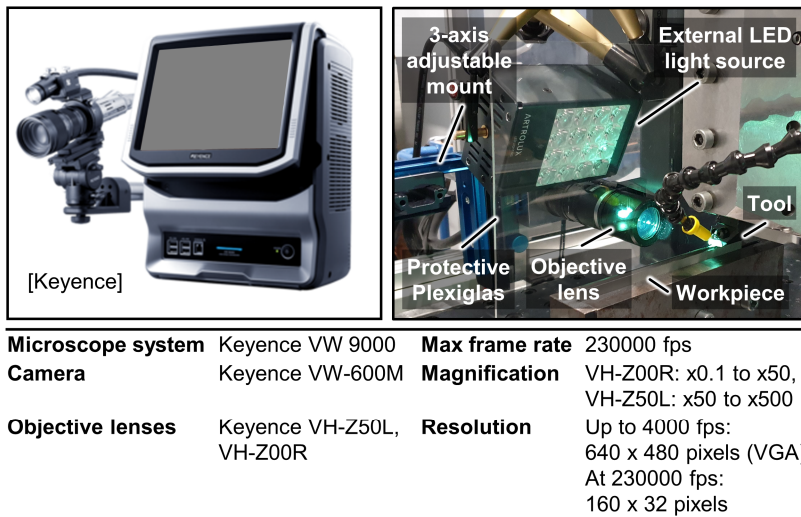


Figure 4.14 High speed video recording setup

4.7 Ex-situ analysis technology

Adhesion marks on the inserts and the progression of tool wear on drilling tools were analyzed through optical measurement using the Keyence VHX 5000 digital light microscope, which provides image magnification of up to x200. Images were captured at regular intervals, and the flank wear was quantified based on the maximum width of the wear mark. Additionally, a microscopic visual inspection was conducted to identify chipping or cracks on the cutting edge. Optical recording of tool wear was complemented by monitoring the drilling torque and feed force. In case of a sudden increase, the test series was halted, and the tool condition was analyzed using the optical microscope.

The analysis of chip surface topography and morphology was performed using the InfiniteFocus G5 measuring device from Alicona Imaging GmbH. This device utilizes the principle of autofocus variation and is suitable for quantitatively describing surface topographies in large-area measurements with sufficient surface roughness and low reflection behavior. It allows the derivation of profile- and area-related surface parameters according to DIN ISO 4287 and DIN EN ISO 25178. The lens used has a magnification of x50 and a vertical resolution of 2 nm.

In addition to the surface topography measurements mentioned above, images were obtained using a scanning electron microscope (SEM) for further assessment of the surfaces. The specific SEM used is the TESCAN MIRA3 XM model. It is equipped with SE and BSE detectors, enabling magnification of up to 50000, while an EDS detector is utilized for chemical composition analysis. Adhesions appearing in BSE images of cutting inserts were quantified using an in-house developed gray level masking (AGLM) method, which will be discussed later in this thesis.

The surface quality of the boreholes is a critical criterion for evaluating process performance. After thorough cleaning of the samples, the analysis of the produced bores regarding their dimensional and shape deviations, as well as surface quality, was conducted. Bore roughness was measured tactically using a Mahr MarSurf GD 120 profilometer. A probe tip with a tip radius of $r = 2 \mu\text{m}$ was

employed at varying drilling depths. The total profile was divided into five individual measuring sections, each with a length corresponding to the cut-off wavelength of $l_i = \lambda_c = 0.8$ mm.

Chapter 5: Adhesion on the Rake Face in Interrupted Orthogonal Cutting

Adhesion is considered one of the topological aspects that characterize tool-chip contact. In this chapter, adhesion appearing on the tool's rake face in orthogonal interrupted machining is investigated. The experimental setup is described, which involves the use of interrupted workpieces with a variable number of interruptions and a constant total cutting length. A method for quantifying the adhesion area appearing in backscatter electron (BSE) images is proposed and utilized for tool-chip contact characterization. In addition to adhesion quantification, tool-chip contact length and mechanical load are considered. The experimental investigations include a comparison between variable cutting speeds, as well as the effect of varying cutting length occurring prior to interruption. A relationship between interruption frequency and tool-chip contact is observed.

5.1 Methodology and experimental setup

Interrupted cutting is utilized in this investigation to allow periodically occurring access to the cutting fluid in the tool-chip interaction zones. During the interruption, the cutting edge disengages from the cutting process, and the chip breaks away, exposing the interaction area to the machining environment. As a result, the cutting medium may have improved access to the interaction area, enabling direct cooling and re-lubrication.

In this investigation, tool-chip disengagement was realized by the number of slots in the workpiece, which acted as cutting interruptions along the cutting path. The influence of interrupted machining on the machining of Inconel 718 was observed by monitoring process forces, coefficient of friction, adhesion area on the rake face, and tool-chip contact length. The estimation of the adhesion area was based on a quantification method using adhesion gray level masking (AGLM) observed in BSE images, which will be discussed in the next section.

5.1.1 Tools and materials

A custom-built CNC machine that allows the fundamental analysis of chip formation in orthogonal cutting was used, as shown in Figure 5.1 (A). The mechanical load was measured by a three-axis piezoelectric dynamometer (Kistler 9263). A clean side of the cutting insert was used in every trial. Synthetic MQL oil Vascomill MMS HD 1 from Blaser Swisslube GmbH was pneumatically atomized by an external MQL preparation device LSJ-mini from HPM Technologie GmbH.

In this investigation, Inconel 718 was used as the workpiece material. The cuboid samples, as sketched in Figure 5.1 (B), were in the annealed and aged condition, with a hardness measured at 470 HV30. The workpieces had a width of $b = 3$ mm and a constant total cutting length of $L_c = 144$ mm. Four different workpieces were prepared with a number of interruption intervals, $n = 0 \dots 3$. The interruption length was kept constant in all workpieces at $L_{int} = 8$ mm.

Tool holder CTFPL2525M16 with uncoated tungsten carbide (WC) inserts TPGN160308H13A from manufacturer Sandvik and TPUN160308FN H10T from manufacturer CERATIZIT S.A. were used in the orthogonal cutting experiments. Uncut chip thickness was kept constant for all trials at $h = 0.1$ mm, as well as rake angle $\gamma_0 = 6^\circ$ and clearance angle $\alpha_0 = 5^\circ$. Cutting speed varied within $v_c = 10 \dots 60$ m/min.

For the orthogonal cutting experiments, a tool holder CTFPL2525M16 with uncoated tungsten carbide (WC) inserts TPGN160308H13A from the manufacturer Sandvik and TPUN160308FN H10T from the manufacturer CERATIZIT S.A. were used. The uncut chip thickness was kept constant for all trials at $h = 0.1$ mm, as well as the rake angle $\gamma_0 = 6^\circ$ and clearance angle $\alpha_0 = 5^\circ$. The cutting speed varied within $v_c = 10 \dots 60$ m/min.

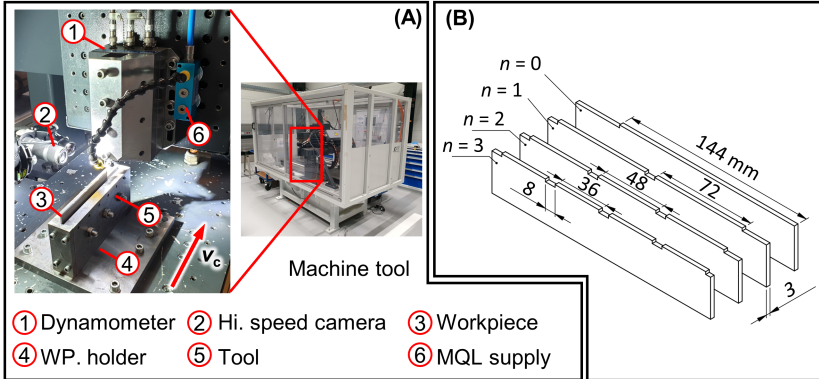


Figure 5.1 (A) Experimental setup, (B) Interrupted workpiece geometry; (Alammari et al., 2021b)

5.1.2 Adhesion area quantification on the rake face using AGLM^a

It has been revealed by machining tribology research that the adhesion of the workpiece material to the cutting tool is an important aspect that governs a number of physical parameters within the tool-chip interface. Adhesion is of particular concern when difficult-to-cut materials such as nickel-based alloys are being machined. Tool wear that leads to premature tool failure or the triggering of other wear modes, hindering machinability and reducing product quality, may be promoted by adhesion. Adhesion quantification, which is an indispensable tool, is currently being investigated by many researchers in order to understand the fundamentals of adhesion wear. While certain types of wear mechanism measurements such as flank wear have been well-documented and standardized (e.g., ISO 3685), adhesion wear quantification is still under investigation. From a tribological perspective, it is an important aspect that can affect the tool-chip contact. Therefore, in this section, an efficient approach based on the Adhesion Gray Level Masking (AGLM) of Backscatter Electron (BSE) images obtained under a scanning electron microscope (SEM) is proposed.

Several techniques for quantifying adhesion wear have been investigated by researchers. A review of classical adhesion quantification techniques, including white light microscopy, elemental mapping using energy dispersive x-ray spectroscopy (EDS) or wavelength dispersive spectrometry (WDS), and laser time of flight mass spectroscopy, was carried out by (M'Saoubi and Chandrasekaran, 2005). An accurate method for quantifying adhesion area is elemental mapping, which distinguishes between tool and workpiece materials more accurately by providing detailed information regarding existing elements. However, it is a slow method that requires the allocation of various resources. Manual image segmentation of optical images of the flank face was employed by (Castejón et al., 2007) to obtain a list of geometric descriptors used in defining wear classes. Adhesion regions from SEM BSE images were manually identified using commercial image editing software by (Kilick and Raman, 2007), who subsequently quantified sticking and sliding zones resulting from the contact between the tool and an aluminum alloy.

^a This section adapted from (Alammari et al., 2021a)

In addition to the above-mentioned 2D quantification methods, adhesion has also been investigated in 3D. Adhesion volume was quantified by (Ponce et al., 2018) through the measurement of the 3D surface profile of the tool before and after machining. (Mainé et al., 2013) utilized the focus variation microscopy (FVM) technique for contactless 3D adhesion quantification. Recently, a 3D chemical and morphology mapping technique based on the fusion of SEM images and EDS with Multiview photogrammetry was developed by (Gontard et al., 2018). This method was applied to uncoated tungsten carbide inserts used for machining aluminum alloy. Although their technique provides a novel insight into 3D characterization and is highly sophisticated, its efficiency can be reduced, especially when examining a large number of samples, due to the high level of complexity and the time required to obtain a high number of SEM images and EDS maps at different orientations.

While adhesion can be quantified using one of the aforementioned methods, most of them can be quite time-inefficient. Therefore, an efficient alternative based on a systematic approach for 2D quantification of the adhesion pixels through image processing of BSE images, known as AGLM, is proposed. AGLM utilizes the inherited properties of BSE images, where the contrast of sample phases is enhanced based on the mean atomic number and assigned a particular gray level. The area of adhesion is thus quantified by counting the total area of adhesion pixels based on a statistically distinguished gray level distribution that can be identified and masked.

In this chapter, the application of AGLM is focused on quantifying the adhesion area on the rake face. The resulting adhesion of Inconel 718 on uncoated tungsten carbide inserts is quantified using this method. Additionally, to compare the performance of AGLM, elemental mapping using EDS and image segmentation using a k-means clustering algorithm are utilized.

Principle of AGLM

For preparation proposes, the inserts after cutting were cleaned by ethanol using an ultrasonic bath for at least 5 minutes. The insert's rake face was then scanned under scanning electron microscope MIRA3 TESCAN using backscatter electron detector. The acceleration voltage, HV, was selected at HV = 10 kV, and working distance was at WD = 30 mm (unless otherwise specified). The advantage of a backscatter electron detector in contrasting the gray level based on the existing phases of the sample is essential in this study to distinguish between tool substrate and adhered material. The different intensities of backscattered electrons based on the mean atomic number of the sample enable a clear identification of the adhesion. Therefore, a contrast between the gray level of adhered material and the background tool material can be observed quite distinctively. The fundamental aspect of the resultant gray level assignment is the bases of this research. The gray level range of adhesion was identified from BSE image gray level histogram, as shown in Figure 5.2.

For preparation purposes, the inserts were cleaned with ethanol using an ultrasonic bath for at least 5 minutes after cutting. Subsequently, the rake face of the inserts was scanned using a scanning electron microscope (SEM) model MIRA3 TESCAN, equipped with a backscatter electron detector. The acceleration voltage was set to HV = 10 kV, and the working distance was set to WD = 30 mm, unless stated otherwise. The backscatter electron detector proves advantageous in this study as it enables contrasting the gray levels based on the existing phases of the sample, facilitating the distinction between the tool substrate and adhered material. The varying intensities of backscattered electrons, determined by the mean atomic number of the sample, allow for clear identification of the adhesion. Consequently, a distinct contrast between the gray level of the adhered material and the background tool material can be observed. The assignment of gray levels serves as a fundamental aspect of AGLM. The gray level range corresponding to the adhesion was determined from the gray level histogram of the backscatter electron (BSE) image, as shown in Figure 5.2.

The analysis area starts just before the cutting edge and extends into the cutting insert, covering the tool-chip interaction region. The gray images obtained from the SEM are 12-bit color images. For AGLM, only 256 gray level bins were considered, as shown on the horizontal axis of the histogram in Figure 5.2 (the black bin with gray level = 1 was excluded for improved clarity). In the histogram, two prominent peaks can be identified: a lighter peak with higher gray level numbers located towards the right, representing the tool material, and a darker peak with lower gray level numbers representing the adhesion. The black bin (bin no. 1) contains pixel counts located outside the cutting insert and beyond the cutting edge. It can be observed that the range of adhesion pixels had to be systematically defined. Therefore, a Gaussian curve was fitted to the distribution of adhesion gray levels as follows:

$$n_p = \frac{1}{\sqrt{2\pi\sigma_g^2}} e^{-\frac{(g-\mu_g)^2}{2\sigma_g^2}} \quad (5.1)$$

where n_p represents the number of adhesion pixels at a specific gray level g , σ_g denotes the standard deviation, and μ_g represents the mean adhesion gray level.

Workpiece mat.	Inconel 718	Cutting tool	TPUN160308FNH10T
Lubrication	Dry	Rake angle γ_o	6°
Uncut chip thick. h	0.1 mm	Flank angle α_o	5°
Width of cut b	3 mm	SEM detector	BSE
Length of cut L_c	144 mm	SEM voltage	10 kV
Cutting speed v_c	50 m/min	SEM work. dist.	30 mm
Number of inter. n	0	Adh. st. div. mult.	1

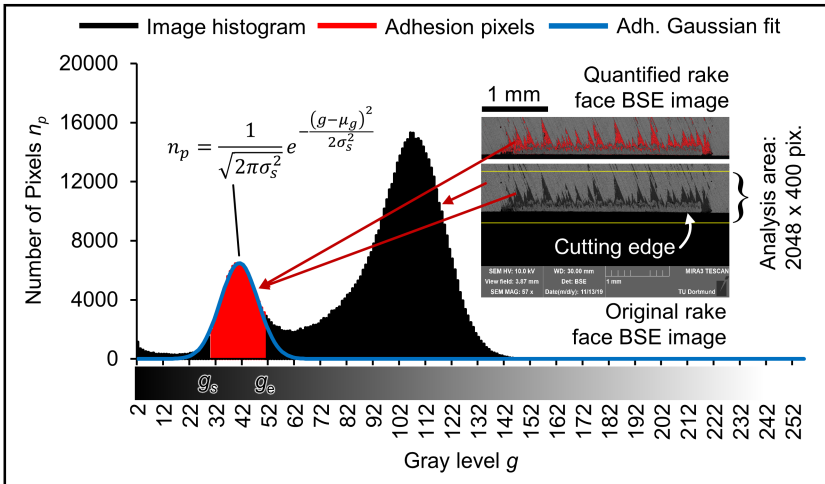


Figure 5.2 AGLM method illustrated on backscatter image histogram; (Alammari et al., 2021a)

The adhesion gray level mean and standard deviation were determined based on the Gaussian equation, Equation (5.1). The red-colored bins in the histogram shown in Figure 5.2 represent one standard deviation around the adhesion gray level mean. The effect of the primary electron

acceleration voltage on the quantified pixels, adhesion gray level mean, and standard deviation of the adhesion gray level distribution was investigated by varying it from HV = 4 to 20 kV.

The adhesion area can be calculated by multiplying the area of each pixel, which varies based on the magnification, by the total number of counted adhesion pixels using the following equation:

$$A_{adh} = \sum_{i=g_s}^{g_e} n_p \cdot A_p \quad (5.2)$$

where A_{adh} represents the total adhesion area, A_p is the size of an individual pixel (basically the square of one pixel's scale dimension), g_s is the lowest adhesion gray level, and g_e is the highest adhesion gray level. The pixel scale dimension can be accurately obtained from the image metadata provided with the BSE image. The values of g_s and g_e are determined based on the selected multiple of the adhesion distribution standard deviation around the mean adhesion gray level.

In the following sections, the adhesion quantification of cutting inserts using the AGLM method to quantify adhesion after orthogonal machining of Inconel 718 with varying cutting speeds without interruptions will be presented and discussed. Comparison results of the proposed quantification method with the k-means clustering algorithm and EDS elemental mapping will be presented. Later, in section 5.3, AGLM will be used to estimate adhesion on the rake face resulting from interrupted machining.

5.2 Assessment of AGLM for adhesion area quantification on the rake face in continuous orthogonal machining^a

Figure 5.3 (A) presents the side-by-side comparison of quantified and original backscatter images. The range around the identified adhesion mean was chosen to be one standard deviation. The adhesion gray level mean and standard deviation were derived from the fitted Gaussian curve using Equation 5.1. Subsequent discussions will explore the impact of the masking range around the identified adhesion gray level distribution mean, as well as the effect of electron acceleration voltage on the quantification results.

For better clarity, the masked adhesion pixels were recolored in red. The masked images clearly demonstrate that the masking method is capable of distinguishing and mapping the adhesion pixels, regardless of their shape or direction. The resulting adhesion quantification, including the total adhesion area within the scanning region, as well as the corresponding adhesion gray level mean and standard deviation, are presented in Figure 5.3 (B) and (C). Figure 5.3 (A) illustrates the quantified adhesion area of different cutting trials, providing insights into the extent of physical interaction within the tool-chip contact zones. The mean (μ_g) and standard deviation (σ_s) of the fitted Gaussian curves are summarized in Figure 5.3 (C). Analysis of Figure 5.3 (C) reveals that the adhesion gray level is consistently centered around a particular value, indicating that the scanning parameters remained unchanged during the acquisition of individual images.

^a This section adapted from (Alammari et al., 2021a)

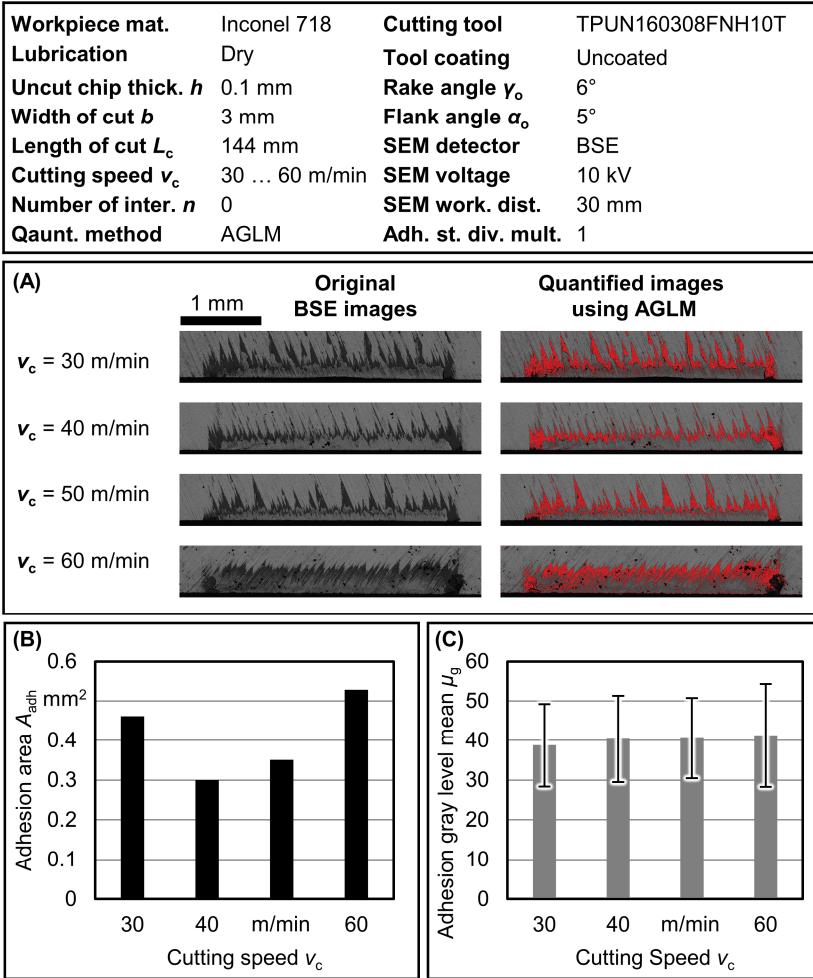


Figure 5.3 Adhesion area quantification in continuous orthogonal machining of Inconel 718, (A) Quantified adhesion BSE images, (B) Adhesion area quantification of variable cutting speeds, (C) Adhesion gray level mean and standard deviation; (Alammari et al., 2021a)

Specifically, for a specific set of scanning conditions when obtaining the BSE images, the adhesion gray level mean was approximately 41. The histograms of the BSE images presented in Figure 5.3 are displayed in Figure 5.4. Adhesion gray level distributions are fitted with Gaussian curves according to Equation (5.1).

Workpiece mat.	Inconel 718	Cutting tool	TPUN160308FNH10T
Lubrication	Dry	Tool coating	Uncoated
Uncut chip thick. h	0.1 mm	Rake angle γ_o	6°
Width of cut b	3 mm	Flank angle α_o	5°
Length of cut L_c	144 mm	SEM detector	BSE
Cutting speed v_c	30 ... 60 m/min	SEM voltage	10 kV
Number of inter. n	0	SEM work. dist.	30 mm

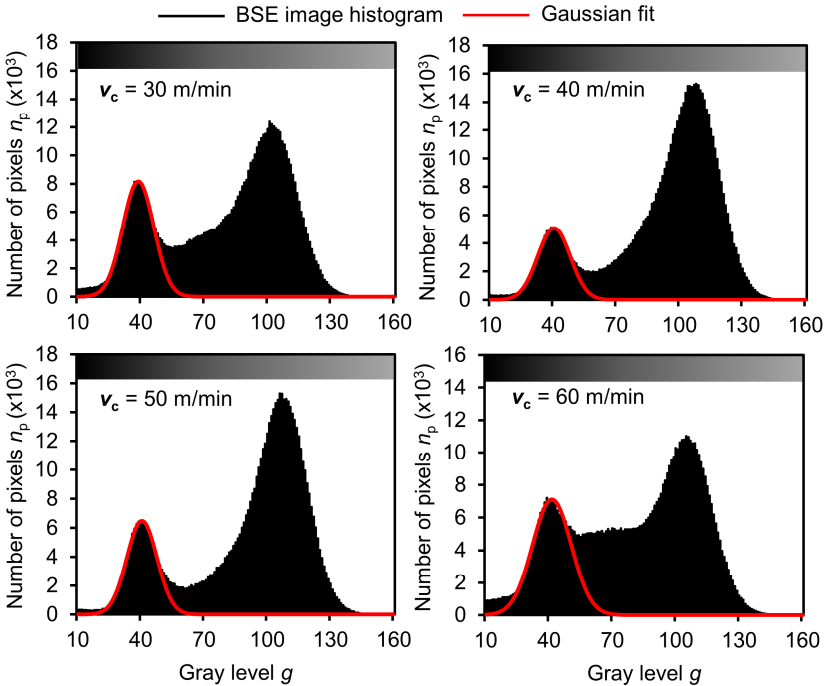


Figure 5.4 BSE image histograms for cutting speeds variation trials; (Alammari et al., 2021a)

The standard deviation varies depending on how adhesion spreads around a specific gray level mean, which can be influenced by tool-chip contact conditions. Consequently, the adhesion gray level distribution becomes wider, and the overlapping region between the adhesion gray distribution and the tool gray distribution can increase, as shown in Figure 5.4 ($v_c = 60$ m/min). This increase in overlapping regions between adhesion and the tool can result in transitional boundaries that impact the BSE intensity, as illustrated in Figure 5.5.

Workpiece mat.	Inconel 718	Cutting tool	TPUN160308FNH10T
Lubrication	Dry	Tool coating	Uncoated
Uncut chip thick. h	0.1 mm	Rake angle γ_o	6°
Width of cut b	3 mm	Flank angle α_o	5°
Length of cut L_c	144 mm	SEM detector	BSE
Cutting speed v_c	50 m/min	SEM voltage	10 kV
Number of inter. n	0	SEM work. dist.	30 mm

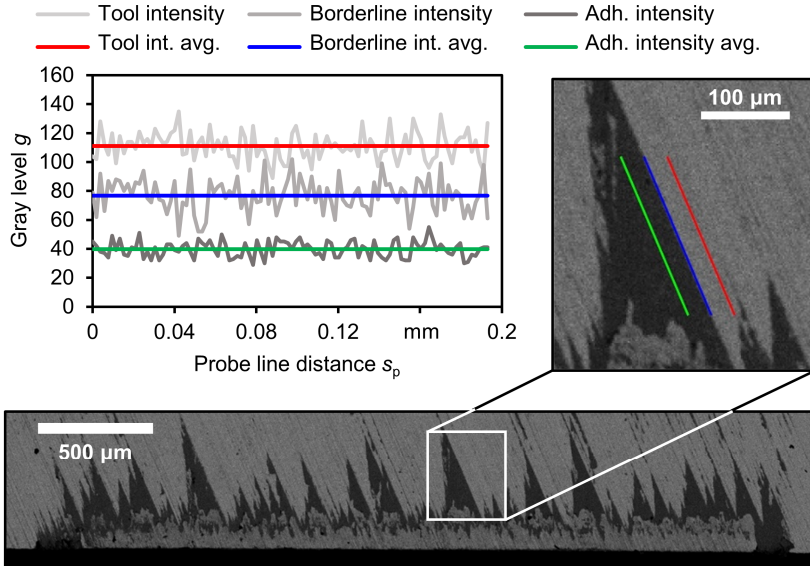


Figure 5.5 Gray level distribution along different regions; (Alammari et al., 2021a)

The tool or adhesion asperities can also contribute to an increase in the overlapping area of gray levels, resulting in a smooth transition in the gray distribution and a less contrasted image. It is well-known that backscatter intensity can vary based on both the composition of the scanned materials and the orientation of the asperities in the scanned area (Goldstein et al., 2018). Additionally, the shape and location of the gray distributions can be affected by the scanning parameters used, such as the acceleration voltage, brightness, and contrast, which should be selected carefully. The subsequent section will discuss the effect of the primary electron acceleration voltage on adhesion quantification.

5.2.1 Sensitivity of AGLM to change in primary electron acceleration voltage

To assess the potential impact of scanning parameters on quantification, the acceleration voltage was varied from 4 to 20 kV. The corresponding mean and standard deviation of the adhesion gray level distribution are presented in Figure 5.6. Variation in acceleration voltage leads to changes in image contrast. To maintain optimal image quality, the SEM's auto BSE contrast/brightness setting was utilized whenever the acceleration voltage was adjusted. The brightness was automatically maintained at a constant value of 93.5%.

Workpiece mat.	Inconel 718	Cutting tool	TPUN160308FNH10T
Lubrication	Dry	Tool coating	Uncoated
Uncut chip thick. h	0.1 mm	Rake angle γ_0	6°
Width of cut b	3 mm	Flank angle α_0	5°
Length of cut L_c	144 mm	SEM detector	BSE
Cutting speed v_c	50 m/min	SEM voltage	4 ... 20 kV
Number of inter. n	0	SEM work. dist.	30 mm

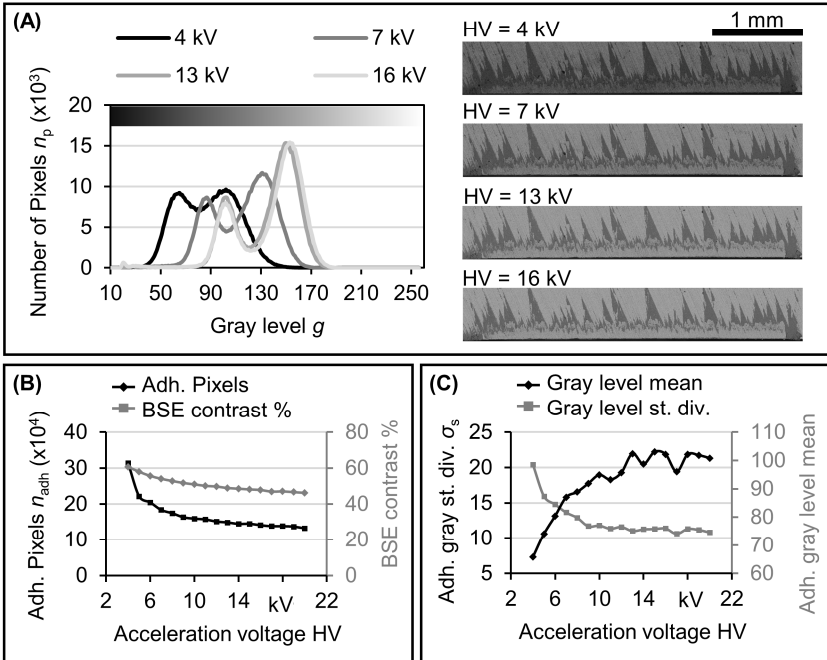


Figure 5.6 Effect of SEM acceleration voltage on adhesion quantification, (A) BSE images and image histograms using different acceleration voltages, (B) The effect of acceleration voltage on the number of quantified adhesion pixels, (C) Adhesion gray level mean and standard deviation at different acceleration voltages; (Alammari et al., 2021a)

As the acceleration voltage increases, the adhesion gray level mean was observed to shift towards the brighter range. This shift is attributed to the increased intensity of backscattered electrons when the interaction volume expands, resulting in more electrons being collected by the detector. Consequently, the overall image brightness increases. On the other hand, the spreading of the adhesion gray distribution becomes narrower as the acceleration voltage increases. This narrowing effect can be attributed to the diminishing influence of topography on the intensity of detected backscattered electrons compared to elemental contrast. As a result, BSE intensity at boundary regions and asperities becomes more pronounced at higher acceleration voltage. These changes in the shape of the adhesion gray distribution may consequently impact the number of counted adhesion pixels, as demonstrated in Figure 5.6 (B).

The quantified adhesion pixels increase as more areas appear darker when the acceleration voltage decreases. Specifically, a more substantial increase in the quantified adhesion pixels is observed when the acceleration voltage is below 10 kV. This rapid change in trend is also evident in Figure 5.6 (C) for the mean and standard deviation. A very low acceleration voltage can result in weak interaction/emission with the sample insert. Consequently, the tool material does not appear sufficiently bright in the resulting image, leading to a significant increase in the assigned gray level for the adhesion. This causes the adhesion distribution to become noticeably wider, resulting in larger standard deviation values, as shown in Figure 5.6 (C). The automatic BSE brightness/contrast tool of the SEM was used to maintain a brightness level of 93.5%, while the contrast decreased with increasing acceleration voltage.

In the following sections, two methods were employed to assess the performance of the proposed method: the k-means clustering algorithm and EDS elemental mapping. The k-means clustering algorithm is widely used in image processing for various applications, including segmentation and pattern recognition. On the other hand, EDS elemental mapping is commonly utilized for elemental identification and mapping in materials analysis.

5.2.2 AGLM in comparison with K-mean clustering algorithm

The k-means clustering algorithm is a widely used classification method, often applied in various applications, including image segmentation (Dhanachandra et al., 2015). In the case of BSE gray images, the algorithm segments the image into a specified number of clusters, or gray levels. Initially, random values are assigned to the cluster centroids. Each pixel's gray level is then randomly assigned to one of the clusters. The difference between the pixel's color and the centroid is calculated, and the centroid value is adjusted to minimize this difference until convergence is reached (i.e., when the previous centroid matrix equals the current centroid matrix). The process continues until each data point is assigned to its nearest cluster. The process flowchart is shown in Figure 5.7 (A).

The k-means clustering algorithm was applied for image segmentation of BSE images. Initially, three clusters were selected, as this choice appeared logical given that three distinct gray level distributions were observed in the BSE image histogram, corresponding to the area beyond the cutting edge, the tool, and the adhesion. It was noted that the resulting cluster centroids were positioned far from the histogram peaks, as illustrated by the red lines in Figure 5.7 (B). Consequently, the number of clusters was doubled to shift a cluster node closer to the adhesion mean. The resulting images after applying the k-means clustering algorithm with 3 and 6 clusters are presented on the right side of Figure 5.7 (B). The segmented images using 6 clusters reveal a greater number of gray levels, corresponding to the increased number of clusters, with the adhesion pixels colored in red for clarity. The centroid values corresponding to the adhesion clusters were identified as the second darkest clusters, with the darkest cluster representing the area beyond the cutting edge. A comparison between the adhesion gray level distribution mean obtained from the BSE image histogram using AGLM and the resulting values of the adhesion centroid using 3 and 6 cluster segmentation is shown in Figure 5.7 (C).

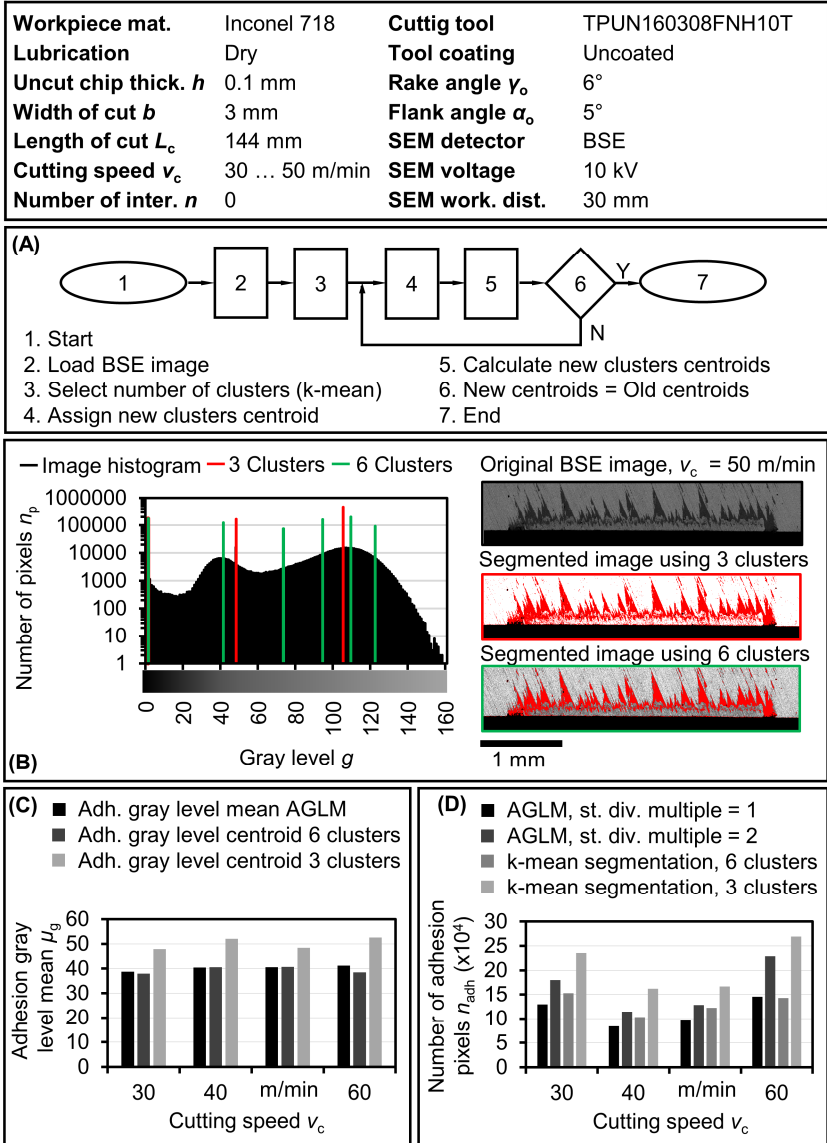


Figure 5.7 (A) K-mean clustering algorithm flow chart, (B) Segmented BSE image and corresponding histogram with the location of segmentation centroids; $v_c = 50$ m/min (C) AGLM adhesion gray level mean with adhesion cluster means, (D) Quantified adhesion pixels of variable cutting speeds trials using AGLM method in comparison with adhesion quantification by k-mean clustering algorithm image segmentation; (Alammari et al., 2021a)

As shown in Figure 5.7 (B) and Figure 5.7 (C), the difference between the adhesion centroid and the identified adhesion gray level distribution mean from the BSE image histogram using AGLM diminishes when more clusters are defined. However, increasing the number of clusters may affect the number of counted pixels within the adhesion cluster, as illustrated in Figure 5.7 (D).

Figure 5.7 (D) illustrates that increasing the preselected number of clusters leads to a decrease in the quantified adhesion pixels, as some pixels are redistributed to other clusters during the k-means clustering algorithm's redistribution process. Additionally, it can be observed that increasing the masking range results in higher adhesion quantification, aligning with statistical expectations and approaching the quantification achieved through the k-means clustering method. However, since the adhesion distribution is not completely isolated from the tool gray level distribution, expanding the masking range around the adhesion gray level mean may be influenced by the tool gray level distribution. Unfortunately, the k-means clustering algorithm alone does not provide an accurate determination of the adhesion distribution masking range. Hence, the quantification using EDS elemental mapping (discussed in the next section) was employed to establish a more precise relationship between the actual count of adhesion pixels and the quantification using variable standard deviations across multiple ranges.

5.2.3 AGLM in comparison with EDS elemental mapping

Energy-dispersive X-ray spectroscopy (EDS) was utilized to quantify the adhesion pixels. The EDS analysis and mapping were conducted using the "octane elect plus" detector equipped with silicon drift detector (SDD) technology from EDAX Inc. Given that the workpiece material is Inconel 718, which consists of nickel, iron, and chromium, any phase containing these elements was identified as adhesion. Consequently, any corresponding elemental map location that yielded counts from these workpiece elements was considered an adhesion pixel. Conversely, tungsten, cobalt, and carbon were designated as the tool phase. An electron acceleration voltage of $HV = 15$ kV and a working distance of $WD = 15$ mm were selected to excite the tool and workpiece elements. The following mapping parameters were chosen: scanning matrix of 1048×400 pixels, dwell time of 200 milliseconds with 512 frames, and an amplification time of 7.68 seconds. The elemental mapping process, conducted using the specified parameters, required approximately 14 hours. The identified adhesion pixels were subsequently counted and compared with the number of adhesion pixels determined using the AGLM method for the same area.

The EDS elemental mapping was performed on a partial insert area due to the limitation of the SEM/EDS field of view at the employed working distance. The adhesion within the same area was also quantified using the AGLM technique applied to the corresponding BSE image. EDS elemental mapping offers a more accurate quantification of the elemental composition and location of the underlying tool or workpiece material. Therefore, it was employed for comparative assessment of the proposed method's statistical parameters, particularly regarding the effect of the selected standard deviation multiples. Figure 5.8 (A) shows the elemental mapping result of the selected insert area at $v_c = 50$ m/min.

In Figure 5.8 (A), the adhesion, tool, overlapping, or unidentified pixels are represented by the colors red, green, yellow, and black, respectively. The cutting edge is visible at the bottom of the image. The histogram of the corresponding BSE scan of the same area is displayed in Figure 5.8 (B). Two gray level distributions, corresponding to the tool and adhesion, can be observed overlapping each other. Additionally, a dark gray distribution associated with the area beyond the cutting edge, where the detected BSE intensity becomes weak, appears towards the black end (i.e., gray level 1).

The ranges of selected gray levels, based on the standard deviation of the adhesion gray distribution, are shown in Figure 5.8 (B). Four ranges are considered for comparison with the quantified adhesion pixels obtained from the elemental mapping analysis. The standard deviation of the adhesion gray distribution is multiplied by different multipliers ($S_m = 1, S_m = 1.5, S_m = 2, \text{ and } S_m = 2.5$) to extend the gray level range around the adhesion gray level mean in both directions. Since the adhesion gray level distribution overlaps with the background tool gray level distribution, a specific range limit cannot be directly observed from the histogram.

Workpiece mat.	Inconel 718	Cutting tool	TPUN160308FNH10T
Lubrication	Dry	Tool coating	Uncoated
Uncut chip thick. h	0.1 mm	Rake angle γ_o	6°
Width of cut b	3 mm	Flank angle α_o	5°
Length of cut L_c	144 mm	SEM detector	BSE, EDS
Cutting speed v_c	50 m/min	SEM voltage	15 kV
Number of inter. n	0	SEM work. dist.	15 mm
Scanning res.	1084x400 pix.	Magnification	X100
ESD dwell time	200 msec	Scanning frames	512 frames

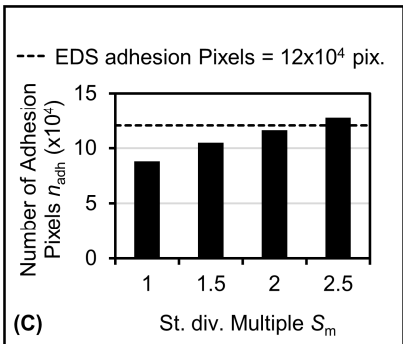
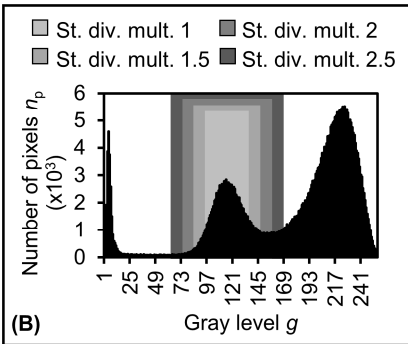
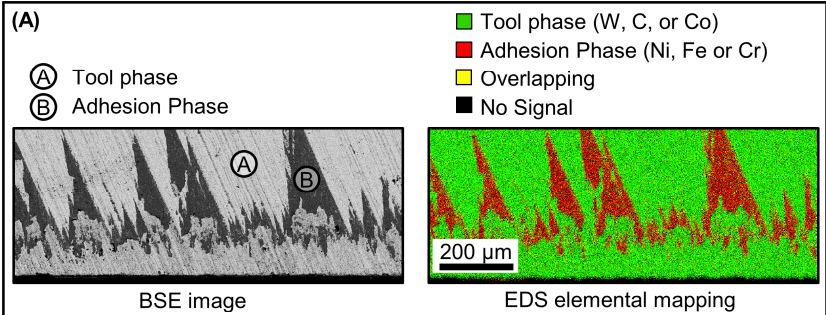


Figure 5.8 (A) Adhesion quantification using EDS elemental mapping, (B) Selection of adhesion gray level range around adhesion gray level mean, (C) AGLM range versus quantified adhesion pixels by EDS elemental mapping; (Alammari et al., 2021a)

As observed in Figure 5.8 (C), the selected quantification range, which depends on the standard deviation multiple, influences the counted adhesion pixels. Due to the overlapping area, the limit of the adhesion distribution is not clearly defined. Therefore, adhesion pixels were only counted around the mean value of the adhesion gray levels, within a range determined by the standard deviation multiples. The standard deviation multiple value was found to be between $S_m = 2$ and $S_m = 2.5$. Standard deviation multiple 2 was found to provide close adhesion quantification as compared to EDS. However, the exact value may vary under different conditions, introducing a significant source of uncertainty. Therefore, the AGLM quantification should primarily be used for qualitative investigations and can be complemented with EDS for improved accuracy in defining the masking range. Alternatively, a smaller masking range can be chosen to obtain statistically representative results of the adhesion, which should be distant from the uncertainty zone within the overlapping region of the BSE image histogram.

Similar to the aforementioned observations, pixels with gray levels located within the overlapping region between the tool gray distribution and the adhesion gray distribution can be attributed to topography variations at the interface between the adhesion and the tool. This is also evident in the EDS map, where the boundaries of the adhesion appear yellow in Figure 5.8 (A), indicating the challenge of differentiating between tool and workpiece materials.

One of the fundamental limitations of elemental mapping is that the field of view becomes restricted to maintain acceptable EDS parameters. As a result, the total interaction area, which could be on the order of several mm^2 , may not be entirely covered and quantified. Additionally, elemental mapping is a resource-intensive technique that demands significant time and resources. In this regard, the AGLM quantification technique could serve as a reasonable alternative, especially when adhesion quantification is required for approximate assessment purposes.

Adhesion quantification for cutting tools is an essential tool for machining tribology research. While some existing techniques offer high accuracy, they suffer from poor efficiency when applied to a large number of experiments. AGLM offers a relatively less complex technique that enables rapid evaluation while maintaining an acceptable degree of accuracy and flexibility. It utilizes the inherent properties of backscatter imaging to contrast the sample's elemental composition. The background of the uncoated tool material and the adhered workpiece material result in two distinct gray distributions in the BSE histogram, allowing for the quantification of the adhesion area by defining the masking range around the adhesion gray distribution mean.

While the AGLM quantification method can be faster (on the order of a few seconds per image) compared to other techniques such as EDS elemental mapping, it may have its limitations. The detected BSE intensity can vary in strength due to sample topography, which can interfere with elemental contrast and potentially affect the quantification accuracy. This effect can be more prominent at the interface between the tool and adhesion regions. Therefore, proper scanning parameters such as acceleration voltage should be utilized to mitigate this challenge. AGLM can also be complemented with EDS elemental mapping for enhanced accuracy in determining the statistical quantification range around the adhesion gray level mean.

Overall, AGLM can provide an acceptable representation for adhesion quantification. However, accurately quantifying adhesion at the tool-adhesion borderlines remains challenging. Therefore, adhesion can be estimated more accurately away from the tool-adhesion borderlines. Hence, a limited masking range around the adhesion gray level mean, positioned away from the gray level zones of uncertainty located between the adhesion and tool gray level distributions in the BSE image

histogram, should be selected. In the next section, interrupted orthogonal machining under MQL is investigated, where AGLM is used to quantify the adhesion area on the rake face.

5.3 Interrupted orthogonal machining of Inconel 718 under MQL^a

In this section, the results for the adhesion of Inconel 718 on the tool rake face during the interrupted orthogonal cutting process under MQL are presented and discussed. Interrupted cutting is employed to enable intermittent exposure to the tool-chip contact area. Adhesion serves as an indicator of the tribological condition within the tool-chip interface, providing insight into the effectiveness of contaminants (e.g., lubricants) in preventing severe contact between the chip and tool. Alongside investigating the influence of machining interruptions on the adhesion area, other factors such as chip-tool contact length, mechanical loads, and coefficient of friction are also observed.

5.3.1 Adhesion area quantification

In addition to the forthcoming analysis of mechanical load and coefficient of friction, the adhesion area on the rake face and the tool-chip contact length, observed from BSE images of the tool's rake face, will be discussed first. Exemplary BSE images are displayed in Figure 5.9. The adhesion area on the rake face was quantified using the adhesion gray level masking (AGLM) method, which was introduced earlier in this chapter. The adhesion area for different cutting speeds and numbers of interruptions along the cutting length is presented in Figure 5.10.

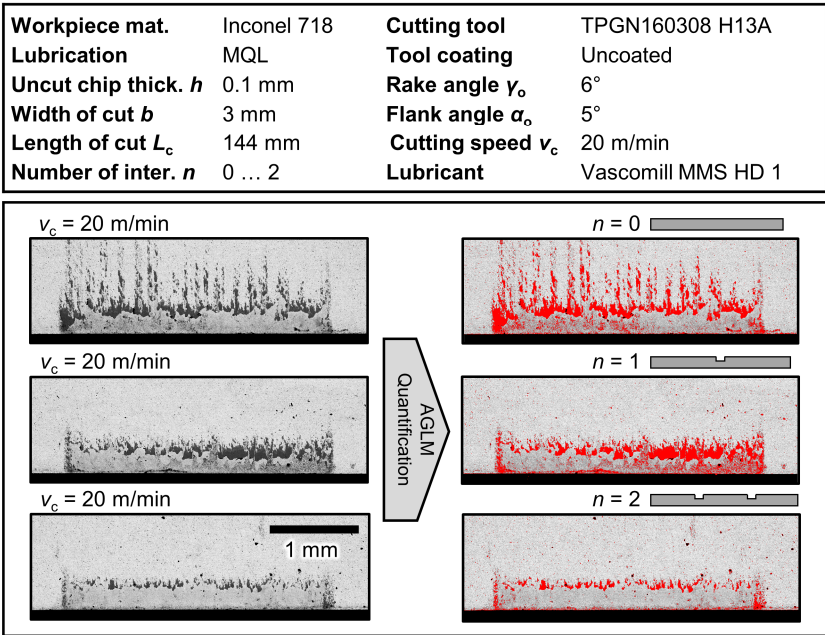


Figure 5.9 Exemplary original and quantified BSE images of adhesion on the rake face using MQL in continuous and interrupted orthogonal cutting of Inconel 718 at $v_c = 20$ m/min; (Alammari et al., 2021b)

^a This section adapted from (Alammari et al., 2021b)

Workpiece mat.	Inconel 718	Cutting tool	TPGN160308 H13A
Lubrication	MQL	Tool coating	Uncoated
Uncut chip thick. h	0.1 mm	Rake angle γ_o	6°
Width of cut b	3 mm	Flank angle α_o	5°
Length of cut L_c	144 mm	Cutting speed v_c	10 ... 50 m/min
Number of inter. n	0 ... 3	Lubricant	Vascomill MMS HD 1

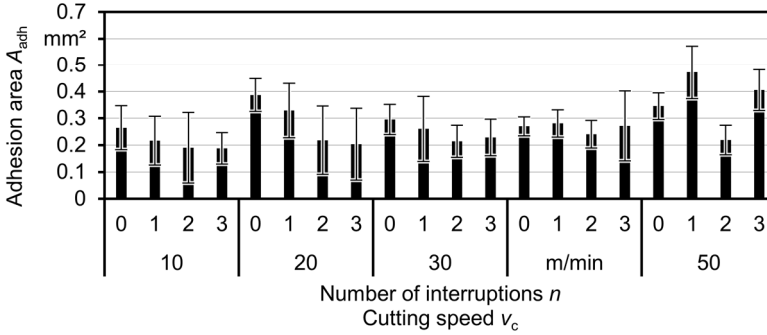


Figure 5.10 Quantified adhesion area using AGLM for Inconel 718 under MQL in continuous and interrupted orthogonal cutting; (Alammari et al., 2021b)

As shown in Figure 5.10, there is a consistent reduction in the adhesion area when the number of interruptions increases at cutting speeds up to $v_c = 30$ m/min. However, at higher cutting speeds (i.e., $v_c = 40$ and 50 m/min), the trend in adhesion area becomes inconsistent. This can be attributed to the intensified increase in adhesion caused by higher temperatures at higher cutting speeds. Furthermore, since the interruption length was constant for all tests at $L_{int} = 8$ mm, the time available for cooling and re-lubricating becomes shorter during interruptions at higher cutting speeds.

5.3.2 Tool-chip contact length

In addition to the presented adhesion area, the chip-tool contact length l_c , which measures the distance from the cutting edge to the average end of adhesion marks (i.e., when the chip disengages from the rake face), provides valuable information. The results of the tool-chip contact length are summarized in Figure 5.11.

Figure 5.11 (A) illustrates the tool-chip contact length, which considers the combined extension of the sliding and sticking zones from the cutting edge. The contact length provides insights into chip tool disengagement, regardless of its severity. Conversely, the extent of adhesion spreading within the chip-tool interface can be determined by the adhesion area.

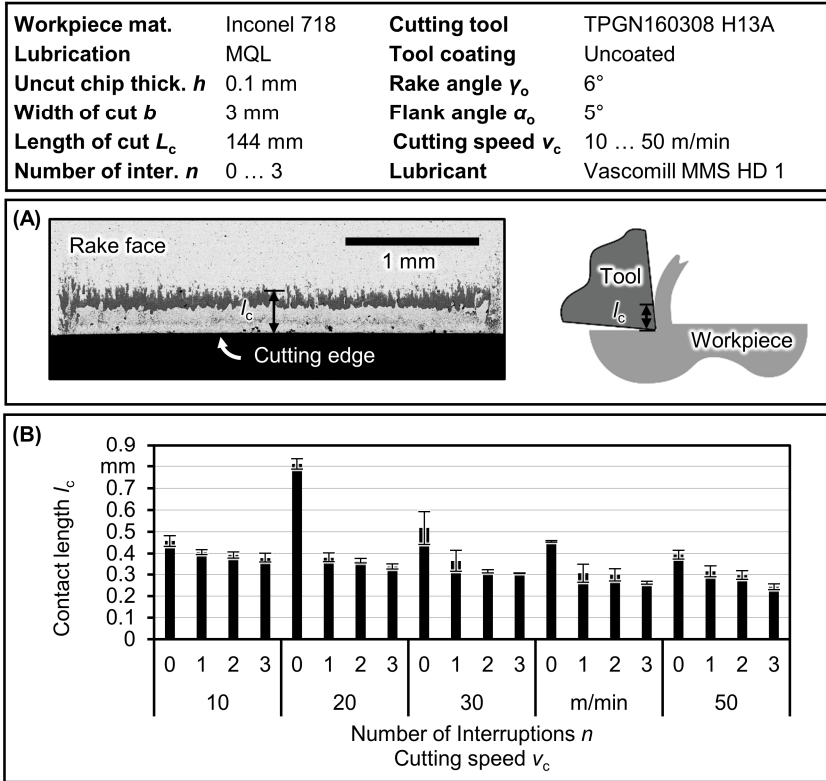


Figure 5.11 Tool-chip contact length results under MQL in continuous and interrupted cutting, (A) BSE image of the rake face indicating contact length measurement, (B) tool-chip contact length results; (Alammari et al., 2021b)

From Figure 5.11 (B), two observations can be made. Firstly, continuous cutting leads to the longest contact length compared to interrupted cutting. Secondly, as the number of interruptions increases, the contact length decreases. The interrupted cutting process allows exposure to the cutting environment, facilitating the renewal of the contamination layer and reducing temperatures. The shorter cutting length and the forced removal of adhered material at the beginning of each subsequent cutting period may contribute to restricting adhesion.

Adhesion area and tool-chip contact length provide crucial information about the contact state within the tool-chip interface. The sliding zone does not start immediately at the cutting edge; it follows a sticking zone. As described by (Childs, 2006), lubricants have the opportunity to influence the tribological conditions in the sliding zone, and cutting fluids can penetrate the interface due to lower contact stresses. In contrast, within the sticking zone, higher stresses occur, and the lubricant may not have the chance to penetrate the interface. In the sticking zone, a stagnant volume of workpiece material can exist and fall off with the chip after the cutting process, resulting in an adhesion-free area. In the sliding zone, where relative motion between the chip and rake face occurs, parts of the

workpiece material remain adhered. In addition to the high contact stresses within the sticking zone, which prevent contaminants from penetrating further towards the cutting edge, high temperatures impose additional restrictions. (Garcia-Gonzalez et al., 2016) measured the maximum contact temperature when machining Inconel 718 to be located at a finite distance from the cutting edge and less than the tool-chip contact length. To examine the combined effect of interruption and cutting speed on the chip-tool contact length from a different perspective, the interruption frequency f_{int} is plotted against the contact length l_c in Figure 5.12.

Workpiece mat.	Inconel 718	Cutting tool	TPGN160308 H13A
Lubrication	MQL	Tool coating	Uncoated
Uncut chip thick. h	0.1 mm	Rake angle γ_o	6°
Width of cut b	3 mm	Flank angle α_o	5°
Length of cut L_c	144 mm	Cutting speed v_c	10 ... 50 m/min
Number of inter. n	0 ... 3	Lubricant	Vascomill MMS HD 1

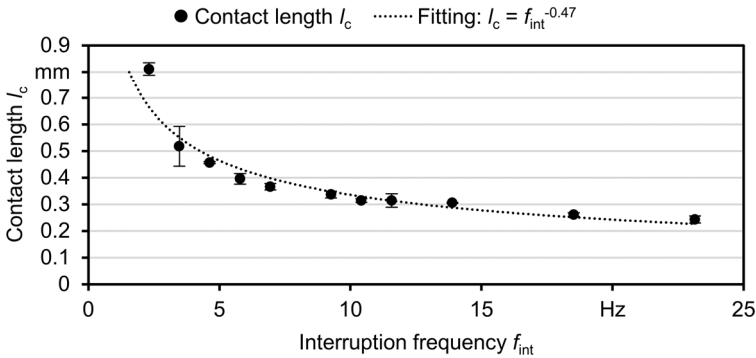


Figure 5.12 Interruption frequency f_{int} versus chip-tool contact length; (Alammari et al., 2021b)

The interruption frequency f_{int} was calculated as $f_{\text{int}} = 1/t_{\text{cut}}$ where t_{cut} is the cutting period between interruptions in seconds. As interruption frequency increases either due to increasing the number of interruptions n or increasing the cutting speed v_c , contact length decreases.

The interruption frequency f_{int} was calculated using: $f_{\text{int}} = 1/t_{\text{cut}}$, where t_{cut} represents the cutting period between interruptions in seconds. As the interruption frequency increases, either by increasing the number of interruptions n or by increasing the cutting speed v_c , the contact length decreases.

5.3.3 Mechanical load

Three force components were measured using the described piezoelectric dynamometer. The cutting force F_c , which is parallel to the direction of cutting speed, and the passive force F_p , which is perpendicular to the cutting force in the direction of chip flow, are the only components considered in this analysis. The third force component is neglected as the cutting process is orthogonal. The averaged cutting force F_c is shown in Figure 5.13 (A).

The forces were evaluated within the stable cutting length just before the end of the cut. The cutting force F_c appears to be less influenced by the number of interruptions or cutting speed. Contrary to

the initial presumption, among the cutting forces at $v_c = 10$ m/min, the cutting force slightly increases as the number of interruptions increases.

Workpiece mat.	Inconel 718	Cutting tool	TPGN160308 H13A
Lubrication	MQL	Tool coating	Uncoated
Uncut chip thick. h	0.1 mm	Rake angle γ_o	6°
Width of cut b	3 mm	Flank angle α_o	5°
Length of cut L_c	144 mm	Cutting speed v_c	10 ... 50 m/min
Interruption length L_{int}	8 mm	Lubricant	Vascomill MMS HD 1
Number of inter. n	0 ... 3		

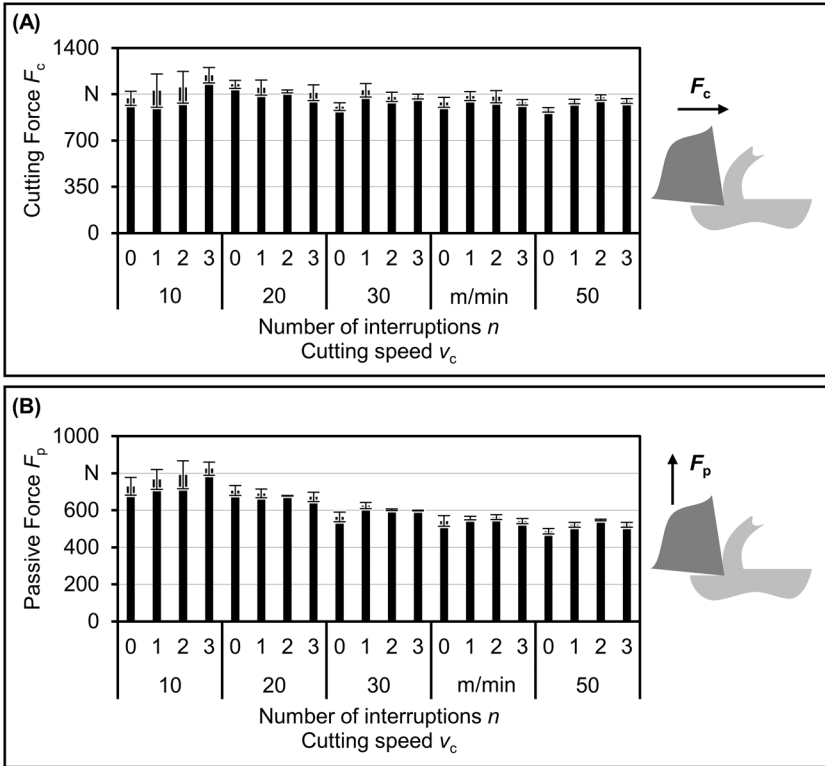


Figure 5.13 Mechanical load in interrupted orthogonal cutting under MQL, (A) Cutting force F_c , (B) Passive force F_p ; (Alammari et al., 2021b)

The increase in mechanical load at low cutting speed (i.e., $v_c = 10$ m/min) with increasing interruptions can be attributed to minimal changes in the tool geometry due to inhibited built-up edge formation. Interrupted machining reduces the cutting length, which reduces the potential for built-up edge accumulation and promotes the frequent removal of built-up edge at the beginning of each cutting interval, minimizing changes in the cutting edge geometry. The relationship between

process forces and built-up edge has been investigated by (Sukvittayawong and Inasaki, 1994) indicating a relationship between built-up edge and increased rake angle. Low rake angles are observed to cause low passive force.

Additionally, as shown in Figure 5.13 (B), passive forces decrease with increasing cutting speed, accompanied by shorter chip-tool contact on the rake face. Interruptions have minimal effect on the average passive force at higher cutting speeds.

Overall, interruptions have limited influence on the mechanical load for the investigated cutting length. This may be because the calculated averages in Figure 5.13 were obtained within the steady-state region, where tribological effects occurring at the beginning of the cutting period have already diminished. These observations suggest a need for a shorter cutting length and further investigation into the transient period which will be considered in the next chapter.

5.3.4 Apparent coefficient of friction

Cutting and passive forces, as described earlier, were utilized to calculate the apparent coefficient of friction (COF) on the rake face, considering a rake angle of $\gamma_o = 6^\circ$. The average COF results are shown in Figure 5.14. Equation (5.3) was employed to calculate the COF using the following formula:

$$COF = \frac{F_p + F_c \tan \gamma_o}{F_c - F_p \tan \gamma_o} \quad (5.3)$$

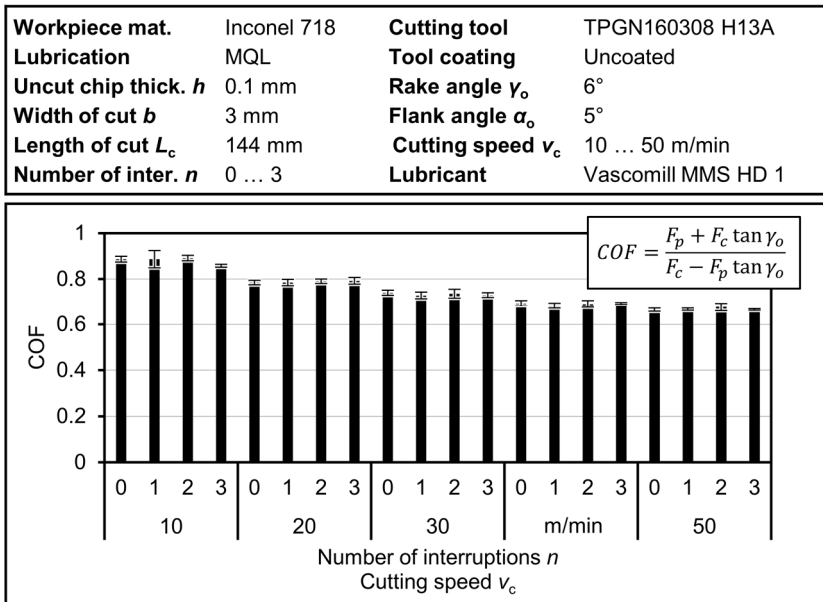


Figure 5.14 Coefficient of friction CO - under MQL; (Alammari et al., 2021b)

As can be observed from Figure 5.14, higher cutting speeds result in lower COF. Interruptions have a negligible effect on the average COF. It is important to note that the results presented in Figure 5.14 represent only the average of data points selected from within a stable region of the COF time series. The COF time-series results for $v_c = 10$ m/min and $v_c = 40$ m/min at $n = 1$ are displayed in Figure 5.15. The following observations can be made from the COF time-series shown in Figure 5.15. At a low cutting speed of $v_c = 10$ m/min in Figure 5.15 (A), the COF gradually increases at the start of the cutting until a steady-state is achieved. The reduced COF observed at the beginning of the cutting period lasts for a shorter period of time during the second cutting interval. At a higher cutting speed of $v_c = 40$ m/min in Figure 5.15 (B), the gradual increase in COF at the beginning of the cutting period becomes difficult to observe from the time-series results. When comparing dry cutting with MQL, negligible difference can be observed.

Workpiece mat.	Inconel 718	Cutting tool	TPGN160308 H13A
Lubrication	MQL	Tool coating	Uncoated
Uncut chip thick. h	0.1 mm	Rake angle γ_o	6°
Width of cut b	3 mm	Flank angle α_o	5°
Length of cut L_c	144 mm	Cutting speed v_c	10, 40 m/min
Number of inter. n	1	Lubricant	Vascomill MMS HD 1

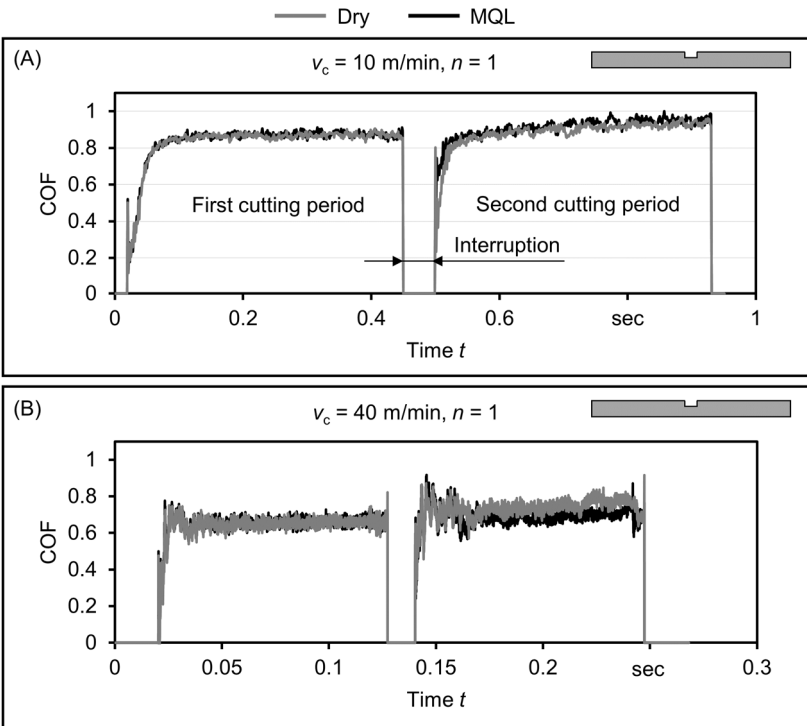


Figure 5.15 COF time-series at $n = 1$, (A) $v_c = 10$ m/min and (B) $v_c = 40$ m/min; (Alammari et al., 2021b)

5.4 Chapter conclusions

Adhesion on the rake face can be influenced by interruptions along the cutting length, as indicated by the quantification of adhesion area using the AGLM method applied to BSE images of the rake face. The AGLM method offers an efficient way to quantify adhesion on the rake face and provides statistically representative results. Quantifying adhesion area as well as the tool-chip contact length can provide valuable information about the contact conditions in an ex-situ manner. However, for a more detailed understanding of time-varying conditions, other measures such as mechanical load may offer more insights.

The average values of the measured mechanical load during steady-state conditions appear to be less affected by the presence of interruptions. However, it is important to note that the time-series results show a clear indication of low contact at the beginning of the cutting period, especially at low cutting speeds. This low mechanical load, reflected as a low apparent coefficient of friction, was not fully captured in the average values, highlighting the importance of considering transient behavior.

Furthermore, the low contact observed in the first cutting interval was not consistently repeatable after the interruption. This suggests that the chosen interruption length in this chapter may not have provided sufficient exposure of the cutting edge to the environment. Therefore, in the next chapter, further investigations will focus on the initial period of chip formation (IPCF) with variable interruption lengths to gain a deeper understanding of the early stages of the cutting process.

Chapter 6: Initial Period of Chip Formation

In the previous chapter, it was discussed that a transient phenomenon occurs at the beginning of the cut, where reduced contact characteristics can be noticed. In this chapter, the initial period of chip formation (IPCF), which occurs during a narrow window of space and time at the beginning of the cut, is closely investigated in an orthogonal machining setup in dry and MQL conditions. During IPCF, low mechanical loads were observed. In addition to mechanical load monitoring, the development of tool-chip contact was observed through measurements of initial chip curl with a transition criteria. Chip underside roughness and the contact marks on the rake face were also observed. The existence of IPCF is further investigated under an interrupted cutting process at prescribed intervals in order to sustain the positive effects occurring during IPCF.

6.1 Methodology and experimental setup^a

In order to investigate the contact condition in IPCF, stepped workpieces were prepared, allowing for variable cutting lengths as shown in Figure 6.1 (A). The evolution of the contact on the tool was examined. The total tool-chip contact length (l_c) on the rake face of the tool was measured, taking into account the development of sticking and sliding zones that progressively appear on the rake face, until the end of adhesion marks. A case study was conducted using Lycopodium powder applied on the rake face immediately after cutting, in order to determine the boundaries of lubricated regions within the tool-chip contact on the tool's rake face. Selected chips were collected and the curvature of the chip contact side was traced and analyzed. Additionally, a case study was conducted where the roughness of the contact side of a chip was measured at incremental locations corresponding to the cutting length. Furthermore, slotted workpieces with variable slot width, as shown in Figure 6.1 (B), were prepared to investigate the influence of interrupted cutting on sustaining IPCF.

As discussed in detail in Chapter 4, the machine tool used was a custom-built CNC machine, which allowed for the fundamental analysis of chip formation in orthogonal cutting, as shown in Figure 4.4. Mechanical load during machining were monitored using a three-axis piezoelectric dynamometer type 9263 (Kistler AG). Synthetic MQL oil Vascomill MMS HD 1 (Blaser Swisslube AG) was applied on the rake face using an airbrush prior to cutting during continuous cuts and supplied as MQL during interrupted cutting trials. An optical microscope VHX5000 (Keyence GmbH) was used to capture images of the rake face and chip side, as well as to quantify tool-chip contact zones. The chip contact-side surface morphology and roughness were measured using an autofocus variation microscope InfiniteFocus G5 from Alicona Imaging GmbH. A rotary holding device was used to assist in measuring the surface of the chip's contact side at different angular positions along the chip. Backscatter electron (BSE) images were obtained using a scanning electron microscope (SEM) MIRA3 XM from the manufacturer TESCAN equipped with a backscatter detector.

The workpiece materials used were austenitic stainless steel alloy X8CrNiS18-9 (1.4305) and Inconel 718. The specimens were separated from round workpieces using waterjet machining. The workpieces had a width of $b = 2$ mm. Stepped workpiece (WP-A) with cutting lengths $L_c = 2 \dots 108$ mm were prepared from stainless steel material, as shown in Figure 6.1 (A). Additionally, slotted workpieces (WP-B) were prepared from austenitic stainless steel 1.4305 and Inconel 718 materials with a cutting length $L_c = 8$ mm and different interruption lengths $L_{\text{int}} = 4, 6, 8, 16,$ and 24 mm, as shown in Figure 6.1 (B).

^aThis section adapted from (Alammari et al., 2023)

Tool holder CTFPL2525M16 with uncoated tungsten carbide (WC) inserts TP(G/U)N160308H13A from manufacturer Sandvik were used. The resultant rake angle was $\gamma_o = 6^\circ$ and the clearance angle of $\alpha_o = 5^\circ$. The cutting insert has a triangular shape with cutting edge radius measured at $r_\beta = 8 \mu\text{m}$. Uncut chip thickness was at $h = 0.2 \text{ mm}$ for stainless steel workpieces and $h = 0.1 \text{ mm}$ for Inconel 718 workpieces. The cutting speed was varied in the range of $v_c = 30, 60, 90$ and 120 m/min for stainless workpieces and $v_c = 10, 20, 30$ and 50 m/min for Inconel 718 workpieces.

The tool holder used was CTFPL2525M16 with uncoated tungsten carbide (WC) inserts TP(G/U)N160308H13A from the manufacturer Sandvik. The resulting rake angle was $\gamma_o = 6^\circ$ and the clearance angle was $\alpha_o = 5^\circ$. The cutting insert had a triangular shape with a cutting edge radius measured at $r_\beta = 8 \mu\text{m}$. The uncut chip thickness was $h = 0.2 \text{ mm}$ for stainless steel workpieces and $h = 0.1 \text{ mm}$ for Inconel 718 workpieces. The cutting speed was varied in the range of $v_c = 30, 60, 90,$ and 120 m/min for stainless steel workpieces, and $v_c = 10, 20, 30,$ and 50 m/min for Inconel 718 workpieces.

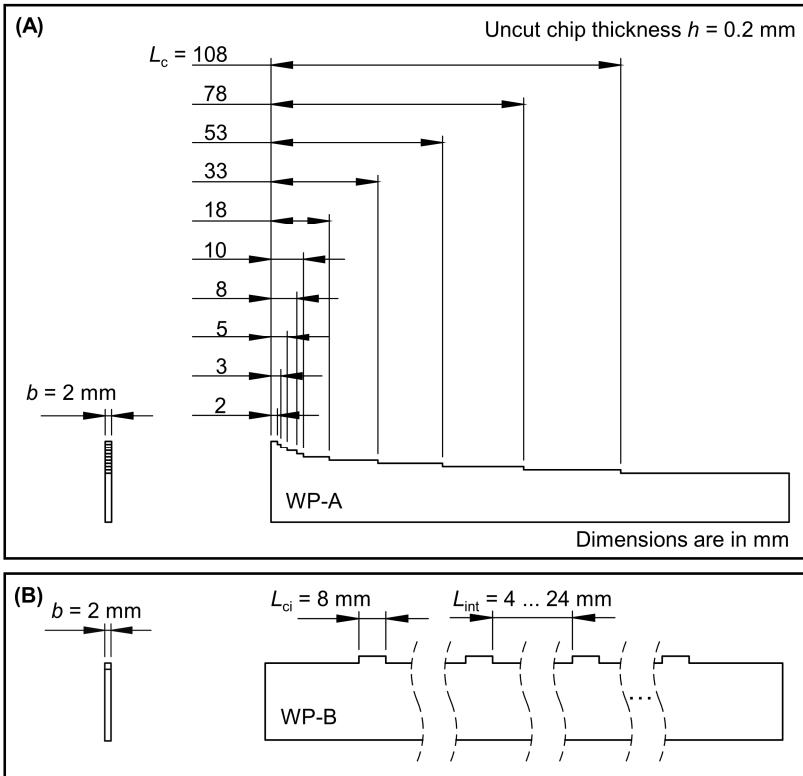


Figure 6.1 Workpieces geometry, (A) Stepped workpiece allowing for variable cutting lengths, (B) Slotted workpiece allowing for variable interruption length; (Alammari et al., 2023)

6.2 Initial period of chip formation (IPCF) and correlated low-tool-chip contact

6.2.1 Mechanical load in IPCF^a

Chip formation undergoes a complex physical evolution during the machining process. Particularly, at the beginning of the cutting interval, a transient behavior emerges, exhibiting an interesting phenomenon where low mechanical loads can be observed. Understanding how this development occurs, its limiting criteria, and influencing factors is highly important from tribological stand point. Figure 6.2 illustrates the measured mechanical loads and calculated coefficient of friction in orthogonal cutting under the specified conditions. IPCF occurs at the start of the cut, as highlighted in Figure 6.2 (A), with the effect of cutting speed on IPCF also shown. The impact of lubricated and dry conditions on IPCF, as well as the calculated apparent coefficient of friction, is presented in Figure 6.2 (B). The coefficient of friction was determined using Equation (5.3). The results shown in the figure correspond to continuous cutting without interruption. Further investigations into interrupted cutting reveal distinct behaviors of IPCF when comparing dry and lubricated conditions.

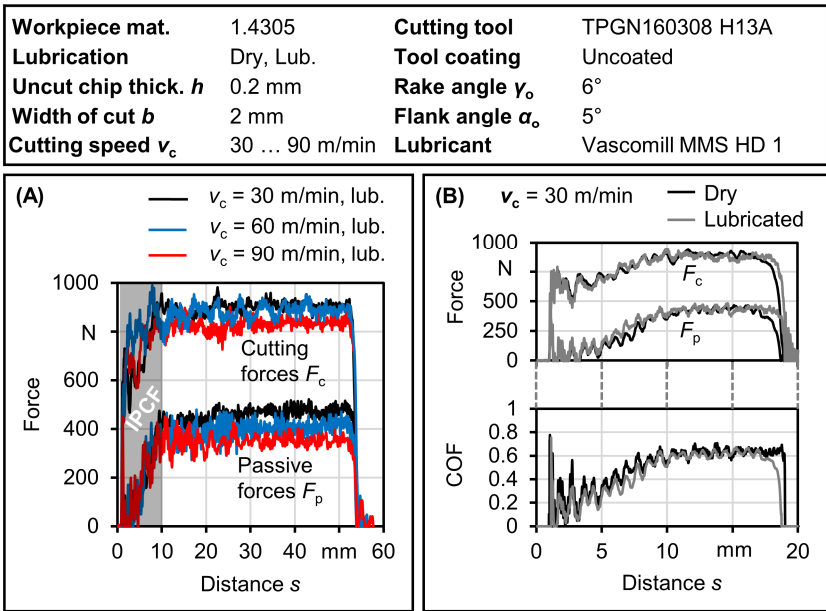


Figure 6.2 IPCF in continuous orthogonal machining, (A) The effect of using different speeds on mechanical load during IPCF, (B) The effect of dry vs. lubricated conditions on mechanical load and the calculated coefficient of friction (COF) during IPCF; (Alammari et al., 2023)

The passive force, F_p , is significantly influenced by friction in the secondary shear zone, where the rake side of the tool comes into contact with the forming chip. Factors such as contaminants (e.g., lubricants and oxides) and tool surface characteristics, including roughness and coatings, play a crucial role in determining the behavior of the tool-chip interface.

^aThis section adapted from (Alammari et al., 2023)

When examining mechanical loads during IPCF, it was observed that low forces were detected, with a greater reduction specifically associated with the passive force, F_p . This reduction in measured forces occurs only at the beginning of the cut. The transient region appears to reach a plateau at a specific cutting length, regardless of the cutting speed. IPCF seems to be more related to the distance traveled rather than the time elapsed, suggesting the possibility of a temperature effect that promotes adhesion and severe friction. Further investigations are required to study this intriguing phenomenon. In the next chapter, thermal modeling of IPCF will be conducted, wherein a critical temperature will be calculated at the transition point between low and high friction conditions.

6.2.2 Contact zone within tool-chip interface in IPCF^a

To examine the contact history during IPCF, adhesion on the rake face resulting from machining various cutting lengths was analyzed. An area of close contact near the cutting edge, where no adhesion marks are present, is referred to as the sticking zone, while the region with adhesion marks is referred to as the sliding zone. Figure 6.3 provides a summary of the measurements of sticking length (l_{cs}) and the total contact length (l_c) on the rake face after different cutting lengths (L_c), as per WP-A shown in Figure 6.1 (A).

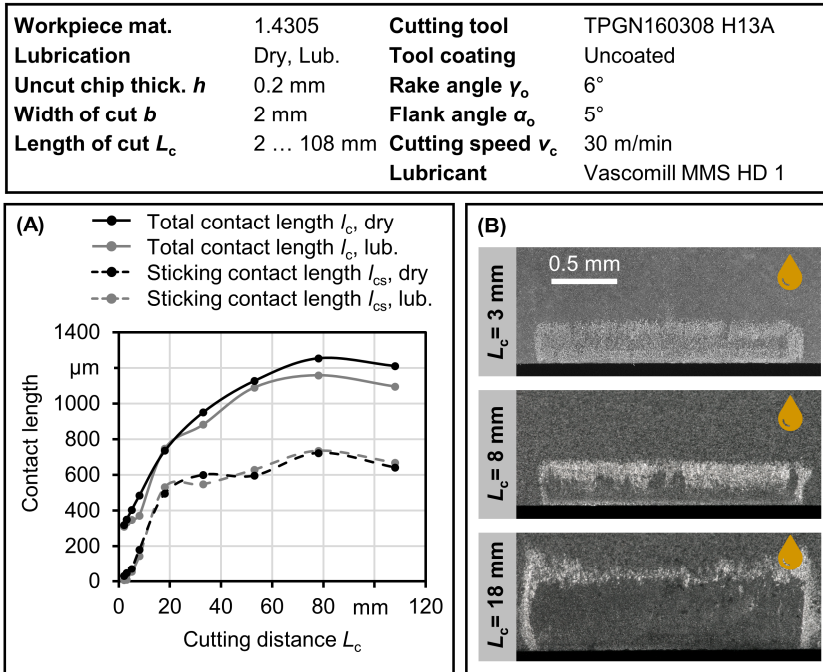


Figure 6.3 Tool-chip contact zones sizes, (A) Sticking and total contact lengths of dry and lubricated cutting, (B) Images of rake face showing adhesion marks resulting after different cutting lengths; (Alammari et al., 2023)

On one hand, the sticking zone gradually develops as the cutting progresses, eventually reaching a stable value after a certain cutting length. Qualitatively, the development of the sticking zone is

^a This section adapted from (Alammari et al., 2023)

similar to observations related to cutting forces. The full contact may have been delayed by contaminants present during initial chip formation. On the other hand, reaching the final total contact length occurs at a delayed cutting length, with a minimal increase in sticking length. The adhesion marks, indicating the sliding zone, start with a length slightly larger than the uncut chip thickness. However, the sticking zone can start from smaller values and rapidly increase to a final value. At short cutting lengths (e.g., $L_c = 2$ mm and $L_c = 3$ mm), the sticking zone is indistinguishable from the sliding zone, as shown in Figure 6.3 (B). The absence of a sticking zone at short cutting distances indicates low stresses, providing a better chance for contaminants to exist and influence tool-chip contact. However, similar to observations on mechanical load in Figure 6.2 (B), no significant difference was observed between dry and lubricated conditions in continuous cutting. IPCF appears to result in lower mechanical load and lower chip-tool contact. However, up to this point, IPCF analysis has been applied to a single cutting occasion in continuous cutting. Since the effects of IPCF are temporary, the goal is to sustain the beneficial effects by interrupting the cutting process, as discussed later in this chapter. Figure 6.4 presents a case study confirming the presence of lubricant within the sliding zone only, where adhesion marks are observed on the rake face.

6.2.3 Lubricant penetration within tool-chip interface

Figure 6.4 illustrates the application of Lycopodium powder to the rake face immediately after a lubricated cutting, revealing the spatial boundaries of lubricant penetration into the tool-chip contact interface. It can be observed that lycopodium particles adhere only within the sliding zone, where adhesion marks are present, and are found far from the cutting edge.

Workpiece mat.	1.4305	Cutting tool	TPGN160308FNH10T
Lubrication	Air brush	Tool coating	Uncoated
Uncut chip thick. h	0.2 mm	Rake angle γ_o	6°
Width of cut b	2 mm	Flank angle α_o	5°
Length of cut L_c	143 mm	Lubricant	Vascomill MMS HD 1
Cutting speed v_c	60 m/min		

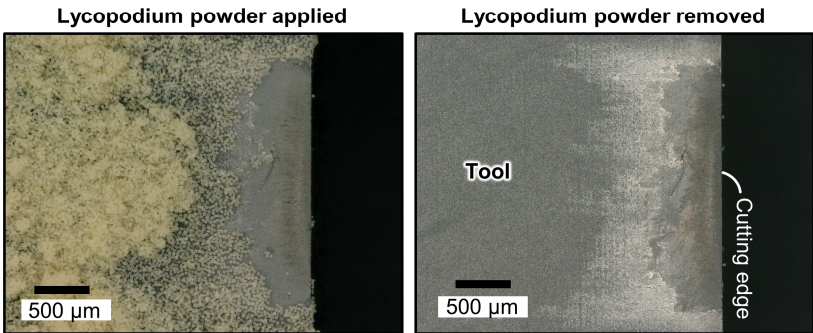


Figure 6.4 Observation of lubricant penetration within the tool-chip contact on the rake face using Lycopodium powder, performed ex-situ.

Two distinctive densities of adhered particles can be observed qualitatively. A low particle density is located within the sliding zone, while a relatively higher particle density appears beyond the sliding zone, far from the cutting edge where there is no tool-chip contact and an abundant quantity

of lubricant is present. Almost no particles are present within the sticking zone, which is immediately close to the cutting edge. The low density of particles may indicate partial penetration of the lubricant fluid. Additionally, it appears that there is no chance for the lubricant fluid to penetrate into the sticking zone under the specified conditions.

While observing the tool's rake face after a cutting operation can provide important insights, as discussed in this section, various other aspects can also be influenced by the contact condition within the tool-chip interface. The produced chips contain several important aspects that can indicate low contact characteristics within IPCF and its boundaries. In the next section, the surface topography of the contact-side of the chip will be measured from the beginning of the cut to determine if there is a transition in chip's contact side surface roughness between low and severe contact conditions along the length of the chip.

6.2.4 Chip contact-side surface condition

The roughness of the chip's contact side was measured at various locations that approximately corresponded to the cutting distance. The cutting distance was estimated by considering the compression ratio and chip length. This method, although not as accurate as other methods for indicating the transition location, can provide an indication of the influence of tool-chip contact on chip formation. Figure 6.5 presents a summary of the surface roughness of the chip's contact side. To obtain these measurements, the chip was mounted on a rotary holding device, with its axis perpendicular to the lens axis of the measurement device, and rotated at prescribed angles.

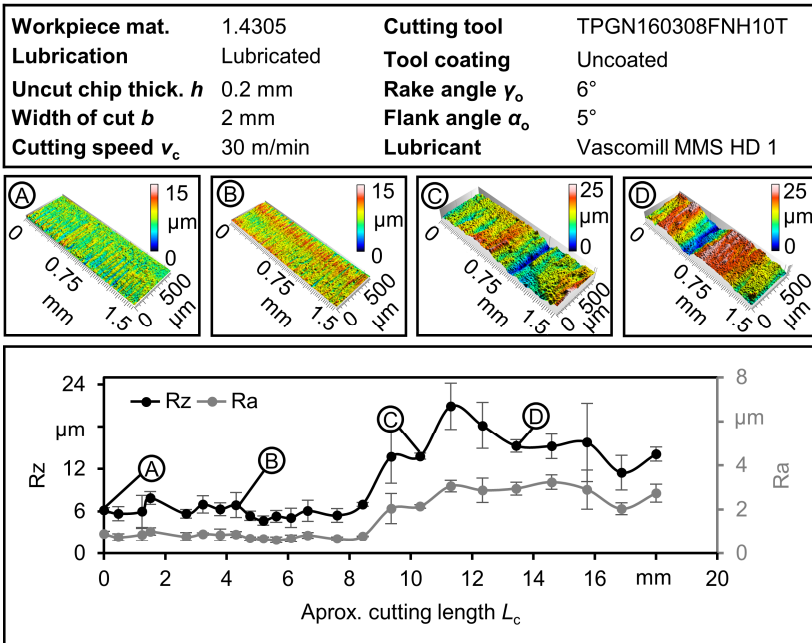


Figure 6.5 Chip's contact side surface roughness

The roughness of the chip's contact side starts with low values and increases as the cutting progresses. The low roughness observed at the beginning of the cutting interval indicates sliding friction on the rake face. This can also affect the calculation of the cutting length reported in Figure 6.5, as the compression ratio may be different. Due to the low friction within the tool-chip interface, the formed chips are longer than the chips formed at higher friction values, which corresponds to low and high shear angles, respectively. High chip roughness values indicate the initiation of buildup edge (BUE) formation, which was observed in high-speed video recordings. The frequent deposition and break-off of the BUE on the rake face have an influence on the roughness of the chip's contact side. The surface roughness of the chip's contact side provides important information about the contact condition within the tool-chip interface. However, it has its limitations in terms of measurement accessibility. The investigated chip had to fit within a limited space, and it becomes quite challenging to conduct measurements for a continuous chip as the multiple turns or winding of the chip obstruct the direct view of internal portions. To quantify the transition between low and high friction conditions and their influences on chip formation, chip curl was also investigated. The initial chip curl was systematically quantified, and a transition criterion was used to identify the end of the initial chip curl.

6.2.5 Chip curl and the identification of a transition criteria

Produced chips contain valuable information about machining conditions, including tool-chip interface friction. Of particular importance is the chip curl that occurs at the beginning of the cutting instance, known as the initial chip curl, in orthogonal machining. The curl radius and the transition point, indicating the transition between an arc and a spiral form, are further investigated for their relationship to IPCF. Figure 6.6 (A) shows that the chip has two distinct forms: the initial chip curl and the subsequent chip curl. The end of the initial chip curl is defined as the transition point.

At the beginning of the cutting instance, the geometrical shape of the chip curl takes the form of an arc. The chip continues to grow with a specific chip curl radius until a transition occurs. As the cutting progresses, the initial chip curl no longer maintains the arc shape, which can be influenced by various factors, including changes in the tribological conditions within the tool-chip interface. By knowing when this transition occurs and the distance to this point, IPCF can be characterized more reliably, and a distinctive transition can be systematically distinguished by examining chip curl aspects. In Figure 6.6 (B), a clear transition can be observed between arc and spiral formation, which is related to the initial and subsequent chip formation, respectively.

To obtain the plot shown in Figure 6.6 (B), several steps are followed. First, the chip outline is recorded and manually digitized as Cartesian coordinates from digital images of the chip side. Then, a logarithmic spiral is fitted to the digitized outline to obtain a continuous and uniformly distributed set of chip outline points. The logarithmic spiral is found abundantly in nature as an optimal path for radial growth. As suggested by (Batzer and Sutherland, 2001) and (Devotta, 2015), a logarithmic spiral can closely approximate the chip form as well. The logarithmic arc outline can be mathematically described in terms of the distance from the spiral center (r_s) and the rotation angle (θ) between the horizontal line and the line connecting the spiral center and the spiral outline. The following equation represents the logarithmic spiral:

$$r_s = a_s e^{\theta \cot(b_s)} \quad (6.1)$$

where a_s and b_s are constants defining the logarithmic spiral. Then, the centers of small arcs, consisting of a few points, moving progressively along the chip profile, are determined and plotted.

Workpiece mat.	1.4305	Cutting tool	TPGN160308H13A
Lubrication	Lubricated	Tool coating	Uncoated
Uncut chip thick. h	0.2 mm	Rake angle γ_o	6°
Width of cut b	2 mm	Flank angle α_o	5°
Cutting speed v_c	60 m/min	Length of cut L_c	8

- Chip Initial curl outline
- Subsequent Chip curl outline
- ✕ End of initial Chip curl
- ✕ Averaged arc center – initial curl
- ✕ Arc centers – initial curl
- ✕ Arc Centers – subsequent curl

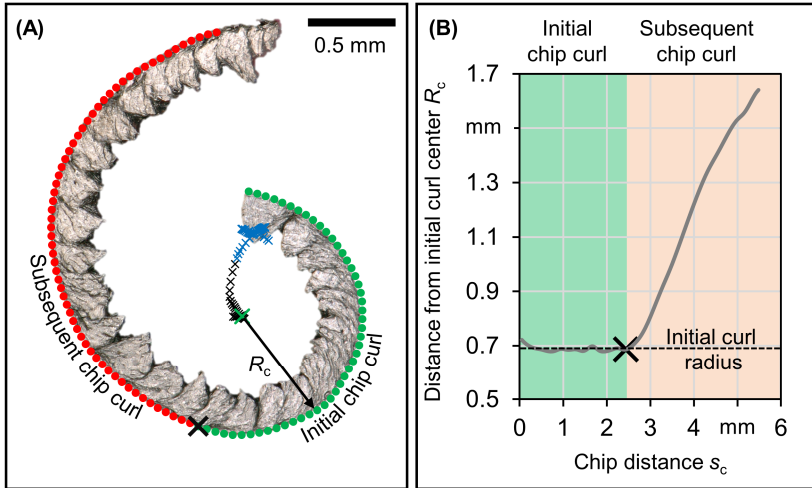


Figure 6.6 Initial chip curl, (A) Illustration of initial chip formation on chip side, (B) Initial chip curl radius and transition criteria

A criterion was established to determine when the next progressive arc center deviates more than the average distance of the previous progressive arc centers. The progressive arc centers are depicted as blue and black crosses in Figure 6.6 (A), with the blue centers representing progressive arcs located within the initial chip curl. The average initial arc center can be determined by averaging the positions of the progressive arc centers located within the initial chip curl. The distance between the initial chip curl and the chip outline, R_c , is plotted in Figure 6.6 (B). The distance R_c is obtained using the circle formula as follows:

$$R_c = \sqrt{(x - x_c)^2 + (y - y_c)^2} \quad (6.2)$$

where x and y represent the Cartesian coordinates of a point located on the chip outline, and x_c and y_c represent the Cartesian coordinates of the initial chip curl center, indicated by a green cross in Figure 6.6 (A). A constant radius, R_c , can be obtained within the initial chip curl and is shown as a horizontal line in Figure 6.6 (B). The distance R_c increases beyond the initial chip curl as the chip distance, s_c , increases. The transition distance between the initial chip curl and the subsequent chip curl can be determined by setting a threshold limit on R_c . The quantification of the initial chip curl radius and length is performed using specialized MATLAB scripts specifically developed to process

the input data and calculate the results. The script requires input data for the chip curl outline as Cartesian coordinates, along with image scale information. Another MATLAB script was used to assist in manually tracing the chip side outline graphically. The results of the initial chip curl and initial chip curl length for different cutting speeds and lubrication conditions are shown in Figure 6.7 for austenitic stainless steel and Inconel 718 workpiece materials.

In Figure 6.7 (A) and (C), the chip curl radius decreases for the lubricated case compared to the dry case for both materials. High cutting speed induces thermal effects that influence chip formation, such as thermal softening, which affects chip curl and tool-chip contact. At relatively low cutting speed for austenitic stainless steel 1.4305, there is a noticeable difference in chip curl radii between the dry and lubricated conditions. However, the difference between lubricated and dry cases becomes less pronounced as the cutting speed increases, as shown in Figure 6.7 (A) for austenitic stainless steel 1.4305.

Workpiece mat.	1.4305, Inconel 718	Cutting tool	TPGN160308FNH10T
Lubrication	Dry, Lub.	Tool coating	Uncoated
Width of cut b	2 mm	Rake angle γ_o	6°
		Flank angle α_o	5°

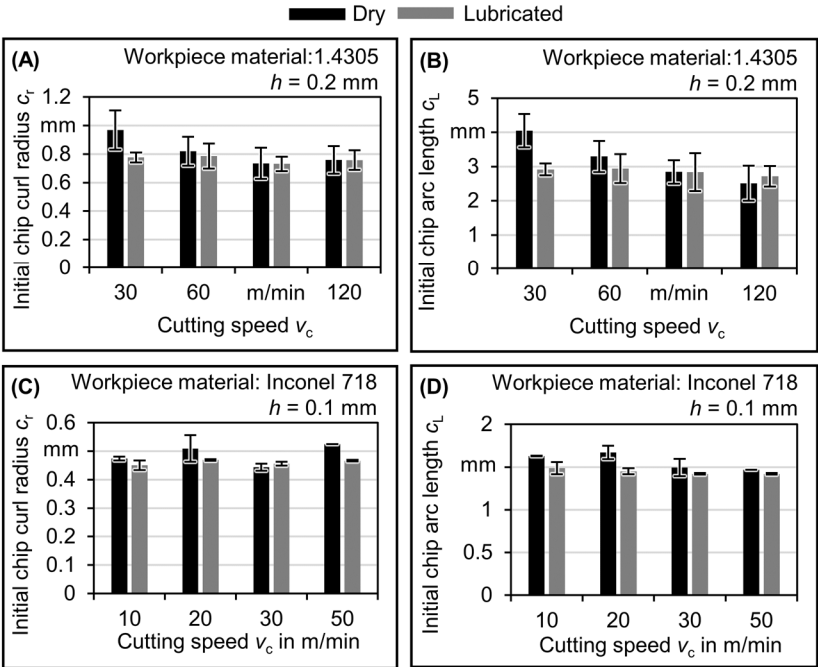


Figure 6.7 Initial chip curl results, (A) and (C) Initial chip curl radius, (B) and (D) Initial chip curl length

It is generally understood that contact temperatures increase with higher cutting speeds. These observations may indicate that external lubrication becomes less effective due to increased temperature at high cutting speeds. The formation of a built-up edge (BUE) influences chip formation at low cutting speeds, as it can alter the geometry of the cutting tool by adhering work-hardened workpiece material during cutting, thereby influencing the angles of the cutting tool. The rake angle may become larger with the presence of a BUE. Based on the results of the chip curl radius, it cannot be conclusively determined if the presence of a BUE influences the initial chip curl results of dry and lubricated cases at low cutting speeds.

The initial chip arc length, as shown in Figure 6.7 (B) and (D), indicates a similar trend for dry cutting. The initial chip curl length becomes shorter as the cutting speed increases. The difference between the dry and lubricated cases decreases as the cutting speed increases, with a longer chip curl observed for dry cutting. This observation suggests that the initial chip curl for lubricated cutting lasts for a shorter distance.

An important observation obtained from high-speed video recordings suggests that the transition of chip curl and the corresponding transition distance may be influenced when the chip contacts the workpiece. The friction between the chip and the workpiece can affect chip curling, as reported by (Batzner and Sutherland, 2001). However, the transition between the initial chip curl and subsequent chip curl is not always influenced by the contact between the chip and the workpiece, as in many cases, the transition can already occur before chip-workpiece contact takes place.

Up to this point, the IPCF analysis has been applied to a single cutting occasion. Since the effects of IPCF are temporary, the goal is to maintain the favorable effects by interrupting the cutting process. It is also essential to observe the repeatability and applicability of IPCF characteristics for interrupted cutting. In the next section, investigations on IPCF using interrupted workpieces will be conducted.

6.3 IPCF in interrupted orthogonal cutting

6.3.1 Austenitic stainless steel 1.4305

As evident from the results of previous investigations, the effects associated with IPCF are transient and cannot be sustained beyond a finite cutting distance. Therefore, interrupted cutting provides an opportunity to maintain the favorable effects associated with IPCF. During cutting interruption, spatial and temporal windows allow for the potential cooling of the tool and the restoration of the contamination layer, such as a lubricant film.

In the interrupted cutting investigations, the cutting length was fixed within the IPCF range at $L_c = 8$ mm. The interruption length, L_{int} , was varied in the range of $L_{int} = 4$ to 24 mm. Each workpiece (designated as WB-B in Figure 6.1) had a constant interruption length. Figure 6.8 illustrates the calculated coefficient of friction (COF) for four consecutive cutting intervals in the two outermost cases, with $L_{int} = 4$ mm shown in Figure 6.8 (A) and $L_{int} = 24$ mm shown in Figure 6.8 (B)

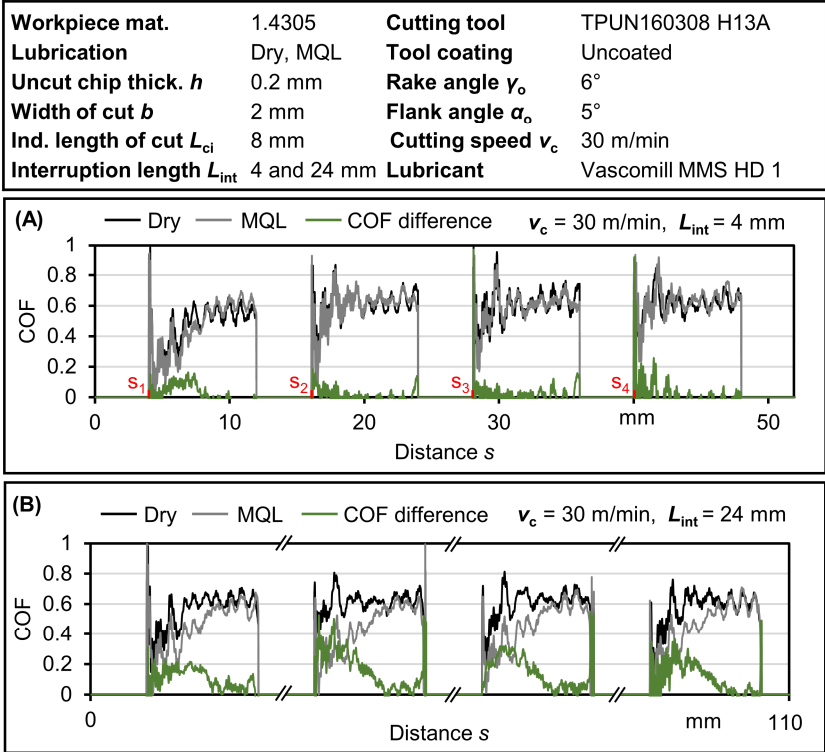


Figure 6.8 Interrupted cutting under MQL with varying interruption length – Austenitic stainless steel 1.4305, (A) At interruption length $L_{int} = 4$ mm, (B) At interruption length $L_{int} = 24$ mm; (Alammari et al., 2023)

Interruption can play a crucial role in sustaining the effects of IPCF. With a short interruption length, there is limited opportunity to clear the chips, cool down the tool, and potentially restore the contamination layer, as shown in Figure 6.8 (A). Conversely, as the interruption duration increases through longer interruption lengths, subsequent cutting intervals exhibit repeatable behavior similar to the first cutting instance, as shown in Figure 6.8 (B). The first cutting instance, illustrated in Figure 6.8 (A), demonstrates a typical behavior where the dry and lubricated cases show no significant difference, exhibiting low COF values similar to the observations presented earlier in Figure 6.2 (B). This raises an important question regarding the initial conditions at the beginning. Prior to the first cutting occasion, the tool temperature is at a relatively low room temperature, which may influence the tribological conditions at the tool-chip interface. Accurately measuring high-speed temperature changes from low temperatures (starting from room temperature) within the tool-chip interface, which subsequently rise to relatively high temperatures (ranging from 500 to 1000°C) during cutting, presents a significant challenge. Therefore, the first cutting occasion is excluded from further analysis.

To quantify the differences between the various conditions, the work per cutting interval is calculated, and the average of all cutting intervals is obtained, excluding the first cutting interval. The following formula is used to calculate the average work per cutting interval.

$$\bar{W} = \frac{\sum_{i=2}^{n_c} \int_{s_i}^{s_{i+1}} F \cdot ds}{N} \quad (6.3)$$

where s_i represents the starting distance of the cutting interval, as shown in Figure 6.8 (A), n_c is the number of cutting intervals, F is the resultant force, and s represents distance. The results of the average work per cutting interval, \bar{W} , excluding the first cutting interval, for different interruption lengths and cutting speeds are shown in Figure 6.9.

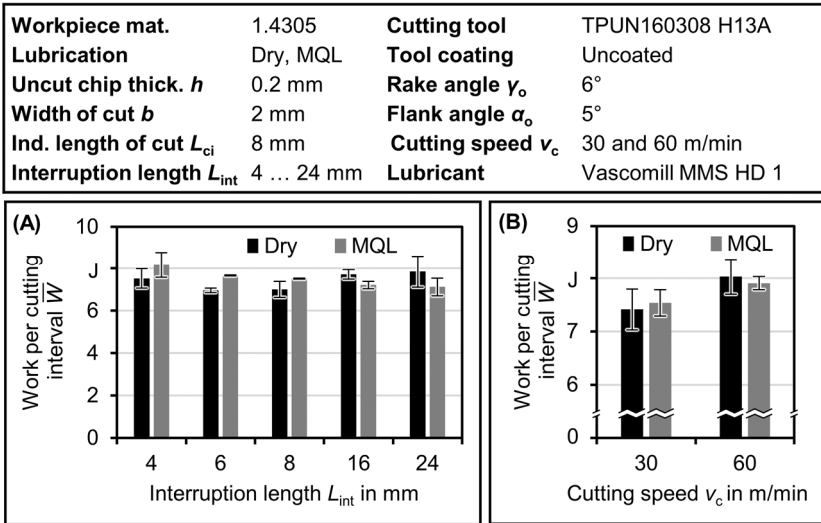


Figure 6.9 Average work per cutting interval, (A) At variable interruption length, (B) Averaged results of work per cutting interval at cutting speed $v_c = 30$ m/min and $v_c = 60$ m/min

As shown in Figure 6.9 (A), the average work per cutting interval continues to decrease as the interruption length increases, demonstrating a direct correlation to interruption effectiveness for lubricated cutting with a cutting speed of $v_c = 30$ m/min. The average work per cutting interval for cutting speed $v_c = 30$ m/min is slightly lower compared to cutting speed $v_c = 60$ m/min, as shown in Figure 6.9 (B). Trials with the same speed and lubrication condition were averaged together. These results can be interpreted in two ways. Firstly, it could be related to temperature, where the interruptions provide less time at higher speeds for the temperature to cool down and be as effective as in the case of lower speeds. Secondly, it may be related to the effect of lubrication in the lubricated cases and the presence of BUE in the dry cutting cases at low cutting speed.

For short interruption lengths (i.e., $L_{int} = 4, 6,$ and 8 mm), the lubricated cases exhibit reversed behavior compared to dry cutting, as shown in Figure 6.9 (A). In these interruption lengths, the average work per cutting interval is lower in dry cutting. High-speed video recordings were examined, revealing the presence of BUE in dry cutting trials at $v_c = 30$ m/min, as shown in Figure 6.10.

Workpiece mat.	1.4305	Cutting tool	TPUN160308 H13A
Lubrication	Dry	Tool coating	Uncoated
Uncut chip thick. h	0.2 mm	Rake angle γ_o	6°
Width of cut b	2 mm	Flank angle α_o	5°
Ind. length of cut L_{ci}	8 mm	Cutting speed v_c	30 m/min
Interruption length L_{int}	4 mm		

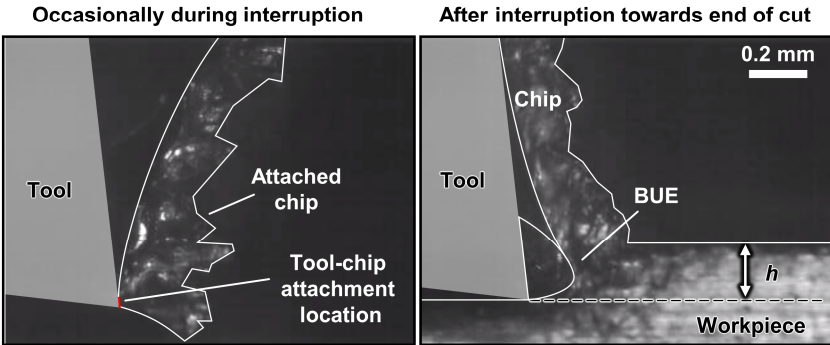


Figure 6.10 Built-up-edge (BUE) at low cutting speed and dry condition after short interruption length

As shown in Figure 6.10, in the case of short interruption lengths and dry cutting, the chip adheres to the cutting edge after cutting interval. This adherence of the chip to the tool, which lasts some time during the interruption, promotes the formation of a built-up edge (BUE) during subsequent cutting. This observation is more pronounced in cutting periods located towards the end of the workpiece. The presence of the BUE affects chip formation, and the measured mechanical load is low as the effective rake angle increases and becomes more positive. In dry cases, the work-hardened material adheres more easily to the rake face of the tool compared to lubricated cases. On the other hand, there is little BUE detected in lubricated cases, especially in trials with long interruption lengths compared to trials with short interruptions in dry machining.

6.3.2 Inconel 718

Previous investigations were conducted using austenitic stainless steel 1.4305. In this section, IPCF in interrupted cutting is also explored for Inconel 718. The range of cutting speeds and uncut chip thicknesses used for Inconel 718 investigations is lower than those employed for machining austenitic stainless steel, as machining Inconel 718 involves higher thermal and mechanical loads. Consequently, a direct comparison between the two materials is not feasible. However, other conditions pertaining to interruption length, cutting length, and lubrication were kept consistent for both workpiece materials. Figure 6.11 illustrates the difference in coefficient of friction for four consecutive cuts at a cutting speed of $v_c = 10$ m/min, with variable interruption lengths at $L_{int} = 8$ mm and $L_{int} = 24$ mm, in dry and lubricated machining.

Workpiece mat.	Inconel 718	Cutting tool	TPGN160308 H13A
Lubrication	Dry, MQL	Tool coating	Uncoated
Uncut chip thick. h	0.1 mm	Rake angle γ_o	6°
Width of cut b	2 mm	Flank angle α_o	5°
Ind. length of cut L_{ci}	8 mm	Cutting speed v_c	10 m/min
Interruption length L_{int}	8 and 24 mm	Lubricant	Vascomill MMS HD 1

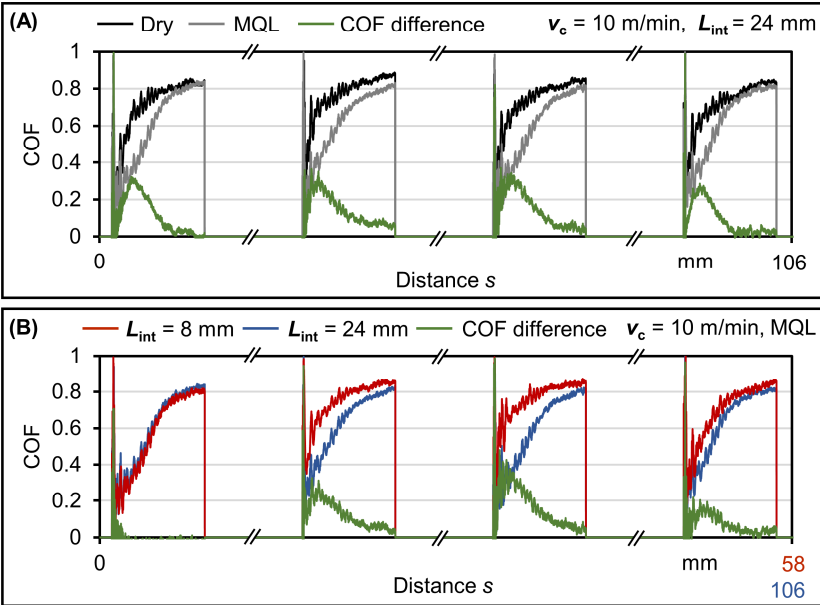


Figure 6.11 Interrupted cutting under MQL with varying interruption length – Inconel 718, (A) Dry versus MQL cutting at interruption length $L_{int} = 24$ mm, (B) Interruption length $L_{int} = 24$ mm versus $L_{int} = 8$ mm

Figure 6.11 (A) demonstrates that at a cutting speed of 10 m/min, MQL is effective in reducing the coefficient of friction (COF) within IPCF when a relatively long interruption length is present between cutting occasions. Conversely, at a shorter interruption length of $L_{int} = 8$ mm, the lubricant is less effective in reducing the COF within IPCF compared to $L_{int} = 24$ mm, as shown in Figure 6.11 (B). It is noteworthy that the calculated COF for the MQL trial with a short interruption length of $L_{int} = 8$ mm is similar to the results obtained in dry cutting with a longer interruption length of $L_{int} = 24$ mm. Figure 6.12 provides a summary of the results of the work per cutting interval, as described by Equation 6.3, for different interruption lengths, cutting speeds, and lubrication conditions.

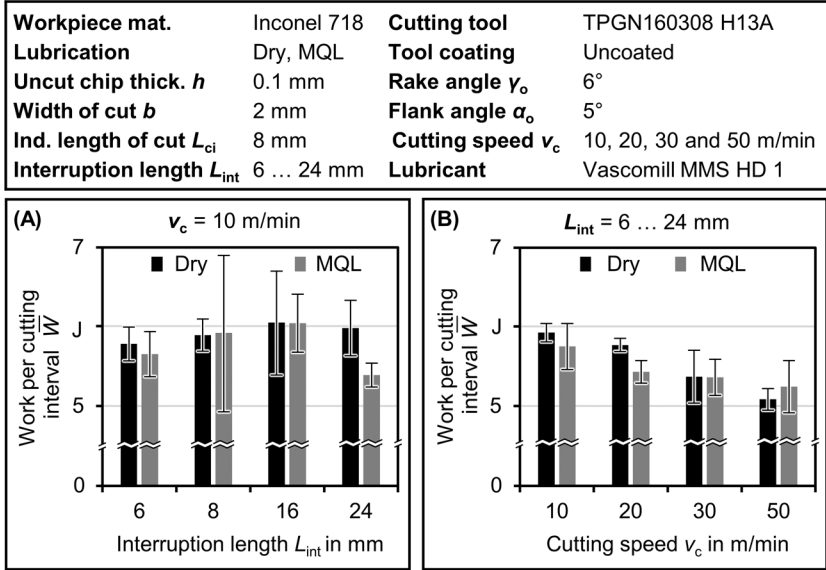


Figure 6.12 Average work per cutting interval for Inconel 718, (A) With varying interruption length, (B) Averaged results of work per cutting interval at variable cutting speed

As depicted in Figure 6.12 (A), the difference between dry and MQL cases is only noticeable at a long interruption length of $L_{int} = 24$ mm and a cutting speed of $v_c = 10$ m/min. Shorter interruption lengths show little difference between MQL and dry machining. Additionally, it can be observed that the work per cutting interval slightly decreases for both MQL and dry machining as the interruption length decreases. This decrease could be attributed to the limited temperature reduction achievable at shorter interruption lengths, where thermal aspects have an effect on chip formation. The short duration available for the tool to cool down and be exposed to the environment might result in reduced effectiveness of MQL in re-wetting the tool-chip contact area during the interruption.

In Figure 6.12 (B), a similar effect can be observed. As the cutting speed increases, there is less time available during the interruption to influence chip formation in the subsequent cutting interval. MQL is less effective at relatively high speeds of $v_c = 30$ m/min and $v_c = 50$ m/min compared to low cutting speeds of $v_c = 10$ m/min and $v_c = 20$ m/min, as shown in Figure 6.12 (B). The effect of BUE for Inconel 718 at low cutting speeds is less prominent compared to the observations for austenitic stainless steel 1.4305.

To investigate IPCF more closely, high-speed video recording was conducted for both MQL and dry cutting. Figure 6.13 presents some video frames captured at different times during IPCF for the case involving a cutting speed of $v_c = 10$ m/min and an interruption length of $L_{int} = 24$ m/min. The corresponding COF results are correlated with the extracted frames, allowing for observation of changes in chip curl, chip thickness, shear angle, and the approximate contact length.

Workpiece mat.	Inconel 718	Cutting tool	TPGN160308 H13A
Lubrication	Dry, MQL	Tool coating	Uncoated
Uncut chip thick. h	0.1 mm	Rake angle γ_o	6°
Width of cut b	2 mm	Flank angle α_o	5°
Ind. length of cut L_{ci}	8 mm	Cutting speed v_c	10 m/min
Interruption length L_{int}	24 mm	Lubricant	Vascomill MMS HD 1

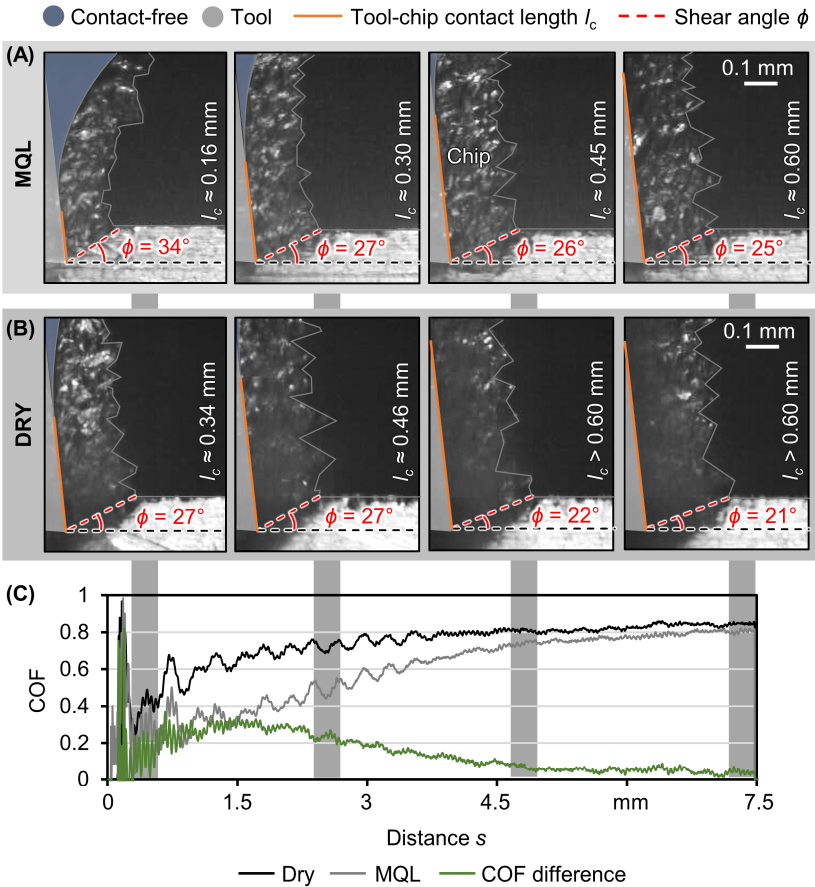


Figure 6.13 Frames extracted from high speed video recording during IPCF, (A) Cutting under MQL, (B) Dry cutting, (C) Corresponding COF results

Chip curl under MQL, as shown in Figure 6.13 (A), starts with a small radius, resulting in a short tool-chip contact length. Additionally, the shear angle is large, indicating low tool-chip contact friction during IPCF. However, as cutting continues, these characteristics of low contact gradually diminish after a certain cutting distance. In dry cutting, as depicted in Figure 6.13 (B), the

characteristics of low tool-chip contact during IPCF only persist for a shorter distance compared to the MQL case.

BSE images of the rake face were taken to observe adhesion occurring after cutting with variable interruption lengths, cutting speeds, and lubrication conditions. Figure 6.14 presents BSE images for cutting speeds of $v_c = 10$ m/min and $v_c = 50$ m/min under dry and lubricated conditions, as well as interruption lengths of $L_{int} = 24$ mm and $L_{int} = 6$ mm.

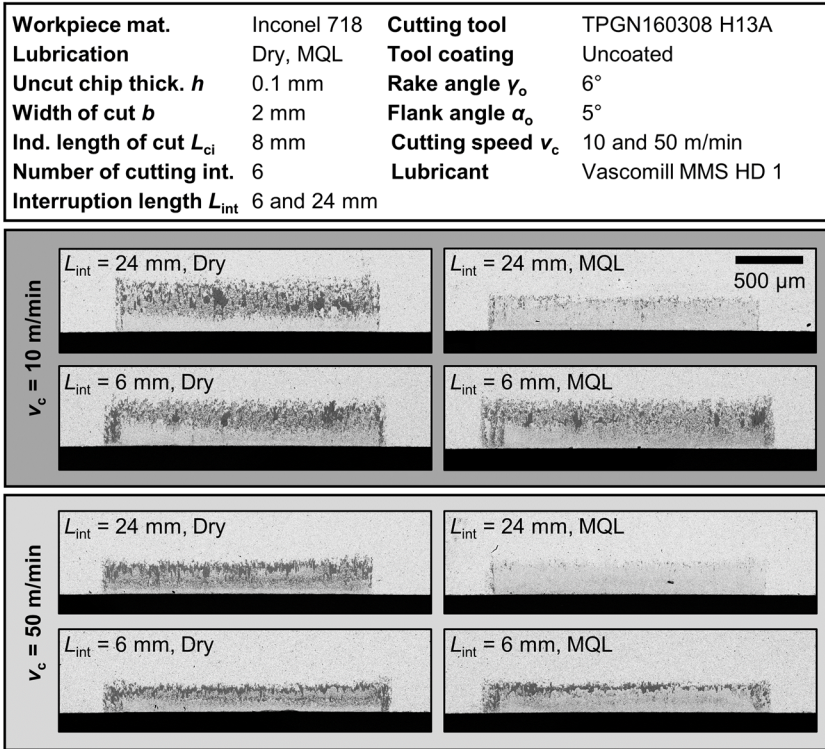


Figure 6.14 BSE images of the adhesion on the rake face after interrupted cutting

Adhesion on the rake face, as depicted in Figure 6.14, appears to be minimal for interruption length $L_{int} = 24$ mm using MQL at both cutting speeds of $v_c = 10$ m/min and $v_c = 50$ m/min. In contrast, shorter interruption lengths and dry cutting conditions result in increased adhesion on the rake face. These results align with the previous observations regarding COF in Figure 6.11, which indicate reduced tool-chip contact as the interruption length increases under MQL. Additionally, it is noteworthy that the contact length at a relatively high cutting speed of $v_c = 50$ m/min appears to be shorter than the contact length at a low cutting speed of $v_c = 10$ m/min, likely due to the thermal effects that occur at higher cutting speeds.

6.4 Chapter conclusions

The initial period of chip formation (IPCF) at the start of the cutting process exhibits reduced mechanical load and low tool-chip contact compared to the steady-state condition. Understanding and characterizing IPCF can be advantageous for improving continuous machining processes through the introduction of interruptions along the cutting path. This enables targeted and efficient application of cutting fluids (CFs) and enhances sustainability.

The investigations conducted in this chapter indicate a finite cutting length where transient IPCF effects occur before diminishing at the steady state. To sustain IPCF, an adequate cutting-free period is required. There appears to be a relationship between the development of contact zones on the tool's rake face and the end of IPCF. The sticking contact gradually develops within IPCF until it reaches its final size, suggesting an apparent relationship between contaminants resistant to ablation and the mechanical loads.

Chip curl, which resembles an arc shape, also indicates the initial chip formation. The radius of the initial chip curl arc can provide insights into the contact condition within the tool-chip interface. A smaller chip curl indicates lower contact within the interface. The initial chip curl has a finite length and undergoes a shape transition at a specific location, which could be an important indicator of the change in tool-chip contact before chip-workpiece contact occurs.

Improved performance of minimum quantity lubrication (MQL) under interrupted cutting within IPCF has been observed. The repeatability of IPCF is influenced by the size of interruptions. IPCF appears to be insensitive to cutting speed, and a finite cutting length can be identified. Modeling IPCF is necessary to investigate thermal effects in chip formation, which are essential for characterizing IPCF and its sustainability in interrupted machining. The next chapter will address the thermal modeling of IPCF to further explore the potential connection between transition distance and temperature in IPCF.

Chapter 7: Thermal Modelling of the Initial Period of Chip Formation

In this chapter, the thermal modeling of the initial period of chip formation (IPCF) is proposed and discussed. Thermal aspects, which were discussed in the previous chapter, may influence IPCF. Periodic heating and cooling occurring during cutting and interruption, respectively, are modeled using a hybrid analytical and finite element (FE) transient thermal model. In addition to identifying a transition distance from apparent coefficient of friction results using a sigmoid function, a transition temperature is also identified using the thermal model. The model is validated experimentally using a two-color pyrometer at a specific cutting distance.

7.1 Transient thermal modelling at IPCF

Heat generation caused by plastic deformation and friction plays an important role in metal cutting. Most of the mechanical energy used in machining is converted into heat, which is transferred to the tool, workpiece, and chip. The remaining heat is released as radiation or kinetic energy in the chip. The majority of the heat generated in the cutting area is removed by the chip. Localized heat generation induces high temperature gradients. Experimental techniques for determining cutting tool temperature are challenging due to the small dimensions of the heat source and the chips produced, making it difficult to observe the cutting region during machining. Therefore, theoretical analysis of cutting temperatures is crucial for understanding heat generation and temperature distribution during cutting operations.

Due to the cyclic behavior in interrupted cutting, where a steady-state condition may or may not be achieved, a transient thermal modeling is required in this case. A transient thermal model proposed by (Karaguzel, 2021) is adapted in the following analysis, with key differences related to the identification of input parameters required to identify heat flux, which are obtained experimentally, and the definition of heat flux reducing factors along the cutting path associated with interruptions and IPCF. The thermal model consists of two main parts: one is related to identifying the heat flux, and the other part is the determination of the temperature field within the tool using a partial differential equation (PDE) solved numerically with a 2D Finite Element Method.

7.1.1 Determination of heat flux at tool-chip interface

In IPCF, the friction within the tool-chip interface varies over a finite cutting distance, resulting in a corresponding influence on the heat flux. Additionally, the distribution of heat flux within the tool-chip interface is influenced by a dual zone model, namely sticking and sliding. Figure 7.1 provides an overview of the heat flux within the tool-chip interface in IPCF.

The primary mechanism in the thermomechanical modeling of the secondary deformation zone is the friction between the tool and the chip. This friction arises from the contact between the two surfaces and is modeled using a dual zone approach (Zorev, 1963). The contact at the rake face of the tool is divided into a sticking region and a sliding region. The sticking region experiences high normal stress, while the sliding region has relatively low normal stress values and follows the Coulomb friction law. The normal and tangential stresses on the rake face of the tool are typically represented as shown earlier in Chapter 2, Figure 2.9.

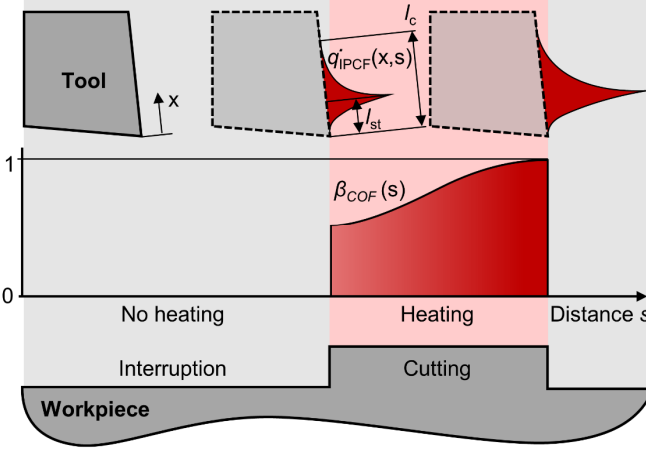


Figure 7.1 Schematic of heat flux in IPCF

According to Coulomb's friction law, the shear stress is directly proportional to the normal stress, with a sliding friction coefficient μ and normal stress p . If the friction coefficient remains constant, as the normal stress increases towards the tool tip, the shear stress also increases. However, the shear stress cannot exceed the material's shear flow stress τ_1 , so it is assumed to be equal to τ_1 in the sticking zone. Therefore, the distribution of shear stress along the contact on the rake face is defined as (Childs, 2006):

$$\tau = \begin{cases} \tau_1, & x \leq l_{st} \\ \mu p(x), & l_{st} < x \leq l_c \end{cases} \quad (7.1)$$

Accordingly, the heat flux within the tool-chip interface, denoted as $\dot{q}(x)$ and representing the function of the distance x away from the cutting edge on the rake face, is given as (Karaguzel, 2021):

$$\dot{q}(x) = \begin{cases} \tau_1 v_{ch}, & 0 \leq x \leq l_{st} \\ \mu v_{ch} p(x), & l_{st} < x \leq l_c \\ 0, & x > l_c \end{cases} \quad (7.2)$$

where l_c represents the total tool-chip contact length, which is measured at the end of adhesion marks appearing on the rake face. l_{st} denotes the sticking zone length and is calculated using the formula proposed by Budak and Ozlu (2008):

$$l_{st} = l_c \left(- \left(\frac{\tau_1}{p_0 \mu} \right)^{\frac{1}{\zeta}} + 1 \right) \quad (7.3)$$

where μ represents the tool-workpiece sliding friction coefficient, which is determined experimentally. τ_1 denotes the material shear flow stress, estimated to be equal to the shear flow stress at the primary shear zone, which is influenced by material properties at high strain rates and elevated temperatures. It is calculated at steady state from measured forces and geometrical parameters, which identify the primary shearing area, as follows (Childs, 2006):

$$\tau_1 = \frac{(F_c \cos \phi - F_p \sin \phi) \cdot \sin(\phi)}{hb} \quad (7.4)$$

where F_c represents the cutting force and F_p denotes the passive force. The angle ϕ represents the shear angle. The uncut chip thickness and width of cut are denoted as h and b , respectively. v_{ch} denotes the chip velocity calculated along the chip-tool contact, following the method proposed by (Li et al., 2013), as follows:

$$v_{ch}(x) = \begin{cases} v_{ch0} \left(\frac{x}{l_{st}} \right)^{\omega_c}, & 0 \leq x \leq l_{st} \\ v_{ch0}, & l_{st} < x \leq l_c \\ 0, & x > l_c \end{cases} \quad (7.5)$$

where ω_c represents the chip velocity distribution exponent, which is assumed to have a constant value of $\omega_c = 2$ in this investigation. v_{ch0} denotes the average chip velocity and can be determined using the following equation:

$$v_{ch0} = v_c \frac{\sin\phi}{\cos(\phi - \gamma_o)} \quad (7.6)$$

where v_c represents the cutting speed, γ_o is the rake angle, and ϕ denotes the shear angle, which can be determined geometrically by knowing the chip thickness ratio $r_c = h / h_c$, where h_c represents the average chip thickness. The relationship is as follows:

$$\phi = \tan^{-1} \left(\frac{r_c \cos\gamma_o}{1 - r_c \sin(\gamma_o)} \right) \quad (7.7)$$

$p(x)$ represents the normal pressure on the rake face and is given by (Budak and Ozlu, 2008):

$$p(x) = p_0 \left(1 - \frac{x}{l_c} \right)^\zeta \quad (7.8)$$

where ζ represents the stress distribution exponent, which is typically considered to be between 2 and 3 and can be determined through split tool experiments. In the current investigation, it was assumed to be $\zeta = 2$. p_0 is calculated as follows (Budak and Ozlu, 2008):

$$p_0 = \tau_1 \frac{h(\zeta + 1)}{l_c \sin\phi} \frac{\cos\lambda_f}{\cos(\phi + \lambda_f - \gamma_o)} \quad (7.9)$$

where λ_f represents the apparent friction angle, which is calculated as $\lambda_f = \tan^{-1}(COF)$, and COF denotes the apparent coefficient of friction obtained from the cutting forces F_c and passive forces F_p , as well as the rake angle, using the following equation:

$$COF = \frac{F_p + F_c \tan \gamma_o}{F_c - F_p \tan \gamma_o} \quad (7.10)$$

The secondary shear zone heat flux partition ratio R_2 is used to determine the portion of the total heat flux \dot{q} that is divided between the tool and the chip. In this investigation, R_2 was found iteratively by comparing the steady-state temperature obtained from the temperature analysis of (Loewen and Shaw, 1954) with the steady-state tool temperature obtained from the proposed model. The tool heat flux is then determined as follows:

$$\dot{q}_{tool}(x) = (1 - R_2)\dot{q}(x) \quad (7.11)$$

Here, \dot{q}_{tool} represents the steady-state heat flux at the tool. The cutting-distance-dependent heat flux in IPCF is determined both during interruption and cutting, as follows:

$$\begin{aligned} \dot{q}_{IPCF}(x, s) &= \begin{cases} \beta_{COF}(s) \cdot \dot{q}_{tool}(x), & i(L_{ci} + L_{int}) \leq s \leq i(L_{ci} + L_{int}) + L_{ci} \\ 0, & i(L_{ci} + L_{int}) + L_{ci} \leq s \leq (i + 1)(L_{ci} + L_{int}) \end{cases} \end{aligned} \quad (7.12)$$

where $i = 0, 1, 2, \dots$, L_{ci} represents the length of each individual cutting interval, and L_{int} denotes the length of the interruption. The distance is related to time by $s = v_c t$. $\beta_{COF}(s)$ is a factor that represents the reduction of steady-state heat flux due to a decrease in friction in IPCF. It is obtained by fitting a sigmoid function to the average COF data of subsequent cutting segments. The sigmoid function for IPCF is defined as follows:

$$COF_{fit}(s) = COF_{min} + \frac{COF_{max}}{1 + e^{-k_1(s-s_0)}} \quad (7.13)$$

$$\beta_{COF}(s) = COF_{fit}(s)/COF_{max} \quad (7.14)$$

where COF_{min} and COF_{max} represent the minimum and maximum COF values in IPCF, respectively. k_1 denotes the evolution rate, and s_0 represents the transition distance at the transition midpoint. If s_0 becomes negative, it indicates that the transition in the COF data has not been detected.

7.1.2. Determination of tool temperature due to heat flux occurring at tool-chip interface

Once the heat flux is determined temporally and spatially, as discussed in the previous section, the temperature can be estimated using the heat equation. The partial differential equation for the temperature field in the tool is given as follows:

$$\rho c \frac{\partial T}{\partial t} = \nabla \cdot (k \nabla T) \quad (7.15)$$

Where T represents the tool rake temperature, ρ is the density, k is the thermal conductivity, and c is the specific heat. Equation 7.15 is solved numerically using the MATLAB Partial Differential Equations (PDE) toolbox. The two-dimensional tool geometry is specified, and boundary conditions are defined on the edges of the tool as follows:

- Heat flux is applied only within chip-tool contact.
- Heat convection is applied on the flank face and the rest of the rake face. The heat convection coefficient is assumed to be $h_{conv} = 10 \text{ W/m}^2$, and the ambient temperature is $T_\infty = T_{room} = 23 \text{ }^\circ\text{C}$.
- The outermost edges of the tool are set to a constant temperature of $T_{room} = 23 \text{ }^\circ\text{C}$.

Figure 7.2 provides a summary of the tool geometry, mesh, and boundary conditions of the setup as applied in the MATLAB PDE toolbox. The "*generateMesh*" command in the MATLAB PDE toolbox was used with *Hmax* and *Hedge* properties. A refined mesh size smaller than 0.02 mm was used along the tool-chip contact, extending up to 1 mm from the cutting edge. The maximum mesh size was 0.5 mm throughout the tool away from the tool-chip contact. The total simulation time was set according to the desired number of heat cycles. The step size was defined by dividing the time of a single heat cycle by 1000.

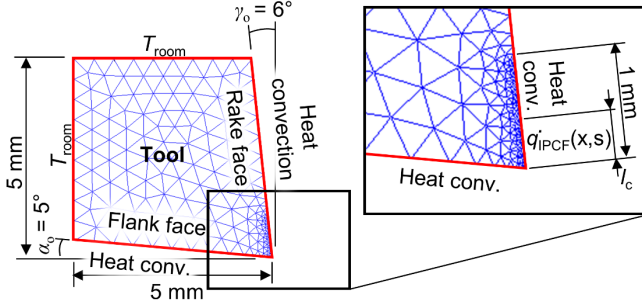


Figure 7.2 Tool geometry, mesh and boundary conditions applied in MATLAB PDE tool box

Temperature-dependent thermal conductivity and specific heat for the tool were utilized in solving the partial differential equation. They were implemented in the MATLAB PDE toolbox as user-defined functions using function handles. In order to determine the heat partition ratio, R_2 , temperature-dependent thermal properties for both the tool and workpiece were employed in the model proposed by (Loewen and Shaw, 1954). Table 7.1 provides an overview of the temperature-dependent thermal properties for the materials of the tool and workpieces. According (Ho and Chu, 1978), the electrical and thermal properties of austenitic stainless steel 304 and 303 (1.4305) are considered to be identical. Hence, the properties for austenitic stainless steel 304 are presented in Table 7.1 and will be utilized in the thermal investigations for austenitic stainless steel 303 (1.4305).

Table 7.1 Temperature-dependent thermal properties and density of tool and workpiece materials

Material	Property	Equation or value
Tool WC/6Co adapted from (Spriggs et al., 2002)	Thermal cond. in W/mK	$k(T^{\circ}C) = 3 \times 10^{-5} T^2 - 0.0715 T + 100.25$
	Specific heat in J/kgK	$c(T^{\circ}C) = -6 \times 10^{-5} T^2 + 0.125 T + 213.07$
	Density in kg/m ³	15160*
Inconel 718 adapted from (Sweet et al., 1987)	Thermal cond. in W/mK	$k(T^{\circ}C) = 0.017 T + 10.73$
	Specific heat in J/kgK	$c(T^{\circ}C) = -2.9 \times 10^{-4} T^2 + 0.44 T + 330$
	Ther. diffusivity in m ² /s	$K(T^{\circ}C) = 2.83 \times 10^{-9} T + 2.82 \times 10^{-6}$
	Density in kg/m ³	8221
Austenitic stainless steel 304 Adapted from (Sweet et al., 1987)	Thermal cond. in W/mK	$k(T^{\circ}C) = 0.0174 T + 14.421$
	Specific heat in J/kgK	$c(T^{\circ}C) = -3.7 \times 10^{-4} (T^2) + 0.61 T + 329$
	Ther. diffusivity in m ² /s	$K(T^{\circ}C) = 4.35 \times 10^{-9} T + 1.59 \times 10^{-6}$
	Density in kg/m ³	7900

*measured

In the following sections, the transient temperature results in IPCF for Inconel 718 and austenitic stainless steel 1.4305 will be discussed.

7.2 Results of transient temperature in IPCF – Inconel 718

7.2.1 Input parameters

As discussed in the previous section, the model requires certain parameters as input. These parameters consist of the apparent coefficient of friction (COF), tool-chip contact length at different cutting speeds, mean chip thickness, and the sliding friction coefficient in both dry and lubricated conditions. The sliding friction coefficient was experimentally measured using an open tribometer, as described by (Puls et al., 2012). Figure 7.3 presents a summary of these experimental results. Furthermore, the heat partition ratio R_2 , obtained through iterative calculations, is also illustrated in Figure 7.3.

Workpiece mat.	Inconel 718	Cutting tool	TPGN160308 H13A
Lubrication	Dry, MQL, Lub.	Tool coating	Uncoated
Uncut chip thick. h	0.1 mm	Rake angle γ_o	6°
Width of cut b	2 mm	Flank angle α_o	5°
Cutting speed v_c	10 ... 50 m/min	Friction tool angle	5°
Relative speed v_r	10 ... 90 m/min		

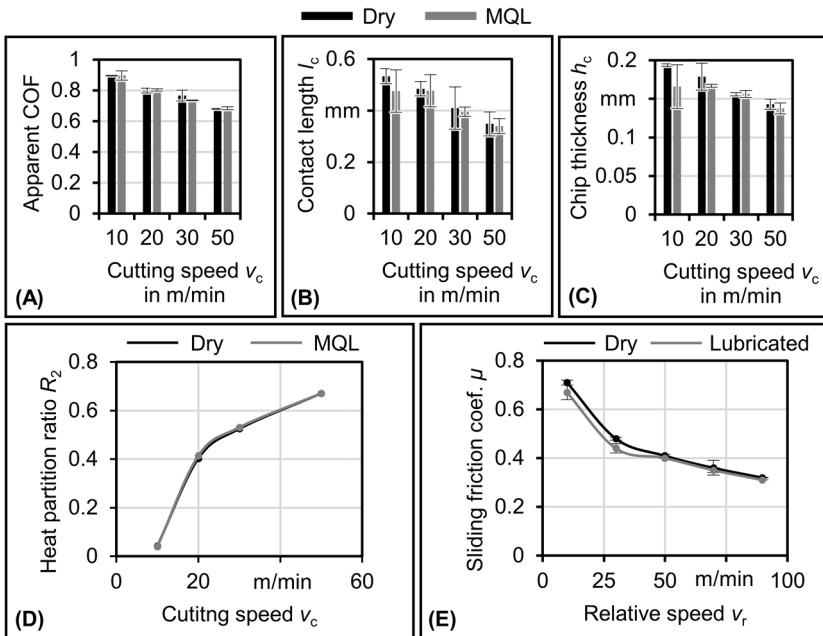


Figure 7.3 Input parameters to IPCF transient temperature model for dry and lubricated cases for Inconel 718, (A) Apparent friction coefficient (COF), (B) Tool-chip contact length l_c , (C) Chip thickness h_c , (D) Heat partition ratio R_2 , (E) Sliding friction coefficient μ

The parameters shown in Figure 7.3 are obtained under steady-state conditions. The apparent coefficient of friction influences the heat flux as it defines the maximum normal stress on the rake

face, as shown in Equation 7.8. The contact length is an important factor that determines the spatial extent of the heat flux and is used to obtain the heat partition ratio in the steady state. The chip thickness and uncut chip thickness are used to calculate the shear angle, considering the rake angle as shown in Equation 7.7. The experimentally obtained sliding friction values are used to define the sliding friction in the sliding zone. As expected, the apparent coefficient of friction, tool-chip contact length, and chip thickness decrease as the cutting speed increases. Furthermore, the use of MQL slightly reduces their values. The heat partition ratio R_2 , which indicates the portion of heat entering the chip, increases with increasing cutting speed. An interesting observation is the minimal influence of lubrication on the sliding friction for Inconel 718, as shown in Figure 7.3 (E).

7.2.2 Model results validation at steady state

The reliability of the proposed model in estimating the steady-state temperature is examined by comparing the results with the results of steady state temperature model of (Loewen and Shaw, 1954). Figure 7.4 (A) provides a summary of the steady-state results. Additionally, a comparison with experimental temperature measurements at a finite distance using a two-color ratio pyrometer on the rake face, as described by Saelzer et al. (2020), is shown in Figure 7.4 (B).

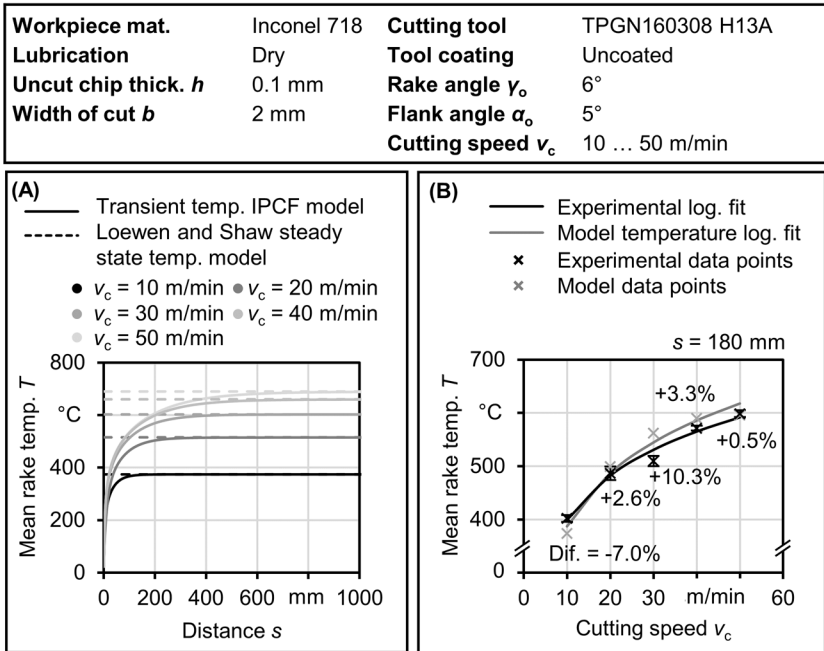


Figure 7.4 (A) Comparison with analytical steady state model by (Loewen and Shaw 1954), (B) Model results in comparison with experimental average rake temperatures obtained using ratio pyrometer at cutting distance $s = 180$ mm

The model predicts the average rake temperature, which is the average temperature along the tool-chip contact length, with reasonable accuracy. The estimated mean rake temperature error is approximately $\pm 10\%$ within the cutting speed range of $v_c = 10$ to 50 m/min for Inconel 718. This

error could be attributed to measurement accuracy issues related to the position of the measuring spot on the rake face, as well as inherent limitations of the model resulting from the calculated sticking zone length using Equation 7.3.

7.2.3 Determination of heat flux reduction factor within IPCF

The steady-state heat flux, which can be determined using the aforementioned parameters, is reduced within IPCF by utilizing the IPCF heat flux reduction factor β_{COF} , as shown in Figure 7.5. This reduction factor accounts for distance-related events such as interruptions where no heat input occurs, as well as the reduction observed in IPCF, which exhibits a decrease in the COF.

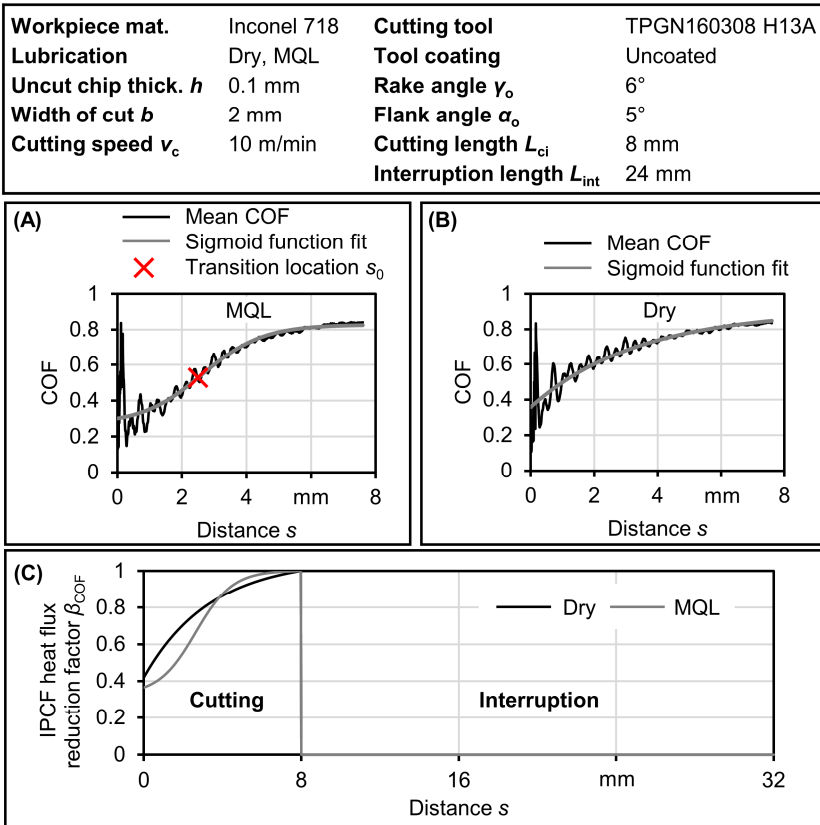


Figure 7.5 Example of the influence of IPCF on heat flux, (A) An MQL case showing mean COF fitted with sigmoid function with identified transition location s_0 , (B) Corresponding dry case showing mean COF fitted with sigmoid function and no transition in COF was identified, (C) The resulting IPCF heat flux reduction factor for a single heating cycle of cases shown in A and B

The sigmoid function fit, as shown in Figure 7.5 (A) and (B), provides a close approximation that describes the reduction in COF observed in IPCF. Whether a transition between low and high

friction occurs or not, the sigmoid function is capable of fitting the data. In cases where no transition is detected, a negative transition value is assigned. The fitted data are then divided by the maximum COF value, which approximates the steady-state condition. The IPCF heat flux reduction factor β_{COF} can be determined for both cutting and interruption segments. The steady-state heat flux within the tool-chip interface is multiplied by the reduction factor along the tool movement, accounting for multiple heat cycles.

7.2.4 Heat flux and temperature results

This section presents the temperature within the tool, resulting from the determined heat flux. Figure 7.6 displays selected temperature results obtained from the model, specifically showing the maximum temperature on the rake face.

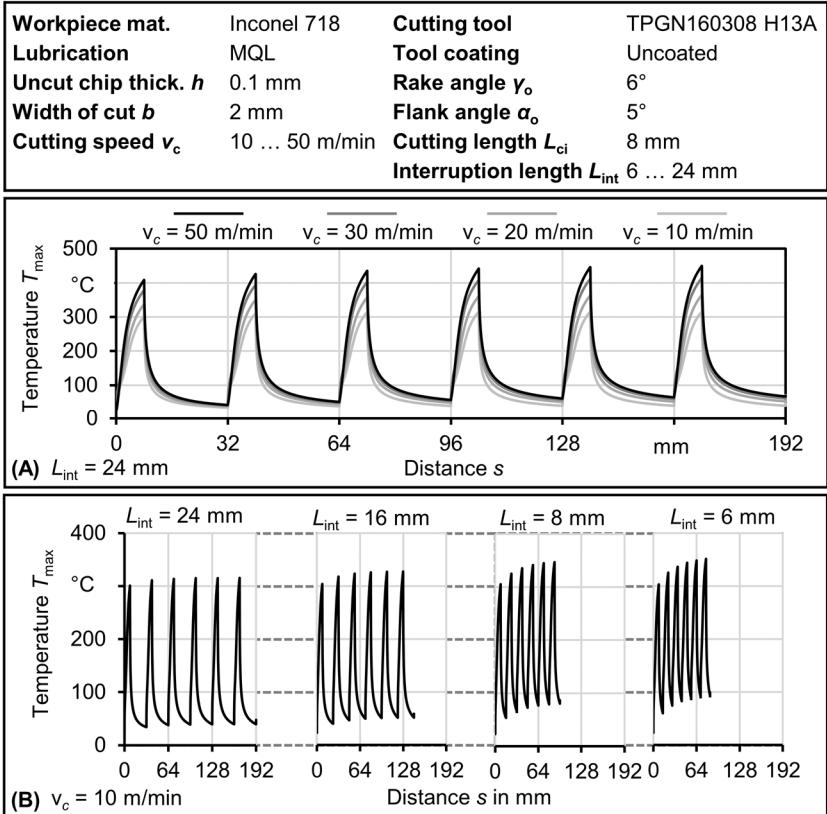


Figure 7.6 Maximum rake temperature at rake face obtained from the model in interrupted cutting for Inconel 718, (A) At different speeds for $L_{int} = 24$ mm, (B) At different interruption length at $v_c = 10$ m/min

Figure 7.6 (A) demonstrates that higher cutting speeds result in higher maximum temperatures at the tool-chip contact, as expected, due to the increased heat flux. However, the heat partition ratio may limit its influence on the tool temperature, as only a small amount of heat enters the tool at high speeds. During cutting, the temperature gradually rises due to the heat supplied by the cutting process, resulting from shearing and friction. When cutting is interrupted, the temperature increase halts and a reduction in temperature occurs. Figure 7.6 (B) shows that shorter interruption lengths lead to higher minimum and maximum temperatures, as the time available for cooling the tool becomes shorter. The temperature change associated with different interruption lengths suggests a potential impact of temperature on the reduced tool-chip contact in lubricated IPCF, where temperature and interruption time become crucial factors. At low speeds and longer interruption lengths, the reduced contact in IPCF becomes more noticeable between the dry and MQL cases. Figure 7.7 reveals that the reduced tool-chip contact friction in IPCF appears to slow down the temperature increase during cutting.

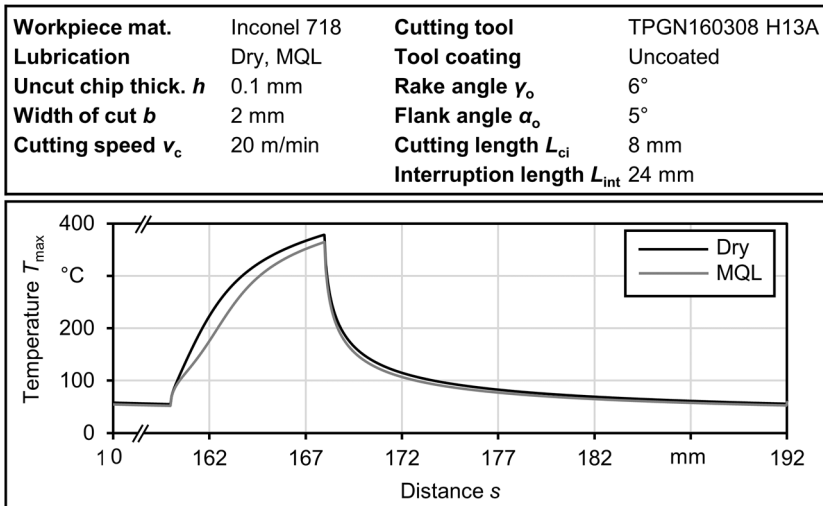


Figure 7.7 Effect of MQL on maximum rake temperature for Inconel 718

Figure 7.7 provides a visualization of a single heating cycle, highlighting the influence of MQL on the maximum temperature at the tool-chip interface. The heat flux reduction factor, β_{COF} , plays an important role in reducing the rate of temperature increase at the beginning of the cutting process. This factor reflects the impact of the low apparent coefficient of friction within IPCF and determines the extent to which a reduction in steady-state heat flux can be achieved. The decrease in heat flux at the start of the cut affects the final temperature before interruption, resulting in a lower maximum temperature achieved with MQL compared to the dry condition.

Figure 7.8(A) illustrates the total heat flux along the tool-chip contact length at the steady-state condition, $\dot{q}(x)$, for different cutting speeds and lubrication conditions. This heat flux, $\dot{q}(x)$, is reduced by the heat partition ratio, R_2 , where a portion flows through the chip while the remaining portion $(1 - R_2)$ enters the tool. Additionally, the heat reducing factor, β_{COF} , allows for a non-uniform heat flux that depends on the tool's position within IPCF. The non-uniform distribution of heat flux along the tool-chip contact length leads to a non-uniform temperature distribution along the contact,

with the maximum temperature located at a certain distance from the cutting edge, as depicted in Figure 7.8(B). The temperature field within the tool at these maximum values is shown in Figure 7.8(C) for different cutting speeds using MQL.

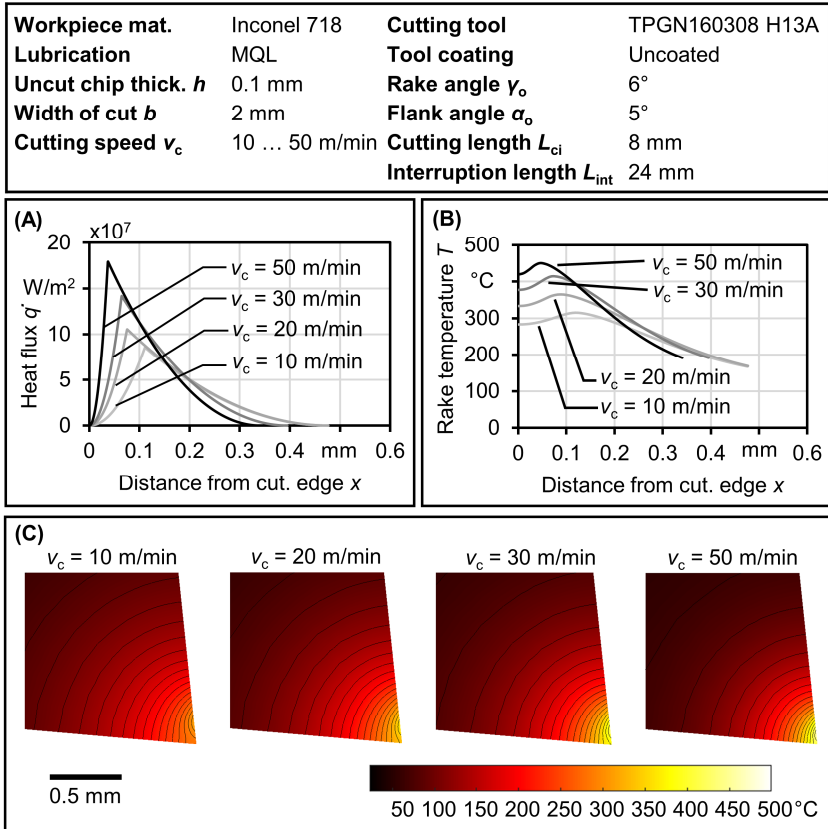


Figure 7.8 Heat flux and tool temperature for Inconel 718, (A) Heat flux along tool-chip contact length at steady state, (B) Temperature along tool-chip contact length before interruption, (C) Temperature field within the tool at different cutting speeds occurring before interruption

The heat flux depicted in Figure 7.8 (A) extends for a finite distance along the tool-chip contact length. The endpoint of the heat flux and the location of the maximum heat flux value (which occurs at the end of the sticking zone) influence the temperature distribution along the contact and within the tool, as shown in Figure 7.8 (B). High temperatures are reached at high cutting speeds, although the temperature field within the tool may vary, as seen in Figure 7.8 (C). At low cutting speeds, a lower maximum temperature is observed, but with an extended temperature field due to the longer tool-chip contact length.

The temperature analysis discussed in this chapter raises an important question regarding the existence of a transition temperature for IPCF and its quantification. Figure 7.9 attempts to provide more detail on this aspect.

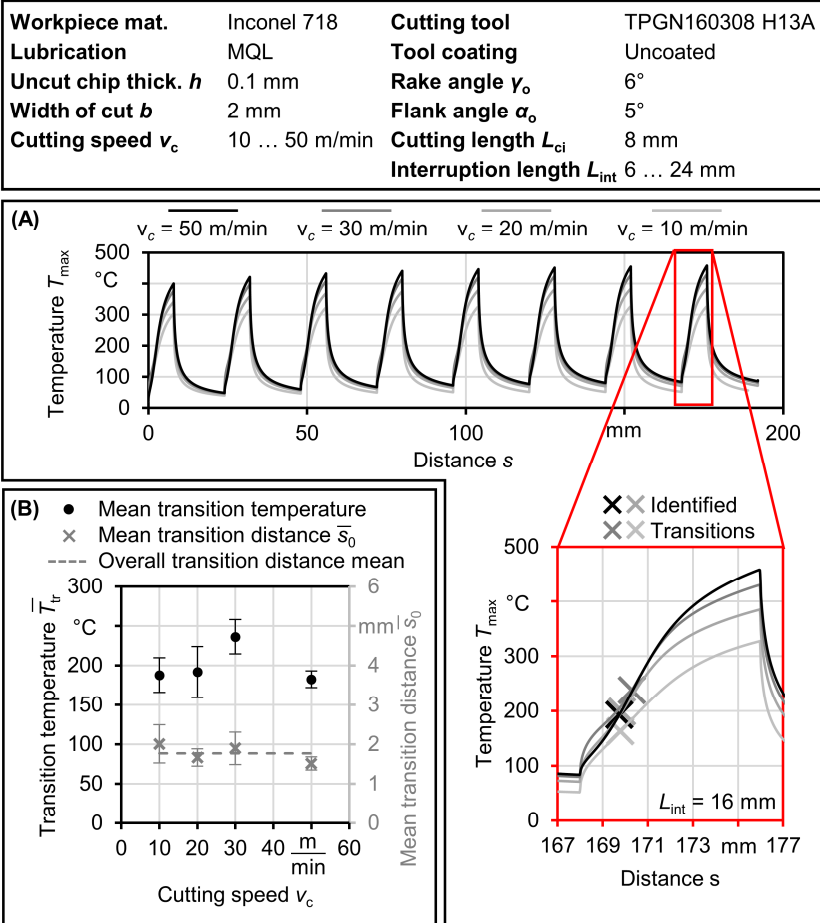


Figure 7.9 Identification of transition temperatures, (A) Example of transition temperature identification, (B) Transition temperature and distance results

As previously shown in Figure 7.5 (A) and (B), a sigmoid function was utilized to fit the data of the apparent coefficient of friction (COF). The transition distance, denoted as s_0 , was determined as the value at the sigmoid's midpoint. In Figure 7.9, the identified transition distance was employed to find the transition temperature at different cutting speeds. It should be noted that for Inconel 718, the transition distance is only valid for cases with MQL; the dry cases either exhibit negative values or very small values that were not considered as transition points. An example illustrating how the transition temperature is identified is presented in Figure 7.9 (A). A summary of the transition results

is provided in Figure 7.9 (B). The transition distance, s_0 , appears to remain constant across different cutting speeds at an average value of $\bar{s}_0 = 1.8$ mm, and the corresponding transition temperature, T_{tr} , falls within a limited range with an average of $\bar{T}_{tr} = 199.5$ °C.

7.3 Results of transient temperature in IPCF – austenitic stainless steel 1.4305

7.3.1 Input parameters

The results presented and discussed in the previous section were focused on Inconel 718. In this section, the results for austenitic stainless steel 1.4305 will be presented. The input parameters for the model are shown in Figure 7.10. These parameters were obtained experimentally. The heat partition ratio R_2 is determined iteratively by comparing the mean steady-state temperature along the contact length predicted by the proposed model with the tool temperature obtained using the method by Loewen and Shaw (1954)

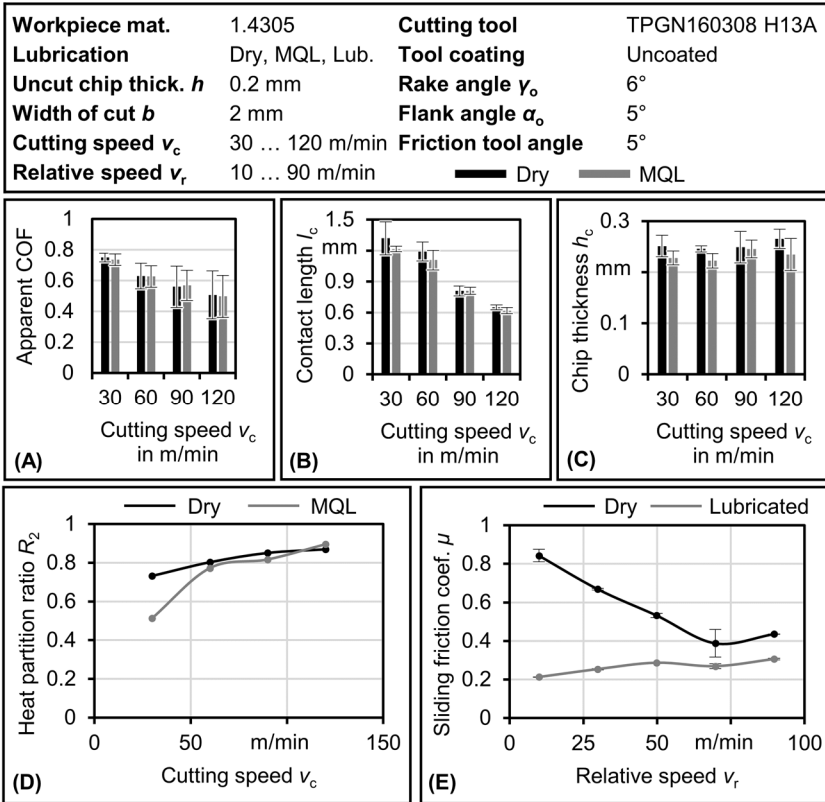


Figure 7.10 Input parameters to IPCF transient temperature model for dry and lubricated cases of 1.4305 workpiece material, (A) Apparent friction coefficient (COF), (B) Tool-chip contact length l_c , (C) Chip thickness h_c , (D) Heat partition ratio R_2 as obtained from Loewen and Shaw temperature model, (E) Experimentally-obtained sliding friction coefficient μ

In Figure 7.10 (A) and (B), it can be observed that the apparent coefficient of friction (COF) and the contact length (l_c) decrease with increasing cutting speed. However, the mean chip thickness remains relatively unchanged, with a slight reduction in the case of MQL, as shown in Figure 7.10 (C). In Figure 7.10 (E), the difference in sliding friction coefficient (μ) between the dry and lubricated cases is more pronounced for austenitic stainless steel 1.4305 compared to Inconel 718. This difference may be influenced by the lower contact stresses and temperatures associated with stainless steel. The sliding friction coefficient (μ) starts at a low value and slightly increases with higher relative speed in lubricated conditions. Conversely, in dry sliding, the coefficient consistently remains higher than in the lubricated condition and decreases as the relative sliding speed increases within the measured speed range. The heat partition ratio R_2 , as shown in Figure 7.10 (D), is almost identical for both dry and MQL cases, except at a low cutting speed of $v_c = 30$ m/min.

7.3.2 Model results validation at steady state

Following a similar procedure as previously demonstrated, the model results for austenitic stainless steel 1.4305 at steady state and at a finite distance of $s = 160$ mm are displayed in Figure 7.11.

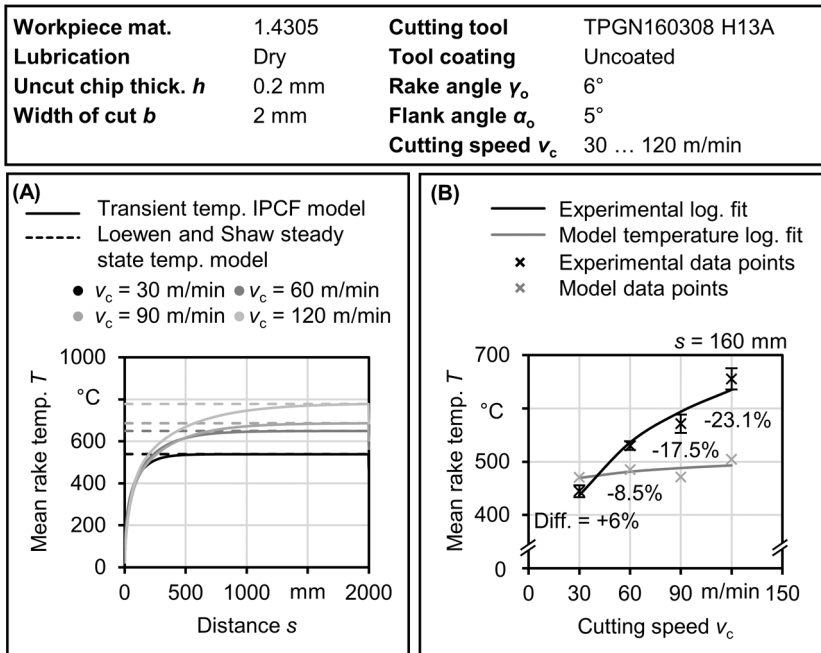


Figure 7.11 Validation of model results for austenitic stainless steel 1.4305, (A) Comparison with analytical steady state model by (Loewen and Shaw 1954), (B) Model results in comparison with experimental average rake temperatures obtained using ratio pyrometer at cutting distance $s = 160$ mm

In Figure 7.11 (A), the steady-state temperatures at four different speeds are compared with the analytical temperature results obtained from the model proposed by (Loewen and Shaw, 1954). The heat partition ratio R_2 of the proposed model was adjusted iteratively to achieve agreement with the

analytical model. The temperatures at $s = 160$ mm, corresponding to the cutting length where rake face measurements were taken using a two-color ratio pyrometer, are presented in Figure 7.11 (B). The temperature evaluation shows reasonable accuracy within a range of $\pm 10\%$ for cutting speeds of $v_c = 30$ and 60 m/min. However, the model underestimates the temperature at higher cutting speeds, with a deviation of up to -23% at $v_c = 120$ m/min. This discrepancy could be attributed to the assumption of constant distribution exponents ω and ζ for different speeds, as well as the influence of the sticking length calculation (Equation 7.3). Therefore, further analysis excludes cutting speeds of 90 and 120 m/min.

7.3.3 Heat flux and temperature results

Figure 7.12 displays the heat flux and temperature distribution along the rake face. Additionally, it presents the temperature field within the tool for both dry and MQL cases.

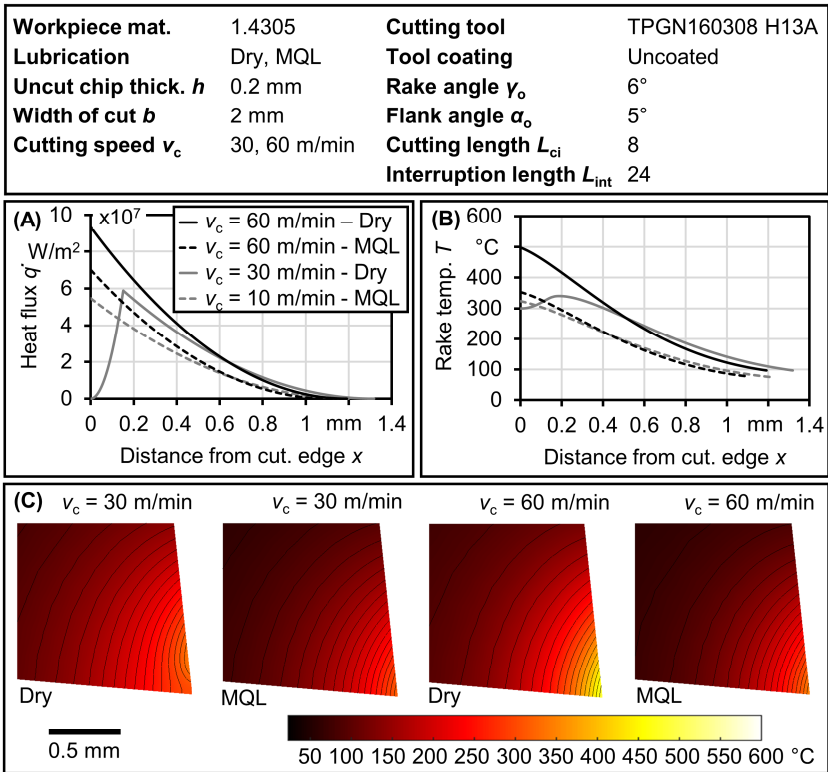


Figure 7.12 Heat flux and tool temperature for austenitic stainless steel 1.4305, (A) Heat flux along tool-chip contact length at steady state, (B) Temperature along tool-chip contact length before interruption, (C) Temperature field within the tool at different cutting speeds and lubrication conditions occurring before interruption

In Figure 7.12 (A), the total heat flux demonstrates a reduction in the cases with MQL at both cutting speeds of $v_c = 30$ and 60 m/min. The sticking zone is only observed at a speed of $v_c = 30$ m/min in the dry condition. However, MQL cases at $v_c = 30$ m/min and all cases at $v_c = 60$ m/min do not exhibit a sticking zone. Consequently, the temperature is highest at the cutting edge, as illustrated in Figure 7.12 (B). Further investigation is required to determine the underlying factors influencing these calculations. It is worth noting that the experimentally identified sticking zone, based on adhesion marks, does not align with the calculated sticking length for both Inconel 718 and austenitic stainless steel 1.4305. It is possible that either the calculation of sticking length does not accurately represent the actual sticking scenario, or the assumption regarding the determination of the sticking zone at the beginning of the adhesion marks from the cutting edge fails to accurately quantify the phenomenon where sliding speed significantly decreases. However, the impact of sticking length on the total input heat flux should have been compensated for during the determination of the heat partition ratio R_2 .

The results for the transition length of IPCF and the corresponding transition temperature for austenitic stainless steel 1.4305 are shown in Figure 7.13.

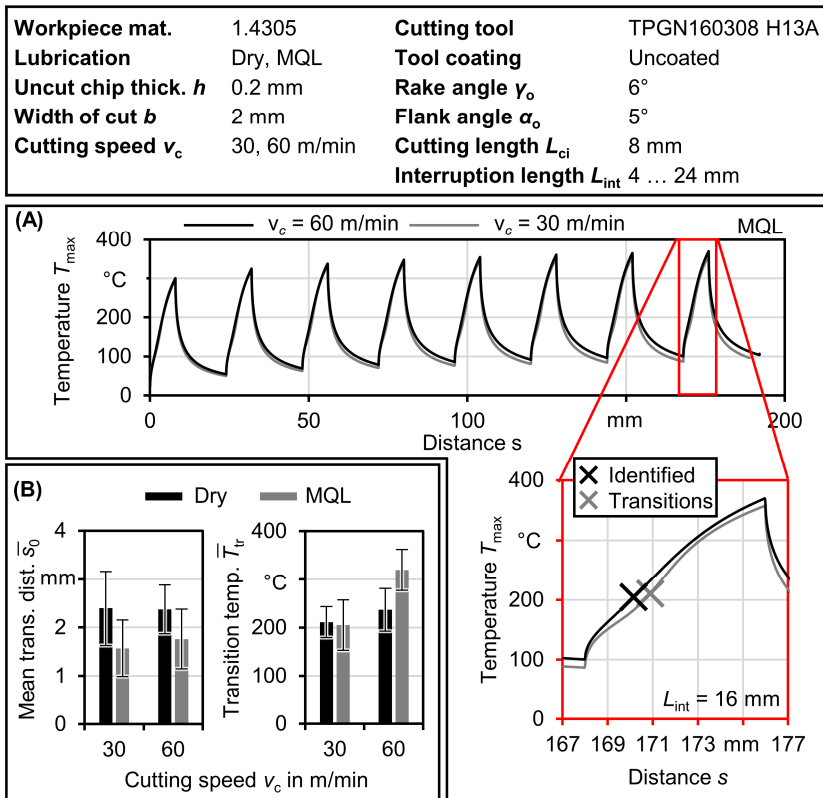


Figure 7.13 Identification of transition temperatures for austenitic stainless steel 1.4305, (A) Example of transition temperature identification, (B) Transition temperature and distance results

The objective of the thermal transient modeling presented in this chapter is to determine the corresponding transition temperature, T_{tr} , at the mean transition distance, \bar{s}_0 . Figure 7.13 (A) illustrates that the transition temperature can be identified from the transient temperature results when the transition distance is known. The transition distance is determined by fitting the Sigmoid function (Equation 7.13) to the experimentally determined apparent coefficient of friction (COF). For the MQL case, the transition distance and temperature are determined as $\bar{s}_0 = 2.4$ mm and $\bar{T}_{tr} = 224$ °C, respectively. In the case of austenitic stainless steel 1.4305, the transition can also be detected in the dry case, whereas for Inconel 718, no reliable transition was detected in the dry condition. For the dry case of 1.4305, the values are $\bar{s}_0 = 1.7$ mm and $\bar{T}_{tr} = 205$ °C, as shown in Figure 7.13 (B). The transition distance is shorter in the dry case. At a cutting speed of $v_c = 60$ m/min, a relatively higher transition temperature of $\bar{T}_{tr} = 320$ °C was calculated. The transition temperature for austenitic stainless steel 1.4305 is slightly higher than those for Inconel 718, which could be further increased by the solid lubrication effect due to the high sulfur content of 1.4305. However, additional investigations are required in order to explore this effect further.

7.4 Chapter conclusions

Thermal modeling of IPCF in interrupted machining enables a deeper understanding of the working mechanism of IPCF. The heat flux in interrupted machining is cyclic, reaching zero during interruption and having a reduced value at IPCF. Consequently, the temperature becomes cyclic with transient behavior that is always present, regardless of the contact condition. In IPCF, the transient temperature rise can be delayed, resulting in a reduced maximum temperature before the next interruption interval. However, for this additional reduction in temperature to be observed, the transition associated with IPCF between low and high friction must occur. This transition was only observed when effective application of lubricant is achieved adequately.

An important observation is that the transition distance, as obtained from fitting a sigmoid function, lies within a very narrow range. A similar observation holds true for the corresponding transition temperature. It is found that for both investigated materials, the transition distance is typically less than a couple of millimeters, and the corresponding transition temperature is within 180 to 220 °C. This indicates that the thermal aspect has a direct influence on IPCF.

Uncertainties related to the accuracy of heat flux determination might also affect the model results. In particular, the calculation of sticking length and the assumption that the pressure distribution exponent ζ and chip velocity distribution exponent ω are constants at variable cutting conditions might contribute to increased uncertainty in determining accurate tool temperature. Further experimental investigations are still required to validate the transient temperature rise on the rake face in real-time, which is still one of the major limitations in machining research.

Based on the fundamental investigations presented in this chapter and previous chapters of this dissertation, it can be inferred that interrupted machining has the potential to improve tribological conditions. In the next chapter, case studies will be conducted to explore the limitations and opportunities of implementing interrupted machining in drilling as a practical application. Drilling is a continuous machining operation known for its demanding thermomechanical challenges. Hence, special process adaptations are necessary to enable interrupted machining in drilling.

Chapter 8: Case Studies on the Influence of Interrupted Machining on Drilling Inconel 718 under MQL

Fundamental investigations, as discussed in previous chapters, serves the purpose of gaining better understanding that can ultimately be applied in practical scenarios. In this chapter, the focus is on the drilling process, which poses significant thermomechanical challenges, particularly when dealing with difficult-to-cut materials at near-dry conditions. Two case studies were conducted: peck drilling and vibration-assisted drilling (VAD). The two methods offer different ranges of cycle frequency. To achieve vibrations with selectable amplitudes and frequencies applied to the workpiece in VAD, a custom-built hydraulic actuator was designed and utilized. The objective of this chapter is to analyze the effects of these techniques on various process variables such as mechanical load, chip form and tool life. Figure 8.1 outlines drilling investigations that will be discussed in this chapter with respect to cycle frequency.

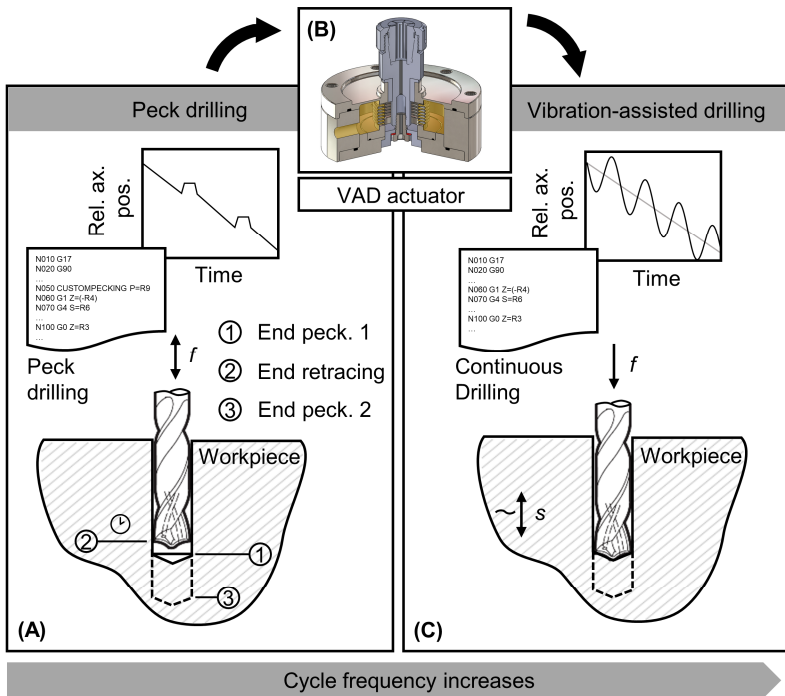


Figure 8.1 Drilling investigations schematic, (A) Peck drilling, (B) Actuator development, (C) Vibration-assisted drilling (VAD)

8.1 Peck drilling Investigations

As shown in Figure 8.1 (A), the pecking cycle enables tool disengagement from the workpiece after prescribed drilling distance l_p . The pecking cycle follows the following sequence. Before drilling begins, the tool approaches position of safety distance to the surface with maximum axis traverse speed, drilling starts at feed speed the first pecking depth with cutting speed v_c and feed f according to the experimental plan. After the tool reaches the end of pecking depth, two dwell revolutions occur to break the chips. The tool then retracts $l_r = 1$ mm from the pecking position and holds its position for dwell time $t_d = 0.4$ s, the cycle repeats and the tool moves to the next pecking length until achieving final drilling depth.

Feed was chosen to be $f = 0.1$ mm, as well as the total interruption time of $t_{int} \approx 1.5$ s which include traverse times. For the MQL system, the oil was supplied at a flow of $Q_{oil} = 25$ ml/h and pressure of $p_{oil} = 14$ bar, whereas the air at a flow of $Q_{air} = 155$ NI/min and pressure of $p_{air} = 10$ bar. MQL parameters were kept within $\pm 20\%$ allowance. Pecking length, drilling depth, cutting speed and tool coating were varied. The pecking lengths was $l_p = 2.0$, $l_p = 5.0$ and $l_p = 8.5$ mm. Drilling depths of $l = 34$ mm, which corresponds to $l/d = 5$, and $l = 43$ mm at tool's maximum recommended drilling depth were investigated. Cutting speed were varied to be either $v_c = 20$ m/min or $v_c = 30$ m/min. Uncoated twist drilling tools as well as multi-layer TiN-TiAlN PVD coated tools were used. Process parameters are summarized in Table 8.1.

Table 8.1 Peck drilling process parameters

Fixed process parameters						
Material	Feed f mm	Interrupt- ion time t_{int} s	MQL oil flow Q_{oil} NI/min	MQL oil pressure p_{oil} bar	MQL air flow Q_{air} NI/min	MQL air pressure p_{air} bar
Inconel 718	0.1	1.5	25	14	155	10
Varied process parameters						
Pecking length l_p mm	Drilling depth l mm	Cutting speed v_c mm	Cutting tool coating	-	-	-
2, 5 and 8.5	34 and 43	20 and 30	Uncoated, TiN- TiAlN	-	-	-

8.1.1 Tool wear and maximum tool life in peck drilling

In Figure 8.2 (A), tool wear using pecking lengths: $l_p = 2$ mm, $l_p = 5$ mm and $l_p = 8.5$ mm are shown. In Figure 8.2 (B), pecking length was kept constant at $l_p = 2$ mm and tool wear resulting from varying cutting speed v_c , tool coating and cutting depth l are shown. The flank wear size were measured at four locations starting from 250 μ m from the outer diameter of the tool. The measuring locations are also 250 μ m apart. The average flank wear \overline{VB} at these locations are reported in Figure 8.2.

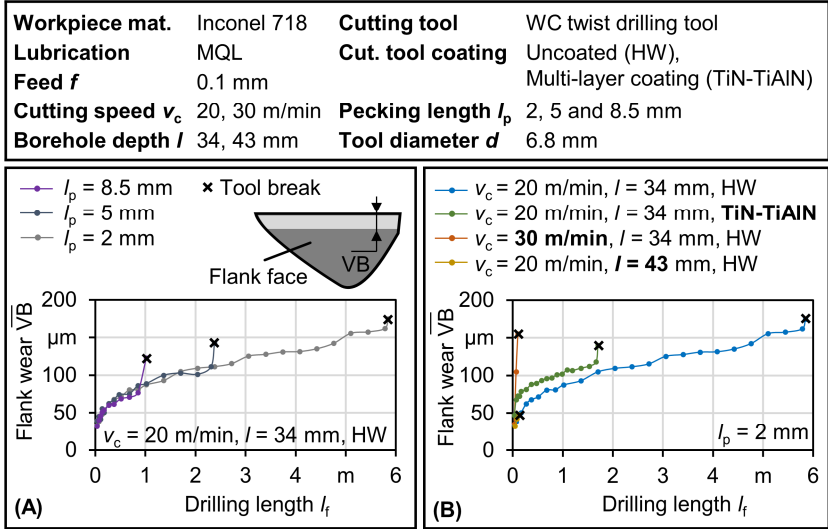


Figure 8.2 Flank wear progress and chipping towards the outer diameter

From Figure 8.2, pecking length l_p was observed to influence tool life using uncoated tools once cutting speed and feed are set properly. Shorter pecking length reveal longer tool life. Interrupting the drilling after short pecking length promotes chip evacuation and constrains the increase in tool temperature which could lead to accelerated tool wear. Limiting thermal load can also contribute in limiting tool thermal expansion which could lead to premature tool failure due to increased torque as shown for $v_c = 30$ m/min in comparison with $v_c = 20$ m/min in Figure 8.3. Cutting speed, as expected, severely reduces tool life when increased from $v_c = 20$ m/min to $v_c = 30$ m/min. Contrary to initial presumption, coated tools lasted approximately one third the life of uncoated tool.

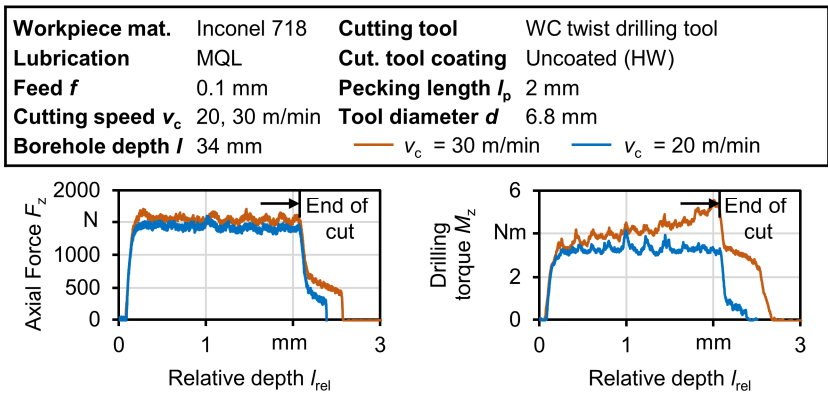


Figure 8.3 Axial force and drilling torque for $v_c = 20$ m/min and $v_c = 30$ m/min shown for a single pecking interval

When observing the cutting edge under optical microscope, the color changes observed around the cutting edge particularly in uncoated tools, are indicative of thermal variations resulting from friction and chip formation. In Figure 8.4, oxidation marks are visible on the flank face towards the outer diameter of the tool. These marks become more pronounced with longer pecking lengths (i.e., $l_p = 8.5$ mm), indicating a higher thermal load. Additionally, larger oxidation marks were observed at relatively higher cutting speed $v_c = 30$ m/min. In this context, the effectiveness of metal working fluids (MWF), especially MQL, in terms of lubrication and cooling becomes quite relevant. It is worth noting that MQL, due to its lower thermal capacity compared to flood coolant, may lead to inadequate dissipation of heat from the cutting zones. This characteristic of MQL contributes to accelerated tool wear, particularly during prolonged contact at long pecking lengths. However, by reducing the pecking length and introducing more frequent interruptions in the cutting process, this issue can be mitigated. Shorter pecking lengths result in more frequent exposure to the cooling and lubricating effects provided by MQL, thus extending the tool life and maintaining more effective cooling and lubrication. It's important to highlight that oxidation marks cannot serve as a quantitative measure of thermal input; rather, they are suitable only for qualitatively assessing the thermal conditions. In addition to oxidation marks, changes in the cutting edge geometry that appear as chipping, result in alterations in the chip form and an increase in axial force. Figure 8.4 illustrates also the occurrence of chipping at the cutting edge.

The increase in drilling length from $l = 34$ mm to $l = 43$ mm decreases tool life significantly. The longer path could have worsened chip evacuation, due to the clogging of the hole and the chip rubbing effect. As a result, mechanical and thermal load increase causing adverse consequences on tool life.

Workpiece mat.	Inconel 718	Cutting tool	WC twist drilling tool
Lubrication	MQL	Cut. tool coating	Uncoated (HW)
Feed f	0.1 mm	Pecking length l_p	2, 5 and 8.5 mm
Cutting speed v_c	20 m/min	Tool diameter d	6.8 mm
Borehole depth l	34 mm		

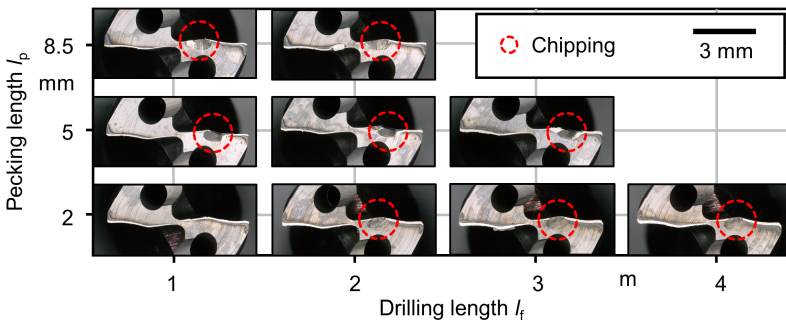


Figure 8.4 Cutting edge condition using different pecking lengths

8.1.2 Chip form in peck drilling

The chip form undergoes changes both along the drilling depth and throughout the tool's lifespan, as shown in Figure 8.5. Initially, at the start of the drilling process, a typical entrance chip formation appears as a continuous helix. When the tool is new and the cutting edges are intact, a small

discontinuous helical chip forms throughout the drilling depth. However, as chipping occurs on the cutting edges after a number of boreholes, the chip thickness increases, and the pitch of the helical chip widens. Moreover, long ribbon-like chips form typically after a certain distance away from the borehole entrance.

Workpiece mat.	Inconel 718	Cutting tool	WC twist drilling tool
Lubrication	MQL	Cut. tool coating	Uncoated (HW)
Feed f	0.1 mm	Pecking length l_p	2 ... 8.5 mm
Cutting speed v_c	20 m/min	Tool diameter d	6.8 mm
Borehole depth l	34 mm		

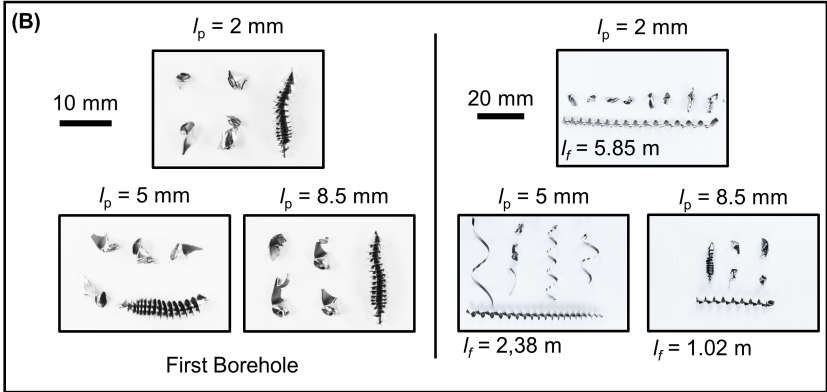
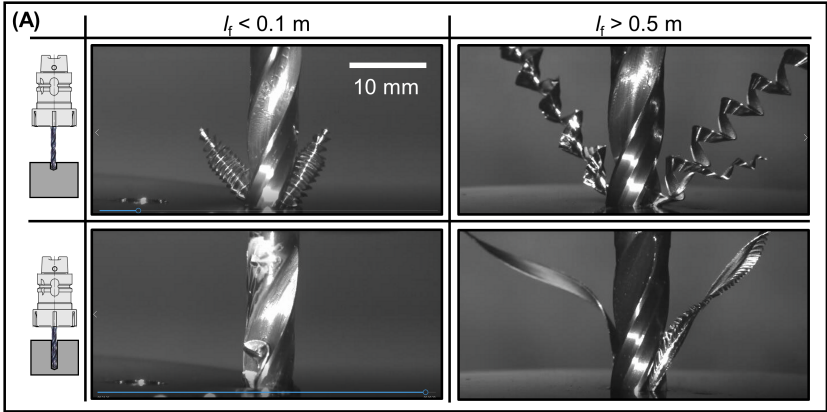


Figure 8.5 Chip shapes in peck drilling, (A) High speed video images comparing between a new (left) and used (right) tool at the beginning (top) and end of the borehole (bottom), (B) Collected chips for a new (left) and used (right) tools with respect to different pecking lengths

A key observation is that the utilization of MQL with peck drilling seems to be enhanced by the presence of long ribbon-like chips. This enhancement can be attributed to improved chip evacuation. Specifically, small helical chips tend to accumulate, unfold and stack upon each other, particularly

when the tool is reaching the bottom of the borehole. This phenomenon has been observed through high-speed video recordings as the chips exit the borehole. The gaseous flow of MQL seems insufficient for rapid evacuation of the accumulated chips from the borehole. However, the presence of long ribbon-like chips aids in mitigating this issue by avoiding chip accumulation during the drilling process.

Chipping, which is observed to take place between the chisel edge and the outer diameter of the tool at the cutting edge, leads to an increase in axial force, as illustrated in Figure 8.6. Chipping appeared in different parts of the cutting edge in every test, but most of the time towards the chisel edge. After it happened, the wear remained stable to continue drilling additional boreholes and the chip form changed. When using pecking lengths of $l_p = 5$ mm and $l_p = 8.5$ mm, chipping in the cutting edge occurs prematurely after drilling only a few boreholes. This significantly limits the tool's lifespan when employing these pecking lengths. The drilling torque appears to be less affected, with minor chipping occurring in the cutting edge, away from the outer diameter. On the other hand, when the cutting edge chips at the outer diameter, the tool consistently fails immediately after a short drilling distance.

Workpiece mat.	Inconel 718	Cutting tool	WC twist drilling tool
Lubrication	MQL	Cut. tool coating	Uncoated (HW)
Feed f	0.1 mm	Pecking length l_p	2, 5 and 8.5 mm
Cutting speed v_c	20 m/min	Tool diameter d	6.8 mm
Borehole depth l	34 mm		

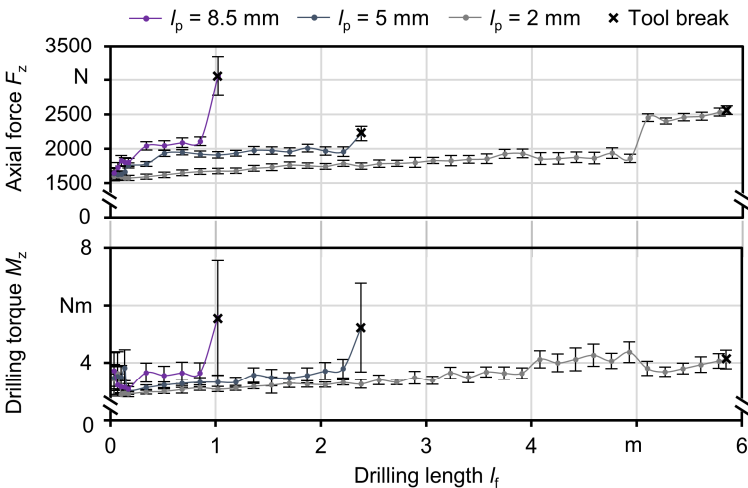


Figure 8.6 Axial drilling force F_z and drilling torque M_z when varying the pecking length throughout the life of the tool

During the initial stages of tool life, a significant variation in drilling torque M_z was observed, particularly towards the bottom of the borehole, regardless of the pecking length tested. This variation can be attributed to the presence of discontinuous helical chips that become obstructed between the tool flute and the borehole walls, resulting in increased resistance to tool rotation.

However, as the drilling process progresses and long helical and ribbon chips begin to form, the drilling torque and its variations are minimized. In contrast, the cutting force F_z consistently increases throughout the tool life without any noticeable discrepancies occurring at the initial stage.

8.1.3 Borehole roughness in peck drilling

In the group of tests with varied pecking lengths as shown in Figure 8.7, the roughness measurements revealed higher values in the first cut compared to the middle of the tool's life, both in terms of R_a and R_z . This can be attributed to the more challenging chip flow during the initial cuts, which leads to chip rubbing against the borehole wall and subsequently lowers the surface quality. Furthermore, the roughness at the bottom of the borehole (Zone C) exhibited slightly better results compared to Zones A and B. This can be attributed to the shorter contact time with evacuated chips in Zone C. Among the boreholes drilled before the tool broke, the one drilled with a pecking length of 2.0 mm displayed the highest borehole roughness. This can be attributed to the higher wear on the tool edges due to the prolonged tool life. Conversely, boreholes drilled with pecking lengths of $l_p = 5.0$ mm and $l_p = 8.5$ mm demonstrated lower roughness in the final borehole. This can be attributed to premature cutting edge chipping, resulting in a considerably shorter tool life and less extensive tool wear compared to shorter pecking lengths (i.e., $l_p = 2.0$ mm).

Workpiece mat.	Inconel 718	Cutting tool	WC twist drilling tool
Lubrication	MQL	Cut. tool coating	Uncoated (HW)
Feed f	0.1 mm	Pecking length l_p	2, 5 and 8.5 mm
Cutting speed v_c	20 m/min	Tool diameter d	6.8 mm
Borehole depth l	34 mm		

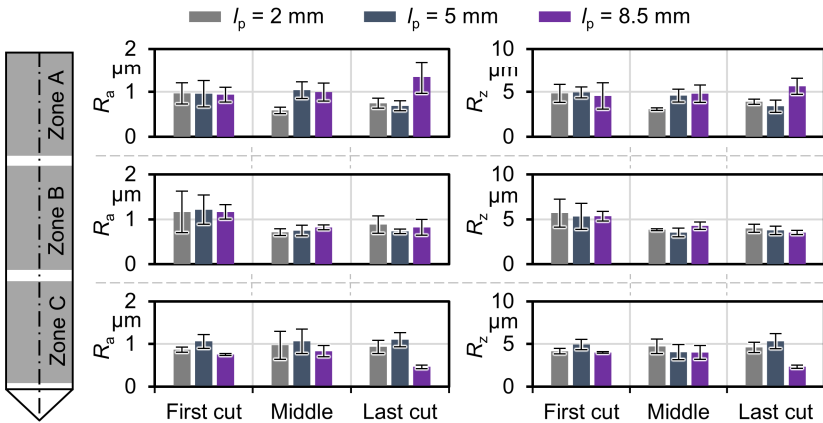


Figure 8.7 Roughness R_a and R_z – Comparison with the first, middle and last cuts measured at various locations along borehole depth

The influence of pecking length, cutting speed, coating, and borehole length on the test results is summarized in Table 8.2. Drilling Inconel 718 under MQL with continuous feed without utilizing peck drilling technique results a significant reduction of tool life. Under the same conditions, tool life increased up to 75 times when comparing continuous drilling peck drilling using $l_p = 2$ mm. Peck drilling length, cutting speed, borehole length and tool coating have influence on tool life.

When comparing drilling using pecking length $l_p = 2$ mm, increasing the cutting speed from $v_c = 20$ to 30 m/min resulted in a significant decrease in tool life by 98%, despite an increase in material removal rate (MRR) by 35% to $MRR = 36.7$ mm³/s. This reduction in tool life can be attributed to the higher heat generated at higher cutting speeds. Despite using same peck drilling conditions, increasing borehole drilling length from $l = 34$ mm to $l = 43$ mm resulted in a significant decrease in tool life, with a reduction of 98% or 5.72 m in total drilling length. This decrease can be attributed to the longer drilling path, which may have hindered chip evacuation from the borehole. The use of a coated tool showed a decreased tool life. However, the specific reasons behind this reduction could not be directly inferred from the obtained results. Further investigations are required to observe the effect of coating material on tool life under similar test conditions. Despite the potential benefits of higher cutting speeds or longer pecking lengths in improving MRR, tool life can be significantly reduced.

Table 8.2 Peck drilling results overview

Variation from reference conditions	Total drilling length l_t	Increase in tool life	Single borehole drilling Time	MRR	Decrease in MRR
	mm (# boreholes)	folds	s	mm ³ /s	%
Reference*	79 (2.3)	-	21.8	56.6	-
$l_p = 2$ mm	5850 (172.0)	75	45.2	27.3	-52
$l_p = 5.0$ mm	2380 (70.0)	30	30.8	40.1	-29
$l_p = 8.5$ mm	1020 (30.0)	12	26.3	46.9	-17
$v_c = 30$ m/min, $l_p = 2$ mm	100 (2.9)	1.3	33.6	36.7	-35
Coated tool, $l_p = 2$ mm	1700 (50.0)	21	45.2	27.3	-52
$l = 43$ mm, $l_p = 2$ mm	130 (3.0)	0.7	57.3	27.3	-52

* Continuous drilling, MQL, $l = 34$ mm, $v_c = 20$ m/min, Uncoated tool

Based on previous findings and discussions, it is apparent that interrupted drilling has a positive impact on drilling Inconel 718 under MQL conditions. However, it can significantly hinder productivity (i.e., MRR). Attempts to enhance the MRR by increasing pecking length or cutting velocity have proven unsuccessful, as they result in a significant decrease in tool life. Therefore, VAD will be investigated further. VAD allows for higher cycle frequencies and the utilization of a constant feed. Unlike peck drilling, where the cycle period is in the order of seconds, VAD offers cycle periods of less than a second. To provide a clearer perspective, the following parameters: cutting speed $v_c = 20$ m/min, feed $f = 0.1$ mm, pecking length $l_p = 2$ mm, and interruption time of $t_{int} = 1.5$ s are found to result in relatively long tool life of $l_t = 5.85$ m. With these values, the calculated cycle frequency is approximately $f_{cycle} = 0.36$ Hz. On the other hand, the cycle frequency in VAD as investigated in the next section can be selected up to 39 Hz. This discrepancy in cycle frequency becomes even more significant when compared to previous investigations where IPCF lasted only a very short time, corresponding to a finite cutting distance.

To facilitate VAD investigations, a hydraulic actuator has been developed to enable sinusoidal translational movement of the workpiece, as elaborated in the following section.

8.2 Design and development of a hydraulic VAD actuator

To enable oscillatory relative movement between the tool and the workpiece, a hydraulic actuator was developed. The actuator is based on the principle of elastic deformation of a plate subjected to hydraulic pressure where the workpiece can be attached. Variable amplitude and frequency can be

selected enabling more flexibility for investigating the influence of VAD parameters on drilling performance. Schematic of the actuator, signal flow, and unloaded testing setup are shown in Figure 8.8.

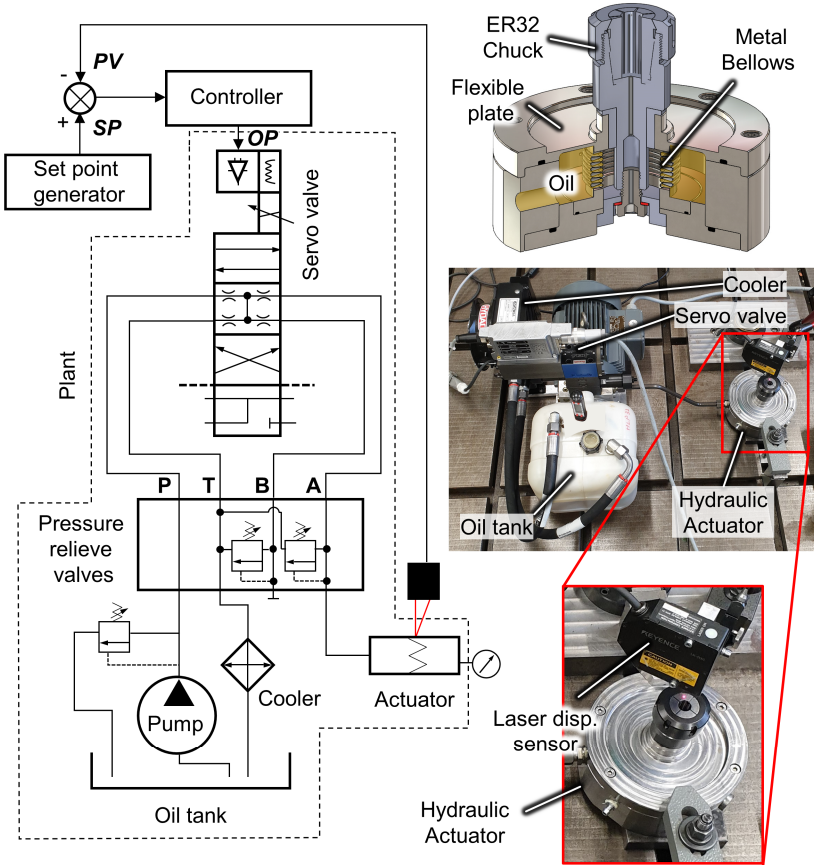


Figure 8.8 Development of a hydraulic actuator for VAD investigations

The hydraulic pressure required for the actuator is generated by a hydraulic gear pump, which is submerged inside a tank. This pressure can be directed proportionally either to the actuator or back to the oil tank, by the utilization of a high-speed hydraulic servo valve. The valve incorporates an electronics module that supplies the necessary power to generate electromagnetic force, enabling the movement of the valve’s spool between three positions. The spool controls the flow of hydraulic oil throughout the system. The actuator’s precise position is determined using a laser position sensor, which serves as the feedback signal (PV) in a closed-loop proportional-integral (PI) control system. The desired actuator position is defined by a sinusoidal signal called the set point (SP), which is generated within the controller. The controller allows for customization of the sinusoidal movement’s amplitude and frequency, ensuring that a proper control signal (OP) is generated

accordingly. The digital control was implemented via LabView 2019 and deployed to real-time controller cRIO-9074 equipped with a field-programmable gate array (FPGA) module from National Instruments Corporation. Unloaded static and dynamic responses are shown in Figure 8.9.

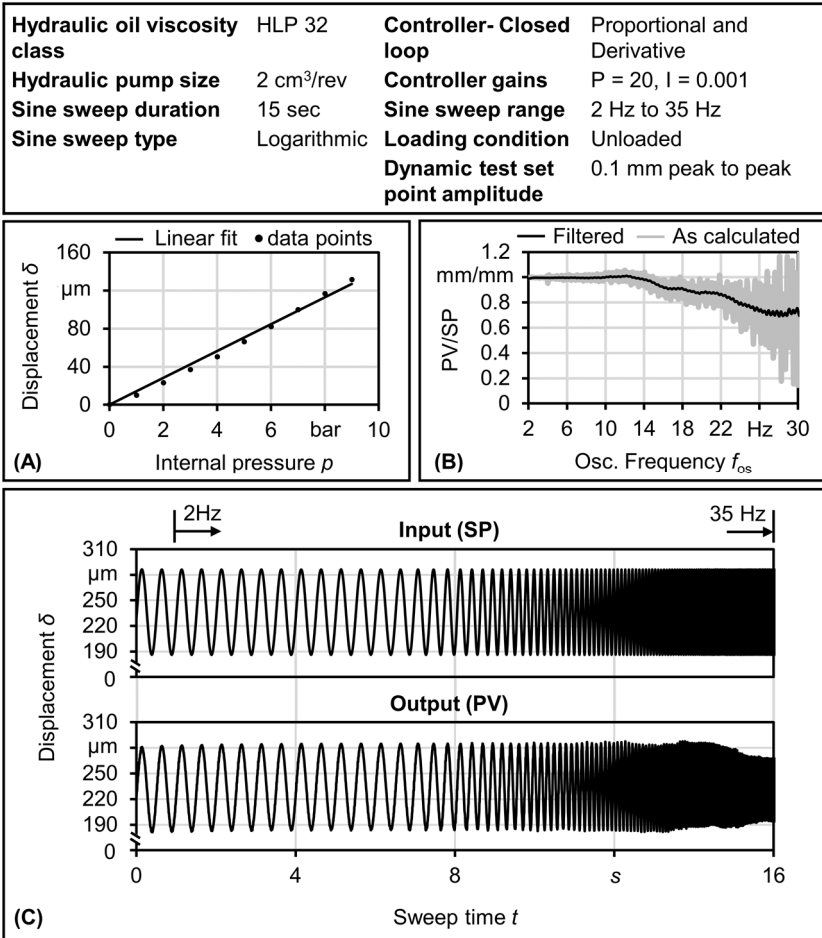


Figure 8.9 Unloaded hydraulic actuator characteristics, (A) Static response, (B) Frequency-domain response, (C) Sine sweep time-domain response

As shown in Figure 8.9 (A), the static response of the hydraulic actuator exhibits linearity and is directly proportional to the internal hydraulic pressure. For the actuator to effectively operate in dynamic applications, the inclusion of an offset displacement or a preload becomes necessary. Figures 8.9 (B) and (C) illustrate the impact of oscillation frequency on the dynamic responses. At lower frequencies, the hydraulic actuator is capable of achieving an amplitude ratio of PV/SP = 1, indicating that the requested amplitude is successfully attained. However, as the frequency

increases, approximately at frequencies higher than $f_{os} = 14$ Hz, the amplitude ratio between the input and output begins to decline, resulting in the actuator generating a smaller amplitude than what was originally requested. It is worth noting that tuning the controller gains can yield different response characteristics. By appropriately adjusting these gains, it is possible to compensate for discrepancies between the input and output, particularly in higher-frequency applications operating at a fixed frequency.

8.3 VAD investigations

In this section, the developed actuator described in the previous section is used in vibration-assisted drilling investigations. The setup of VAD investigations is described, along with discussions on the experimental limitations and constraints, followed by VAD results.

8.3.1 VAD experimental setup

The developed actuator, as discussed in the previous section, was utilized for conducting VAD experiments in a horizontal machining center, as shown in Figure 8.10. The actuator serves the purpose of holding the workpiece, thereby facilitating the supply of oscillatory movement from the workpiece side.

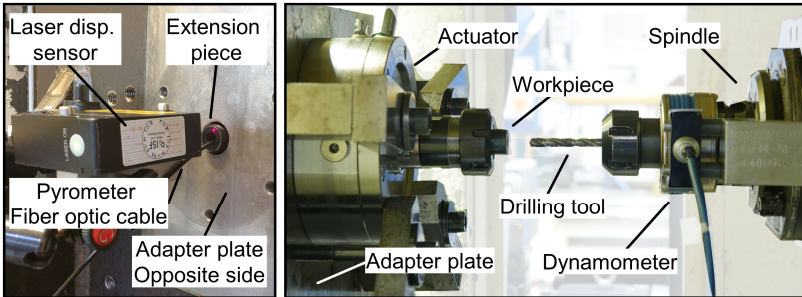


Figure 8.10 Vibration assisted drilling (VAD) setup in horizontal machining center

The attachment of the actuator to the machine using a 90-degree adapter plate and clamps with a set of step blocks are illustrated in Figure 8.10. To facilitate direct measurement of the displacement of the collet chuck, a hole is incorporated into the supporting plate. Through this hole, a laser displacement sensor is directed to the back of the actuator equipped with a magnetic extension piece attached to it. The displacement sensor is positioned to measure the surface of the magnetic extension piece, which is attached to a screw that fastens the collet chuck against a set of disk springs. By employing this configuration, the displacement of the collet chuck can be directly measured from the rear side of the actuator. Additionally, the mechanical load exerted during the drilling process is measured from the tool side. This measurement is made possible by a rotary dynamometer that is attached to the machine spindle, allowing for the simultaneous assessment of the mechanical load in addition to workpiece displacement. The investigations were initiated by utilizing the Kistler 9125A rotary dynamometer. Furthermore, anticipating higher mechanical loads under certain VAD parameters, the Kistler 9170A rotary dynamometer with an extended measurement range was employed. Temperature measurements were conducted using a two-color ratio pyrometer, with the pyrometer's fiber optic cable passing through the actuator.

8.3.2 VAD experimental plan and constraints

The selection of amplitude and frequency for VAD investigations is determined from the kinematic model of VAD which is described previously in chapter 2. As can be inferred from the kinematic model, even values of K_f , which is the ratio between rotation frequency and oscillation frequency, does not result in variable uncut chip thickness. Therefore, the constraints for VAD frequency selection is bounded by this phenomenon. Moreover, the amplitude selection can only be limited by actuator capability limits. In general, only small amplitudes can be produced at relatively high frequencies. Figure 8.11 is an overview of VAD investigation limits with respect to frequencies and amplitudes that can be investigated under the constraints imposed by VAD kinematic characteristics and used actuator capabilities.

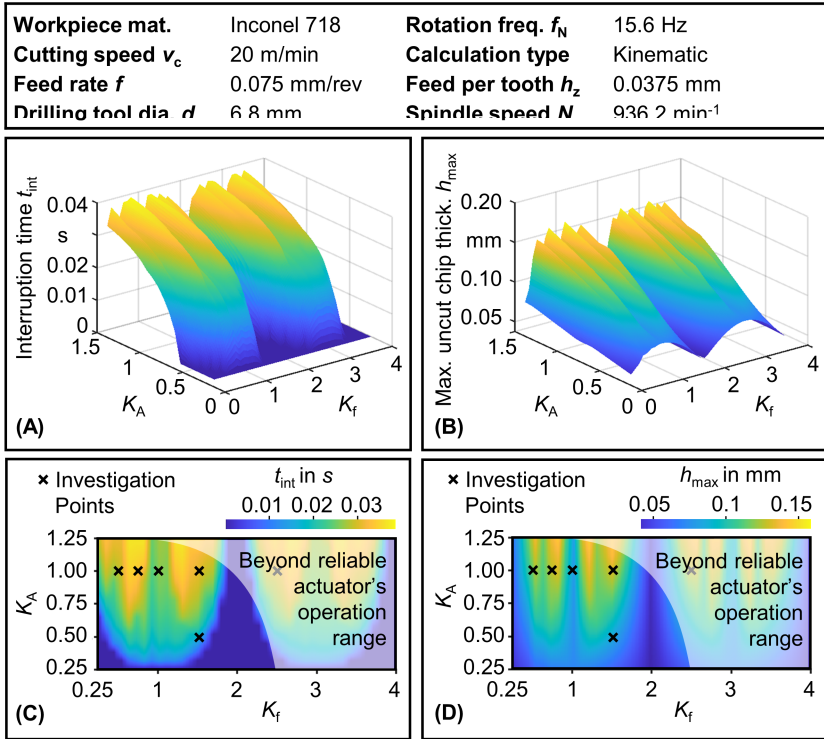


Figure 8.11 VAD characteristics and investigations overview, (A) Interruption time as function of amplitude and frequency ratios, (B) Maximum uncut chip thickness as function of amplitude and frequency ratios, (C) and (D) Illustrate investigations points and actuator usable range overlaid on interruption time and maximum uncut chip thickness maps, respectively

In Figure 8.11 (A) and (C), the average interruption time per revolution, t_{int} , is shown, indicating the duration during which the tool disengages from the cutting process kinematically. Both the amplitude ratio, given as $K_A = A/f$, and the frequency ratio, given as $K_f = f_{os}/f_N$, play significant roles in achieving interruptions in VAD. The interruption time begins to rise when the oscillation

amplitude exceeds about 25% of the feed. However, as the amplitude ratio increases further, the rapid increase in interruption time reduces. Conversely, when the oscillation frequency is an even multiple of the rotation frequency (specifically, $K_f = 2$ and $K_f = 4$), the frequency ratio results in continuous cutting, and no interruptions occur. Only a slight decrease in interruption time occurs when the frequency ratio takes on odd values or falls in the middle between odd and even frequency ratios.

The presence of interruptions in VAD, despite its aim to enhance MWF access to the contact zones and the production of small chips, carries a drawback that can impede its intended performance. Figures 8.11 (B) and (D) demonstrate that the maximum uncut chip thickness per cutting edge can be up to multiple times higher compared to continuous drilling. This increase in maximum uncut chip thickness leads to an increase in mechanical load, which will be discussed in further detail later. Similar to the observations made for interruption time, the behavior of the amplitude and frequency ratios also affects the maximum uncut chip thickness. As the amplitude ratio increases, the maximum uncut chip thickness also increases. When the frequency ratio takes on even values, the maximum uncut chip thickness becomes equal to that of continuous drilling. This is due to the absence of a phase shift between the current tool path and the generated surface from cutting instances in current or previous revolutions, resulting in a constant oscillating uncut chip thickness. In the literature, similar observations regarding the impact of amplitude and frequency ratios on interruption time and maximum uncut chip thickness have been reported (Mann et al., 2011; Ladonne et al., 2015; Miyake et al., 2018; Bleicher et al., 2019). Table 8.3 summarizes VAD investigations parameters and tool life.

Table 8.3 VAD investigated parameters and tool life

Tool coating	v_c m/min	f mm	f_{os} Hz	A mm	K_f --	K_A --	t_f mm (# boreholes)
C1	20	0.075	--	--	Cont.	--	1054 (31.0)
C2	20	0.100	--	--	Cont.	--	408 (12.0)
C3	20	0.075	7.8	0.075	0.50	1.0	57 (1.7)
C4	20	0.075	15.7	0.075	1.00	1.0	170 (5.0)
C5	20	0.075	23.4	0.075	1.50	1.0	1059 (31.1)
C6	20	0.100	15.7	0.050	1.00	0.5	408 (12.0)
C7	20	0.100	23.4	0.050	1.50	0.5	1863 (54.8)
C8	20	0.100	7.8	0.100	0.50	1.0	58 (1.7)
C9	20	0.100	15.7	0.100	1.00	1.0	102 (3.0)
C10	20	0.100	23.4	0.100	1.50	1.0	25 (0.7)
C11	25	0.100	29.3	0.050	1.50	0.5	204 (6.0)
C12	20	0.075	23.4	0.035	1.50	0.5	510 (15.0)
C13	20	0.075	39.0	0.075	2.50	1.0	25 (0.7)
U1	20	0.075	--	--	Cont.	--	850 (25.0)
U2	20	0.100	--	--	Cont.	--	79 (2.3)
U3	20	0.075	7.8	0.075	0.50	1.0	68 (2.0)
U4	20	0.075	15.7	0.075	1.00	1.0	680 (20.0)
U5	20	0.075	23.4	0.075	1.50	1.0	204 (6.0)
U6	20	0.100	15.7	0.500	1.00	0.5	181 (5.3)
U7	20	0.100	23.4	0.500	1.50	0.5	1428 (42.0)
U8	20	0.100	7.8	0.100	0.50	1.0	23 (0.7)
U9	20	0.100	15.7	0.100	1.00	1.0	41 (1.2)
U10	20	0.100	23.4	0.100	1.50	1.0	34 (1.0)
U11	20	0.075	11.7	0.075	0.75	1.0	816 (24)

C: coated tool, U: uncoated tool, Lubrication: MQL, Workpiece material: Inconel 718

Because of the hydraulic actuator's limited capability to achieve the necessary amplitudes at relatively high frequencies while drilling Inconel 718, the investigation points were restricted. As a result, the investigations were conducted at relatively low oscillation amplitudes with amplitude ratios $K_A = 0.5$ and 1 , and within the frequency ratio range of $K_f = 0.5$ to 1.5 . The cutting speed was $v_c = 20$ m/min and $v_c = 25$ m/min and the feed was varied between $f = 0.075$ and $f = 0.1$ mm.

While comparing the frequency ratios in the range of $K_f = 0.25 \dots 2$ and the range of $K_f = 2 \dots 4$, the interruption time per revolution and the maximum uncut chip thickness demonstrate similarities. However, when a higher frequency ratio is utilized, an increased number of oscillations per revolution is observed, leading to the possible generation of smaller chips. It is essential to note that the above discussions solely pertain to the kinematic analysis. The actual scenario, which takes into account the mechanical loads resulting from chip formation, is expected to differ in terms of interruption occurrence and duration and the magnitude of the maximum uncut chip thickness.

8.3.3 VAD experimental results

The maximum number of boreholes that can be drilled before tool breaks in comparison between continuous drilling and different drilling conditions using various VAD parameters are shown in Figure 8.12.

Workpiece mat.	Inconel 718	Cutting tool	WC twist drilling tool
Cutting speed	20 m/min	Cut. tool coating	Coated and Uncoated
Feed	0.075 & 0.1 mm	Tool diameter d	6.8 mm
VAD freq. ratio K_f	0 ... 1.5	Borehole length l	34 mm
VAD amp. ratio K_A	0.5 & 1	Drilling type	Continuous and VAD
Lubrication	MQL		

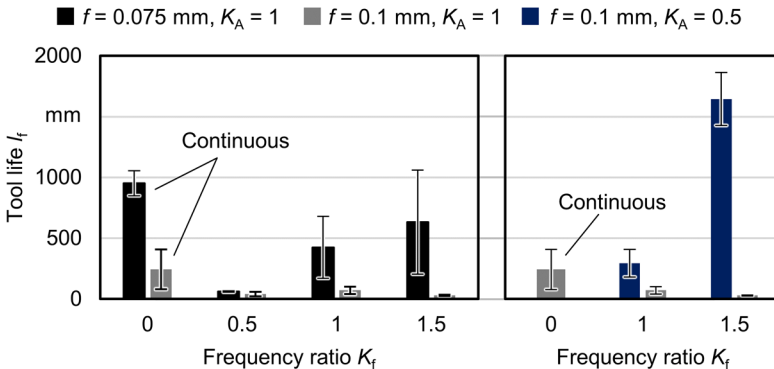


Figure 8.12 Tool life in VAD in comparison with continues drilling

Figure 8.12 demonstrates that a low feed at $f = 0.075$ mm results in a longer tool life when compared to the cases using a feed of $f = 0.1$ mm, both in continuous drilling and VAD. Using a feed of $f = 0.075$ mm, tool life improves when increasing the vibration frequency ratio. However, an improvement in tool life was not observed using a larger feed of $f = 0.1$ mm and VAD. When using VAD amplitude ratio of $K_A = 1$, continuous drilling always outperforms VAD. However, when

reducing the amplitude ratio to $K_A = 0.5$, VAD results in a longer tool life up to 6.7 times. These observations indicate that a high amplitude ratio might bring about adverse outcomes due to frequent exit-reentry events affecting cutting edge integrity, which results in premature chippings. In contrast, a low amplitude ratio ensures continuous engagement with the workpiece with a variable uncut chip thickness. Further investigations are required to determine if a work-hardening layer exists, which could pose challenges in initiating chip formation immediately after the interruption event ends and at the start of the next tool-workpiece engagement period in VAD. Furthermore, it is worth noting that both continuous drilling and VAD, as opposed to peck drilling discussed earlier in this chapter, leads to a significant decrease in tool life. The maximum drilling torque (M_z) and axial force (F_z) in VAD surpass those in continuous drilling, primarily because of the temporarily increased uncut chip thickness. Figure 8.13 illustrates the disparity in time-resolved mechanical load between VAD and continuous drilling.

Workpiece mat.	Inconel 718	Cutting tool	WC twist drilling tool
Lubrication	MQL	Cut. tool coating	Uncoated (HW),
Cutting speed v_c	20 m/min	Tool diameter d	6.8 mm
Feed	0.075 mm	Borehole length l	34 mm
VAD freq. ratio K_f	1.5	Drilling type	Continuous and VAD
VAD Amp. ratio K_A	1		

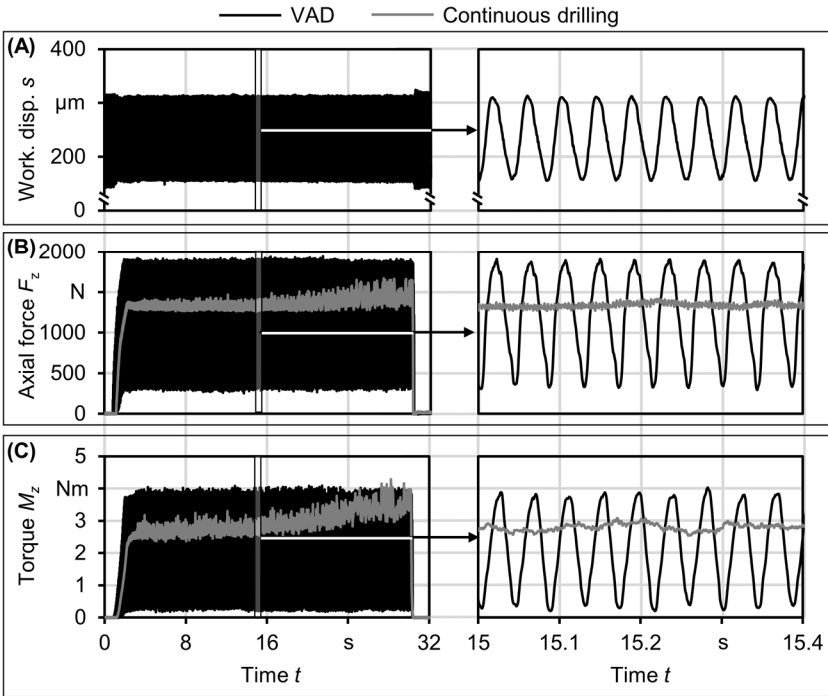


Figure 8.13 Mechanical load in VAD versus continuous drilling, (A) Workpiece displacement in VAD, (B) Axial force F_z and (C) Drilling torque M_z

The minimum axial force in VAD does not reach zero, indicating residual loading when the workpiece moves away from the tool. Although the kinematic model suggests complete disengagement for the parameters indicated in Figure 8.13, factors such as system compliance and uncut material near the chisel edge contribute to some resistance, resulting in residual axial force during maximum workpiece retraction. Conversely, the drilling torque (M_z) approaches zero at maximum workpiece retraction, with small residual torque attributed to friction between the tool and borehole walls, as well as the resistance caused by the chips occurring during chip evacuation. Additionally, a notable difference between continuous drilling and VAD is the observed increase in mechanical load towards the bottom of the borehole in continuous drilling, which is absent in VAD. This observation suggests improved thermal regulation and enhanced overall chip evacuation in VAD. The occurrence of interruption in VAD is discussed further in Figure 8.14.

Workpiece mat.	Inconel 718	Cutting tool	WC twist drilling tool
Lubrication	MQL	Tool diameter d	6.8 mm
Cutting speed v_c	20 m/min	Borehole length l	34 mm
Feed	0.075 mm	VAD freq. ratio K_f	1 and 1.5
VAD Amp. ratio K_A	0.5 and 1		

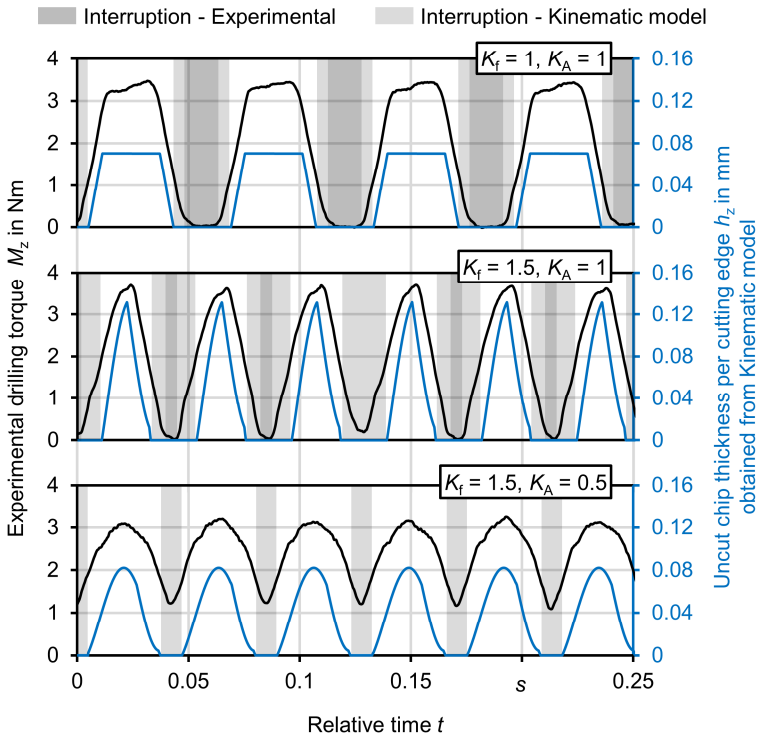


Figure 8.14 Uncut chip thickness per cutting edge - obtained from VAD kinematic - overlaid over drilling torque for different frequency and amplitude ratios

The interruption in VAD can be affected by frequency and amplitude ratios. Previous results from the kinematic model, shown in Figure 8.11, suggested that interruption is likely to occur in most cases of K_f and K_A . However, relying solely on system kinematics does not provide a complete understanding of the situation. The accuracy of interruption occurrence and its characteristics cannot be accurately predicted by the kinematic model alone. The drilling torque, M_z , as shown in Figure 8.14, can experimentally characterize interruption and exhibits a very close tendency to the uncut chip thickness predicted by the kinematic model.

When the oscillation frequency matches the rotation frequency (i.e., $K_f = 1$), the profile of uncut chip thickness per cutting edge (h_z) closely resembles a trapezoidal shape. This allows for a nearly constant uncut chip thickness between interruptions, with the uncut chip thickness per cutting edge becoming almost equal to the feed. However, it remains high at approximately twice the value observed during continuous drilling. As the frequency ratio increases, less time is available between cutting occasions, although the interruption time per revolution is minimally affected. At $K_f = 1.5$, the uncut chip thickness per cutting edge profile takes on a spike shape with a sharp peak. Despite a significant increase in the maximum value of h_z , the drilling torque does not exhibit the same trend, and the maximum level of drilling torque at $K_f = 1.5$ remains comparable to that observed at $K_f = 1$.

When reducing the amplitude ratio from $K_A = 1$ to $K_A = 0.5$ while maintaining the same frequency ratio of $K_f = 1.5$, no interruptions were observed, and the maximum value of M_z slightly decreased. In this case, the kinematic model suggests the presence of interruptions; however, they do not occur in reality, and only a temporary reduction in mechanical load was observed. By reducing the amplitude ratio, non-interrupted drilling with oscillating uncut chip thickness can be achieved, leading to the drilling of more boreholes and improving tool life. To investigate the thermal loading in VAD in comparison with continuous drilling, the rake face temperature was measured using a two-color ratio pyrometer. The temperature results are summarized in Figure 8.15.

Workpiece mat.	Inconel 718	Cutting tool	WC twist drilling tool
Cutting speed	20 m/min	Cut. tool coating	Uncoated
Feed	0.075 & 0.1 mm	Tool diameter d	6.8 mm
VAD freq. ratio K_f	0 ... 1.5	Borehole length l	34 mm
VAD amp. ratio K_A	0.5 & 1	Drilling type	Continuous and VAD
Lubrication	MQL		

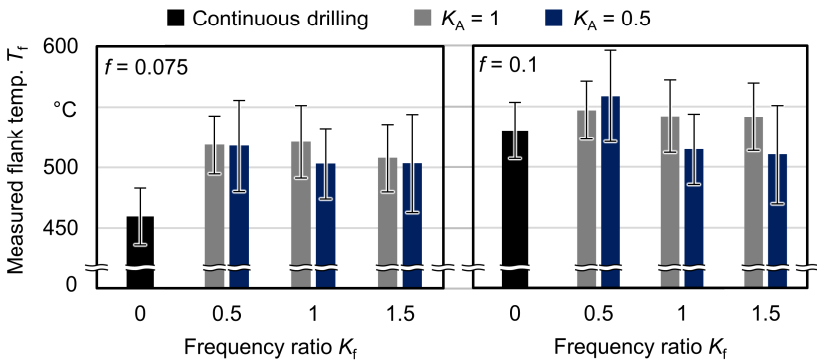


Figure 8.15 Measured flank temperature in continuous drilling and VAD with MQL

While the results of flank temperature shown in Figure 8.15 indicate minor differences, there are a few interesting observations that can be discussed further. On one hand, the flank temperature results indicate that increasing the vibration frequency K_f leads to a decrease in the flank temperature in VAD. This reduction in flank temperature is more pronounced when using a feed of $f=0.1$ mm. On the other hand, the flank temperature in continuous drilling is generally lower than or very close to the corresponding VAD results in most cases.

It's important to consider the influence of the characteristic increase in uncut chip thickness associated with VAD. This influence could explain the recorded temperature variations, resulting in higher temperatures for VAD when compared to continuous drilling. This can also explain the slightly higher temperature using amplitude ratio $K_A = 1$ in comparison with $K_A = 0.5$. In addition to thermal effects, cutting edge integrity is quite important for tool life.

In VAD and continuous drilling, the first sign of tool failure is observed to be small chippings of the tool. These chipping occur at different locations as shown in Figure 8.16. In continuous and peck drilling, chipping occurs in the middle of the cutting edge. Usually, the tool can still drill once chipping occurs at this location. However, in VAD, chipping occur more frequently at or very close to the chisel edge followed by almost immediate tool failure. In seldom cases, chipping occurs at the cutting edge towards the outer diameter of the tool which causes accelerated tool failure as well.

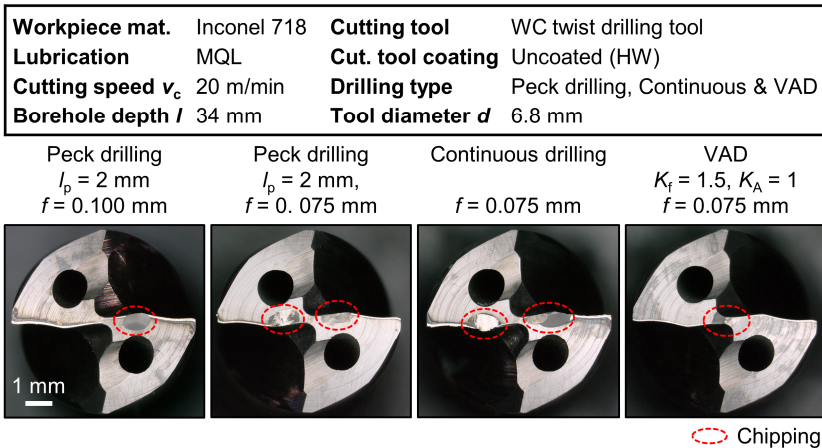


Figure 8.16 Examples of cutting edge chipping onset and its location in peck drilling, continuous drilling and VAD

The form of chips in VAD and continuous drilling is significantly influenced by changes in uncut chip thickness, resulting in distinct differences between the two techniques, as illustrated in Figure 8.17. In the case of continuous drilling, uncut chip thickness is uniform resulting in a continuous helical chip that is formed at the entrance of the borehole. As drilling progresses, the chips transform into smaller, discontinuous helical chips with a short tail. On the other hand, VAD consistently produces short chips with a C-shape, even at the borehole entrance.

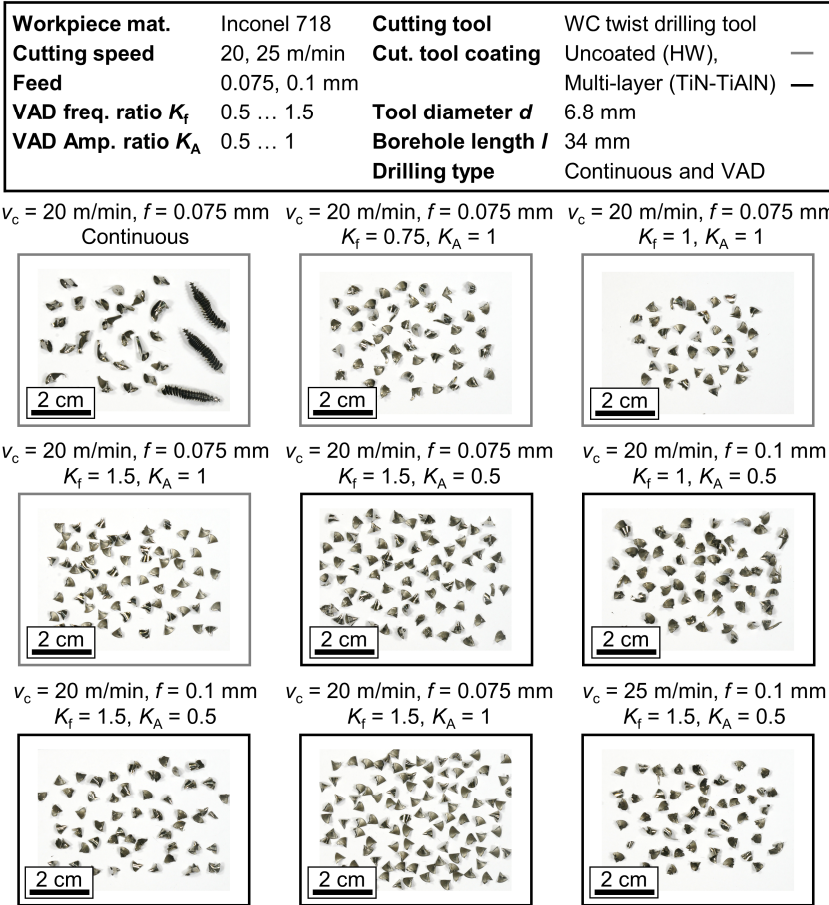


Figure 8.17 Chip forms in continuous drilling and VAD at different parameters

Figure 8.15 demonstrates that the alterations in chip form when utilizing different VAD parameters are in general not substantial. Moreover, adjusting the feed from $f = 0.075$ mm to $f = 0.1$ mm or the cutting speed from $v_c = 20$ m/min to $v_c = 25$ m/min does not yield significant variations in chip shape and size. When employing an amplitude ratio of $K_A = 0.5$, chips that would otherwise be separate appear to be connected with a small chip thickness. Furthermore, there is a slight qualitative reduction in chip size as the frequency ratio increases from $K_f = 0.75$ to $K_f = 1.5$. It should be noted that chip form can also be influenced by tool wear and cutting edge condition.

8.4 Chapter conclusions

In this chapter, case studies on interrupted machining techniques, namely peck drilling and Vibration-Assisted Drilling (VAD), were examined for their application in drilling Inconel 718 under MQL. Peck drilling involves retracting the drilling tool after a specified drilling distance, resulting in a non-continuous feed. It was observed that shorter pecking lengths contribute to longer tool life, although the total drilling time increases, and the material removal rate is hindered. On the other hand, VAD offers the advantage of higher cycle frequency compared to peck drilling, as the feed is continuous and an oscillatory motion is generated by an actuator where the workpiece is attached. VAD generates smaller chips compared to continuous drilling and shows improvement in reducing the increase in mechanical load experienced near the end of the borehole. However, VAD also leads to higher maximum mechanical loads and premature tool failure due to chipping near or at the chisel edge.

The potential benefits associated with tribological effects in interrupted machining may have been overlooked due to the premature failure of the tool in VAD, particularly in interrupted VAD. Non-interrupted VAD has demonstrated relatively promising results in terms of tool life. However, in all VAD cases, peck drilling consistently outperforms in terms of tool life when compared to VAD and continuous drilling.

It is worth noting that the VAD case study only covers a limited range of frequency and amplitude ratios due to constraints imposed by the used actuator. Therefore, future investigations should consider exploring higher frequency and amplitude ratios, achieved through actuator performance development or alternative VAD actuation techniques, to further understand the impact of VAD on the drilling performance of Inconel 718 under MQL. Furthermore, it might be necessary to introduce modifications to the cutting edge geometry of the drilling tool, particularly at the chisel edge. These modifications aim to enhance its resistance to chipping, which can occur due to the increased load experienced during VAD.

Chapter 9: Summary and Outlook

This dissertation explores the impact of interruptions on the tribological conditions during the machining of difficult-to-cut materials under near-dry conditions. The research involves fundamental investigations using an orthogonal cutting setup with variable interruption geometry machined on the workpiece along the cutting path. Additionally, case studies discussing a possible application of interrupted machining in drilling operation were also examined. The investigations involved two materials: Austenitic stainless steel 1.4305 and nickel-based superalloy Inconel 718 with more focus on the latter. The delivery method for metalworking fluids was the minimal quantity lubrication (MQL) technique. Throughout the study, mainly uncoated tools were utilized. Enhancement of MQL through interrupted machining and the utilization of uncoated tools were expected to contribute into improving machining sustainability.

Preliminary investigations have revealed the significant potential of interrupted machining to enhance tribological conditions within the tool-chip interface compared to continuous machining. By providing intermittent exposure to the machining environment, interrupted machining enables cutting fluids to better reach the contact zones, resulting in less adhesion on the rake face. To quantify the adhesion resulting from severe tool-chip contact, adhesion gray level masking (AGLM) of backscatter electron (BSE) images was employed. The results from adhesion area quantification and tool-chip contact length on the rake face emphasize the influence of interrupted machining in reducing chip-tool contact, particularly at low cutting speeds. Moreover, a noteworthy observation points to a relationship between increased interruption frequency and reduced tool-chip contact length. It is worth noting that the mechanical load and apparent coefficient of friction showed only limited influence beyond a finite cutting length, indicating a transient behavior that deserves further investigation to explore its behavior and factors influencing it.

Further experimental investigations aimed to study the transient behavior occurring at the beginning of the cutting period after the interruption were conducted. The length of interruptions was varied to investigate its impact on tool-chip contact. The results revealed that a specific finite cutting length, coinciding with the end of the initial period of chip formation (IPCF), was observed to exhibit considerable reductions in mechanical load and tool-chip contact compared to the steady-state condition. Valuable insights into optimizing MQL application for enhanced machining performance were offered by this finding, as reduced tool-chip contact leads to decreased work during machining. The potential benefits of understanding and characterizing IPCF for improving continuous machining by incorporating interruptions along the cutting path were emphasized. Interestingly, a relationship between the development of contact zones on the tool's rake face and the end of IPCF was observed, with sticking contact gradually forming within IPCF until it reached a final size. This suggested a possible link between contaminants resistant to ablation and mechanical loads.

Another significant indicator of IPCF is the chip curl, which takes on an arc shape. The arc radius of the initial chip curl was directly correlated with the contact condition within the tool-chip interface, with small chip curls indicating low contact in this interface. Notably, the initial chip curl exhibited a finite length, undergoing a shape change at a specific transition location. This transition between initial chip formation and subsequent chip formation within IPCF could serve as an essential indicator of changes in tool-chip contact before chip-workpiece contact occurs. The existence of IPCF was found to be dependent on an adequate cutting-free period. The size of interruptions influenced the repeatability of IPCF. The IPCF appeared relatively insensitive to

cutting speed, indicating the existence of a finite critical cutting length. The critical length was found to be within 1.5 to 2.5 mm as obtained from fitting a sigmoid function to the time resolved apparent coefficient of friction. The critical cutting length might indicate a thermal-related phenomenon initiated by the mechanical ablation of contaminants on the rake face of the cutting tool. To investigate the thermal effects further, thermal modeling of IPCF became necessary.

A hybrid analytical and finite element approach is employed to model the transient temperature increase occurring at IPCF. The analytical method, utilizing experimentally obtained input parameters, precisely considers the determination and distribution of input heat flux along the flank face, considering its magnitude during both interruption and cutting intervals. Numerical solutions of the partial differential heat equation are used to obtain a 2D section of the tool's temperature field, allowing the determination of critical transition temperatures corresponding to finite cutting distances at the end of IPCF. The average temperature of the rake face at variable cutting speeds obtained from the thermal model at a defined distance was validated experimentally using a two-color pyrometer directed at the rake face through a milled slot in the workpiece along the cutting path. The thermal model predicts temperatures that are very close to the experimental measurements, particularly at low cutting speeds. The transient thermal model in combination with the critical distance obtained from IPCF allows for the determination of a transition temperature which is found to be within 180 to 220 °C for both investigated materials even when different cutting parameters were used.

Case studies were conducted to investigate potential challenges and opportunities when a continuous machining operation is interrupted to establish a link between fundamental investigations and practical application. The drilling of Inconel 718 was investigated in these case studies. To assess the influence of interrupted drilling, the interruption cycle frequency is systematically varied using different drilling techniques. These include low-frequency peck drilling and relatively higher frequency vibration-assisted drilling (VAD). The VAD investigation utilizes a custom-built hydraulic actuator to control vibration amplitude and frequency, covering an extended range of parameter variations. Peck drilling involves the drilling tool being retracted after a specified drilling distance, resulting in a non-continuous feed. It was observed that longer tool life is achieved using shorter pecking lengths, although the total drilling time is increased, and the material removal rate is hindered. On the other hand, the advantage of higher cycle frequency, compared to peck drilling, is offered by VAD, as the feed is continuous and an oscillatory motion is generated by an actuator where the workpiece is attached. Smaller chips compared to continuous drilling are generated by VAD, and an improvement in reducing the increase in mechanical load experienced near the end of the borehole is shown. However, higher maximum mechanical loads and premature tool failure due to chipping near or at the chisel edge are also brought about by VAD. The potential benefits associated with tribological effects in interrupted machining may have been overlooked due to the premature failure of the tool in VAD, particularly in interrupted VAD. Relatively promising results in terms of tool life have been demonstrated by non-interrupted VAD. However, in terms of tool life, peck drilling consistently outperforms VAD and continuous drilling in all VAD cases.

Utilizing MQL for machining difficult-to-cut materials through interrupted machining has shown promising feasibility. However, a key concern that emerges is related to tool life, where premature tool failure can occur due to small chippings of the cutting edge. To address this challenge, further investigations aimed at optimizing cutting edge geometry and cutting edge preparation are needed to effectively mitigate these issues and improve tool longevity. It is important to acknowledge that the VAD case study covers a limited range of frequency and amplitude ratios due to constraints imposed by the used actuator. Hence, future investigations should explore higher frequency and amplitude ratios, achieved through actuator performance development or alternative VAD actuation

techniques. This approach will provide more insights into the impact of VAD on the drilling performance of difficult-to-cut materials under MQL. Additionally, considering the overall energy consumption when active means are used to introduce interruptions in continuous machining operations can be highly relevant to the sustainable evaluation of the process. Exploring this aspect will contribute to a more comprehensive understanding of the sustainable impact of interrupted machining techniques. The combination of minimal consumption of metalworking fluids, reduced energy usage, and the use of uncoated tools directly contributes to sustainability. These promising attributes serve as strong motivation for conducting further research focused on improving tool life during interrupted machining, particularly in drilling operations. By such advancements being achieved, not only is an environmentally friendly approach embraced, but also cost savings are achieved, and machining performance is enhanced, making interrupted machining a viable and sustainable solution for difficult-to-cut materials.

References

- Aggarwal, A., Singh, H., Kumar, P., & Singh, M. (2008). Optimizing power consumption for CNC turned parts using response surface methodology and Taguchi's technique—a comparative analysis. *Journal of materials processing technology*, 200, 373–384.
- Ahmed, N., Mitrofanov, A. V., Babitsky, & Silberschmidt, V. V. (2007). Analysis of forces in ultrasonically assisted turning. *Journal of Sound and Vibration*, 308, 845–854.
- Akasawa, T., Sakurai, H., Nakamura, M., Tanaka, T., & Takano, K. (2003). Effects of free-cutting additives on the machinability of austenitic stainless steels. *Journal of Materials Processing Technology*, 143, 66–71.
- Alam, K., Mitrofanov, A. V., & Silberschmidt, V. V. (2009). Measurements of surface roughness in conventional and ultrasonically assisted bone drilling. *American Journal of Biomedical Sciences*, 1, 312–320.
- Alammari, Y., Iovkov, I., Berger, S., Saelzer, J., & Biermann, D. (2021a). Adhesion area estimation using backscatter image gray level masking of uncoated tungsten carbide tools. *Wear*, 476, 203666.
- Alammari, Y., Iovkov, I., Saelzer, J., Wolf, T., & Biermann, D. (2021b). Adhesion of Inconel 718 on uncoated tungsten carbide inserts in interrupted orthogonal machining under MQL. *Procedia CIRP*, 103, 194-199.
- Alammari, Y., Saelzer, J., Berger, S., Iovkov, I., & Biermann, D. (2023). Initial Period of Chip Formation: Observations towards Enhancing Machining Sustainability. In: Kohl, H., Seliger, G., Dietrich, F. (eds) *Manufacturing Driving Circular Economy*. GCSM 2022. *Lecture Notes in Mechanical Engineering*, 193–201.
- Armarego, E. J. A., Karri, V., & Smith, A. J. R. (1994a). Fundamental studies of driven and self-propelled rotary tool cutting processes—I. Theoretical investigation. *International Journal of Machine Tools and Manufacture*, 34, 785–801.
- Armarego, E. J. A., Karri, V., & Smith, A. J. R. (1994b). Fundamental studies of driven and self-propelled rotary tool cutting processes—II. Experimental investigation. *International Journal of Machine Tools and Manufacture*, 34(6), 803-815.
- Arrazola, P. J., Özel, T., Umbrello, D., Davies, M., & Jawahir, I. S. (2013). Recent advances in modelling of metal machining processes. *CIRP Annals*, 62, 695–718.
- Arul, S. V., Vijayaraghavan, L., Malhotra, S. K., & Krishnamurthy, R. (2006). The effect of vibratory drilling on hole quality in polymeric composites. *International Journal of Machine Tools and Manufacture*, 46, 252–259.
- Asmael, M., Safaei, B., Zeeshan, Q., Zargar, O., & Nuhu, A. A. (2021). Ultrasonic machining of carbon fiber–reinforced plastic composites: a review. *The International Journal of Advanced Manufacturing Technology*, 113, 3079–3120.
- Augspurger, T., Da Silva, G., Schraknepper, D., Mattfeld, P., & Bergs, T. (2020). Model-based monitoring of temperatures and heat flows in the milling cutter. *The International Journal of Advanced Manufacturing Technology*, 107, 4231–4238.
- Babitsky, V. I., Kalashnikov, A. N., Meadows, A., & Wijesundara, A. A. (2003). Ultrasonically assisted turning of aviation materials. *Journal of materials processing technology*, 132, 157–167.
- Babitsky, V. I., Mitrofanov, & Silberschmidt, V. V. (2004). Ultrasonically assisted turning of aviation materials: simulations and experimental study. *Ultrasonics*, 42, 81–86.
- Baghlani, V., Mehbudi, P., Akbari, J., & Sohrabi, M. (2013). Ultrasonic assisted deep drilling of Inconel 738LC superalloy. *Procedia Cirp*, 6, 571–576.

- Batzer, S. A., & Sutherland, J. W. (2001). A geometric analysis of semi-spiral chip morphology in orthogonal machining. *Machining science and technology*, 5, 63–76.
- Beck, J. V., Blackwell, B., & Clair Jr, C. R. (1985). *Inverse heat conduction: Ill-posed problems*. James Beck.
- Beer, N., Özkaya, E., & Biermann, D. (2014). Drilling of Inconel 718 with geometry-modified twist drills. *Procedia CIRP*, 24, 49–55.
- Bhushan, B. (2013). *Introduction to tribology*. John Wiley & Sons.
- Bleicher, F., Reiter, M., & Brier, J. (2019). Increase of chip removal rate in single-lip deep hole drilling at small diameters by low-frequency vibration support. *CIRP Annals*, 68, 93–96.
- Bleicher, F., Wiesinger, G., Kumpf, C., Finkeldei, D., Baumann, C., & Lechner, C. (2018). Vibration assisted drilling of CFRP/metal stacks at low frequencies and high amplitudes. *Production Engineering*, 12, 289–296.
- Boothroyd, G. (1988). *Fundamentals of metal machining and machine tools* (Vol. 28). CRC Press.
- Brehl, D. E., & Dow, T. A. (2008). Review of vibration-assisted machining. *Precision engineering*, 32, 153–172.
- Brehl, D. E., Dow, T. A., Garrard, K., & Sohn, A. (2006). Micro-structure fabrication using elliptical vibration-assisted machining (EVAM). *Proc. 21st Annu. ASPE meet. ASPE*.
- Brinksmeier, E., Pecat, O., & Rentsch, R. (2015). Quantitative analysis of chip extraction in drilling of Ti6Al4V. *CIRP Annals*, 64(1), 93-96.
- Brooks, J. W., Bridges, P. J., & others. (1988). Metallurgical stability of Inconel alloy 718. *Superalloys*, 88, 33–42.
- Bücker, M., Oezkaya, E., Hensler, U., & Biermann, D. (2020). A new flank face design leading to an improved process performance when drilling high-temperature nickel-base alloys. *Proceedings of the Machining Innovations Conference (MIC)*.
- Bücker, M. (2022). *Neue Methoden zur Entwicklung und Herstellung von Hochleistungswerkzeugen für die Bohrbearbeitung von Inconel 718*. Dissertation, Universität Dortmund, Vulkan Verlag, Essen, 2021, ISBN: 978-3-8027-8922-9.
- Budak, E., & Ozlu, E. (2008). Development of a thermomechanical cutting process model for machining process simulations. *CIRP annals*, 57, 97–100.
- Campatelli, G. (2009). Analysis of the environmental impact for a turning operation of AISI 1040 steel. *IPROMS Conference*, (pp. 6–17).
- Camposeco-Negrete, C. (2013). Optimization of cutting parameters for minimizing energy consumption in turning of AISI 6061 T6 using Taguchi methodology and ANOVA. *Journal of Cleaner Production*, 53, 195–203.
- Castejón, M., Alegre, E., Barreiro, J., & Hernández, L. K. (2007). On-line tool wear monitoring using geometric descriptors from digital images. *International Journal of Machine Tools and Manufacture*, 47, 1847–1853
- Castle, W. F. (2007). Fifty-years' development of cryogenic liquefaction processes. *Cryogenic Engineering*, 146–160.
- Cerniway, M. A., & others. (2002). Elliptical diamond milling: kinematics, force and tool wear.
- Chapman, P. F., & Roberts, F. (2013). *Metal Resources and Energy: Butterworths Monographs in Materials*. Elsevier.
- Chern, G.-L., & Chang, Y.-C. (2006). Using two-dimensional vibration cutting for micro-milling. *International Journal of Machine Tools and Manufacture*, 46, 659–666.
- Chhabra, P. N., Ackroyd, B., Compton, W. D., & Chandrasekar, S. (2002). Low-frequency modulation-assisted drilling using linear drives. *Proceedings of the Institution of Mechanical Engineers, Part B: Journal of Engineering Manufacture*, 216, 321–330.
- Childs, T. H. (2006). Friction modelling in metal cutting. *Wear*, 260, 310–318.

- Chu, N.-H., Nguyen, V.-D., & Do, T.-V. (2018). Ultrasonic-assisted cutting: A beneficial application for temperature, torque reduction, and cutting ability improvement in deep drilling of Al-6061. *Applied Sciences*, 8, 1708.
- Conti, J., Holtberg, P., Diefenderfer, J., LaRose, A., Turnure, J. T., & Westfall, L. (2016). International energy outlook 2016 with projections to 2040. Tech. rep., USDOE Energy Information Administration (EIA)
- Cselle, T. (1995). New Directions in Drilling, Dry and Near-dry Machining Will Impact High Productivity Drilling in the Next Decade. *Manufacturing Engineering*, SME, Dearborn, MI.
- Dahmus, J. B., & Gutowski, T. G. (2004). An environmental analysis of machining. *ASME international mechanical engineering congress and exposition*, 47136, pp. 643–652.
- Dambhare, S., Deshmukh, S., & Borade, A. (2015). Machining parameter optimization in turning process for sustainable manufacturing. *International Journal of Industrial Engineering Computations*, 6, 327–338.
- Davies, M. A., Ueda, T., M'saoubi, R., Mullany, B., & Cooke, A. L. (2007). On the measurement of temperature in material removal processes. *CIRP annals*, 56, 581–604.
- Davim, J. P., Davim, & Castro. (2019). *Measurement in Machining and Tribology*. Springer.
- De Bartolomeis, A., Newman, S. T., Jawahir, I. S., Biermann, D., & Shokrani, A. (2021). Future research directions in the machining of Inconel 718. *Journal of Materials Processing Technology*, 297, 117260.
- Debnath, S., Reddy, M. M., & Yi, Q. S. (2014). Environmental friendly cutting fluids and cooling techniques in machining: a review. *Journal of cleaner production*, 83, 33–47.
- Denkena, B., Bergmann, B., Grove, T., & Pape, O. (2017). Increasing productivity in turning of hard-to-cut materials by means of modified flank faces. *Procedia Manufacturing*, 14, 97–104.
- Denkena, B., Krödel, A., & Beblein, S. (2021). A novel approach to determine the velocity dependency of the friction behavior during machining by means of digital particle image velocimetry (DPIV). *CIRP Journal of Manufacturing Science and Technology*, 32, 81-90.
- Devillez, A., Le Coz, G., Dominiak, S., & Dudzinski, D. (2011). Dry machining of Inconel 718, workpiece surface integrity. *Journal of Materials Processing Technology*, 211, 1590–1598.
- Devotta, A. M. (2015). Characterization & modeling of chip flow angle & morphology in 2D & 3D Turning process. Ph.D. dissertation, University West.
- Dhanachandra, N., Manglem, K., & Chanu, Y. J. (2015). Image segmentation using K-means clustering algorithm and subtractive clustering algorithm. *Procedia Computer Science*, 54, 764–771.
- Dhananchezian, M., & Kumar, M. P. (2011). Cryogenic turning of the Ti–6Al–4V alloy with modified cutting tool inserts. *Cryogenics*, 51, 34–40.
- Ding, H., Ibrahim, R., Cheng, K., & Chen, S.-J. (2010). Experimental study on machinability improvement of hardened tool steel using two dimensional vibration-assisted micro-end-milling. *International Journal of Machine Tools and Manufacture*, 50, 1115–1118.
- Dong, S., Liao, W., Zheng, K., & Ma, W. (2020). Investigation on thrust force in rotary ultrasonic drilling of CFRP/aluminum stacks. *Proceedings of the Institution of Mechanical Engineers, Part C: Journal of Mechanical Engineering Science*, 234, 394–404.
- Doyle, E. D., Horne, J. G., & Tabor, D. (1979). Frictional interactions between chip and rake face in continuous chip formation. *Proceedings of the Royal Society of London. A. Mathematical and Physical Sciences*, 366(1725), 173-183.
- El Baradie, M. A. (1996). Cutting fluids: Part I. characterisation. *Journal of materials processing technology*, 56, 786–797.

- Ezugwu, E. O., Bonney, J., Fadare, D. A., & Sales, W. F. (2005). Machining of nickel-base, Inconel 718, alloy with ceramic tools under finishing conditions with various coolant supply pressures. *Journal of materials processing technology*, 162, 609–614.
- Feng, Y., Zhang, M., Zhu, Z., Jia, B., & Wang, X. (2019). Axial cutting force prediction model of titanium matrix composites TiBw/TC4 in ultrasonic vibration-assisted drilling. *The International Journal of Advanced Manufacturing Technology*, 105, 121–135.
- Fernando, W. L., Karunathilake, H. P., & Gamage, J. R. (2021). Strategies to reduce energy and metalworking fluid consumption for the sustainability of turning operation: A review. *Cleaner Engineering and Technology*, 3, 100100.
- Finnveden, G., Hauschild, M. Z., Ekvall, T., Guinée, J., Heijungs, R., Hellweg, S., . . . Suh, S. (2009). Recent developments in life cycle assessment. *Journal of environmental management*, 91, 1–21.
- Forestier, F., Gagnol, V., Ray, P., & Paris, H. (2012). Model-based cutting prediction for a self-vibratory drilling head-spindle system. *International Journal of Machine Tools and Manufacture*, 52, 59–68.
- Furrer, D., & Fecht, H. (1999). Ni-based superalloys for turbine discs. *Jom*, 51, 14–17.
- Ghani, J. A., Rizal, M., & Haron, C. H. (2014). Performance of green machining: a comparative study of turning ductile cast iron FCD700. *Journal of cleaner production*, 85, 289–292.
- Ghosh, S., Rao, P. V., & others. (2015). Application of sustainable techniques in metal cutting for enhanced machinability: a review. *Journal of Cleaner Production*, 100, 17–34.
- Goldstein, J. I., Newbury, D. E., Michael, J. R., Ritchie, N. W., Scott, J. H., & Joy, D. C. (2017). *Scanning electron microscopy and X-ray microanalysis*. Springer.
- Goldwitz, J. A. (2002). *Productivity Gains and Environmental Impact of Turning Tools*. Ph.D. dissertation, Massachusetts Institute of Technology, Department of Mechanical Engineering.
- Gontard, L. C., Batista, M., Salguero, J., & Calvino, J. J. (2018). Three-dimensional chemical mapping using non-destructive SEM and photogrammetry. *Scientific Reports*, 8, 11000.
- Guibert, N., Paris, H., & Rech, J. (2008). A numerical simulator to predict the dynamical behavior of the self-vibratory drilling head. *International Journal of Machine Tools and Manufacture*, 48, 644–655.
- Guo, P., & Ehmann, K. F. (2013). An analysis of the surface generation mechanics of the elliptical vibration texturing process. *International Journal of Machine Tools and Manufacture*, 64, 85–95.
- Gutowski, T., Murphy, C., Allen, D., Bauer, D., Bras, B., Piwonka, T., & Wolff, E. (2005). Environmentally benign manufacturing: observations from Japan, Europe and the United States. *Journal of Cleaner Production*, 13, 1–17.
- Hanafi, I., Khamlichi, A., Cabrera, F. M., Almansa, E., & Jabbouri, A. (2012). Optimization of cutting conditions for sustainable machining of PEEK-CF30 using TiN tools. *Journal of Cleaner Production*, 33, 1–9.
- Heginbotham, W. B., & Gogia, S. L. (1961). Metal cutting and the built-up nose. *Proceedings of the Institution of Mechanical Engineers*, 175, 892–917.
- Heisel, U., Wallaschek, J., Eisseler, R., & Potthast, C. (2008). Ultrasonic deep hole drilling in electrolytic copper ECu 57. *CIRP annals*, 57, 53–56.
- Ho, C. Y., & Chu, T. K. (1977). *Electrical resistivity and thermal conductivity of nine selected AISI stainless steels* (p. 36). Center for Information and Numerical Data Analysis and Synthesis, Purdue University.
- Hsu, C. Y., Huang, C. K., & Wu, C. Y. (2007). Milling of MAR-M247 nickel-based superalloy with high temperature and ultrasonic aiding. *The International Journal of Advanced Manufacturing Technology*, 34, 857–866.

- Huang, C., Lee, S., Sullivan, J. P., & Chandrasekar, S. (2007). In situ measurement of fluid film thickness in machining. *Tribology Letters*, 28, 39–44.
- Hucks, H. (1951). *Plastizitätsmechanische Grundlagen und Kenngrößen der Zerspanung*. Ph.D. dissertation, Rheinisch-Westfälische Technische Hochschule, Aachen.
- Hussein, R., Sadek, A., Elbestawi, M. A., & Attia, M. H. (2018). Low-frequency vibration-assisted drilling of hybrid CFRP/Ti6Al4V stacked material. *The International Journal of Advanced Manufacturing Technology*, 98, 2801–2817.
- Hwang, J., & Chandrasekar, S. (2011). Contact conditions at the chip-tool interface in machining. *International Journal of Precision Engineering and Manufacturing*, 12, 183–193.
- Isaev, A. I., & Anokhin, V. S. (1961). Application of Ultrasonic Vibrations of the Tool during Cutting Metals. *Vestn. Mashinostr.*, 56–62.
- Itoigawa, F., Takeuchi, D., Nakamura, T., & Childs, T. H. (2007). Experimental study on lubrication mechanism in MQL intermittent cutting process. *Machining Science and Technology*, 11, 355–365.
- Jallageas, J., K'nevez, J. Y., Chérif, M., & Cahuc, O. (2013). Modeling and optimization of vibration-assisted drilling on positive feed drilling unit. *The International Journal of Advanced Manufacturing Technology*, 67, 1205–1216.
- Jawahir, I. S., Attia, H., Biermann, D., Dufflou, J., Klocke, F., Meyer, D., . . . others. (2016). Cryogenic manufacturing processes. *CIRP annals*, 65, 713–736.
- Jayal, A. D., Badurdeen, F., Dillon Jr, O. W., & Jawahir, I. S. (2010). Sustainable manufacturing: Modeling and optimization challenges at the product, process and system levels. *CIRP Journal of Manufacturing Science and Technology*, 2, 144–152.
- Jen, T.-C., & Anagonye, A. U. (2001). An improved transient model of tool temperatures in metal cutting. *J. Manuf. Sci. Eng.*, 123, 30–37.
- Jen, T.-C., Eapen, S., & Gutierrez, G. (2003). Nonlinear numerical analysis in transient cutting tool temperatures. *J. Manuf. Sci. Eng.*, 125, 48–56.
- Jiang, F., Liu, Z., Wan, Y., & Shi, Z. (2013). Analytical modeling and experimental investigation of tool and workpiece temperatures for interrupted cutting 1045 steel by inverse heat conduction method. *Journal of Materials Processing Technology*, 213, 887–894.
- Karaguzel, U., Olgun, U., Uysal, E., Budak, E., & Bakkal, M. (2015). Increasing tool life in machining of difficult-to-cut materials using nonconventional turning processes. *The International Journal of Advanced Manufacturing Technology*, 77, 1993–2004.
- Karaguzel, U., Bakkal, M., & Budak, E. (2016). Modeling and measurement of cutting temperatures in milling. *Procedia CIRP*, 46, 173–176.
- Karaguzel, U. (2021). Transient multi-domain thermal modeling of interrupted cutting with coated tools. *The International Journal of Advanced Manufacturing Technology*, 116, 345–361.
- Kataoka, R., & Shamoto, E. (2019). Influence of vibration in cutting on tool flank wear: Fundamental study by conducting a cutting experiment with forced vibration in the depth-of-cut direction. *Precision Engineering*, 55, 322–329.
- Kilic, D. S., & Raman, S. (2007). Observations of the tool–chip boundary conditions in turning of aluminum alloys. *Wear*, 262, 889–904.
- Kim, D.-H., & Lee, C.-M. (2014). A study of cutting force and preheating-temperature prediction for laser-assisted milling of Inconel 718 and AISI 1045 steel. *International Journal of Heat and Mass Transfer*, 71, 264–274.
- Kitagawa, T., Kubo, A., & Maekawa, K. (1997). Temperature and wear of cutting tools in high-speed machining of Inconel 718 and Ti-6Al-6V-2Sn. *wear*, 202, 142–148.
- Klocke, F. A., & Eisenblätter, G. (1997). Dry cutting. *CIRP Annals*, 46, 519–526.

- Komanduri, R., & Hou, Z. B. (2000). Thermal modeling of the metal cutting process: part I—temperature rise distribution due to shear plane heat source. *International Journal of Mechanical Sciences*, 42, 1715–1752.
- Komanduri, R., & Hou, Z. B. (2001a). Thermal modeling of the metal cutting process—Part II: temperature rise distribution due to frictional heat source at the tool–chip interface. *International Journal of Mechanical Sciences*, 43, 57–88.
- Komanduri, R., & Hou, Z. B. (2001b). Thermal modeling of the metal cutting process—Part III: temperature rise distribution due to the combined effects of shear plane heat source and the tool–chip interface frictional heat source. *International Journal of Mechanical Sciences*, 43, 89–107.
- Kordonowy, D. N. (2002). A power assessment of machining tools. Ph.D. dissertation, Massachusetts Institute of Technology.
- Kountanya, R. (2008). Cutting tool temperatures in interrupted cutting—the effect of feed-direction modulation. *Journal of Manufacturing Processes*, 10, 47–55.
- Kronenberg, M. (1952). *Grundzüge der Zerspanungslehre: Theorie und Praxis der Zerspanung für Bau und Betrieb von Werkzeugmaschinen*. Springer Berlin Heidelberg.
- Ladonne, M., Cherif, M., Landon, Y., K'nevez, J.-Y., Cahuc, O., & De Castelbajac, C. (2015). Modelling the vibration-assisted drilling process: identification of influential phenomena. *The International Journal of Advanced Manufacturing Technology*, 81, 1657–1666.
- Lawal, S. A., Choudhury, I. A., & Nukman, Y. (2013). A critical assessment of lubrication techniques in machining processes: a case for minimum quantity lubrication using vegetable oil-based lubricant. *Journal of Cleaner Production*, 41, 210–221.
- Lazoglu, I., & Altintas, Y. (2002). Prediction of tool and chip temperature in continuous and interrupted machining. *International Journal of Machine tools and manufacture*, 42, 1011–1022.
- Lee, E. H., & Shaffer, B. W. (1951). The theory of plasticity applied to a problem of machining. *Journal of applied Mechanics*, 18(4), 405–413.
- Lei, S., & Liu, W. (2002). High-speed machining of titanium alloys using the driven rotary tool. *International journal of machine tools and manufacture*, 42, 653–661.
- Li, L., Li, B., Ehmann, K. F., & Li, X. (2013). A thermo-mechanical model of dry orthogonal cutting and its experimental validation through embedded micro-scale thin film thermocouple arrays in PCBN tooling. *International Journal of Machine Tools and Manufacture*, 70, 70–87.
- Liao, Y. S., Chen, Y. C., & Lin, H. M. (2007). Feasibility study of the ultrasonic vibration assisted drilling of Inconel superalloy. *International Journal of Machine Tools and Manufacture*, 47, 1988–1996.
- Liu, C. S., Zhao, B., Gao, G. F., & Zhang, X. H. (2005). Study on ultrasonic vibration drilling of particulate reinforced aluminum matrix composites. *Key Engineering Materials*, 291, pp. 447–452.
- Loewen, E. G., & Shaw, M. C. (1954). On the analysis of cutting-tool temperatures. *Transactions of the American Society of Mechanical Engineers*, 76, 217–225.
- Lotfi, M., & Amini, S. (2018). Effect of ultrasonic vibration on frictional behavior of tool–chip interface: Finite element analysis and experimental study. *Proceedings of the Institution of Mechanical Engineers, Part B: Journal of Engineering Manufacture*, 232, 1212–1220.
- Madhavan, V., Chandrasekar, S., & Farris, T. N. (2002). Direct observations of the chip-tool interface in the low speed cutting of pure metals. *J. Trib.*, 124, 617–626.
- Mainé, J. M., Batista, M., García-Jurado, D., Shaw, L., & Marcos, M. (2013). FVM based methodology for evaluating adhesion wear of cutting tools. *Procedia CIRP*, 8, 552–557.

- Mann, J. B., Saldana, C., Chandrasekar, S., Compton, W. D., & Trumble, K. P. (2007). Metal particulate production by modulation-assisted machining. *Scripta Materialia*, 57, 909–912.
- Mann, J. B., Shankar, M. R., Chandrasekar, S., Compton, W. D., & Moscoso, W. (2009, December). Machining method to controllably produce chips with determinable shapes and sizes. Patent.
- Mann, J. B. (2010). Modulation-assisted machining. Ph.D. dissertation, Purdue University.
- Mann, J. B., Guo, Y., Saldana, C., Compton, W. D., & Chandrasekar, S. (2011). Enhancing material removal processes using modulation-assisted machining. *Tribology International*, 44, 1225–1235.
- Masoudi, S., Vafadar, A., Hadad, M., & Jafarian, F. (2018). Experimental investigation into the effects of nozzle position, workpiece hardness, and tool type in MQL turning of AISI 1045 steel. *Materials and Manufacturing Processes*, 33, 1011–1019.
- Mativenga, P. T., & Rajemi, M. F. (2011). Calculation of optimum cutting parameters based on minimum energy footprint. *CIRP annals*, 60, 149–152.
- McGuire, M. F. (2008). *Stainless steels for design engineers*. Asm International.
- Merchant, M. E. (1944). Basic mechanics of the metal-cutting process. *Journal of applied Mechanics*, 11(3), A168-A175
- Merchant, M. E. (1945). Mechanics of the metal cutting process. II. Plasticity conditions in orthogonal cutting. *Journal of applied physics*, 16, 318–324.
- Mia, M., & Dhar, N. R. (2015). Effect of high pressure coolant jet on cutting temperature, tool wear and surface finish in turning hardened (HRC 48) steel. *Journal of Mechanical Engineering*, 45, 1–6.
- Mignanelli, P. M., Jones, N. G., Pickering, E. J., Messé, O. M., Rae, C. M., Hardy, M. C., & Stone, H. J. (2017). Gamma-gamma prime-gamma double prime dual-superlattice superalloys. *Scripta Materialia*, 136, 136–140.
- Mitrofanov, A. V., Babitsky, V. I., & Silberschmidt, V. V. (2005). Thermomechanical finite element simulations of ultrasonically assisted turning. *Computational materials science*, 32, 463–471.
- Miyake, A., Kitakaze, A., Katoh, S., Muramatsu, M., Noguchi, K., Sannomiya, K., . . . Sasahara, H. (2018). Chip control in turning with synchronization of spindle rotation and feed motion vibration. *Precision Engineering*, 53, 38–45.
- Moriwaki, T., & Shamoto, E. (1991). Ultraprecision diamond turning of stainless steel by applying ultrasonic vibration. *CIRP annals*, 40, 559–562.
- Moriwaki, T., Shamoto, E., & Inoue, K. (1992). Ultraprecision ductile cutting of glass by applying ultrasonic vibration. *CIRP annals*, 41, 141–144.
- Moriwaki, T., & Shamoto, E. (1995). Ultrasonic elliptical vibration cutting. *CIRP annals*, 44, 31–34.
- Moscoso, W., Olgun, E., Compton, W. D., & Chandrasekar, S. (2005). Effect of low-frequency modulation on lubrication of chip-tool interface in machining. *J. Trib.*, 127, 238–244.
- Moura, R. R., da Silva, M. B., Machado, Á. R., & Sales, W. F. (2015). The effect of application of cutting fluid with solid lubricant in suspension during cutting of Ti-6Al-4V alloy. *Wear*, 332, 762–771.
- M'Saoubi, R., & Chandrasekaran, H. (2005). Innovative methods for the investigation of tool-chip adhesion and layer formation during machining. *CIRP annals*, 54, 59–62.
- Müller, B. (2004). Thermische analyse des Zerspanens metallischer Werkstoffe bei hohen Schnittgeschwindigkeiten. Ph.D. dissertation, Bibliothek der RWTH Aachen.
- Nategh, M. J., Razavi, H., & Abdollah, A. (2012). Analytical modeling and experimental investigation of ultrasonic-vibration assisted oblique turning, part I: Kinematics analysis. *International Journal of Mechanical Sciences*, 63, 1–11.

- Nath, C., Rahman, M., & Andrew, S. S. (2007). A study on ultrasonic vibration cutting of low alloy steel. *Journal of Materials Processing Technology*, 192, 159–165.
- Nath, C., & Rahman, M. (2008). Evaluation of ultrasonic vibration cutting while machining Inconel 718. *International Journal of Precision Engineering and Manufacturing*, 9, 63–68.
- Neugebauer, R., & Stoll, A. (2004). Ultrasonic application in drilling. *Journal of materials processing technology*, 149, 633–639.
- Okamura, K., Sasahara, H., Segawa, T., & Tsutsumi, M. (2006). Low-frequency vibration drilling of titanium alloy. *JSME International Journal Series C Mechanical Systems, Machine Elements and Manufacturing*, 49, 76–82.
- Oxley, P. L. (1988). Modelling machining processes with a view to their optimization and to the adaptive control of metal cutting machine tools. *Robotics and computer-integrated manufacturing*, 4, 103–119.
- Oxley, P. L. B. (1989). *Mechanics of Machining: An Analytical Approach to Assessing Machinability*. Ellis Horwood series in Mechanical Engineering, John Wiley & Sons, New York, USA.
- Özel, T., Biermann, D., Enomoto, T., & Mativenga, P. (2021). Structured and textured cutting tool surfaces for machining applications. *CIRP Annals*, 70, 495–518.
- Paris, H., Tichkiewitch, S., & Peigne, G. (2005). Modelling the vibratory drilling process to foresee cutting parameters. *CIRP annals*, 54, 367–370.
- Patil, S., Joshi, S., Tewari, A., & Joshi, S. S. (2014). Modelling and simulation of effect of ultrasonic vibrations on machining of Ti6Al4V. *Ultrasonics*, 54, 694–705.
- Paulsen, T., Guba, N., Sölter, J., & Karpuschewski, B. (2020). Influence of the workpiece material on the cutting performance in low frequency vibration assisted drilling. *CIRP Journal of Manufacturing Science and Technology*, 31, 140–152.
- Pecat, O., & Meyer, I. (2013). Low frequency vibration assisted drilling of aluminium alloys. *Advanced materials research*, 769, 131–138.
- Pecat, O., & Brinksmeier, E. (2014). Low damage drilling of CFRP/titanium compound materials for fastening. *Procedia Cirp*, 13, 1–7.
- Pecat, O., & Brinksmeier, E. (2014). Tool wear analyses in low frequency vibration assisted drilling of CFRP/Ti6Al4V stack material. *Procedia Cirp*, 14, 142–147.
- Pecat, O., Paulsen, T., Katthöfer, P., Brinksmeier, E., & Fangmann, S. (2016). Vibration assisted drilling of aerospace materials. *Tech. rep.*, SAE Technical Paper.
- Peigne, G. (2014). Ring-rolling bearing with axial displacement and shaping tooling equipped with such a bearing. Ring-rolling bearing with axial displacement and shaping tooling equipped with such a bearing. Google Patents.
- Pervaiz, S., Kannan, S., & Kishawy, H. A. (2018). An extensive review of the water consumption and cutting fluid based sustainability concerns in the metal cutting sector. *Journal of Cleaner Production*, 197, 134–153.
- Piispanen, V. (1948). Theory of formation of metal chips. *Journal of Applied Physics*, 19, 876–881.
- Ponce, M., Del Sol Illana, I., Fernandez-Vidal, S. R., & Salguero Gomez, J. (2018). Experimental parametric model for adhesion wear measurements in the dry turning of an AA2024 alloy. *Materials*, 11, 1598.
- Popova, E., & Popov, V. L. (2015). The research works of Coulomb and Amontons and generalized laws of friction. *Friction*, 3, 183–190.
- Potdar, Y. K., & Zehnder, A. T. (2003). Measurements and simulations of temperature and deformation fields in transient metal cutting. *J. Manuf. Sci. Eng.*, 125, 645–655.
- Puls, H., Klocke, F., & Lung, D. (2012). A new experimental methodology to analyse the friction behaviour at the tool-chip interface in metal cutting. *Production engineering*, 6, 349–354.

- Pusavec, F., Krajnik, P., & Kopac, J. (2010a). Transitioning to sustainable production—Part I: application on machining technologies. *Journal of Cleaner production*, 18, 174–184.
- Pusavec, F., Kramar, D., Krajnik, P., & Kopac, J. (2010b). Transitioning to sustainable production—part II: evaluation of sustainable machining technologies. *Journal of Cleaner Production*, 18(12), 1211–1221.
- Pusavec, F., Sterle, L., Kalin, M., Mallipeddi, D., & Krajnik, P. (2020). Tribology of solid-lubricated liquid carbon dioxide assisted machining. *CIRP annals*, 69, 69–72.
- Rahim, E. A., & Sasahara, H. (2011). A study of the effect of palm oil as MQL lubricant on high speed drilling of titanium alloys. *Tribology International*, 44, 309–317.
- Rajemi, M. F., Mativenga, P. T., & Jaffery, S. I. (2009). Energy and carbon footprint analysis for machining titanium Ti-6Al-4V alloy. *Journal of Machine Engineering*, 9.
- Ramkumar, J., Aravindan, S., Malhotra, S. K., & Krishnamurthy, R. (2004). An enhancement of the machining performance of GFRP by oscillatory assisted drilling. *The International Journal of Advanced Manufacturing Technology*, 23, 240–244.
- Rao, D. N., & Krishna, P. V. (2008). The influence of solid lubricant particle size on machining parameters in turning. *International Journal of Machine Tools and Manufacture*, 48, 107–111.
- Razavi, H., Nategh, M. J., & Abdullah, A. (2012). Analytical modeling and experimental investigation of ultrasonic-vibration assisted oblique turning, part II: Dynamics analysis. *International Journal of Mechanical Sciences*, 63, 12–25.
- Reddy, N. S., Nouari, M., & Yang, M. (2010). Development of electrostatic solid lubrication system for improvement in machining process performance. *International Journal of Machine Tools and Manufacture*, 50, 789–797.
- Reed, R. C. (2008). *The superalloys: fundamentals and applications*. Cambridge university press.
- Rowe, G. W., & Spick, P. T. (1967). A new approach to determination of the shear-plane angle in machining. *Journal of Manufacturing Science and Engineering*, 89(3): 530–538.
- Sadek, A., Meshreki, M., & Attia, M. H. (2014). Effect of tool kinematics on the drilling forces and temperature in low frequency high amplitude vibration assisted drilling. *ASME International Mechanical Engineering Congress and Exposition*, 46438, p. V02AT02A035.
- Saelzer, J., Alammari, Y., Zabel, A., Biermann, D., Lee, J., & Elgeti, S. (2021). Characterisation and modelling of friction depending on the tool topography and the intermediate medium. *Procedia CIRP*, 102, 435–440.
- Saelzer, J., Berger, S., Iovkov, I., Zabel, A., & Biermann, D. (2020). In-situ measurement of rake face temperatures in orthogonal cutting. *CIRP Annals*, 69, 61–64.
- Saelzer, J., Berger, S., Iovkov, I., Zabel, A., & Biermann, D. (2020). In-situ measurement of rake face temperatures in orthogonal cutting. *CIRP Annals*, 69, 61–64.
- Schultheiss, F., Zhou, J., Gröntoft, E., & Ståhl, J.-E. (2013). Sustainable machining through increasing the cutting tool utilization. *Journal of Cleaner Production*, 59, 298–307.
- Schulz, H., & Spur, G. (1990). High speed turn-milling—a new precision manufacturing technology for the machining of rotationally symmetrical workpieces. *CIRP annals*, 39, 107–109.
- Schumski, L., Paulsen, T., Sölter, J., & Karpuschewski, B. (2021). Finite element simulation of low frequency vibration-assisted drilling with modification of oscillation modes. *Procedia CIRP*, 102, 168–173.
- Shamoto, E., & Moriwaki, T. (1999). Ultraprecision diamond cutting of hardened steel by applying elliptical vibration cutting. *CIRP Annals*, 48, 441–444.
- Shamoto, E., Suzuki, N., Tsuchiya, E., Hori, Y., Inagaki, H., & Yoshino, K. (2005). Development of 3 DOF ultrasonic vibration tool for elliptical vibration cutting of sculptured surfaces. *CIRP annals*, 54, 321–324.

- Shaw, M. C., Cook, N. H., & Finnie, I. (1953). The shear-angle relationship in metal cutting. *Transactions of the American Society of Mechanical Engineers*, 75, 273–283.
- Shaw, M. C. (1984). *Metal Cutting Principles*. Oxford University Press.
- Shaw, M. C. (1993). Some observations concerning the mechanics of cutting and grinding.
- Shaw, M. C., & Cookson, J. O. (2005). *Metal cutting principles* (Vol. 2). Oxford university press New York.
- Shokrani, A., Dhokia, V., & Newman, S. T. (2012). Environmentally conscious machining of difficult-to-machine materials with regard to cutting fluids. *International Journal of machine Tools and manufacture*, 57, 83–101.
- Siniawski, M., & Bowman, C. (2009). Metal working fluids: finding green in the manufacturing process. *Industrial Lubrication and tribology*. *Industrial Lubrication and Tribology*, 61(2), 60-66.
- Skelton, R. C. (1968). Turning with an oscillating tool. *International Journal of Machine Tool Design and Research*, 8, 239–259.
- Spriggs, G. E. (2002). 13.4 Properties of hardmetals and cermets: 13 Hard materials. *Powder metallurgy data. Refractory, hard and intermetallic materials*, 86-117.
- Standard ASTM A582/A582M-21, Standard Specification for Free-Machining Stainless Steel Bars, ASTM International
- Standard ASTM B637-18 Standard Specification for Precipitation-Hardening and Cold Worked Nickel Alloy Bars, Forgings, and Forging Stock for Moderate or High Temperature Service, ASTM International
- Standard DIN EN 10088-3:2014-12, Nichtrostende Stähle – Teil 3: Technische Lieferbedingungen für Halbzeug, Stäbe, Walzdraht, gezogenen Draht, Profile und Blankstahlerzeugnisse aus korrosionsbeständigen Stählen für allgemeine Verwendung, Beuth Verlag GmbH
- Standard DIN EN 10302:2008-06, Warmfeste Stähle, Nickel- und Cobaltlegierungen, Beuth Verlag GmbH
- Standard DIN EN ISO 25178-1:2016-12, Geometrische Produktspezifikation (GPS) - Oberflächenbeschaffenheit: Flächenhaft – Teil 1: Angabe von Oberflächenbeschaffenheit, Beuth Verlag GmbH, Beuth Verlag GmbH,
- Standard DIN EN ISO 4287:2010-07, Geometrische Produktspezifikation (GPS) - Oberflächenbeschaffenheit: Tastschnittverfahren - Benennungen, Definitionen und Kenngrößen der Oberflächenbeschaffenheit, Beuth Verlag GmbH
- Standard ISO 3685:1993, Tool-life testing with single-point turning tools, ISO
- Stark, R., Seliger, G., & Bonvoisin, J. (2017). *Sustainable manufacturing: Challenges, solutions and implementation perspectives*. Springer Nature.
- Stephenson, D. A., & Ali, A. (1992). Tool temperatures in interrupted metal cutting.
- Sterle, L., Kalin, M., & Pušavec, F. (2018). Performance evaluation of solid lubricants under machining-like conditions. *Procedia CIRP*, 77, 401–404.
- Sugihara, T., & Enomoto, T. (2016). Ultra-low-frequency vibration assisted machining of Ti-6Al-4V alloy. *International Journal of Automation Technology*, 10, 647–653.
- Sui, H., Zhang, X., Zhang, D., Jiang, X., & Wu, R. (2017). Feasibility study of high-speed ultrasonic vibration cutting titanium alloy. *Journal of Materials Processing Technology*, 247, 111–120.
- Sweet, J. N., Roth, E. P., & Moss, M. (1987). Thermal conductivity of Inconel 718 and 304 stainless steel. *International journal of thermophysics*, 8, 593–606.
- Takeyama, H., & Kato, S. (1991). Burrless drilling by means of ultrasonic vibration. *CIRP annals*, 40, 83–86.
- Timmerhaus, K. D., & Reed, R. P. (2007). *Cryogenic engineering: fifty years of progress*.

- Toews Iii, H. G., Compton, W. D., & Chandrasekar, S. (1998). A study of the influence of superimposed low-frequency modulation on the drilling process. *Precision engineering*, 22, 1–9.
- Tong, J., Wei, G., Zhao, L., Wang, X., & Ma, J. (2019). Surface microstructure of titanium alloy thin-walled parts at ultrasonic vibration-assisted milling. *The International Journal of Advanced Manufacturing Technology*, 101, 1007–1021.
- Trent, E. M. (1977). *Metal cutting*. Butterworths, London.
- Trigger, K. J., & Chao, B. T. (1951). An analytical evaluation of metal-cutting temperatures. *Transactions of the American Society of Mechanical Engineers*, 73, 57–66.
- Ueda, K., Iwata, K., & Nakayama, K. (1980). Chip formation mechanism in single crystal cutting of β -brass. *CIRP annals*, 29, 41–46.
- Usui, E., Gujral, A., & Shaw, M. C. (1961). An experimental study of the action of CCl_4 in cutting and other processes involving plastic flow. *International Journal of Machine Tool Design and Research*, 1, 187–197.
- Usui, E., Hirota, A., & Masuko, M. (1978). Analytical prediction of three dimensional cutting process—Part 1: basic cutting model and energy approach. *Journal of Manufacturing Science and Engineering*, 100(2): 222-228
- Van Luttervelt, C. A., Childs, T. H., Jawahir, I. S., Klocke, F., Venuvinod, P. K., Altintas, Y., . . . others. (1998). Present situation and future trends in modelling of machining operations progress report of the CIRP Working Group ‘Modelling of Machining Operations’. *CIRP Annals*, 47, 587–626.
- Verma, G. C., & Pandey, P. M. (2019). Machining forces in ultrasonic-vibration assisted end milling. *Ultrasonics*, 94, 350–363.
- Warnecke, G. (1974). *Fertigungstechnische Berichte: Spanbildung bei metallischen Werkstoffen*. Technischer Verlag Resch. Germany
- Weinert, K., Inasaki, I., Sutherland, J. W., & Wakabayashi, T. (2004). Dry machining and minimum quantity lubrication. *CIRP annals*, 53, 511–537.
- Wertheim, R., Rotberg, J., & Ber, A. (1992). Influence of high-pressure flushing through the rake face of the cutting tool. *CIRP annals*, 41, 101–106.
- Williams, J. A., & Tabor, D. (1977). The role of lubricants in machining. *Wear*, 43, 275–292.
- Wright, P. K. (1990). Transparent sapphire tools. *Journal of Manufacturing Systems*, 9, 292–302.
- Xu, J., Li, C., Chen, M., & Ren, F. (2019). A comparison between vibration assisted and conventional drilling of CFRP/Ti6Al4V stacks. *Materials and Manufacturing Processes*, 34, 1182–1193.
- Xu, W., Zhang, L. C., & Wu, Y. (2014). Elliptic vibration-assisted cutting of fibre-reinforced polymer composites: understanding the material removal mechanisms. *Composites Science and Technology*, 92, 103–111.
- Yang, H., Ding, W., Chen, Y., Laporte, S., Xu, J., & Fu, Y. (2019). Drilling force model for forced low frequency vibration assisted drilling of Ti-6Al-4V titanium alloy. *International Journal of Machine Tools and Manufacture*, 146, 103438.
- Zareena, A. R., Rahman, M., & Wong, Y. S. (2005). Binderless CBN tools, a breakthrough for machining titanium alloys. *Journal of Manufacturing Science and Engineering, Transactions of the ASME*, 127 (2), 277-279
- Zhang, R. Y., Qin, H. L., Bi, Z. N., Li, J., Paul, S., Lee, T. L., Dong, H. B. (2020). Evolution of lattice spacing of gamma double prime precipitates during aging of polycrystalline Ni-base superalloys: an in situ investigation. *Metallurgical and Materials Transactions A*, 51, 574–585.
- Zhao, G. Y., Liu, Z. Y., He, Y., Cao, H. J., & Guo, Y. B. (2017). Energy consumption in machining: Classification, prediction, and reduction strategy. *Energy*, 133, 142–157.

- Zheng, L., Chen, W., & Huo, D. (2020). Review of vibration devices for vibration-assisted machining. *The International Journal of Advanced Manufacturing Technology*, 108, 1631–1651.
- Zhou, J., Bushlya, V., Avdovic, P., & Ståhl, J. E. (2012). Study of surface quality in high speed turning of Inconel 718 with uncoated and coated CBN tools. *The International Journal of Advanced Manufacturing Technology*, 58, 141–151.
- Zorev, N. N. (1963). Inter-relationship between shear processes occurring along tool face and shear plane in metal cutting. *International research in production engineering*, 49, 143–152.
- Zorev, N. N. (1966). *Metal cutting mechanics*. Pergamon. England.
- Zou, P., Xu, Y., He, Y., Chen, M., & Wu, H. (2015). Experimental investigation of ultrasonic vibration assisted turning of 304 austenitic stainless steel. *Shock and Vibration*, 2015.

Students work

In the context of this dissertation the following student works have been planned and supervised. Selected data and results of these works are used in dissertation content. I would like to express my gratitude to the students for their dedication and diligence as well as for the scientific exchange.

Elkholiy, A: The Influence of Interrupted Machining on Adhesive Tool Wear during Orthogonal Cutting of Inconel 718. Master project work, ISF, TU Dortmund, 2021

Mistry, K. A.: Observations of Initial Chip Formation in Orthogonal Machining of Austenitic Stainless-Steel Alloy X8CrNiS19-9. Master project work, ISF, TU Dortmund, 2021

Reis, F. B.: Influence of Interrupted Drilling of Inconel 718 under MQL. Master project work, ISF, TU Dortmund, 2022

Haberland, J. and Protsch P.: Static and Dynamic Evaluation of a Hydraulic Actuator for Vibration Assisted Drilling. Bachelor project work, ISF, TU Dortmund, 2023

Bisherige Bände in der Schriftenreihe des ISF

- Band H3 Surmann, T.: Simulation der Dynamik von Dreh- und Fräsprozessen. Habilitationsschrift, Technische Universität Dortmund, Vulkan Verlag, Essen, 2017, ISBN 978-3-8027-8794-2
- Band H2 Zabel, A.: Prozesssimulation in der Zerspanung – Modellierung von Dreh- und Fräsprozessen. Habilitationsschrift, Technische Universität Dortmund, Vulkan Verlag, Essen, 2010, ISBN 978-3-8027-8752-2
- Band H1 Mehnen, J.: Mehrkriterielle Optimierverfahren für produktionstechnische Prozesse. Habilitationsschrift, Universität Dortmund, Vulkan Verlag, Essen, 2005, ISBN 3-8027-8760-9
- Band 109 Kipp, M.: Feinstbearbeitung von Hartmetall unter Einsatz elastisch gebundener Diamantschleifwerkzeuge zur Präparation von Spannuten. Dissertation, Universität Dortmund, Vulkan Verlag, Essen, 2023, ISBN: 978-3-8027-8925-0
- Band 108 Nickel, J.: Analyse und Modellierung der thermomechanischen Beeinflussung der Randzoneneigenschaften beim Einlippentiefbohren von Bauteilen aus Vergütungsstahl. Dissertation, Universität Dortmund, Vulkan Verlag, Essen, 2023, ISBN: 978-3-8027-8924-3
- Band 107 Zelinko, A.: Magnetabrasives Polieren auf Bearbeitungszentren. Dissertation, Universität Dortmund, Vulkan Verlag, Essen, 2022, ISBN: 978-3-8027-8923-6
- Band 106 Bücken, M.: Neue Methoden zur Entwicklung und Herstellung von Hochleistungswerkzeugen für die Bohrbearbeitung von Inconel 718. Dissertation, Universität Dortmund, Vulkan Verlag, Essen, 2021, ISBN: 978-3-8027-8922-9
- Band 105 Jaeger, J.: Wendeltiefbohren kleinster Durchmesser in schwer zerspanbare Werkstoffe mit kryogener Minimalmengenschmierung. Dissertation, Universität Dortmund, Vulkan Verlag, Essen, 2021, ISBN: 978-3-8027-8921-2
- Band 104 Bathe, T.: Untersuchungen zur Topographie- und Umfangsgestaltoptimierung von Einlippentiefbohrwerkzeugen. Dissertation, Universität Dortmund, Vulkan Verlag, Essen, 2020, ISBN: 978-3-8027-8919-9
- Band 103 Hannich, S.: Experimentelle und simulative Untersuchungen zum stirnseitigen Fließbohren von Leichtmetallen. Dissertation, Universität Dortmund, Vulkan Verlag, Essen, 2020, ISBN: 978-3-8027-8920-5
- Band 102 Kansteiner, M.: Grundlagenuntersuchungen zum Einsatzverhalten von diamantimprägnierten Werkzeugen beim Kernbohren von hochfestem Beton. Dissertation, Universität Dortmund, Vulkan Verlag, Essen, 2019, ISBN: 978-3-8027-8918-2
- Band 101 Fuß, M.: Entwicklung eines Verfahrens zur Herstellung von tiefen nicht kreisförmigen Bohrungen. Dissertation, Universität Dortmund, Vulkan Verlag, Essen, 2019, ISBN: 978-3-8027-8917-5
- Band 100 Metzger, M.: Innenkonturieren und Walzen tiefgebohrter Grundbohrungen. Dissertation, Universität Dortmund, Vulkan Verlag, Essen, 2019, ISBN: 978-3-8027-8916-8
- Band 99 Aßmuth, R.: Schneidkantenpräparation durch Druckluft- Nassstrahlspanen mit Industrierobotern. Dissertation, Universität Dortmund, Vulkan Verlag, Essen, 2019, ISBN: 978-3-8027-8915-1

- Band 98 Wolf, M.: Abstimmung der Präparationsprozesse in der Herstellungskette von PVD-beschichteten Vollhartmetall-Wendelbohrern. Dissertation, Universität Dortmund, Vulkan Verlag, Essen, 2019, ISBN: 978-3-8027- 8913-7
- Band 97 Freiburg, D.: Hochvorschubfräsen zur Strukturierung von Werkzeugoberflächen für die Blechmassivumformung. Dissertation, Universität Dortmund, Vulkan Verlag, Essen, 2019, ISBN 978-3802789120
- Band 96 Tiffe, M.: Charakterisierung grundlegender Mechanismen für die Simulation der Spanbildung mithilfe der FEM. Dissertation, Universität Dortmund, Vulkan Verlag, Essen, 2018, ISBN 978-3-8027-8911-3
- Band 95 Schumann, S.: Mehrskalige Modellierung und Simulation des Hochleistungs-Innenrundschälenschleifens. Dissertation, Universität Dortmund, Vulkan Verlag, Essen, 2019, ISBN: 978-3-8027-8914-4
- Band 94 Böhmer, J.: Untersuchung und Simulation des Randschichtverhaltens inhomogener Spritzstrukturen beim Honen. Dissertation, Universität Dortmund, Vulkan Verlag, Essen, 2018, ISBN 978-3-8027-8799-7
- Band 93 Hense, R.: Simulation und Optimierung der Fräsbearbeitung von Turbinenschaufeln. Dissertation, Universität Dortmund, Vulkan Verlag, Essen, 2018, ISBN 978-3-8027-8798-0
- Band 92 Krebs, E.: Simulationsgestützte Mikrofräsbearbeitung gehärteter Werkzeugstähle zur Herstellung filigraner Formelemente und funktionaler Oberflächenstrukturen. Dissertation, Universität Dortmund, Vulkan Verlag, Essen, 2017, ISBN 978-3-8027-8797-3
- Band 91 Habermeier, J.: Technologische Untersuchungen der Bearbeitung nickelreduzierter Stahlgusslegierungen für Turbinengehäuse. Dissertation, Universität Dortmund, Vulkan Verlag, Essen, 2017, ISBN 978-3-8027- 8796-6
- Band 90 Liu, Y.: Technologische Untersuchungen zum flexiblen Einsatz des Fließbohrers. Dissertation, Universität Dortmund, Vulkan Verlag, Essen, 2017, ISBN 978-3-8027-8795-9
- Band 89 Özkaya, E.: FEM-based software system for the efficient 3D tapping simulation and tool optimization using CFD simulation. Dissertation, Universität Dortmund, Vulkan Verlag, Essen, 2016, ISBN 978-3-8027- 8793-5
- Band 88 Abrahams, A.: Untersuchungen zum Führungsleistenverschleiß und zur Prozessdynamik beim BTA-Tiefbohren austenitischer Stähle. Dissertation, Universität Dortmund, Vulkan Verlag, Essen, 2016, ISBN 978-3-8027-8792-8
- Band 87 Kirschner, M.: Tiefbohren von hochfesten und schwer zerspanbaren Werkstoffen mit kleinsten Durchmessern. Dissertation, Universität Dortmund, Vulkan Verlag, Essen, 2016, ISBN 978-3-8027-8791-1
- Band 86 Goeke, S.: Oberflächenstrukturierung tribologisch beanspruchter Funktionsflächen durch Microfinishes Dissertation, Universität Dortmund, Vulkan Verlag, Essen, 2016, ISBN 978-3-8027-8790-4
- Band 85 Iovkov, I.: Technologische Analyse des Tiefbohrers mit Minimalmengenschmierung und simulationsbasierte Kompensation des Mittenverlaufs. Dissertation, Universität Dortmund, Vulkan Verlag, Essen, 2016, ISBN 978-3-8027-8787-4
- Band 84 Rautert, C.: Untersuchungen zum Bohrschleifen faserverstärkter Werkstoffe. Dissertation, Universität Dortmund, Vulkan Verlag, Essen, 2016, ISBN 978-3-8027-8789-8

- Band 83 Hartmann, H.: Analyse der Außenlängsdreh- und Einlippentiefbohrbearbeitung hochfester bainitischer und vergüteter Stähle. Dissertation, Universität Dortmund, Vulkan Verlag, Essen, 2016, ISBN 978-3-8027- 8788-1
- Band 82 Rausch, S.: Modellgestützte Endbearbeitung hartstoffbeschichteter Tiefziehwerkzeuge. Dissertation, Universität Dortmund, Vulkan Verlag, Essen, 2016, ISBN 978-3-8027-8785-0
- Band 81 Beer, N.: Systematische Untersuchung von Vollhartmetall- Wendelbohrern zum Bearbeiten von Inconel 718 . Dissertation, Universität Dortmund, Vulkan Verlag, Essen, 2016, ISBN 978-3-8027-8784-3
- Band 79 Steiner, M.: Grundlagenuntersuchungen zur Mikrofräsbearbeitung des austenitischen Edelstahl X5CrNi18-10. Dissertation, Universität Dortmund, Vulkan Verlag, Essen, 2015, ISBN 978-3-8027-8783-6
- Band 78 Bleckmann, T.: Simulationsbasierte Auslegung von Fräsprozessen für die Großserienfertigung. Dissertation, Universität Dortmund, Vulkan Verlag, Essen, 2015, ISBN 978-3-8027-8781-2
- Band 77 Heymann, T.: Schleifen und Polierschleifen von wendelförmigen Spannuten an Vollhartmetallbohrwerkzeugen. Dissertation, Technische Universität Dortmund, Vulkan Verlag, Essen, 2015, ISBN 978-3-8027-8778-2
- Band 76 Ungemach, E.: Simulationsbasierte Adaption von NC-Fräsprogrammen zur Vermeidung von Ratterschwingungen. Dissertation, Universität Dortmund, Vulkan Verlag, Essen, 2015, ISBN 978-3-8027-8780-5
- Band 75 Upmeier, T.: Einlippentiefbohren teilkristalliner thermoplastischer Kunststoffe. Dissertation, Technische Universität Dortmund, Vulkan Verlag, Essen, 2015, ISBN 978-3-8027-8782-9
- Band 74 Peuker, A.: Werkzeugentwicklung für die Transplantation thermisch gespritzter mikrostrukturierter Funktionsschichten auf Druckgusswerk- stücke. Dissertation, Technische Universität Dortmund, Vulkan Verlag, Essen, 2015, ISBN 978-3-8027-8779-9
- Band 73 Schlenker, J.: Spanende Mikrobearbeitung von Titan und Titanlegierungen. Dissertation, Technische Universität Dortmund, Vulkan Verlag, Essen, 2015, ISBN 978-3-8027-8777-5
- Band 72 Zhang, L. J.: Untersuchungen zum Drehen und Bohren der Nickelbasislegierung Inconel 718. Dissertation, Technische Universität Dortmund, Vulkan Verlag, Essen, 2014, ISBN 978-3-8027-8776-8
- Band 71 Wagner, T.: Planning and Multi-Objective Optimization of Manufacturing Processes by Means of Empirical Surrogate Models. Dissertation, Technische Universität Dortmund, Vulkan Verlag, Essen, 2013, ISBN 978-3-8027-8775-1
- Band 70 Sacharow, A.: Kompensation von Formabweichungen durch adaptive Freiformdeformation der CAD/CAM-Daten. Dissertation, Technische Universität Dortmund, Vulkan Verlag, Essen, 2013, ISBN 978-3-8027- 8774-4
- Band 69 Baschin, A.: Analyse und Simulation der Prozessdynamik und -stabilität beim NC-Mikrofräsen. Dissertation, Technische Universität Dortmund, Vulkan Verlag, Essen, 2012, ISBN 978-3-8027-8773-7
- Band 68 Feldhoff, M.: Modellgestützte Werkzeug- und Prozessentwicklung des Bohrschleifens faserverstärkter Duromere. Dissertation, Technische Universität Dortmund, Vulkan Verlag, Essen, 2012, ISBN 978-3-8027- 8771-3

- Band 67 Machai, C.: Grundlagenuntersuchung zur Zerspanung von β - Titanlegierungen unterschiedlicher Mikrostruktur. Dissertation, Technische Universität Dortmund, Vulkan Verlag, Essen, 2012, ISBN 978-3- 8027-8772-0
- Band 66 Heilmann, M.: Tiefbohren mit kleinen Durchmessern durch mechanische und thermische Verfahren – Prozessgestaltung und Verfahrenskombination. Dissertation, Technische Universität Dortmund, Vulkan Verlag, Essen, 2012, ISBN 978-3-8027-8770-6
- Band 65 Scheidler, A. V.: Simulation des NC-Formschleifprozesses mit unterschiedlichen CBN-Schleifscheibenformen. Dissertation, Technische Universität Dortmund, Vulkan Verlag, Essen, 2012, ISBN 978-3-8027- 8768-3
- Band 64 Pantke, K.: Entwicklung und Einsatz eines temperatursensorischen Beschichtungssystems für Zerspanwerkzeuge. Dissertation, Technische Universität Dortmund, Vulkan Verlag, Essen, 2012, ISBN 978-3-8027- 8769-0
- Band 63 Terwey, I.: Steigerung der Leistungsfähigkeit von Vollhartmetallwendelbohrern durch Strahlspanen. Dissertation, Technische Universität Dortmund, Vulkan Verlag, Essen, 2011, ISBN 978-3-8027-8766-9
- Band 62 Würz, E.: Schleifbearbeitung von Keramik-Hartmetall-Verbunden. Dis- sertation, Technische Universität Dortmund, Vulkan Verlag, Essen, 2011, ISBN 978-3-8027- 8767-6
- Band 61 Engbert, T.: Fließbohrbearbeitung und Innengewinfertigung an Leichtbaustrukturen. Dissertation, Technische Universität Dortmund, Vulkan Verlag, Essen, 2011, ISBN 978-3-8027-8764-5
- Band 60 Felderhoff, J. F.: Prozessgestaltung für das Drehen und Tiefbohren schwefelarmer Edelbaustähle. Dissertation, Technische Universität Dort- mund, Vulkan Verlag, Essen, 2012, ISBN 978-3-8027-8765-2
- Band 59 Kessler, N.: Thermische Mittenverlaufsbeeinflussung beim BTA- Tiefbohren. Dissertation, Technische Universität Dortmund, Vulkan Verlag, Essen, 2011, ISBN 978-3-8027-8763-8
- Band 58 Paffrath, K.-U.: Untersuchungen zum kraftgeregelten Langhubhonen auf multifunktionalen Bearbeitungszentren. Dissertation, Technische Universität Dortmund, Vulkan Verlag, Essen, 2011, ISBN 978-3-8027- 8762-1
- Band 57 Faraz, A.: Experimental Study On Delamination, Mechanical Loads and Tool Wear in Drilling of Woven Composite Laminates. Dissertation, Technische Universität Dortmund, Vulkan Verlag, Essen, 2011, ISBN 978-3-8027-8761-4
- Band 56 Hossam, M.: Chatter Occurrence at Different Natural Frequencies of Milling Machine Axes. Dissertation, Technische Universität Dortmund, Vulkan Verlag, Essen, 2011, ISBN 978-3-8027-8759-1
- Band 55 Kersting, P.: Simulation und Analyse regenerativer Werkstückschwin- gungen bei der NC-Fräsbearbeitung von Freiformflächen. Dissertation, Technische Universität Dortmund, Vulkan Verlag, Essen, 2011, ISBN 978-3-8027-8757-7
- Band 54 Marschalkowski, K.: Beitrag zur Prozessentwicklung für das Hochleistungsinnenrund-Schälenschleifen mit galvanisch gebundenen CBN-Schleifscheiben. Dissertation, Technische Universität Dortmund, Vulkan Verlag, Essen, 2011, ISBN 978-3-8027-8758-4
- Band 53 Weckerle, T.: Konzeption und Entwicklung einer standardisierten Datenübertragung von Schleifoperationen für Werkzeugschleifmaschinen. Dissertation, Technische Universität Dortmund, Vulkan Verlag, Essen, 2010, ISBN 978-3-8027-8756-0

- Band 52 Kahleyß, F.: Grundlagenuntersuchungen und simulationsbasierte Optimierung zur fünffachsignen Mikrofräsbearbeitung von NiTi- Formgedächtnislegierungen. Dissertation, Technische Universität Dortmund, Vulkan Verlag, Essen, 2010, ISBN 978-3-8027-8753-9
- Band 51 Mohn, T.: Schleifen thermisch gespritzter Verschleißschutzschichten auf Bearbeitungszentren – Prozessgestaltung und Simulation. Dissertation Technische Universität Dortmund, Vulkan Verlag, Essen, 2010, ISBN 978-3-8027-8751-5
- Band 49 Rautenberg, J.: Simultane fünffachsigne Fräsbearbeitung von Aluminiumstrukturbauteilen. Dissertation Technische Universität Dortmund, Vulkan Verlag, Essen, 2010, ISBN 978-3-8027-8754-6
- Band 48 Enk, D.: Untersuchungen zum dynamischen Stabilitätsverhalten von Fräsworkzeugen zur HSC-Bearbeitung. Dissertation Technische Universität Dortmund, Vulkan Verlag, Essen, 2009, ISBN 978-3-8027-8748-5
- Band 47 Kersting, M.: Entwicklung und Anwendung eines adaptiven Schwingungsdämpfers für das Einlippentiefbohren. Dissertation, Technische Universität Dortmund, Vulkan Verlag, Essen, 2009, ISBN 978-3-8027- 8749-2
- Band 46 Bergmann, S.: Beitrag zur Zerspanung intermetallischer γ - Titanaluminide durch Bohren, Gewindebohren und Fräsen. Dissertation Technische Universität Dortmund, Vulkan Verlag, Essen, 2009, ISBN 978-3-8027-8746-1
- Band 45 Kahnis, P.: Analyse von Größeneinflüssen bei einer Herabskalierung des Fräsprozesses in den Mikrobereich. Dissertation Technische Universität Dortmund, Vulkan Verlag, Essen, 2008, ISBN 978-3-8027-8745-4
- Band 44 Noyen, M.: Analyse der mechanischen Belastungsverteilung in der Kontaktzone beim Längs-Umfangs-Planschleifen. Dissertation Technische Universität Dortmund, Vulkan Verlag, Essen, 2008, ISBN 978-3-8027- 8744-7
- Band 43 Jansen, T.: Entwicklung einer Simulation für den NC-Formschleifprozess mit Torusschleifscheiben. Dissertation Technische Universität Dortmund, Vulkan Verlag, Essen, 2007, ISBN 978-3-8027-8743-0
- Band 42 Hammer, N.: Spanende Bearbeitung endlos stahlverstärkter Aluminiummatrixstrangpressprofile. Dissertation Universität Dortmund, Vulkan Verlag, Essen, 2007, ISBN 978-3-8027-8742-3
- Band 41 Kress, J.: Auswahl und Einsatz von polykristallinem kubischem Bornitrid beim Drehen, Fräsen und Reiben. Dissertation Universität Dortmund, Vulkan Verlag, Essen, 2007, ISBN 978-3-8027-8741-6
- Band 40 Wittkop, S.: Einlippentiefbohren nichtrostender Stähle. Dissertation Universität Dortmund, Vulkan Verlag, Essen, 2007, ISBN 978-3-8027- 8740-9
- Band 39 Webber, O.: Untersuchungen zur bohrtiefenabhängigen Prozessdynamik beim BTA-Tiefbohren. Dissertation Universität Dortmund, Vulkan Verlag, Essen, 2007, ISBN 978-3-8027-8739-3
- Band 38 Zhang, L.: Accuracy Enhancement of a Hexapod Machine Tool. Dissertation Universität Dortmund, Vulkan Verlag, Essen, 2007, ISBN 978-3-8027-8738-6
- Band 37 Petzoldt, V.: Formgedächtnistechnik – Tiefbohren und Mikrofräsen von NiTi. Dissertation Universität Dortmund, Vulkan Verlag, Essen, 2006, ISBN 3-8027-8737-4, 978-3-8027-8737-9
- Band 36 Kötter, D.: Herstellung von Schneidkantenverrundungen und deren Einfluss auf das Einsatzverhalten von Zerspanwerkzeugen. Dissertation Universität Dortmund, Vulkan Verlag, Essen, 2006, ISBN 3-8027-8736- 6, 978-3-8027-8736-2

- Band 35 Hesterberg, S.: Trockenbearbeitung nichtrostender Stähle - Prozess- gestaltung für das Drehen und Bohren mit Wendeschneidplatten. Dis- sertation Universität Dortmund, Vulkan Verlag, Essen, 2006, ISBN 3-8027-8735-8, 978-3-8027-8735-5
- Band 34 Damm, P.: Rechnergestützte Optimierung des 5-Achsen- Simultanfräsens von Freiformflächen. Dissertation Universität Dortmund, Vulkan Verlag, Essen, 2006, ISBN 3-8027-8734-X, 978-3- 8027-8734-8
- Band 33 Surmann, T.: Geometrisch-physikalische Simulation der Prozessdynamik für das fünfachsige Fräsen von Freiformflächen. Dissertation Universität Dortmund, Vulkan Verlag, Essen, 2006, ISBN 3-8027-8733-1, 978-3-8027-8733-1
- Band 32 Stautner, M.: Simulation und Optimierung der mehrachsigen Fräsbearbeitung. Dissertation Universität Dortmund, Vulkan Verlag, Essen, 2006, ISBN 3-8027-8732-3, 978-3-8027-8732-4
- Band 31 Peters, C.: Herstellung und Einsatzverhalten von Keramik-Hartmetall- Verbundbohrwerkzeugen. Dissertation Universität Dortmund, Vulkan Verlag, Essen, 2006, ISBN 3-8027-8731-5, ISBN 978-3-8027-8731-7
- Band 30 Hagedorn, M.: Herstellung von Verbundbauteilen durch Einwalzen - Verfahrensentwicklung und experimentelle Grundlagen. Dissertation Universität Dortmund, Vulkan Verlag, Essen, 2006, ISBN 3-8027-8730- 7, ISBN 978-3-8027-8730-0
- Band 29 Kalveram, M.: Analyse und Vorhersage der Prozessdynamik und Pro- zessstabilität beim Hochgeschwindigkeitsfräsen. Dissertation Universität Dortmund, Vulkan Verlag, Essen, 2005, ISBN 3-8027-8729-3, 978-3-8027-8729-4
- Band 28 Koehler, W.: Analyse des Einflusses der Schneidenform auf den Hoch- leistungsbohrprozess. Dissertation Universität Dortmund, Vulkan Verlag, Essen, 2004, ISBN 3-8027-8728-5
- Band 27 Loichinger, A.: Analyse und Optimierung der Kühlschmierstoffversor- gung rotierender Werkzeuge. Dissertation Universität Dortmund, Vulkan Verlag, Essen, 2004, ISBN 3-8027-8726-9
- Band 26 Du, S.: Simulation and Tool Path Optimization for the Hexapod Milling Machine. Dissertation Universität Dortmund, Vulkan Verlag, Essen, 2004, ISBN 3-8027-8726-9
- Band 25 Schulte, M.: Profilschleifen von Hartlegierungen und Hartverbund- werkstoffen mit konventionellen Schleifmitteln. Dissertation Universität Dortmund, Vulkan Verlag, Essen, 2004, ISBN 3-8027-8725-0
- Band 24 Lange, M.: Prozessgestaltung bei der spanenden Bearbeitung von kurzfaserverstärkten Magnesiumlegierungen. Dissertation, Universität Dortmund, Vulkan Verlag, Essen, 2003, ISBN 3-8027-8724-2
- Band 23 Guntermann, G.: Aspekte des Hochgeschwindigkeits-Hartfräsens im Werkzeug- und Formenbau. Dissertation, Universität Dortmund, Vulkan Verlag, Essen, 2004, ISBN 3-8027-8723-4
- Band 22 Johlen, G.: Prozessoptimierung für die Hartfeinbearbeitung durch die Kombination von Hartdrehen und Schleifen. Dissertation, Universität Dortmund, Vulkan Verlag, Essen, 2003, ISBN 3-8027-8722-6
- Band 21 Schwietering, C.: Technologische Aspekte der mikromechanischen Fräs- bearbeitung mit Schaftwerkzeugen. Dissertation, Universität Dortmund, Vulkan Verlag, Essen, 2003, ISBN 3-8027-8721-8

- Band 20 Zabel, A.: Simulationsgestützte Vorhersage des Verschleißverhaltens von Fräswerkzeugen beim Fräsen von Freiformflächen. Dissertation, Universität Dortmund, Vulkan Verlag, Essen, 2003, ISBN 3-8027-8720X
- Band 19 Opalla, D.: Hochleistungsbohren metallischer Werkstoffe mit Wendelbohrern. Dissertation, Universität Dortmund, Vulkan Verlag, Essen, 2003, ISBN 3-8027-8716-1
- Band 18 Löbbe, H.: Tiefbohren auf Bearbeitungszentren. Dissertation, Universität Dortmund, Vulkan Verlag, Essen, 2003, ISBN 3-8027-8718-8
- Band 17 Finke, M.: Untersuchungen zur Auslegung und Optimierung des Innenrund-Längsschleifens von Futterteilen. Dissertation, Universität Dortmund, Vulkan Verlag, Essen, 2003, ISBN 3-8027-8717-X
- Band 16 Liedschulte, M.: Untersuchungen zum Bohren von Magnesiummatrix-Verbundwerkstoffen. Dissertation, Universität Dortmund, Vulkan Verlag, Essen, 2003, ISBN 3-8027-8719-6
- Band 15 Buschka, M.: Formgedächtnistechnik - Prozessgestaltung beim Drehen und Bohren von NiTi-Formgedächtnislegierungen. Dissertation, Universität Dortmund, Vulkan Verlag, Essen, 2002, ISBN 3-8027-8715-3
- Band 14 Meng, J.: Freiformflächenmanipulation für den Werkzeug-, Formen- und Modellbau. Dissertation, Universität Dortmund, Vulkan Verlag, Essen, 2001, ISBN 3-8027-8714-5
- Band 13 Bruchhaus, T.: Tribologische Untersuchungen zur Optimierung von BTA-Tiefbohrwerkzeugen. Dissertation, Universität Dortmund, Vulkan Verlag, Essen, 2001, ISBN 3-8027-8713-7
- Band 12 Mehnen, J.: Evolutionäre Flächenrekonstruktion. Dissertation, Universität Dortmund, Vulkan Verlag, Essen, 2000, ISBN 3-8027-8712-9
- Band 11 Schulte, K.: Stahlbearbeitung mit Wendeschneidplatten-Bohrern bei reduzierten Kühlschmierstoffeinsatz. Dissertation, Universität Dortmund, Vulkan Verlag, Essen, 2000, ISBN 3-8027-8710-2
- Band 10 Schroer, M.: Reiben von Vergütungsstahl mit Einschneiden-Reibahlen. Dissertation, Universität Dortmund, Vulkan Verlag, Essen, 2000, ISBN 3-8027-8711-0
- Band 9 Schneider, M.: Auswirkungen thermomechanischer Vorgänge beim Werkzeugschleifen. Dissertation, Universität Dortmund, Vulkan Verlag, Essen, 1999, ISBN 3-8027-8708-0
- Band 8 Albersmann, F.: Simulationsgestützte Prozessoptimierungen für die HSC-Fräsbearbeitung. Dissertation, Universität Dortmund, Vulkan Verlag, Essen, 1999, ISBN 3-8027-8709-9
- Band 7 Mumm, A.: Analyse und Gestaltung von Werkzeugversorgungssystemen in der spanenden Fertigung. Dissertation, Universität Dortmund, Vulkan Verlag, Essen, 1999, ISBN 3-8027-8705-6
- Band 6 Gillmeister, F.: Passive und aktive sekundäre Maßnahmen zur Reduzierung der Hand-Arm-Schwingungsbelastung. Dissertation, Universität Dortmund, Vulkan Verlag, Essen, 1999, ISBN 3-8027-8706-4
- Band 5 Thamke, D.: Technologische und ökonomische Aspekte der Trocken- und Minimalmengenbearbeitung am Beispiel des Einlippentiefbohrrens. Dissertation, Universität Dortmund, Vulkan Verlag, Essen, 1999, ISBN: 3-8027-8707-2
- Band 4 Enselmann, A.: HSC-Hartfräsen von Formen und Gesenken. Dissertation, Universität Dortmund, Vulkan Verlag, Essen, 1999, ISBN 3-8027-8703- X

- Band 3 Willsch, Ch.: Außenrund-Einsteichschleifen von Cermet. Dissertation, Universität Dortmund, Vulkan Verlag, Essen, 1998, ISBN 3-8027-8702-1
- Band 2 Friedhoff, J.: Aufbereitung von 3D-Digitalisierdaten für den Werkzeug-, Formen- und Modellbau. Dissertation, Universität Dortmund, Vulkan Verlag, Essen, 1997, ISBN 3-8027-8701-3
- Band 1 Adams, F.-J.: Einsatzverhalten von symmetrischen, hartmetallbestückten Kurzlochbohrern. Dissertation, Universität Dortmund, Vulkan Verlag, Essen, 1996, ISBN 3-8027-8700-5